Benchmarking of SSB, reference cells and optimization of the cathode composite

Dem Fachbereich Biologie und Chemie
der Justus-Liebig-Universität Giessen

vorgelegte
Dissertation
zur Erlangung des akademischen Grades

Doktor der Naturwissenschaften
− Dr. rer. nat. −

von
Simon Randau

Giessen, März 2021

Dekan / Dean	Prof. Dr. Jürgen Janek
1. Gutachter / 1st Reviewer	Prof. Dr. Jürgen Janek (Justus-Liebig-Universität Giessen)
2. Gutachter / 2nd Reviewer	Prof. Dr. Bernd Smarsly (Justus-Liebig-Universität Giessen)

Danksagung

Ein besonderer Dank gilt Prof. Dr. Jürgen Janek für die Betreuung während meiner Promotionszeit und für die Möglichkeit, auf diesem spannenden Thema die Promotion durchzuführen. In vielen Diskussionen und Gesprächen hat er geholfen, Ziele und Herausforderungen zu erkennen. Diese Unterstützung trug maßgeblich zum Erfolg dieser Promotion bei.

Für die Übernahme des Koreferats dieser Arbeit danke ich Prof. Dr. Bernd Smarsly. Prof. Dr. Siegfried Schindler und Prof. Dr. Richard Göttlich danke ich für die Zusage, Teil der Prüfungskommission zu sein.

Ganz besonders danke ich Dr. Dominik A. Weber, der mich in meinem ersten Jahr der Promotion betreut hat. Bei fachlichen, sowie persönlichen Anliegen fühlte ich mich immer bestens aufgehoben. Die gemeinsamen Diskussionen empfand ich stets als besonders ergiebig und äußerst angenehm. Durch diese wurde im Speziellen mein Blick auf eine vollumfängliche Betrachtung der Fragestellungen geschult.

Nach Dr. Dominik A. Weber folgte Dr. Felix H. Richter als Betreuer. Seine Expertise und sein Blick auf die Feinheiten und Details der jeweiligen Fragestellung halfen maßgeblich bei der erfolgreichen Durchführung der Promotion. Sein umfangreiches und direktes Feedback zu wissenschaftlichen Texten hat diese immer auf eine besondere Weise komplementiert.

Den Kollegen in der Arbeitsgruppe von Prof. Dr. Janek danke ich für die familiäre Arbeitsatmosphäre. Nicht nur im Labor sondern auch in Kaffeepausen, während dem Sport und vielen Freizeitaktivitäten habe ich hier nicht nur Kollegen, sondern auch Freunde gefunden. Ein besonderes Dankeschön gilt dabei Bianca Helm, Justine Ruhl, Luise Riegger, Philip Minnmann, Florian Lotz, Florian Ritz, Christoper Gawlig, Fabian Simon, Adrian Schürmann, Raika Oppermann und Kathrin Michel.

Mein größter Dank gilt meiner Familie, meinem Vater Hermann-Josef, meiner Mutter Gabriele und meinem Onkel Reinhard, die mich stets unterstützt haben, meine Träume, Wünsche und Ziele zu verfolgen und zu erreichen. Durch ihre Geduld und aufbauenden Worte haben sie mich immer unterstützt und motiviert.

Eidesstattliche Erklärung

Die vorliegende Arbeit wurde im Zeitraum vom 01.05.2016 bis 31.10.2020 am Physikalisch-Chemischen Institut der Justus-Liebig-Universität Gießen unter Betreuung von Prof. Dr. Jürgen Janek angefertigt.

Ich erkläre: Ich habe die vorgelegte Dissertation selbstständig und ohne unerlaubte fremde Hilfe und nur mit den Hilfen angefertigt, die ich in der Dissertation angegeben habe. Alle Textstellen, die wörtlich oder sinngemäß aus veröffentlichten Schriften entnommen sind, und alle Angaben, die auf mündlichen Auskünften beruhen, sind als solche kenntlich gemacht. Ich stimme einer evtl. Überprüfung meiner Dissertation durch eine Antiplagiat-Software zu. Bei den von mir durchgeführten und in der Dissertation erwähnten Untersuchungen habe ich die Grundsätze guter wissenschaftlicher Praxis, wie sie in der „Satzung der Justus-Liebig-Universität Gießen zur Sicherung guter wissenschaftlicher Praxis“ niedergelegt sind, eingehalten.

Giessen, 01.03.2021

Simon Randau

Abstract

Due to their potentially higher energy and power density, lower influence of the ambient temperature (freezing of liquid electrolyte) and higher safety compared to liquid electrolyte based lithium ion batteries, solid electrolyte based lithium batteries are gaining more and more interest. A variety of anode concepts, solid electrolytes and cathode concepts have been developed. All battery characteristics, such as energy and power density, cycle stability, but also the chemical stability between the materials can be influenced by a wide variety of combinations. Additionally, it may be necessary to use further additives or protection concepts.

The first goal of this dissertation was to make a comprehensive comparison of the current literature and to put it into context with own battery data as a reference. This was necessary because results are sometimes not classified in the existing literature, no reference is added or no consistent data on masses and manufacturing methods are given. With this first work it was possible to draw in-depth conclusions about the minimal information needed for reproduction, but also to make recommendations for future research goals. Furthermore, an application for the calculation of battery performance was designed, where the calculations are based on minimal information. In the evaluation of the literature it was found that in the majority of publications carbon additives are used in the cathode composites. In the second publication, the focus was on the optimization of battery performance using carbon additives and the influence of their carbon morphology and surface. Cycling experiments and microstructure-resolved simulations show that with fibrous carbons a higher utilization of the cathode active material can be achieved. However, carbon additives lead to an increased capacity loss due to the decomposition of the solid electrolyte. The latter was investigated in more detail by means of cyclovoltammetry, X-ray photoelectron spectroscopy and cyclization experiments. The degree of degradation is directly related to the carbon morphology and surface. To prevent the reactions caused by the use of carbon additives, a protective concept was developed and tested.

The results of this dissertation form the context for a comprehensive comparison of different cell concepts. The basic parameters are presented and discussed. Thus, the current state of the art in the field of solid-state batteries is summarized and evaluated. Recommendations and goals for a successful further development of solid-state batteries can be derived from this thesis. In the second part of the thesis such an optimization was carried out. The positive influence of carbon additives was examined more closely and the existing decomposition was reduced by a novel protection concept.

Zusammenfassung

Aufgrund ihrer potentiell höheren Energie- und Leistungsdichte, dem geringerem Einfluss der Umgebungstemperatur (Gefrieren des Flüssigelektrolyten) und höherer Sicherheit im Vergleich zu flüssigelektrolytbasierten Lithiumionenbatterien gewinnen festelektrolytbasierte Lithium-Batterien zunehmend an Bedeutung. Es haben sich eine Vielzahl von Anodenkonzepten, Festelektrolyten und Kathodenkonzepten entwickelt. Über die verschiedensten Kombinationen können alle Kenngrößen der Batterie, wie die Energie- und Leistungsdichte, Zyklenstabilität, aber auch die chemische Stabilität zwischen den Materialien beeinflusst werden. Zusätzlich kann es nötig sein, weiter Additive oder Schutzkonzepte einzusetzen.

Das erste Ziel dieser Dissertation war es, einen umfassenden Vergleich der aktuellen Literatur durchzuführen und diese mit eigenen Batteriedaten als Referenz in Kontext zu bringen. Dies war nötig, da in der Literatur Ergebnisse teilweise nicht in die vorhandene Literatur eingeordnet werden, keine Referenz beigefügt oder keine konsistenten Angaben zu Massen und Herstellungsmethoden gemacht werden. Mittels dieser ersten Arbeit konnten tiefgreifende Rückschlüsse auf die minimal nötigen Informationen für eine Reproduktion, aber auch Empfehlungen für zukünftige Forschungsziele getroffen werden. Weiterhin wurde eine Anwendung zur Berechnung der Batterieleistung entworfen, bei der die Berechnungen mittels minimaler Angaben erfolgt. Bei der Auswertung der Literatur wurde festgestellt, dass in der Mehrzahl der Publikationen Kohlenstoffadditive in den Kathodenkompositen verwendet werden. In der zweiten Veröffentlichung lag der Schwerpunkt auf der Optimierung der Batterieleistung mittels Kohlenstoffadditiven und dem Einfluss der Kohlenstoffmorphologie und Oberfläche auf Diese. Zyklisierungsversuche und mikrostrukturaufgelöste Simulationen zeigten, dass mit faserförmigen Kohlenstoffen eine höhere Ausnutzung des Kathodenaktivmaterials erreicht werden kann. Allerdings führen Kohlenstoffadditive zu einem erhöhten Kapazitätsverlust aufgrund der Zersetzung des Festelektrolyten. Letzteres wurde mit Hilfe der Zyklovoltammetrie, der Röntgen-Photoelektronenspektroskopie und von Zyklisierungsversuchen näher untersucht. Der Grad der Abreaktion steht dabei im direkten Zusammenhang mit der Kohlenstoffmorphologie und Oberfläche. Um die durch die Verwendung von Kohlenstoffadditiven verursachten Reaktionen zu unterbinden, wurde ein Schutzkonzept entwickelt und getestet.

Die Ergebnisse dieser Dissertation bilden den Kontext für einen umfassenden Vergleich verschiedener Batteriekonzepte. Die grundlegenden Parameter werden vorgestellt und diskutiert. So wird der aktuelle Stand der Technik im Bereich der Feststoffbatterien zusammengefasst und bewertet. Aus dieser Arbeit können Empfehlungen und Ziele für eine erfolgreiche Weiterentwicklung von Feststoffbatterien abgeleitet werden. Im zweiten Teil der Arbeit wurde eine solche Optimierung durchgeführt. Der positive Einfluss von Kohlenstoffadditiven wurde näher untersucht und die bestehende Zersetzung durch ein neuartiges Schutzkonzept reduziert.

List of Abbreviations

CAM	cathode active material
AAM	anode active material
SE	solid electrolyte
SSB	solid-state battery
LIB	lithium-ion battery
SEI	solid electrolyte interface
BEV	battery electric vehicle
VGCF	vapor grown carbon fibers
XPS	X-ray photoelectron spectroscopy
ToF-SIMS	time-of-flight secondary ion mass spectrometry
SEM	scanning electron microscope

Table of Contents

1 Introduction

1.1 Motivation

In recent years, the awareness increased that the use of non-renewable goods must be reduced and that the climate on our planet must be treated more carefully. Especially, in the last 40 years, carbon-based energy production resulted in an explicit increase of atmospheric carbon dioxide.[1,2] This results in a transformation from a purely consumerist society to a modern society that is conscious of the available resources and aware of their limitations. Social developments, such as the desire for a rapid exit from energy production using coal and nuclear power, the desire to base future mobility on electric vehicles or the efforts to develop new climate goals illustrate the rise of this new awareness.[3] Considering this transformation, the development of new ideas for energy supply is an important step.

Renewable resources such as wind, water and solar energy must be used more intensively.[3] The greatest challenge in using these energy sources is to be able to balance the natural fluctuations in their availability. In addition to the optimization of other aspects in the modern energy supply chain, such as production processes or the transport of energy, a new field will establish itself in this system, namely energy storage. Centralized or decentralized energy storage enables the compensation of production fluctuations. Storage of the produced energy is possible with rechargeable battery systems. In order to be able to use battery electric vehicles (BEV) – vehicles with internal combustion engine are responsible for 20 % of global CO_2 emissions[4] - modern and rechargeable battery systems are necessary, specially adapted to the requirements in the area of mobility.[5]

The financial funding of BEVs and increased use of renewable energies leads to a significant grow in demand for current state-of-the-art lithium-ion batteries (LIBs).[6] For many companies, battery manufacturing is a core competence and should be developed and produced in-house. This also enables the possibility of specific designs for the respective requirements and ensures a stable supply.[7] In particular, power and energy density are key parameters for batteries in the automotive sector. The power density enables fast battery charging, while high energy densities enable long range of vehicles and compact design of batteries. Since 1991 the energy density of liquid electrolyte-based LIBs increased by a factor of four. But a physicochemical limit will soon be reached.[8] This is manly defined by the limited capacity of the graphite electrode (372 $mAh \cdot g^{-1}$). Therefore, lithium metal with a superior capacity of 3860 $mAh \cdot g^{-1}$ attracts increasing attention as anode material.

In the case of liquid electrolyte systems, inhomogeneous lithium deposition and dissolution during charge and discharge can lead to lithium dendrite formation. These grow through the electrolyte, as soon as they reach the cathode side, self-discharge along the dendrite occurs, resulting in heat formation and in a possible ignition of the liquid organic electrolyte.[7] Due to these safety concerns "beyond LIB" systems are becoming more attractive for industry and research. These often include a solid electrolyte (SE). The high shear modulus and high Li^+ transference number of SEs potentially prevent the dendrite growth.[9] SEs have transference numbers of around 1 and liquid electrolytes around 0.5. These so-called solid-state batteries (SSB) are promising candidates for future high-energy applications.[8]

The properties of the SE are of particular importance for the success of solid-state batteries. SEs can be classified as solid polymer electrolytes and inorganic SE. Inorganic electrolytes are further divided into oxide-based and thiophosphate-based electrolytes.

For the polymer electrolyte class polyethylene oxide (PEO) is one of the most extensively studied polymers. In the polymer a lithium salt (e.g. Lithium bis(trifluoromethanesulfonyl)imide, LiTFSI) must be solved to achieve the needed ionic conductivity. These electrolytes benefit from low manufacturing costs due to established roll-to-roll processing. The good electrical contact to the adjacent cell components and the stability against lithium metal are positive for the application as well. The ratio of binder, lithium salt and other additives makes the development of these electrolytes very complex. Furthermore, the polymer electrolytes show only low conductivities at room temperature. To obtain sufficient conductivity, batteries must be operated at elevated temperatures (approx. 60 °C).

The class of oxide-based electrolytes is characterized by easy handling in atmosphere and resistance against dendrites, due to a compact composition.[10] LLZO is one of the most popular representatives of these electrolytes. However, sintering of the electrolyte is necessary to obtain the compact composition and to reduce the otherwise too high grain boundary resistances within the electrolyte. Sintering steps are associated with high efforts and costs for the industry. Furthermore, the interfacial resistance to other battery components is usually high, as carbonate impurities are easily formed on the surface.[11]

The class of sulfide electrolytes is currently one of the most likely candidates for industrial application (e.g. Li_3PS_4 and Li_6PS_5Cl). These electrolytes show room temperature conductivities comparable to liquid electrolytes. Their good malleability leads to easy processing and low grain boundary and interfacial resistances. The synthesis is potentially scalable and liquid phase-based syntheses seem to be possible as well. One of the challenges of this material class is clearly the small thermodynamic stability window. This results in the formation of a solid electrolyte interphase (SEI) upon contact with lithium metal. This results in poorly conducting products (e.g. polysulfides, Li_2S, P_2S_5) that reduce battery performance.[12]

However, SEI formation is kinetically inhibited, which enables batteries with good performance data on a laboratory-sized scale. For industrial applications, protection concepts at the lithium metal/SE interface or alternatives to lithium metal will be necessary.

On the cathode side, the SE is combined with a cathode active material (CAM) and possible further additives. Due to the good contact and low porosity during compacting, mainly sulfide-based electrolytes are used. For the active material there is again a wide range of possible materials. The best known are $LiCoO_2$, nickel-rich intercalation materials (e.g. $Li(Ni_xCo_yMn_z)O_2$, NCM), $LiFePO_4$ and high-voltage spinels such as $LiNi_{0.5}Mn_{1.5}O_4$. $LiCoO_2$ and $LiFePO_4$ have too low capacities for solid-state cells with high power and energy densities. Due to the large potential difference between spinels (low chemical potential of lithium) and anode (high chemical potential of lithium), a pronounced degradation results when used with sulfide electrolytes. The nickel-rich intercalation materials are already being used in liquid cells and experience is available. They are known for their high capacities. Successful coating strategies allow further reduction of the occurring reactions with the SE.

The multitude of possible combinations for battery materials and the current focus of research on batteries leads to a very high number of publications in this field. Competitive thinking and also commercial interest result in the fact that the way of publication is not uniform. That could imply that information on masses, volume ratios or manufacturing methods are omitted or not fully reported. Therefore, it is difficult to reproduce results mathematically (e.g. calculation of energy densities) or to reproduce results practically in the laboratory. Additionally, reference data of unmodified systems are missing often. Critical parameters such as power, energy or current density are influenced by many different parameters. Uniform guidelines for publications and understanding the relationships between the individual parameters would be very helpful. A comprehensive evaluation of publications is extremely difficult and is hardly found in the literature. This is the motivation for the first publication of this thesis.

After evaluating the current state of the literature, a single aspect within the solid-state cell can be studied more closely and optimized. It has been found that within the cathode the use of carbon additives can have positive and negative effects. The right ratio between ionic (thiophosphate SE) and electronic (carbon additives) percolation paths is crucial for batteries with high power and energy densities. The second publication of the thesis focuses on this field of research.

1.2 Outline

With the beginning of this thesis project, a main research question was whether the use of a lithium metal anode in combination with a sulfidic electrolyte (β-Li_3PS_4) is possible. Already published studies have shown thermodynamically small stability windows of this SE.[13] Furthermore, the degradation of the SE could be demonstrated by *in-situ* X-ray photoelectron spectroscopy (XPS) studies for a sulfide electrolyte.[12] However, the practical application in an SSB showed acceptable battery performance, which was even comparable to SSBs already using protection concepts. Furthermore, the energy density of such an SSB could be increased to over 100 Wh/L by adapting the cell composition (publication 1). Although the SE decomposes at the anode interface, it is kinetically hindered and enables batteries to be cycled for more than 200 cycles. However, a classification of the experiments carried out in the context of current literature has shown to be difficult. The majority of publications apply already modified battery components. These may be protected CAM, additional protective layers on the anode side or even other anode concepts which do not show instability towards the sulfide electrolyte. Furthermore, it has been found that often not all necessary information for a reproduction is included in the publications. For example, information on the masses used for the separator and the anode are usually missing.

This provides the motivation for the first publication. The performance of current SSB concepts should be compared in broad terms and with a common reference. The reference are the own battery data, since no protection concepts are used. As common battery concepts thiophosphate-, oxide-, phosphate- and polymer- based SSB are compared. To allow a quick comparison, the performance parameters are calculated from fundamental equations. Due to the extensive comparison of the publications, many conclusions could be drawn about the complex relationships between the parameters, the minimum necessary information for a reasonable reproduction of data and recommendations for future research goals. Additionally, a benchmarking tool is created which allows the calculation of the performance parameters for batteries out of the fundamental equations and parameters. The performance evaluation, classification and optimization of SSBs is a central part of this thesis.

During the evaluation of the literature, it was noticed that in the majority of the publications carbon additives are used in the cathode composites. However, publications have shown that carbon additives can have negative effects on battery performance due to induced redox activity of the SE.[14–16] At the same time, there are also publications that prove a positive influence of carbon in the cathode, based on the high electronic conductivity of the carbon additives.[17,18] After the first publication the focus is on optimizing the battery performance. Since the influence of carbon additives is not yet known in detail, this is part of the further research for this thesis.

Therefore, in a first joint work with Felix Walther, the influence of one carbon species was considered separately.[19] Batteries with this carbon additive showed increased long term fading of the capacity, suggesting a degradation mechanism to be present. In this work, the focus is on the analysis of this mechanism. The mechanism could be elucidated by depth profile XPS and time-of-flight secondary ion mass spectrometry (ToF-SIMS) investigations. Within the potential range of the battery sulfate, sulfite and phosphate formation takes place at the Carbon/SE interphase.

The above-mentioned work is followed by the second publication for this thesis. In this paper carbon additives with different morphology and surfaces are compared and their influence on the battery performance is investigated. Simulations of the cathode composite show a lack of electronic conduction paths when no additives are used. However, carbon additives always induce the mentioned degradation of the SE, which could not be simulated. Furthermore, the degree of degradation is different for the different types of carbon. Vapor grown carbon fiber (VGCF) showed the least amount of degradation and also a positive influence on battery performance. Nevertheless, the continuing degradation significantly reduced the long-term performance of batteries. For this reason, a protection concept was developed which has similarities to an insulated cable. The decomposition was reduced and the positive influence of the carbon additive was maintained.

The results of this Ph.D. thesis provide the context for a comprehensive comparison of different battery concepts. The fundamental parameters are presented and discussed. Thus, the current state of the art in SSB performance is summarized and evaluated. From this thesis recommendations and goals for a successful further development of SSBs can be derived. In the second part of the thesis such an optimization was addressed. The positive influence of carbon additives was studied in more detail and the existing decomposition was reduced by a novel protection concept.

The following chapter will discuss in detail the publication by Lee *et al.*[20] and the applied techniques will be embedded in the context of battery research. This work was published at the same time as the first publication of this thesis and could therefore not be included in this comparison and evaluation. The battery presented by Lee *et al.*[20] represents a significant improvement compared to the current state of research. Therefore, the special features of this battery concept will be discussed and their influence will be presented and positive as well as negative aspects are shown.

2 On the way to commercial solid-state batteries

2.1 Solid-state batteries: general design

The subject of solid-state batteries has been common in research for some years, but the focus on this topic by large companies such as Volkswagen, Toyota or Samsung has significantly increased the momentum in research. A large number of national and international research projects and a whole series of newly founded startups have been created. The main motivation for the application of SSBs is based on the potentially higher safety, the higher energy density and the possibility to realize fast charging of batteries.

Due to the high shear modulus of the SEs, they are intended to serve as physical barrier for dendrites. This would allow the use of a lithium metal anode, which can significantly increase energy densities.[21–23] In addition, the SEs are resistant to thermal runaway and can be used in a much wider temperature range.[24] SEs are single-ion conductors. This means that the transport of lithium ions takes place through the crystal structure, preventing concentration gradient buildup across the electrolyte. This means that high current densities can be achieved, which can enable the fast charging of batteries.[25]

An idealized and minimalistic SSB consists of a lithium metal anode, a SE separator layer and a cathode composite, which is a mixture of the SE and a CAM (e.g. $LiCoO_2$, $Li(Ni_xCo_yMn_z)O_2$). The SE layer is sufficient as separator of anode and cathode. During charging, lithium ions are removed from the CAM (oxidation), move through the SE towards the anode and are deposited as lithium on the anode again (reduction). Because the SE does not conduct electrons, these migrate from the cathode to the anode via an external circuit and thereby operate an electronic consumer. The reverse process takes place during discharging. Figure 1 illustrates the differences between liquid electrolyte and solid-state batteries and the functional principle of state-of-the art batteries.

However, due to various additional, unwanted reactions, which decompose components or build up poorly conducting interlayers, a reduction in battery performance can occur. Therefore, it is necessary to apply additional protective layers or coatings between cell components or on components itself. It may also be necessary to use additives such as carbons to compensate for limitations caused by insufficient conduction pathways. This is the reason for the complexity of this research area and the wide variation of different anodes, SEs, cathode materials and cathode composite compositions.

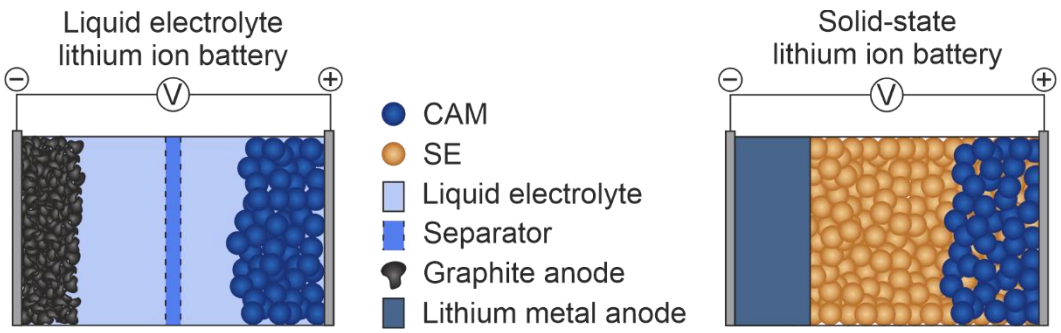

Figure 1: Conventional liquid electrolyte battery containing a CAM (e.g. NCM), a liquid electrolyte including a separator and a graphite anode. A solid-state battery is constructed by substitution of the liquid electrolyte by an inorganic solid electrolyte. The SE also functions as a separator. In this example the graphite anode is replaced by a lithium metal anode.

2.2 The best solid-state battery published: An analysis of the "Samsung cell"

The recently published work of Lee *et al.*[20] impressively demonstrates the possibilities of SSBs. By the right choice of materials, manufacturing methods and additives a solid-state cell with high energy density (546 $Wh \cdot kg^{-1}$, to anode, SE and cathode mass) and free of dendrite formation could be demonstrated. Furthermore, the existing decomposition reactions were addressed by the choice of materials and coating material. Thus, an SSB could be operated for 1000 cycles with only low losses. Another important aspect of this battery was that it had a capacity of 0.6 Ah, which was significantly larger than conventional laboratory cells (ca. 1.5 mAh). The long-term cycling was also carried out at a relatively high current density of 3.4 $mA \cdot cm^{-2}$ (0.5 C).

The anode consists of an Ag-C composite and enables the cell to operate without excess lithium. The resulting anode is therefore very thin (7.5 µm), which is an important factor in increasing energy density. Furthermore, this anode leads to a homogeneous lithium deposition and thus to the possibility of applying higher current densities. However, the exact working principle of this layer has not been fully clarified. The process is described in such a way, that lithium is incorporated into both carbon and silver nanoparticles at the beginning of the charging process. This leads to the formation of an Ag-Li alloy and to the expansion of the particles. During further charging, the silver nanoparticles/silver lithium alloy particles shrink, which is associated with the beginning of the deposition of metallic lithium on the current collector. This also causes the Ag particles to crack. Furthermore, the Ag nanoparticles move towards the current collector, where they are supposed to promote homogeneous lithium deposition. It is also observed that the lithium deposition takes place between the Ag-C composite and the current collector, which has never been observed before. The exact role of

carbon is not clear. It could be responsible for a homogeneous contact with the SE and a more homogeneous nucleation of lithium. Furthermore, the paper refers to the ionically conductive and mechanically stabilizing properties of carbon. However, it is questionable why lithium is deposited between the current collector and the Ag-C interlayer, as this does not seem to be explainable on the background of current knowledge about lithium deposition on electronic conductors.

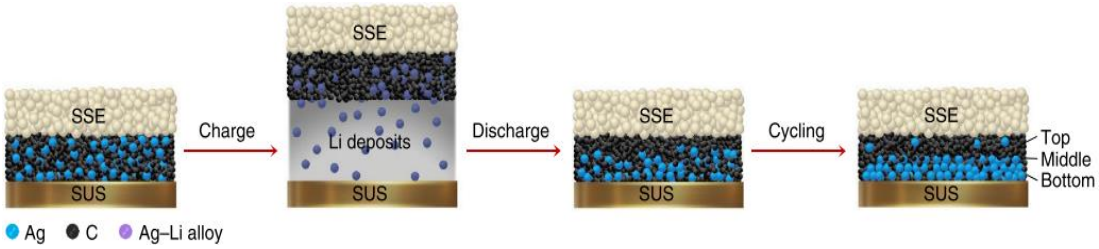

Figure 2: Functional principle of the Ag-C interlayer during charging and discharging. Reprinted with permission from Nat. Energy Copyright 2020 Springer Nature.[20]

It is important that the performance is demonstrated at 60 °C and with an external pressure of 2 MPa (20 bar). At this temperature the problem of dendrite growth is often reduced considerably compared to room temperature.[26] In addition, the combination of external pressure and elevated temperature leads to easier/accelerated dissolution kinetics of lithium, since the contact loss due to pore formation can be suppressed by faster vacancy diffusion.[27]

An important factor for the good performance of the battery is due to the argyrodite based SE, which has high ionic conductivity and is prepared dense. A dense SE reduces the probability of dendrite formation, improves the contacting of the CAM within the cathode, reduces grain boundary resistances and can contribute to lower interfacial resistances. The SE is Li_6PS_5Cl (σ_{RT} = 1.8 mS·cm^{-1}) with a particle size of 3 µm. This particle size is already extraordinarily small and thus results in a dense composition. An additional compacting is achieved by the warm isostatic pressing (WIP) during cell production. Here, the electrodes and the SE are pressed and compacted at an elevated temperature and a pressure of 490 MPa. Details on the applied temperature are not given. Corresponding SEM cross-sections illustrate the effect of additional pressing (Figure 3). Hardly any pores are visible in the SE and the cathode.

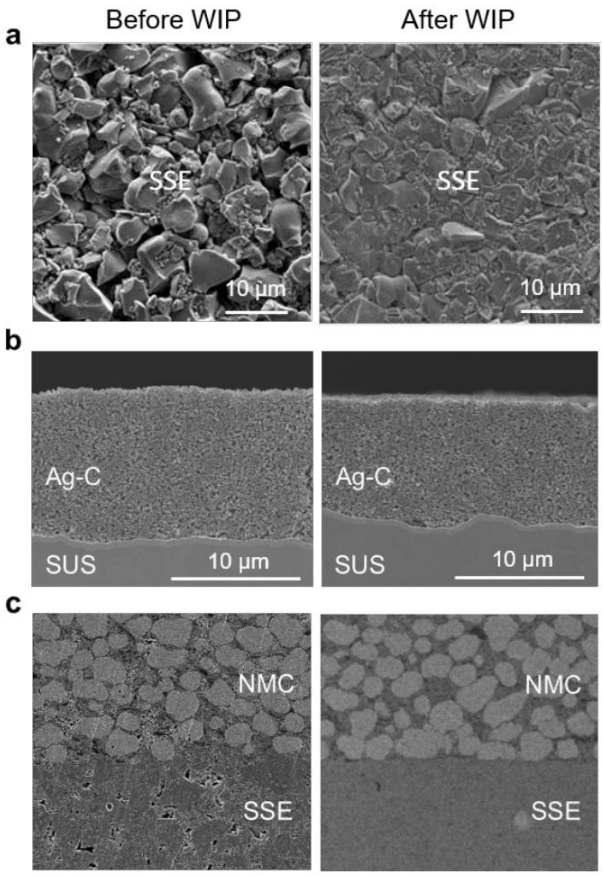

Figure 3: Changes in interfacial properties of SE and cathode by applying warm isostatic pressing (WIP) at elevated temperature and 490 MPa. Reprinted with permission from Nat. Energy *Copyright 2020 Springer Nature.*[20]

The achievable discharge capacity and the resulting energy density in the cathode composite is determined substantially by the CAM used. In the work of Lee *et al.* a nickel rich NCM intercalation material ($LiNi_{0.90}Co_{0.05}Mn_{0.05}O_2$) was used. This material is additionally coated with Li_2O-ZrO_2 to prevent reactions with the SE. The CAM content is relatively high with 85 wt.%. This results in an area loading of 6.8 $mAh \cdot cm^{-2}$. In the cathode composite, an argyrodite-based SE is also used, but this has a different morphology than the separator electrolyte between the anode and cathode. In the publication is a particle size < 1 µm reported, which results in a further reduction of the porosity and an improvement of the contact between SE and CAM. The SE in the cathode must be particularly oxidation stable, as it is in direct contact with the CAM.

The mentioned characteristics of the battery result in excellent energy densities. The small-particle SE and the carbon fibers in the cathode composite lead to very good contacting of all NCM particles. In combination with the homogeneous lithium deposition, high current densities can be realized. Above 1 C, however, there is also a build-up of a significant overvoltage. The reason for this can be a limitation due to the ionic or electronic conductivity in the cathode composite. Long-term cycling is carried out at 3.4 $mA \cdot cm^{-2}$ (0.5 C) and at a

temperature of 60 °C. The following Figure 4 is taken from the publication and illustrates the battery performance.

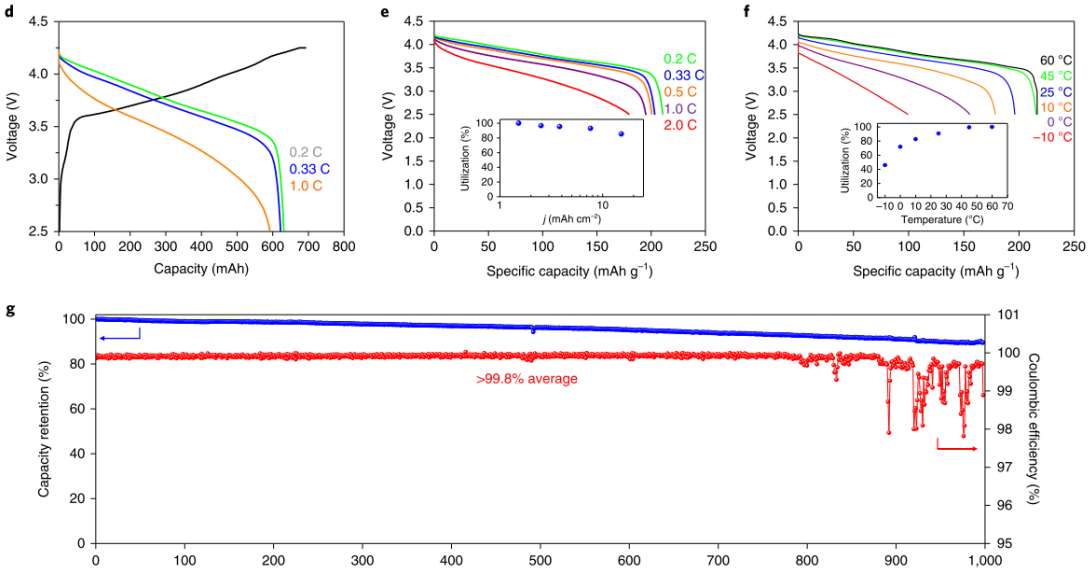

Figure 4: Electrochemical performance for a SSB with the composition Ag-C|Li_6PS_5Cl|$LiNi_{0.90}Co_{0.05}Mn_{0.05}O_2$/$Li_6PS_5Cl$. Reprinted with permission from Nat. Energy Copyright 2020 Springer Nature.[20]

Based on the information in the manuscript, the specific energy and the specific power of the presented battery can be calculated. The two values were calculated ignoring the packaging of the battery materials, so that they do not correspond to the data in the manuscript. This allows the comparison of the results with the performance of previously published solid-state batteries.[28,29,38–47,30,48–53,31–37] The comparison is shown in Figure 5 in the form of a Ragone-Plot. The additional literature values are taken from Randau *et al.*[54] and the reference numbers in the Figure are taken from the publication.

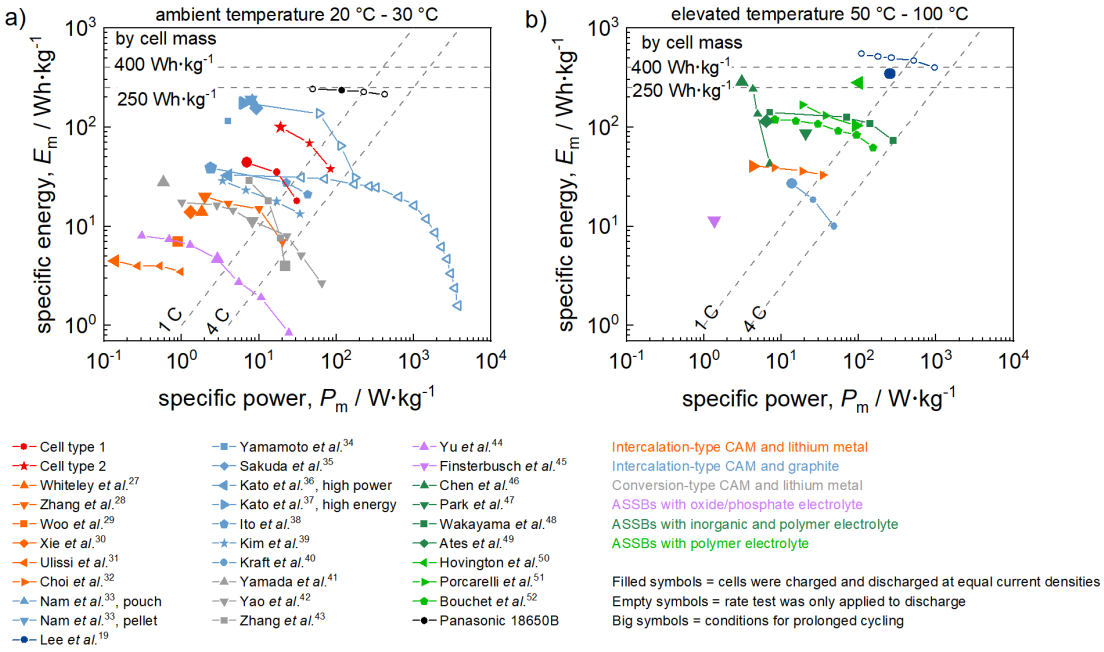

Figure 5: Ragone plots for cells cycled at a) ambient and b) elevated temperature. [54]

After the paper by Lee *et al.*[20] was described in more detail and the composition and influence of the chosen materials and concepts on the battery were described, a broader discussion should take place. Here, the three main factors responsible for good battery performance will be discussed in more detail. The solutions of Lee *et al*. will be compared to the current literature and alternatives or further improvements will be presented. The following discussion is divided into the area of the anode, the SE and the cathode.

For the anode discussion it is important to understand the function and task of the anode and to compare and evaluate the different anode concepts. In the discussion of the solid electrolyte the focus lies on the possibilities of synthesis and implementation of a small-particle and dense separating SE layer. The cathode discussion highlights the properties of different CAM types, the influence of the cathode composite composition, the stability issues of CAMS and a general discussion on coating strategies for CAMs. A comprehensive presentation of all possible CAM coating materials will not be given, as this will not be possible in the context of this thesis.

2.3 Anodes for lithium ion and solid-state batteries

In the field of battery development and electrochemistry it is common to speak of an anode and cathode, if the negative or positive electrode is meant. Depending on whether the battery is being charged or discharged, however, the terms change. If the battery is discharged, in a classical LIB the graphite electrode is the anode and the electrode with the active material, e.g. NCM, is the cathode. This description should be maintained to simplify the following

discussions. An anode can be described in simple terms as a host structure for lithium ions. In the charging step of a battery, lithium ions are incorporated, which are removed again during the discharge step.[55]

An ideal active anode must fulfil a number of requirements: (1) It should be as light as possible and at the same time be able to accommodate a high lithium content. The mass of the host structure material is electrochemically not active and has a direct negative influence on the energy and power density. [54,55] (2) The redox potential of the electrode against Li^+/Li must be as low as possible. In addition, the redox potential should not be influenced by the lithium concentration in the electrode. This potential has to be subtracted from the potential of the cathode in order to obtain the cell voltage. This property influences the energy and power density as well.[56] (3) The anode must have a high electronic and ionic conductivity. Depending on the charging or discharging of the battery, the reduction or oxidation of lithium takes place in the anode. The better electrons and lithium ions can be transported into or out of the anode, the higher current densities are possible, because of lower charge transfer resistances. Resulting in higher power densities.[17,37] (4) In the case of a LIB with liquid electrolyte, the anode must not dissolve in this solution or react with the electrolyte or other components in it (lithium salts). The same applies to cells with an SE. The decomposition products which form in both cases are mainly binary compounds (e.g. PF_5, LiF, HF, Li_2S, P_2S_5) with small ionic and electronic conductivities, or isolating properties. This will result in a buildup of resistances and reduced electrochemical performance. (5) A homogeneous and reversible lithium deposition or dissolution must be realized. In the first instance, a non-homogeneous deposition/dissolution reduces the achievable current densities. If this takes place over many cycles, the formation of lithium dendrites is likely. These build up through the electrolyte and can reach the cathode. If this is the case, the cell will self-discharge. High currents flow along the dendrite, which can lead to heating and finally to decomposition of the liquid electrolyte and burning of the battery. This is called thermal runaway. An SE can prevent a fire of the battery, but also SEs can be prone to dendrites depending on their morphology. Dendrite formation is increased when a SEs shows grain boundaries. Large SE particles and low malleability increase the amount of grains in a SE. Dendrite formation takes place along the grains and a short circuit is possible with an SE. Along the formed dendrite the decomposition of the SE is increased as well. With synthesis and after syntheses methods dense SEs can be received (chapter 2.4)[9,20] (6) The materials used must be cheap and environmentally friendly. With the increasing presence of LIB in the commercial market, the question of the recycling of old battery cells must be addressed.[57]

2.3.1 Graphite in LIBs and SSBs

Graphite is the most commonly used anode material in LIBs. The possibility of storing lithium in graphite by intercalation was first published in 1955.[58] Lithium is stored between the graphene planes and this process involves several phase transitions with increased lithium contend until LiC_6 is formed (Eqs. 1-5). These phase transformations are strongly depending on the anode morphology (porous and small particle) and the used liquid electrolyte. Exfoliation of the anode and cointercalation of Li and solvent molecules must be prevented.[59,60] The proof of the reversible storage was published in 1976 by Besenhard and Eichinger.[61,62] Increasing the Li content in LiC_6 is possible[59], but no reversible cycling beyond LiC_6 could be obtained. The graphite anode can thus be cycled between C_6 and LiC_6, with a theoretical capacity of 372 $mAh \cdot g^{-1}$.

$$C_6 + 0.083Li^+ + 0.083e^- \rightleftharpoons Li_{0.083}C_6 \quad (1)$$

$$Li_{0.083}C_6 + 0.083Li^+ + 0.083e^- \rightleftharpoons Li_{0.166}C_6 \quad (2)$$

$$Li_{0.166}C_6 + 0.056Li^+ + 0.056e^- \rightleftharpoons Li_{0.222}C_6 \quad (3)$$

$$Li_{0.222}C_6 + 0.278Li^+ + 0.278e^- \rightleftharpoons Li_{0.5}C_6 \quad (4)$$

$$Li_{0.5}C_6 + 0.5Li^+ + 0.5e^- \rightleftharpoons LiC_6 \quad (5)$$

The potential of the graphite electrode is approximately 0.15 - 0.25 V against Li^+/Li. A reduction of the cell voltage between AAM and CAM and the associated influence on the energy density is therefore only minor.[56] Graphite is a semi-metal with an high electronic conductivity at room temperature of about 10^{-3} $S \cdot cm^{-1}$. LiC_6 has a high Li-ion diffusion coefficient of 10^{-8} - 10^{-10} $cm^2 \cdot s^{-1}$. These values are sufficient for battery applications and higher current rates (approx. 1C).[56]

In a battery with liquid electrolyte, graphite must be protected from the electrolyte. Otherwise the electrolyte or additional lithium ions would intercalate into the graphite planes. Additionally, electrolyte decomposition can lead to gas formation. The intercalation and gas formation lead to an expansion of the anode and a cracking of this. To prevent this and realize the high reversibility of the graphite anode, ethylene carbonate (EC) is used as electrolyte or major portion of it. During the first charge EC is reduced due to the high potentials. The formed decomposition products and resulting SEI consist of $(CH_2OCO_2Li)_2$, CH_3OLi, CH_3OCO_2Li, Li_2CO_3. These products adhere compact onto the graphite anode and act as a passivation layer to prevent massive reduction of other electrolyte species. The chemical composition and thickness are crucial for the positive effect of the SEI. However, the use of the chemical related, but higher conductive solvent propylene carbonate (PC) is not suitable, because the resulting SEI is too thick and not homogeneous. Increased decomposition and gas formation

of other electrolyte components will be the result.[60] In general the lithium ion flow must be small enough to give the ions time to diffuse into the graphite.[63,64] Otherwise the Li deposition is not homogeneous and additional safety problem will result (dendrite formation and thermal runaway). This fact clearly limits the maximum achievable current density in batteries with a liquid electrolyte and a graphite anode. An overview of the different interphase challenges is shown in comparison to a Li/SE interphase in Figure 7.

One aim of the research is to further increase the capacity of the anode. However, in order to effectively increase the total capacity of the battery cell, the balancing of the capacities of CAM and anode active material (AAM) is crucial. Typical CAM show capacities of 140-200 $mAh \cdot g^{-1}$ [65], the gain in capacity of the total cell by increasing that of the anode element alone is thus limited. If the specific capacity of a typical 18650 cell is calculated as a function of the anode capacity, taking into account a cathode capacity of 200 $mAh \cdot g^{-1}$ and all package components, the total cell capacity will increase till saturation above an anode capacity of approximately 1200 $mAh \cdot g^{-1}$. This illustrates the interdependence of the cathode and anode capacities and at the same time shows that an increase in capacity for the AAM is still reasonable.[65]

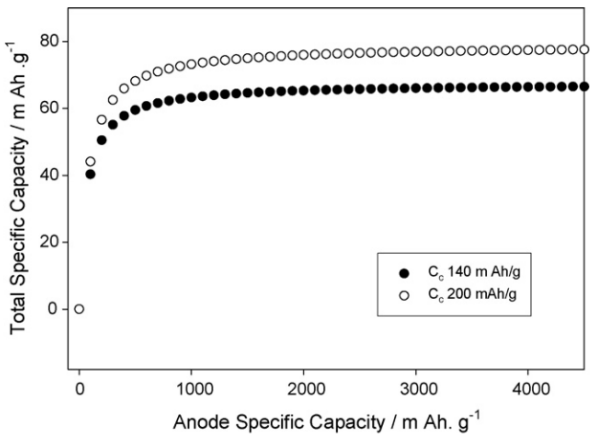

Figure 6: Total capacity of a 18650 LIB as a function of the anode capacity, for two cathodes having capacities of 140 and 200 mAh g-1. Reprinted with permission from J. Power Sources Copyright 2006 Elsevier B.V.[65]

Beside the thermal runaway and dendrite formation, especially the SEI formation is a strong motivation for the replacement of liquid electrolytes by an SE. The SEI formation must be done by the manufacturer and is time and cost intensive. SEs have a lithium transference number close to 1 (liquid electrolyte ≈ 0,5)[8,66,67] and in the last years SE conductivities have been achieved which are comparable to those of liquid electrolytes or even higher.[37,68,69] Resulting in an more homogeneous lithium deposition and dissolution due the absence of an lithium concentration gradient and fast lithium ion diffusion kinetics. SE are unaffected by a

thermal runaway, suppress dendrite formation and the formation of an SEI is not necessary. These advantages allow potentially the realization of much higher current densities.[37]

However, the use of SE also raises new challenges. The contact between SE, AAM and current collector is very important. A bad contact would result in high interfacial resistances. Due to the viscous character of the liquid electrolytes, they always have good contact and can compensate volume effects of active materials. When a SE is applied the volume extension of the AAM (due to LiC_6 formation) is difficult to compensate, due to its solid character. The intercalation of Li^+ into the graphite lattice results in an expansion of the unit cell by almost 46 %.[70] This significant expansion will further compact the SE or lead to cracks within the SE. If Li^+ is now removed again during discharge, the graphene lattice shrinks. Since most SEs are not elastic in this way, there will be a contact loss between AAM and SE. Additionally, SEs show various degradation mechanism due to the chemical potential of lithium in the battery. Decomposition reactions on the anode are discussed in chapter 2.3.2 and for the cathode side in chapter 2.5.3.

In recent publications, however, it has been found that carbons can cause decomposition reactions in combination with a sulfidic SE. The electronic contact, low chemical potential of lithium and potentials above approx. 2 V vs. Li^+/Li lead to a formation of a redox pair. The SE is oxidized to long-chain polysulfides with S^0 character.[15,16,19] These products have lower ionic conductivities than the intact SE and therefore cause resistances to build up within the battery cell, which leads to a decrease in cell performance. However, these decomposition reactions are monitored in symmetrical cells and a transfer of these findings to the battery anode should be possible.[71] The exact relationships and influences within SSBs need to be investigated more closely.

2.3.2 Lithium metal anode

The lithium metal anode is considered to be the most promising anode for modern and future battery concepts. However, the use of this anode is hindered for batteries with liquid electrolytes, due to severe dendrite formation. Low transference numbers and concentration gradients in liquid electrolytes result in an non homogeneous lithium plating, a locally thicker lithium and after several cycles dendrites can cause a short circuit. [72,73] Therefore, the use of a lithium metal anode is only practical in combination with an SE and the following discussions refers to solid-state cell systems.

Lithium has the lowest electrochemical potential at -3.04 V compared to the standard hydrogen electrode. This allows the highest voltage differences between cathode and anode to be achieved. Therefore, the energy and power densities are influenced positively by usage of

this anode material. The theoretical capacity of 3860 $mAh \cdot g^{-1}$ is also exceptionally high. As a result, only small amounts of lithium metal are needed as host structure, or as lithium source, if the CAM is not lithiated. Furthermore, a small excess of lithium metal can have additional benefits for the battery performance, as lithium loss due to e.g. SEI formation can be compensated to a certain degree. Additionally, lithium also has a low density of 0.534 $g \cdot cm^{-3}$. This means that if lithium is needed in the system, it will have only a small negative effect on the total mass of the cell.

The ductility of lithium also allows easy pressing onto the current collector or the SE. Thus, a low interfacial resistance can be obtained. A respective example is provided by the work of Krauskopf *et al*.[11] This work shows that the interfacial resistance between SE and pure lithium can be reduced to practically 0 $\Omega \cdot cm^2$ with an external pressure of 400 MPa. Impurities on the surfaces (carbonate species), or SE decomposition products cause a higher resistance. When using lithium metal in solid systems, particular care must therefore be taken to ensure clean materials and surfaces. In systems with liquid electrolyte, it would be possible to remove impurities via electrolyte additives or to remove them from the system via degassing. This is not possible in solid-state cells.

It must be mentioned, that solid-state cells require a certain pressure, which compresses the cell components during cyclization. This can improve the contact between anode and SE. Typical pressures are 2 - 100 MPa. A homogeneous contact also reduces the probability of dendrite formation. An external pressure can also be combined with an elevated temperature. In general, the aim is to operate the cells at room temperature and achieve high performances. This simplifies the application and it may not be necessary to use additional energy from the battery for heating. However, the temperature has a strong influence on the lithium deposition or dissolution. At higher temperatures, the problem of dendrite growth is often greatly reduced.[26] The combination of external pressure and elevated temperature improves the kinetics of lithium dissolution or deposition. The loss of contact due to pore formation is suppressed by the rapid vacancy diffusion.[27]

In addition, lithium is very reactive due to its low electrochemical potential. Especially contamination of the atmosphere with carbonates, N_2 and H_2O leads to a rapid passivation of the surface. It is likely that during fabrication of the lithium foils a passivation layer is formed. In general an outer Li_2CO_3/LiOH layer with a 1-20 nm thickness is superimposed on a Li_2O layer (10-100 nm).[74] The lithium ions can then no longer diffuse through the passivation layer. If lithium is added to water, highly flammable hydrogen is produced. The handling of lithium is therefore connected with a greater expense. Gloveboxes filled with argon are used on a laboratory scale. This would be too expensive for industry, which is why the focus is on dry rooms with low boiling points. However, operating these is also a large cost factor.

The low potential of lithium can also lead to reactions at the interface to the SE. If a sulfide electrolyte is used, these reactions take place due to the small stability window of the SE. Oxide and polymer SEs, on the other hand, have wider stability windows, which does not lead to decomposition. For example, if $Li_{10}GeP_2S_{12}$ is used as a sulfidic SE, phosphorus is reduced from +5 to +3 and germanium from +4 to 0, resulting in Li_2S, Li_3P and Ge as decomposition products. Wenzel *et al.*[12] investigated this reaction in detail by *in situ* XPS and the growth rates are determined. For $Li_{10}GeP_2S_{12}$ a rate of $3.60 \cdot 10^{-7}$ $cm \cdot h^{-0.5}$ and for $Li_7P_3S_{11}$ a rate of $2.33 \cdot 10^{-8}$ $cm \cdot h^{-0.5}$ is found. After one year the formed SEI of $Li_{10}GeP_2S_{12}$ shows a thickness of 370 nm and for $Li_7P_3S_{11}$ of 23 nm. This would result in significant overvoltage and the corresponding cells would only deliver low performance. These experiments clearly show that sulfide SEs are thermodynamically unstable, but the reaction is kinetically hindered. Thus, practical batteries on a laboratory scale are possible. However, for industrial application, this decomposition must be prevented. An overview of the different interphase challenges is shown in Figure 7.

This can be done either by using other anode concepts (e.g. LiIn alloy or Ag-C anode by Lee *et al.*[20]) or by investigating protection concepts, as is already being done for CAM. The development of anode protection concepts is still in its early stages and literature is rare. An example is the work of Zhang *et al.*[29] where lithium metal is coated with phosphoric acid to form LiH_2PO_4. This protective layer prevents the reduction of $Li_{10}GeP_2S_{12}$ SE, because elemental Lithium is not in contact with the SE. The protection layer forms a uniform surface and shows only a lithium ion conductivity. Battery cells could be operated with more than 500 cycles without major losses of capacity.

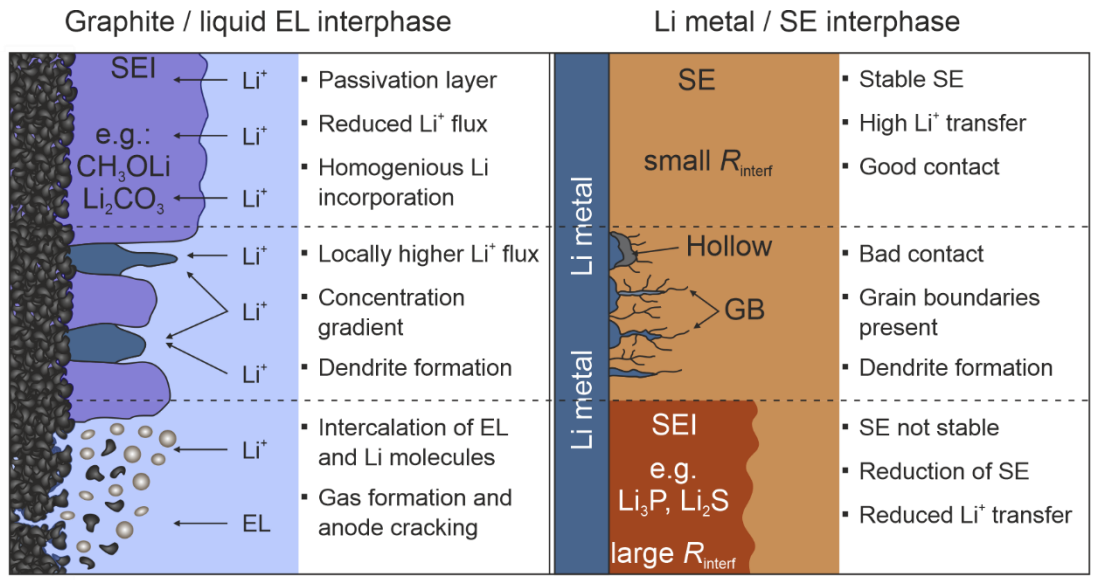

Figure 7:Overview for the anode/electrolyte interphases of liquid electrolyte and SE based batteries and for different interphase properties. For a liquid electrolyte battery, a thin and dense SEI is needed for stable cycling. The SEI promotes a homogeneous Li incorporation into the graphite anode. Is the SEI not fully close, locally higher a Li^+ flux will lead to dendrite formation. The absence of an SEI, or the use of high conducting electrolytes (e.g. PC) can lead to an intercalation of lithium and electrolyte molecules. Gas formation and anode cracking are the result. For an anode SE interphase, a stable SE will lead to high Li^+ transference numbers and a small interphase resistance. A bad contact due to the presence of hollows or grain boundaries can result in a fast formation of dendrites. The SE can as well show chemical instabilities and decompose to products with small ionic conductivities, resulting in higher interphase resistances.

2.3.3 *In situ* formed anodes

To describe this concept, it is first necessary to define the term *in situ* formed anode and to put it into context with other terms in the literature. The aim of this type of anode concept is to avoid the use of AAM on the anode side when building the battery. The lithium ions are obtained from the CAM only and must shuttle completely reversibly between the anode and cathode when operating the battery. In addition, there is no host material, such as graphene, in which the lithium ions could be stored. The lithium ions must be deposited as lithium metal on the anode current collector. There is no excess lithium in the system. As a result, it is assumed that the more complex handling of lithium metal in production can be replaced in order to save costs. Furthermore, an attempt is made to replace the established graphite anode for LIB. This will increase the energy density, since no electrochemically inactive material (graphite) is used.

In the literature the term *anode-free battery* is often used for this concept. This is of course not a correct term, as a battery must have an anode at which oxidation takes place during discharge, and a better term would be *lithium metal-free* or *lithium metal reservoir-free*. As already described at the beginning of the chapter, the anode alternates between the

battery electrodes depending on whether it is charged or discharged. The term *in situ* formed anode is therefore more suited for this type of concept.

As already mentioned, the graphite anode is dominant in the field of LIBs. For SSB, the focus of research is on the lithium metal anode due to the use of SEs and the high capacity and low atomic mass of lithium metal. Further research is needed to show whether the *in situ* formed anode can be applied successfully in SSBs and whether they will have advantages over the lithium metal anode.

In literature, several approaches to implement an *in situ* formed anode for LIB are known. The first approach is focused on the modification of the liquid electrolyte used. The composition of the liquid electrolyte is changed to achieve a higher ionic conductivity. It is intended that this will lead to a more homogeneous lithium deposition and dissolution. In this example a 4 M LiFSi-DME electrolyte was used.[75] Usually electrolyte concentrations of 1 M are used in the literature.

A similar approach was reported by Jote *et al*.[76] However, they also consider the resulting SEI formation at the liquid electrolyte/anode interface. Without the modification of the liquid electrolyte the resulting SEI shows mainly $ROCO_2Li$ and Li_2CO_3 as components. By adding FEC/TTE/DEC a LiF enriched SEI is formed. In the resulting SEI the Li_2CO_3 concentration was reduced and a high concentration of LiF was present. The high Li^+ conductivity of LiF prevents dendrite formation and improves the Coulomb efficiency of the batteries.

The common current collector on the anode side is copper. Zhang *et al*.[77] have coated this copper foil with tin. At the beginning of the charging step a Li-Sn alloy is formed on the current collector. Further lithium is now deposited on this alloy. Due to the high lithium diffusivity of the alloy, it acts as a mediator for reversible deposition and dissolution of lithium.

Polymers are widely used to address interface problems. They are notable for their simple processing and good contact with adjacent components. Assegie *et al*.[78] has coated the widely used polymer (PEO) onto the copper current collector. The liquid electrolyte diffuses into the PEO and allows ionic conductivity. When the battery is charged, lithium deposits between copper and PEO. This allows reversible lithium deposition and dissolution to be achieved.

Wondimkun *et al*.[79] coated the copper current collector with graphene oxide. The graphene oxide is additionally wetted with fluoroethylene carbonate (FEC). The use of these interface agents resulted in homogeneous lithium deposition between the copper current collector and the graphene oxide. The Coulomb efficiency of corresponding batteries was improved and lithium dendrites were apparently avoided.

Finally, a reference needs to be made to the work of Neudecker *et al.*[55] In this paper an *in situ* formed anode for a thin film battery is demonstrated, i.e. lithium was deposited between the LIPON solid electrolyte and the copper current collector. The use of a gas tight overlayer for the anode is crucial for the function of the battery.

The literature presented misses one crucial issue that significantly influences the concept of the *in situ* formed anode. In LIBs as well as ASSBs there is currently always the formation of different SEIs, both in the cathode and at the anode interfaces. As far as known, lithium is consumed in the formation of these SEIs. Since all lithium in this concept is provided by the active material, lithium consumption through SEI formation has a much stronger influence on battery performance than when there is excess lithium in the system.[55] Therefore, it may be reasonable to accept a slightly reduced energy density and the more expensive production due to lithium metal, if the battery performance remains more constant for high cycle numbers.

2.3.4 Evaluation of the anode concept from Lee *et al.*

The design and the functional principle of the Ag-C composite anode by Lee *et al.*[20] has already been described in detail in chapter 2.2. If this anode is now compared with the other anodes presented, the concept of Lee *et al.* can be assigned to the field of an *in situ* formed anode. According to our knowledge, this publication is the first to present an *in situ* formed anode for SSBs with comprehensive data.

A quantitative comparison between an Ag-C composite anode and lithium metal anode is very difficult because it is not clear how a pure lithium metal anode would appear and influence the battery performance. The crucial point is whether excess lithium is required on the anode side as host structure. If not, and a homogeneous deposition of lithium metal between SE and current collector is possible, the improvement in energy density would be significant. The Ag-C composite could be completely spared. On the anode side, only the deposition of lithium metal from the CAM would have to be considered. This would be the same for both cases and is therefore negligible.

If excess lithium is required on the anode side, an improvement in energy density can still be achieved by using lithium metal. The density of lithium is five times lower than that of the Ag-C composite. This would directly affect the gravimetric energy density. Since the same dimensions (thickness 7.5 µm) are assumed for the lithium metal as for the Ag-C anode, there is no improvement in the volumetric energy density.

The theoretical maximum capacity of the two anode concepts will be identical, since in both cases elemental lithium is deposited, which represents the AAM.

According to the current state of the art, however, the concept of the Ag-C anode by Lee *et al.* is still the best solution. The instability of the sulfidic SE compared to lithium metal, the formation of dendrites when using a pure lithium metal anode and the technically high effort for the production of very thin lithium metal foils currently prevent the use of lithium metal for the battery concept of Lee *et al*. If these challenges are solved, a further significant increase in energy density can be achieved by using lithium metal as anode.

2.4 Compact separating electrolyte

Like any electrochemical device, a lithium ion battery or SSB consists of two electrodes (anode and cathode) and an electrolyte. The electrolyte separates anode and cathode electronically to prevent self-discharge and avoids mechanical short circuit. It needs to have a sufficient ionic conductivity to enable repeated shuttling of Li^+ ions between anode and cathode. The type and properties of the electrolyte are determined by the choice of anode and cathode. This means that the chemistry of the two electrode-electrolyte interfaces determines the properties of the optimum electrolyte. These properties of an ideal electrolyte can be summarized: (1) A large window of phase stability (e.g. no decomposition). Usually only certain phases of a compound show the desired electrochemical properties (e.g. conductivity, 3D Li diffusion), these phases may in addition not be the energetically most stable phases. Such compounds have to be produced by specific synthesis routes (stoichiometric ratio, temperature programs, quenching). A phase change must not take place during operation of the battery, e.g. caused by temperature effects; (2) A wide electrochemical stability window, as the chemical potentials adjacent to the electrolyte influence its stability. High chemical potentials of lithium lead to a reduction of the electrolyte, low potentials of lithium lead to oxidation. The decomposition products usually have lower conductivities and thus reduce the battery performance; (3) Non-flammability; (4) Non-toxicity; (5) robust against electrical, mechanical and thermal strains; (6) good electrode-electrolyte contact. Resulting in small interfacial resistances; (7) Abundant availability; (8) Non-corrosive to battery components; (9) Environmentally friendly.

The large amount of work published on lithium ion batteries, solid-state batteries and solid electrolytes in general, shows that an “ideal” electrolyte does not exist. A general overview on the properties of the three main types of electrolytes (oxide, polymer and sulfide) is given in chapter 1.1. The task is to find an electrolyte suited for the specific combination of anode and cathode, with enough combination of desirable properties for an acceptable commercial battery. There are several review papers published giving a broad overview on SEs.[80–82]

As already mentioned in chapter 1.1, the class of sulfide electrolytes is the most promising due to their good mechanical properties. A first relevant representative of this class is the β-Li_3PS_4. Besides this phase, Li_3PS_4 can be found amorphous, in α- and in γ-phase. β-Li_3PS_4 shows higher conductivities than the α-phase and is, in contrast to the γ-phase, obtainable via synthesis. The space group is *Pnma* and the ionic conductivity is about $1.7 \cdot 10^{-4}$ $S \cdot cm^{-1}$, with an activation energy of about 0.36 eV. However, the conductivity of this electrolyte is not sufficient to operate batteries with high active material loadings and high C-rates.[83,84]

For this reason, recent literature increasingly uses another sulfide electrolyte, namely Li_6PS_5Cl. This electrolyte shows a significantly higher ionic conductivity of about 1.8 $mS \cdot cm^{-1}$ at room temperature. This value is comparable to liquid electrolytes and therefore high current densities are possible. The activation energy is 0.35 eV and the space group is *F3m*. In addition, this electrolyte shows a higher chemical stability against a lithium metal anode than the β-Li_3PS_4.[85]

The following chapter will address a property of the SE which is not as present in the current literature as e.g. the optimization of the ionic conductivity. This property is the morphology of the SE, or more precisely the possibilities of obtaining a compact SE. The work of Lee *et al.*[20] shows in a remarkable way the strong influence of this property. In this work the SE shows almost no porosity. A dense SE reduces the probability of the formation of lithium dendrites.[86] Dense pellets increase the mechanical stability, whereby the thickness of the SE can be reduced.[86] Thus, the energy density can be significantly increased.[54] Furthermore, a thin SE reduces the corresponding resistance and therefore allows higher current densities for a battery. [86]

2.4.1 Syntheses of solid electrolytes with small particle size

A first approach would be to modify the synthesis of the SE and then investigate the influence of the resulting particle size. In general, the focus of research is more on optimizing conductivity than on the resulting particle size. Therefore, there are currently only few works on the topic of particle size and its correlation with electrochemical performance.

An example is provided by Liu *et al.*[84] Here the solid electrolyte β-Li_3PS_4 was synthesized. The starting materials were dissolved in THF, and a $Li_3PS_4 \cdot 3THF$ complex was formed. The solvent was removed by heating, followed by a temperature treatment of the amorphous Li_3PS_4 to obtain nanoporous β-Li_3PS_4. The annealing can take place at different temperatures, which has an influence on the resulting crystallite size. At 140 °C 80 nm and at

200 °C 200 nm large crystallites were obtained (Figure 8). The conductivity was higher for small crystallites ($\sigma_{25°C}$ = 2.1·10^{-4} S·cm^{-1}) than for larger crystallites ($\sigma_{25°C}$ = 1.7·10^{-4} S·cm^{-1}).

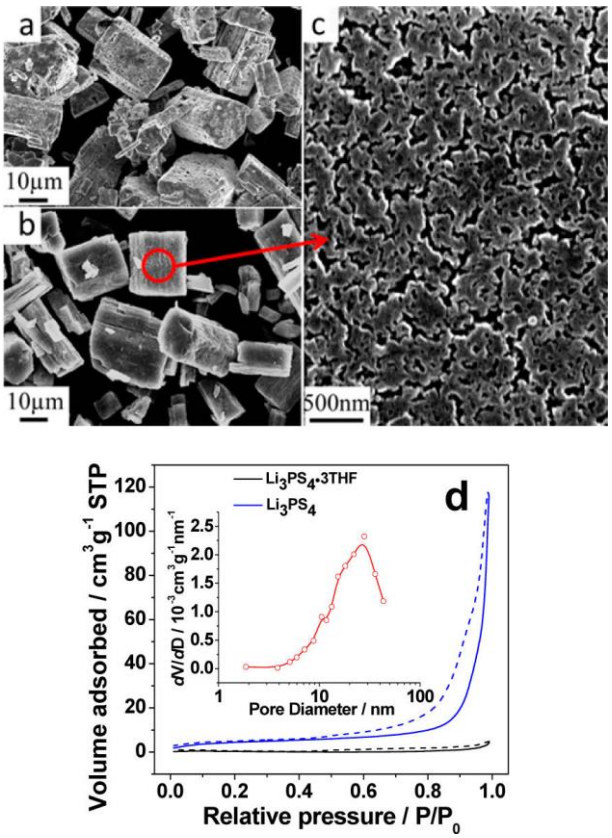

Figure 8: SEM images of SE particles received by the synthesis route described by Liu et al. Respective pore diameters for the SE particles. Reprinted with permission from J. Am. Chem. Soc. Copyright 2013, American Chemical Society.[84]

A work based on this synthesis method was published by Wang *et al.*[87] This work makes use of the small crystallites on the one hand, but on the other hand it extends the synthesis in such a way that very thin layers were produced. The synthesis of β-Li_3PS_4 is similar to the work of Liu *et al.*[84] The used solvent was replaced by ACN and the crystallization of the SE took place at 200 °C. Crystallites with lateral sizes of 1 to 2 µm and thicknesses of 80 nm were obtained ($\sigma_{25°C}$ = 1.2·10^{-4} S·cm^{-1}). The solid electrolyte was again suspended with ACN and was dip coated onto a Ni foil. The solvent was removed during a temperature treatment. Depending on the suspension concentration or how often the dip coating step was repeated, the resulting thickness on the carrier foil was adjusted. Thicknesses from 8 to 50 µm were achieved. Layers with 30 to 50 µm could be produced freestanding.

When comparing the voltages observed for Li stripping and plating experiments in symmetrical Li|SE|Li cells, an eight times reduction (to 0.01 V) was observed when using a 50 µm membrane compared to a 500 µm membrane, which are typical layer thicknesses of cold pressed SE powders. This indicates the possibility of achieving significantly higher current densities in full cells. For stable cold pressed pellets, considerably higher amounts of

SE material are required than for the methods described in this chapter. 20 % porosity is expected for cold pressed pellets, which significantly reduces the mechanical stability of corresponding SE pellets. Furthermore, the number density of grain boundaries is higher than for more compact pellets. Along these grain boundaries the growth of lithium dendrites is typically enhanced. To avoid these issues, more material has to be used. Pellet thicknesses of approx. 500 µm are the result, which means lower energy densities and higher resistances within the batteries.

2.4.2 Methods to reduce solid electrolyte porosity after synthesis

The adjustment of the particle size during the synthesis is limited. The synthesis conditions are specific for the respective product, and if they are not met, other products may be obtained. Furthermore, the synthesis routes are often not published in detail by the manufacturers, which makes it difficult to optimize the particle size during production on a laboratory scale. Methods for adjusting the particle size or compacting after the synthesis therefore seem promising. The aim is always to keep the porosity of the resulting SE pellets as low as possible.

Due to the good ductility, cold uniaxial pressing of powders dominates in the field of sulfide SEs. This gives good results, with common SE pellets having approx. 15-20 % porosity.[17] The publication discussed in the previous chapter and of Lee *et al.*[20] clearly show that more compact SEs are beneficial.

An extension of cold pressing is pressing at elevated temperature. The industry differentiates between warm (> 500 °C) and cold (approx. 100-300 °C) pressing. It is possible to compact the material uniaxially or isostatically. Uniaxial pressing can also be realized continuously, which is called calendaring. When low temperatures are used, the material will soften. Is pressure applied, pores can be closed and compact pellets are obtained. The corresponding temperatures depend on the respective SE and should always be well below the synthesis temperature. For sulfide-type SE, not more than approx. 200 °C should be used. If the temperature is too high, phase transformations or recrystallization may occur. In comparison, significantly higher temperatures (> 1000 °C) are required for compacting oxide-type SE (e.g. LLZO). At these high temperatures a sintering process takes place in addition to compaction due to softening. During sintering, impurities from the material are transported to the surface of the material by solid-state diffusion. This step can additionally result in lower porosity. A first publication that shows the positive effect of pressing at elevated temperatures is the work of Hood *et al.*[88] This work produces freestanding LPS membranes with thicknesses between 6 and 35 µm. By pressing the SE uniaxially at 200 °C and 200 MPa, membranes with

a porosity of 2-5 % were obtained (Figure 9). Stripping and plating experiments with lithium were performed with these membranes. It was possible to prepare thin membranes with thicknesses of down to 12 and 6 µm. The 12 µm membrane of β-Li_3PS_4 shows a conductivity of $7.2 \cdot 10^{-5}$ S·cm^{-1} at 25 °C. The voltage for reversible lithium stripping and plating was very low at 0.01 V. Lithium stripping and plating was demonstrated at current densities of 0.1 and 0.3 mA·cm^{-2} for up to 580 hours without the formation of lithium dendrites.

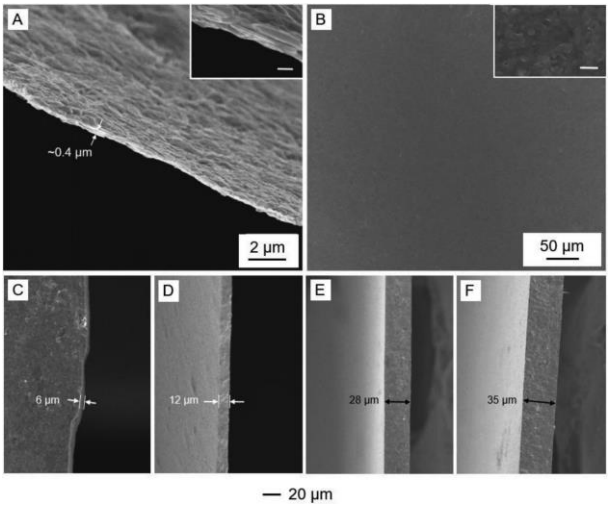

Figure 9: SEM images of β-Li_3PS_4 freestanding thin films with various thicknesses. Reprinted with permission from Adv. Energy Mater. Copyright 2018 WILEY-VCH.[88]

Lee *et al.*[20] extends this procedure once again. In this work the cathode, anode and SE were pressed together isostatically. Thus, in addition to the low porosity, the individual battery components show very good contact with the adjacent battery components. This is represented by a cell resistance of only 50 Ω·cm^2 at 25 °C after the first charging step. Isostatic pressing is performed at elevated temperatures (not specified) and 490 MPa. This procedure contributes substantially to the extraordinarily good battery performance (see chapter 2.2)

2.4.3 Evaluation of warm isostatic pressing of Lee *et al.*

The advantages and effects of a compact SE have already been described in detail in sections 2.2 and 2.4. Beside the high ionic conductivity (σ_{RT} = 1.8 mS·cm^{-1}) and the oxidation stability of the Li_6PS_5Cl SE, the compact SE pellet is crucial for the high battery performance. The compact pellets in the work of Lee *et al.*[20] were obtained by firstly using a SE synthesized with small particle size (3 µm) and secondly isostatic pressing at elevated temperature for all battery components. The pressing provides very good results on a laboratory scale. However, it is not suitable for industrial applications because it cannot be operated continuously. The resulting costs would be too high.[89] The aim therefore should be to realize a continuous compacting at elevated temperature. The calendaring method would be suitable for this

purpose. The influence of this method on LIBs is still part of the current research.[90] Work on this method for SSB is currently awaiting publication.

2.5 The Cathode

Charging/discharging of a battery is an electrochemical process. The movement of electrons from the cathode to the anode is induced by an external power source during charging. This also results in the migration of lithium ions from the cathode to the anode. The CAM is therefore delithiated and the anode is lithiated. During discharging, this process is reversed, lithium ions diffuse from the anode to the cathode and a consumer can be operated by an external power circuit by the electrons. The battery performance (e.g. capacity and working voltage) depends mainly on the structure and type of the CAM. The capacities of common CAM are approx. 130 to 220 $mAh \cdot g^{-1}$ and significantly lower than those of AAM (graphite: 372 $mAh \cdot g^{-1}$, Li metal: 3860 $mAh \cdot g^{-1}$).[91] The voltage difference between cathode and anode is also significantly influenced by the CAM. Graphite shows only a slightly higher redox potential than lithium metal (chapter 2.3.1), which has the lowest redox potential of the elements (chapter 2.3.2). Potentials for CAM can range from about 2 V to 5 V vs. Li^+/Li. This strongly influences the energy and power density.[91] In most cases, about 50 % of the battery manufacturing costs can be attributed to cathode processing.[92]

Beside the choice of the CAM, the cathode performance is influenced by several factors (e.g. material contact, chemical stability, mechanical stability, mixing ratios, additives). If CAM particles are not contacted, they cannot be delithiated/lithiated. Another important aspect is the chemical stability of the components used in the cathode. This includes on the one hand the stability of the CAM as such and on the other hand the interaction between CAM and SE. The stability of the CAM itself is not a major challenge. With intercalation CAM (lithium ions are built into the structure) only a certain amount of lithium can be removed reversibly. If more lithium is removed, the CAM structure is irreversibly damaged (Chapter 2.5.1).[93] With conversion-type CAM (active material reacts chemically with lithium) only as much active material can be converted as is present and contacted in the cathode.[94] Both limitations can be clearly seen from the cell voltage and the limits are known for each CAM, batteries can therefore be cycled accordingly.

Table 1: Electrochemical and material properties of common CAM.[95,96]

CAM	Capacity / mAh·g^{-1}	Mean cell voltage vs Li^+/Li / V	Density / g·cm^{-3}
$LiCoO_2$	137	3.8	4.79
$LiNi_{0.6}Mn_{0.2}Co_{0.2}O_2$	170-190	3.7	4.78
$LiNi_{0.8}Co_{0.15}Al_{0.05}O_2$	199	3.6	
$LiFePO_4$	170	3.2	2.7
$LiMn_2O_4$	148	4.1	4.29

The narrow stability window of different SEs and the resulting oxidation of the SE has a much stronger influence. This aspect will be described in a separate chapter in the following (Chapter 2.5.3). Due to this topic a separate field of research has developed. Coatings for the CAM have become a focus of current research, as it has been found to be difficult to further improve the stability of the SE without losing its positive properties (structure and ionic conductivity).

Furthermore, certain CAM may have special properties. The focus here is on the mechanical breaking of intercalation CAM particles, due to the reversible change in structure caused by delithiation. This affects the contact surface between CAM and SE. At freshly formed CAM/SE interfaces, degradation reactions can occur repeatedly. Another important issue is the diffusion of lithium ions within a CAM particle. If this is limited, an overvoltage can build up in the CAM, which reduce the maximum current density and can lead to an early interruption of a charging step due to the earlier reach of the upper cut-off potential. This results in a non-complete usage of the CAM. These mentioned points represent the most important aspects of cathode research and are therefore discussed in separate chapters in the following. An overview on problems and the influence of coating materials on the CAM/SE interphase is shown in Figure 10.

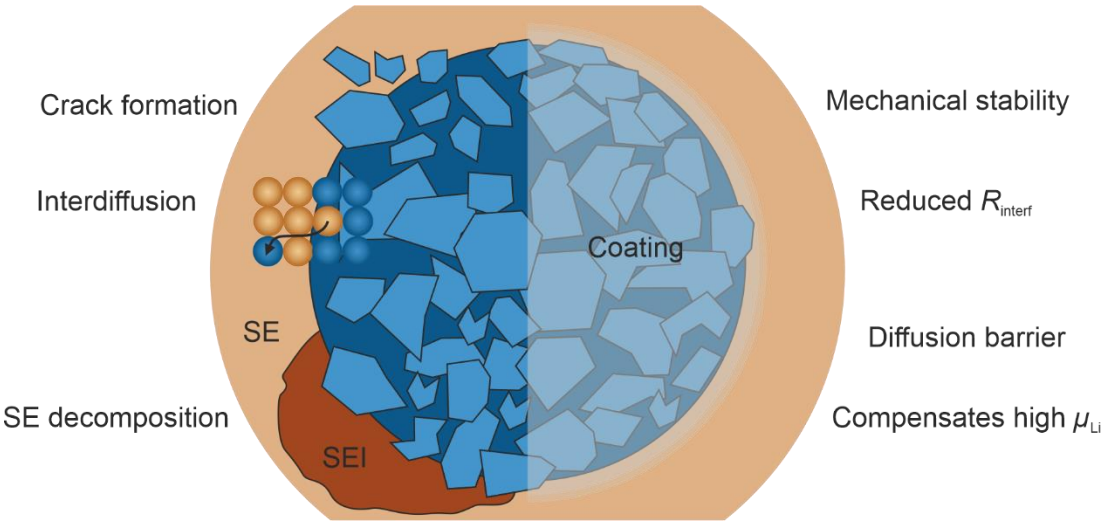

Figure 10: Overview on CAM/SE interphase instabilities and positive effects of coating materials on the interphase.

2.5.1 Cathode active materials

The first commercially used CAM for LIBs is $LiCoO_2$. This is the parent phase for the formula group of $LiMO_2$ (M = Co, Mn, Ni). This intercalation compound was first suggested by Goodenough and Mizushima *et al.*[97] It was commercialized in the 1990s by Sony.[98] Depending on the synthesis method, two crystallographically different phases can result. The material with layered lattice shows better electrochemical performance compared to the cubic spinel lattice. In the fully lithiated state $LiCoO_2$ shows a layered structure with a hexagonal unit cell. The crystal structure is compared to α-$NaFeO_2$, which has the space group $R\bar{3}m$. The unit cell consists of three slabs of edge-sharing CoO_6 octahedra, separated by interstitial layers of Li. This phase is called O_3 phase. With the removal of Li, nonstoichiometric $Li_{1-x}CoO_2$ is formed and Co^{3+} is oxidized to Co^{4+}. From $LiCoO_2$, 50 % of lithium can be reversibly removed. When more lithium is removed, the structure changes from hexagonal to monoclinic. Due to this intrinsic structural instability the maximum achievable discharge capacity is 137 $mAh \cdot g^{-1}$. The average discharge potential for this CAM is 3.7 V vs Li^+/Li.[92] However, $LiCoO_2$ is undesirable for the application in the field of BEVs due to its high costs, safety concerns due to the use of Co and relatively low energy density in resulting cathode composites.

Great efforts are therefore made to develop new CAM and to improve them. The aim is to reduce the Co content or replace Co completely. Three main classes of materials have emerged from this, namely α-$NaFeO_2$-type layered oxide, poly-anion oxide and spinel-type oxide. Representatives of these groups are $LiNi_xCo_yMn_{1-x-y}O_2$, $LiFePO_4$, and $LiMn_2O_4$.

The $LiNi_xCo_yMn_{1-x-y}O_2$ is a further development out of $LiCoO_2$ and $LiNi_{0.5}Mn_{0.5}O_2$, a first substitution attempt of Co from Ohzuku *et al.*[99] The $LiNi_xCo_yMn_{1-x-y}O_2$ class is mainly used in

state-of-the-art LIBs. In $LiNi_{0.5}Mn_{0.5}O_2$ the redox pairs Ni^{2+}/Ni^{4+} and Mn^{2+}/Mn^{4+} are electrochemically active. The Mn^{4+} stabilizes the structure during processing. However, extensive characterization revealed a Li/Ni disorder presence in the pristine material.[100,101] Eight to ten percent lithium-nickel exchange was observed. The similar ion radii of Li^+ and Ni^{2+} are the reason for the exchange. The presence of Ni in the Li layer impedes the lithium extraction and blocking the lithium diffusion path. Since the Li/Ni disordering was the major issue, new CAM materials were investigated. In 2001, Ohzuku *et al.*[102] reported a class of CAM with three transition metal ions, Co, Mn, Ni with the composition $LiNi_xCo_yMn_{1-x-y}O_2$. This CAM shows a comparable mean discharge voltage as $LiCoO_2$ (3.7 V vs Li^+/Li). $LiNi_{0.33}Co_{0.33}Mn_{0.33}O_2$ is a commercially available CAM of this class and many other compositions for $LiNi_xCo_yMn_{1-x-y}O_2$ are used in laboratory scale and commercial applications. A practical capacity for $LiNi_{0.33}Co_{0.33}Mn_{0.33}O_2$ is 195 $mAh \cdot g^{-1}$ at 1 C.[103] The presence of Co in the structure reduces the Li/Ni disorder to 6 % for $LiNi_{0.33}Co_{0.33}Mn_{0.33}O_2$. During charging lithium is extracted and the oxidation states of Ni change from +2 to +4 via +3 and of Co from +3 to +4, whereas Mn remains +4 during charge/discharge of the CAM. Since the oxygen 2*p* band overlaps with the M^{3+}/M^{4+} band, some fraction of electrons could be extracted from the oxygen and oxygen loss occurs when charging beyond 4.5 V.[104] This results in an irreversible structural change and should be avoided.

$LiFePO_4$ was first reported by Padhi *et al.*[105] This CAM was considered a promising CAM due to its low cost, abundant availability, low toxicity, low volume effect (6.81 % reduction during oxidation)[106], relatively high specific capacity, low capacity fade and high safety. $LiFePO_4$ has a flat discharge plateau at 3.4 V and a theoretical specific discharge capacity of 170 $mAh \cdot g^{-1}$.[107] $LiFePO_4$ belongs to the space group *Pnma* with Li, Fe and P atoms occupying octahedral 4a, 4c and tetrahedral 4c sites, respectively. Oxygen atoms are in a slightly distorted, hexagonal close-packed arrangement. The separation of the FeO_6 octahedra by PO_4 polyanions significantly reduces the electronic conductivity (10^{-9} $S \cdot cm^{-1}$). The low ionic conductivity results from the slow 1D migration of Li ions limited by the close-packed hexagonal oxygen atoms. Both effects significantly reduce the practical discharge capacity.[108] Different methods were used to increase the electronic conductivity of this CAM. This can be achieved by reducing particle/grain sizes or by applying a conductive layer. Nanostructured $LiFePO_4$ shows significantly improved rate capability.[109] But the synthesis effort is also increased.[110] The increased surface leads to pronounced decomposition reactions and formation of an SEI at the interface to the SE. This significantly reduces the long-term stability of the capacity.[111] Carbon coatings are the most efficient method to increase the electronic conductivity of this CAM and has become an established technique. Electronic conductivity has been increased to 10^{-2} $S \cdot cm^{-1}$ and batteries show very good performance at room temperature.[112]

The various positive properties seem to make $LiFePO_4$ a good candidate for batteries. But its properties are not sufficient for use in the BEV area. The low volumetric energy density is the main disadvantage. This is due to its low density ($\rho_{LiFePO4}$ = 3.53 g·cm^{-3}) compared to other CAM (ρ_{LiCoO2} = 5.05 g·cm^{-3}, $\rho_{LiNi0.3Co0.3Mn0.3O2}$ = 4.78 g·cm^{-3}). It is further reduced if a carbon coating is used on the surface of the CAM. The discharge potential of 3.4 V is lower than with comparable CAM as well. Therefore, it is not possible to achieve energy densities of 800 Wh/L, which is required for BEVs.

Michael Thackeray first proposed $LiMn_2O_4$ for the use as CAM in LIB in the early 1980s.[113] Compared to other oxide-based CAM it is low cost and environmentally friendly. The MnO_2 framework of the structure provides a fast three-dimensional diffusion of lithium-ions. In this oxide the metal cation occupies ¾ of the octahedral sites in the lithium layer, with the other ¼ of octahedra sites vacant. The lithium ions occupy the tetrahedral sites and are face sharing with the empty octahedral site. Excellent rate capability is provided by the 3D Li diffusion path in this CAM. While the average discharge voltage of 4.1 V vs Li^+/Li is particularly high, the theoretical discharge capacity is rather low at 148 mAh·g^{-1}. This prevents batteries with high energy densities, but applications in niche markets where high power densities are needed are possible.

The $LiMn_2O_4$ additionally suffers from severe capacity fading especially at elevated temperatures. Two main mechanisms are known. 1) Dissolution of Mn^{2+} into the electrolyte by corrosion of H^+ ions and 2) irreversible structural transformation from a spinel to tetragonal structure due to the Jahn-Teller active Mn^{3+} ions.[114,115] The dissolution of Mn ions proceeds by the disproportion reaction of Mn^{3+} to Mn^{4+} and Mn^{2+}. An important strategy to suppress the Mn dissolution is doping the CAM. Various dopants such as Ni, Mg, Al, Cr, Zn, Ti, Fe, Co, Ni, Cu, Nd and La were tried to suppress the formation of Mn^{3+} and increase the electrochemical performance.[116] The Ni-doped $LiNi_{0.5}Mn_{1.5}O_4$ shows the best electrochemical performance with a reversible discharge capacity of around 155 mAh·g^{-1} and a discharge voltage of 4.8 V vs Li^+/Li.[117]

2.5.2 Cathode composite

A cathode is influenced by more than just the active material. In a cathode composite, both ionic and electronic percolation paths must be present in order to contact the active material with the separator electrolyte on the one hand and with the current collector on the other. Lithium ions diffuse through the cathode electrolyte and the separator electrolyte towards the anode. The electrons must reach the current collector in order to diffuse to the anode via the external circuit. Furthermore, the cathode composite ideally has contact to all

active material particles. The electrolyte used in the cathode is usually identical to the separator electrolyte. This reduces interfacial resistance between the two components.

Many CAMs show intrinsic electronic conductivity, including $LiCoO_2$, $LiFePO_4$ and the NCM materials.[118] However, depending on the mixing ratios, morphology of the CAM and the desired current density, it may be necessary to add additional additives that provide electronic percolation paths. This is mainly done with different types of carbons. This will be discussed in more detail later in this chapter.

The mixing ratios of the cathode components are decisive for the adequate contacting of the CAM. First the simplest case will be considered, only an electrolyte is added to the CAM. By simulating the microstructure of the cathode, clear conclusions can be drawn about the ionic and electronic percolation paths. This was the central question in the work of Bielefeld *et al.*[17] Depending on the volume ratio of the two cathode components the utilization of the CAM particles during the operation of a battery could be simulated by Bielefeld *et al*.[17] The calculations showed that an optimal mixture contains 86 wt.% CAM and 14 wt.% SE. The optimum ratio is also largely determined by the porosity of the cathode composite, where a realistic value of 20 % porosity was assumed. In earlier publications reporting laboratory experiments, batteries with a ratio of 70:30 wt.% CAM to SE have shown better battery performance than mixtures with ratios of 60:40 or 80:20 wt.%.[119] A possible explanation for the differences may be the mixing of the cathode composite. In practical cells, the components are mixed using a mortar and pestle. In this process and the following pressing, CAM agglomerate and domains are formed which are not electronically contacted. It is difficult to systematically investigate the influence of the preparation technique, therefore only assumptions can be made.

From the simulation by Bielefeld *et al.*[17] it is also seen that the porosity within the cathode composite significantly influences the properties. There are various possibilities to reduce the porosity. Chapter 2.4 focuses on the realization of compact SEs. These considerations can also be applied to the cathode. Examples are also given in this chapter. Small SE particles and compacting at high pressures and elevated temperatures reduce the porosity. In addition, the particle size of the CAM can be reduced, which also results in a reduction of porosity. This improves the contacting of the CAM particles and thus increases the battery performance.[120]

As already mentioned, a mixing ratio of 70:30 wt.% has established itself for the cathode composite. The simulation work of Bielefeld *et al.*[17] and Neumann *et al.*[118] indicates that there are electronic limitations for these mixing ratios. On the one hand, this reduces the discharge capacities, on the other hand, only lower current densities can be realized. The limitation is due to a lack of electronic conduction pathways, based on low contact area between spherical CAM particles. Therefore, not all CAM particles are electronically contacted, these particles

cannot be delithiated/lithiated during battery cycling. Additionally, during delithiation of contacted CAM, the particles shrink. Resulting in a further reduction of contact area and in a possible isolation of certain CAM particles. This volume change can be balanced by liquid electrolytes, but compact SEs compensate this only to a small degree. Furthermore, the electronic conductivity within the CAM particle is reduced for contacted particles during lithiation. If such a particle is only locally connected, high polarization resistances are the result, leading to higher overvoltages and an early reaching of the cut off potential and a non-homogeneous lithiation can result.

The addition of conductive additives to the cathode composite can compensate these problems. Carbon is a suitable material for this purpose, as shown and already established in the field of LIBs. However, there are publications that see a positive impact on SSB performance. Shi *et al.*[18] have shown a positive effect with an addition of 5 wt.% of VGCF. Higher discharge capacities and better performance at higher current densities are the result. However, there are also publications that demonstrate a negative influence on battery capacities. Zhang *et al.*[14] have used various particulate carbons. All of them show an additional decomposition in the charging step of batteries. Dewald *et al.*[15] could prove a redox activity between sulfide electrolytes and carbons by cyclic voltammetry investigations. The influence of carbon additives on cathode composites is therefore part of current research. Walther *et al.*[19] were able to elucidate the underlying degradation mechanism using XPS and ToF-SIMS analysis. The follow-up to this publication is the second publication of this thesis. In this publication carbons with different morphologies and specific surfaces are compared. It is found that the degree of decomposition depends on the specific surface. The morphology of the carbons mainly influences the contact to the CAM. The carbon with the lowest decomposition is identified and a protection concept is developed to further reduce decomposition.

2.5.3 Stability issues and coating strategies

The CAM themselves usually show wide stability windows, even at high potentials. As mentioned in the previous chapter, some CAMs can be irreversibly changed in their structure by too excessive delithiation. This problem can easily be eliminated by using the appropriate potential limits. A central challenge in the use of high-performance CAMs is the narrow stability window of the SEs used. Using thermodynamic calculations, these were evaluated for a large number of SEs.[13] Especially the sulfide SEs have very small stability windows and tend to oxidize during battery discharging (approx. 1.8 - 2.1 V vs Li^+/Li). The resulting decomposition reactions are defined by the applied potential range during battery cycling. At every SE interface, polysulfides and phase changes of the sulfidic electrolyte are present.

Sulfate/sulfite and phosphate formation requires an oxygen source. All common CAM (see chapter 2.5.1) are oxides, therefore these decomposition products are formed at the CAM/SE interface. Additionally, oxygen impurities can be found on the surface of the current collector, carbon additives, battery housing materials (e.g. PEEK) or in the passivation layer of the lithium metal. The products block the ion flow within the cathode composite and CAM particles can be isolated. The capacities and battery performance are reduced.[121,122]

Zhu *et al.*[13] calculated the stability window of various SEs. With higher potentials an oxidation and with lower potentials a reduction of the SE can be present. In the cathode a low chemical potential of lithium is present. When this is beyond the stability window of the cathode an oxidation takes place at the CAM/SE interface. In that paper, the influence of an additional interphase was also calculated. This interphase is intended to compensate the chemical potential difference. The interphase is stable against the low chemical potential (oxidation stable) and shows no electronic conductivity. This is the basis for one of the most active fields of research in the field of cathode research for SSB, i.e. the development of coating concepts of the CAM. For practical reasons, these coatings are applied to the CAM particles by various methods. To give a review of investigated coatings would exceed the scope of this thesis. An overview of known coatings and theories on the functional principle of these coatings can be found in the work of Culver *et al.*[123] In summary, it can be stated that oxide-based coatings both reduce the interfacial resistance and increase the stability of the CAM or SE. $LiNbO_3$ has turned out to be a prototype coating, which is often used. LiO_2-ZrO_2 is also frequently reported. The mechanism behind the function of the coating is still the subject of current research and systematic studies are necessary for an understanding.

Besides the chemical stability problems, the mechanical stability of CAM materials is also critical. The most commonly used NCM consists of spherical secondary particles, which consist of primary particles. The secondary particles are optimized for liquid electrolyte-based cells. It is not yet clear whether this morphology is also advantageous for SSB. The particular feature of $LiCoO_2$ and NCM materials is the volume effect of the CAM. During charging a CAM particle shrinks. Cracks form, which leads to the breaking of the secondary particle. In LIBs this is an advantage, because now the liquid electrolyte can flow into the CAM particle, the contact area is significantly increased and the diffusion paths for lithium ions are reduced. An SE usually cannot fill these newly created cracks and no positive effects are the result. Rather, the diffusion paths increase in this case and a non-homogeneous lithiation of the CAM particle is likely. In addition, fresh contact surfaces can be created between the SE and the CAM particle, which allow the decomposition of the SE to take place.[124]

It is conceivable that suitable coating materials for the CAM particles can have a positive effect. $Ti(OH)_4$ coated CAM showed a reduced crack formation and a more stable cycling

compared to a pristine sample. Especially, the increase in charge transfer resistance between the CAM and the SE for prolonged cycling is reduced with reduced crack formation.[125] But more studies are needed to understand the formation of anisotropic strain and develop methods to reduce CAM crack formation.

2.5.4 Evaluation of the cathode composite of Lee *et al.*

As already mentioned, only the combination of all components (anode, SE and cathode) will result in a battery with high performance. Regarding the cathode, Lee *et al.*[20] used a CAM with a high discharge capacity, but also designed the cathode composite optimally. Lee *et al*. used a nickel-rich NCM ($LiNi_{0.9}0Co_{0.05}Mn_{0.05}O_2$) as CAM, which is characterized by a high discharge capacity of about 200 $mAh \cdot g^{-1}$ at 1C.[126] This discharge capacity is also achieved in the practical cell. Furthermore, the CAM content is high with 85 wt.%, which is in the optimal range, based on the simulations by Bielefeld *et al.*[17]

The CAM also has a LiO_2-ZrO_2 coating to prevent the SE from decomposition. As already mentioned, there are a variety of possible protective layers for the CAM.[123] Besides $LiNbO_3$, LiO_2-ZrO_2 is also a known protective layer, which prevents decomposition. While it has been clearly proven that oxide-based coatings can reduce interfacial contact resistances and improve the stability, the number of detailed systematic studies is still relatively low, and the mechanism behind the functionality of the coatings is not yet well understood. Whether the protective layer used represents the optimal solution must be proven in future systematic studies.

The applied SE is a good choice. The high conductivity (σ_{RT} = 1.8 $mS \cdot cm^{-1}$) is in the range of the conductivity of liquid electrolytes and allows a sufficiently fast transport of lithium ions. The narrow stability window of this SE is addressed by the CAM coating, and a reaction is kept to a minimum. Very small SE particles were used (< 1 µm). This improves the contacting and the porosity of the cathode composite.

Furthermore, carbon nanofibers were used in the cathode composites. These lead to sufficient electronic percolation paths. As already mentioned in chapter 2.5.2, the literature shows that carbon additives induce SE degradation in the cathode. This problem is not addressed in the concept of Lee *et al.*[20] However, it is not commented if the carbon additive is modified by the author or the supplier. It can be concluded that the cathode composite represents the current state of research and addressed most of the potential problems.

3 Results and Discussion

Calculations show that a lithium metal anode has distinct positive properties on energy density and is therefore preferable to a graphene or In/Li anode. At the time of the start of the thesis, an In/Li alloy was mostly used for cells on a laboratory scale. Thus, problems of instability at the An/SE interface could be avoided.

However, when using lithium metal as anode in solid-state batteries, batteries with reasonable performance were obtained (publication 1). The degradation reaction at the Li/SE interface appears to be kinetically inhibited to an extent that cycling is possible. The large number of publications on the topic of solid-state batteries and the inconsistent information in the publications has made it very difficult to classify our own work in the context of the literature. Therefore, it was necessary to review and evaluate the existing literature. The own battery data then serve as comparison for a minimalistic battery cell. For a reasonable review of the published literature it was also necessary to describe the theoretical and mathematical correlations of the parameters for the evaluation of batteries. The first publication therefore provides in summary reliable battery data for an unmodified (no protection concepts) battery cell (Li|LPS|NCM-622), an evaluation of the current literature, the theoretical background to the battery performance and a tool for calculating the battery performance from the basic battery data.

After the performance of the battery cells was shown without modifications, an optimization was performed (publication 2). Simulations of the cathode composite have suggested that there is a deficiency of electronic percolation paths. The focus of the second publication was thus on the investigation of the influence of different carbon additives on cell performance. To a different degree, carbons induce an additional decomposition of the SE in the cathode. The carbon with the smallest degree of decomposition induced was identified. To further reduce the decomposition, a protection concept was developed, which functions according to the principle of an insulated cable, thus reducing the decomposition but not preventing the positive effect of the carbon additives on the battery performance.

3.1 Publication 1: Benchmarking the Performance of All-Solid-State Lithium Batteries

The first publication of this thesis evaluates the performance of solid-state batteries. A general evaluation is often difficult to derive from published reports, due to interdependence of performance measure, due to a lack of a basic reference system and due to missing data. A

battery cell reduced to the minimum of compounds was presented to benchmark the performance of cell reported in literature. In a Ragone-type graph literature data for thiophosphate, oxide-, phosphate- and polymer-based solid-state batteries were compared. Key performance parameters are discussed and calculated by fundamental equations. As a result, research targets could be identified.

The publication was written by the author and edited by the co-authors. The experiments were designed by the author, D. A. Weber, W. G. Zeier, F. H. Richter and J. Janek. The experimental work was carried out by the author and O. Kötz. R. Koerver carried out the XPS measurements. P. Braun, A. Weber and E. Ibers-Tiffée carried out the DRT analysis. Reprinted with permission from *Nat. Energy* Copyright 2020 Springer Nature.

S. Randau, D. A. Weber, D. A.; Kötz, O.; Koerver, R.; Braun, P.; Weber, A.; Ivers-Tiffée, E.; Adermann, T.; Kulisch, J.; Zeier, W. G.; Richter, F. H.; Janek, J., Benchmarking the Performance of All-Solid-State Lithium Batteries, *Nat. Energy*, **2020**, *5* (3), 259–270.

nature energy

ANALYSIS

https://doi.org/10.1038/s41560-020-0565-1

Check for updates

Benchmarking the performance of all-solid-state lithium batteries

Simon Randau[1], Dominik A. Weber[1,4], Olaf Kötz[1], Raimund Koerver[1,5], Philipp Braun[2], André Weber[2], Ellen Ivers-Tiffée[2], Torben Adermann[3], Jörn Kulisch[3], Wolfgang G. Zeier[1], Felix H. Richter[1]✉ and Jürgen Janek[1]✉

Increasing the specific energy, energy density, specific power, energy efficiency and energy retention of electrochemical storage devices are major incentives for the development of all-solid-state batteries. However, a general evaluation of all-solid-state battery performance is often difficult to derive from published reports, mostly due to the interdependence of performance measures, but also due to the lack of a basic reference system. Here, we present all-solid-state batteries reduced to the bare minimum of compounds, containing only a lithium metal anode, β-Li_3PS_4 solid electrolyte and $Li(Ni_{0.6}Co_{0.2}Mn_{0.2})O_2$ cathode active material. We use this minimalistic system to benchmark the performance of all-solid-state batteries. In a Ragone-type graph, we compare literature data for thiophosphate-, oxide-, phosphate- and polymer-based all-solid-state batteries with our minimalistic cell. Using fundamental equations for key performance parameters, we identify research targets towards high energy, high power and practical all-solid-state batteries.

Electrochemical energy storage devices, such as rechargeable batteries, are increasingly important for mobile applications as well as for grid-scale stationary storage. Batteries with simultaneously high energy, power, energy efficiency and energy retention are generally preferred. Lithium-ion battery technology, which uses organic liquid electrolytes, is currently the best-performing energy storage method, especially for powering mobile applications and electric vehicles[1].

However, the recent discovery of new types of highly lithium-ion conducting solid electrolytes has triggered a surge of interest in the all-solid-state battery (ASSB)[2]. In particular, thiophosphate-based solid electrolytes with high ionic conductivity have been developed to reduce internal resistance and improve the rate performance of ASSBs[3]. Oxide-, phosphate- and polymer-based electrolytes have also been developed to create ASSBs, with graphite or lithium metal anode active material (AAM) and intercalation- or conversion-type cathode active material (CAM)[4–7]. Improvements in rate performance[3] due to the large lithium transfer number of most solid electrolytes and potentially negligible interface resistance with AAMs, such as graphite[3] or lithium[8], may result in ASSB cell performance exceeding that of lithium-ion batteries[9].

A central goal in the development of next-generation battery technologies is to maximize the attainable specific energy (cell energy per cell mass) and energy density (cell energy per cell volume). One path to increasing these is by maximizing the anode capacity by using solely lithium metal as the AAM[10]. However, the implementation of a lithium metal anode is hampered by interface reactions, which degrade cell performance, and by dendrite-like growth of lithium, which short-circuits the cells during battery operation[11,12]. Therefore, protective coatings that modify the anode and cathode interfaces with the solid electrolyte are developed to achieve ASSBs with minimized internal resistance and stable cycling[13,14]. Furthermore, many of the cells reported thus far also use polymer binders to help with cell processing, and carbon additives to create sufficient electronic conduction in the cathode composite[15,16].

The interdependence of cell performance measures and the lack of a basic reference system make it difficult to evaluate overall ASSB performance across different cell chemistries. What complicates this further is that many studies focus on demonstrating particular aspects of ASSBs, and the full cell performance is not always described by the same parameters. Therefore, reviews of the ASSB literature usually summarize the cell performance in extensive tables that list a varied selection of parameters[17,18]. Here, we analyse the ASSB literature in relation to minimalistic cells and quantify the target parameters in back-of-the-envelope-style calculations, thus highlighting the main goals for ASSB research.

Literature analysis of model cells

Table 1 lists details of the ASSBs[3–7,15,16,19–37] included in our analysis and compiles the information on the cell components, cycling conditions and selected performance measures, such as specific capacity, C-rate (C), specific energy, specific power and energy efficiency. We include all ASSBs from the literature that allowed us to carry out a consistent full cell analysis. In some cases we selected representative examples, as the inclusion of all reports would have exceeded the scope of this analysis. Most of the cells included in our analysis are not optimized for energy and power, which the reader should bear in mind when interpreting the results. Although industry is in the process of developing optimized ASSBs, data currently available on these are insufficient for a complete analysis. We exclude cells with an indium anode, as this is not considered a viable AAM for practical applications due to its density and cost. We also exclude hybrid cells that use liquids or gels. Whenever available, we include data specified in the original reference. All remaining values are

[1]Institute of Physical Chemistry & Center for Materials Research, Justus-Liebig-University Giessen, Giessen, Germany. [2]Karlsruhe Institute of Technology, Institute for Applied Materials, Karlsruhe, Germany. [3]BASF SE, Ludwigshafen am Rhein, Germany. [4]Present address: Volkswagen AG, Group Research, Wolfsburg, Germany. [5]Present address: BMW Group, München, Germany. ✉e-mail: felix.h.richter@phys.chemie.uni-giessen.de; Juergen.Janek@phys.Chemie.uni-giessen.de

Table 1 | Comparison of battery composition of cell type 1 and cell type 2 with that of previously reported ASSB cells

Reference	Cell composition					Temperature
	Cathode composite			Solid electrolyte	Anode	*T* (°C)
	CAM	Coating	Carbon		AAM	
ASSBs with thiophosphate electrolyte						
Minimalistic cell						
Cell type 1	NCM622	–	–	β-Li_3PS_4	Li	25
Cell type 2	NCM622	–	–	β-Li_3PS_4	Li	25
Intercalation-type CAM and lithium metal						
Whiteley et al.[19]	NCM111	Al_2O_3	Super C65	$Li_{10}SiP_2S_{12}$	Li	25
Zhang et al.[20]	$LiCoO_2$	$LiNbO_3$	–	$Li_{10}GeP_2S_{12}$ with LiH_2PO_4 coating to Li	Li	25
Woo et al.[21]	$LiCoO_2$	Al_2O_3	AB	Catholyte: $Li_{3.35}Ge_{0.35}P_{0.65}S_4$, separator: $77.5Li_2S$–$22.5P_2S_5$	Li	25
Xie et al.[22]	$LiCoO_2$	$LiNbO_3$	–	Catholyte: $Li_{10}GeP_2S_{12}$, separator: $Li_3P_{1-x}Sb_xS_{4-2.5x}O_{2.5x}$	Li	25
Ulissi et al.[23]	NCA	Li_2ZrO_3	Super C65	$75Li_2S$-$25P_2S_5$	Li–C	25
Choi et al.[24]	NCM622	–	Super P	$Li_7P_2S_8I$	Li	55
Intercalation-type CAM and graphite						
Nam et al.[15]	NCM622	$LiNbO_3$	Graphite	Li_6PS_5Cl	Graphite	25
Nam et al.[15]	NCM622	$LiNbO_3$	Graphite	Li_6PS_5Cl	Graphite	25
Yamamoto et al.[25]	NCM111	$LiNbO_3$	Graphite	Li_3PS_4 glass	Graphite	25
Sakuda et al.[16]	NCM111	$LiNbO_3$	AB	$75Li_2S$-$25P_2S_5$	Graphite	30
Kato et al.[3]	$LiCoO_2$	$LiNbO_3$	AB	Catholyte and separator: $Li_{10}GeP_2S_{12}$, anolyte and separator: $Li_{9.6}P_3S_{12}$	Graphite	25
Kato et al.[26]	$LiCoO_2$	$LiNbO_3$	AB	Catholyte: $Li_{10}GeP_2S_{12}$, separator and anolyte: LiI-Li_2S-P_2S_5	Graphite	25
Ito et al.[27]	NCA	Li_2O–ZrO_2	VGCF	$80Li_2S$-$20P_2S_5$	Graphite	25
Kim et al.[28]	$LiCoO_2$	$LiNbO_3$	Super P	Li_6PS_5Cl	Graphite	30
Kraft et al.[29]	NCM622	–	–	$Li_{6.6}P_{0.4}Ge_{0.6}S_5I$	$Li_4Ti_5O_{12}$	60
Conversion-type CAM and lithium metal						
Yamada et al.[30]	S	–	CNF	Li_3PS_4 glass	Li	20
Yao et al.[6]	Co_9S_8	$Li_3P_3S_{11}$	Super P	Catholyte: $Li_{10}GeP_2S_{12}$, separator: $70Li_2S$-$29P_2S_5$-$1P_2O_5$	Li	25
Zhang et al.[31]	NiS–CNT	$Li_{10}GeP_2S_{12}$	Super P	Catholyte: $Li_{10}GeP_2S_{12}$, separator: $70Li_2S$-$29P_2S_5$-$1P_2O_5$	Li	25
ASSBs with oxide/phosphate electrolyte						
Yu et al.[4]	$Li_3V_2(PO_4)_3$	Carbon	Super P	$Li_{1.3}Al_{0.3}Ti_{1.7}(PO_4)_3$	$LiTi_2(PO_4)_3$	30
Finsterbusch et al.[5]	$LiCoO_2$	–	–	$Li_{6.6}La_3Zr_{1.6}Ta_{0.4}O_{12}$	Li	100
ASSBs with inorganic and polymer electrolyte						
Chen et al.[32]	$LiFePO_4$	–	In_2O_5Sn	Composite of PEO–LiTFSI and Al-$Li_{6.75}La_3Zr_{1.75}Ta_{0.25}O_{12}$	Li	60
Park et al.[33]	NCM622	–	Super P	Composite of PBA–$LiClO_4$ and $Li_{1.5}Al_{0.5}Ge_{1.5}(PO_4)_3$	Li	55
Wakayama et al.[34]	$LiCoO_2$	–	–	Catholyte: $Li_7La_3Zr_2O_{12}$, separator: PEO–LiTFSI	Li	50
Ates et al.[35]	NCM622	–	VGCF	Catholyte: β-Li_3PS_4, separator: PEO–LiTFSI	Li	60
ASSBs with polymer electrolyte						
Hovington et al.[7]	$LiFePO_4$	Carbon	AB	PEO–LiTFSI	Li	70
Porcarelli et al.[36]	$LiFePO_4$	–	–	SI–PEO–LiTFSI	Li	70
Bouchet et al.[37]	$LiFePO_4$	Carbon	C65	SI–PEO–LiTFSI	Li	80
Lithium-ion battery						
Panasonic LIB[46]	NCA	ND	ND	Liquid electrolyte	Graphite	25

Panasonic LIB, lithium-ion battery NCR18650B; CAM, cathode active material; NCM622, $Li(Ni_{0.6}Co_{0.2}Mn_{0.2})O_2$; NCM111, $Li(Ni_{0.3}Co_{0.3}Mn_{0.3})O_2$; NCA, $Li(Ni_{0.8}Co_{0.15}Al_{0.05})O_2$; AB, acetylene black; VGCF, vapour-grown carbon fibres; CNF, carbon nanofibres; PEO, poly(ethylene oxide); PBA, poly(1,4-butylene adipate); SI, single ion; LiTFSI, lithium bis(trifluoromethanesulfonyl)imide ($LiC_2F_6NO_4S_2$); AAM, anode active material; ND, no data available. For details, we refer to the corresponding literature sources. Additional information on cell dimension and composition is summarized in Supplementary Table 4, and on cell capacity, voltage and energy efficiency is in Supplementary Table 5.

calculated from the available parameters using the equations specified in Supplementary Table 1 and, if necessary, using approximations listed in Supplementary Tables 2 and 3. Additional information on cell dimensions and composition is summarized in Supplementary Table 4, and on cell capacity, voltage and energy efficiency in Supplementary Table 5.

The literature analysis benefits from comparing with a minimalistic cell, which contains only the bare minimum of compounds and can be assembled by simple pelletization at ambient temperature. We chose to construct cells with lithium metal foil as AAM, β-Li_3PS_4 (LPS) solid electrolyte and $Li(Ni_{0.6}Co_{0.2}Mn_{0.2})O_2$ (NCM) as CAM and did not use protective coatings, carbon additives and binders. It should be noted, however, that Li_2CO_3 and LiOH impurities, stemming from synthesis and storage, may be present on the NCM surface and may influence cell performance[38,39]. We chose β-Li_3PS_4 as the solid electrolyte as it forms a comparatively suitable interphase with lithium metal[40,41]. In addition, sufficient densification of thiophosphate solid electrolytes is achieved by uniaxial stress at ambient temperature[42]. Furthermore, good cycling performance of ASSBs was demonstrated using NCM and β-Li_3PS_4 solid electrolyte in combination with an indium anode[41,43]. A detailed analysis of the cells can be found in Supplementary Figs. 1–9 and Supplementary Tables 6–8.

First, we focus on the initial cell performance. Typically, the obtainable cell energy depends on the power applied during cycling. Both are plotted in a Ragone-type graph[44] excluding the weight of current collectors and cell casing for ASSBs, as the research focus still lies on the cell chemistry before the casing of ASSBs can be optimized (Fig. 1). As indicated by the target region in the top-right corner of the Ragone diagram, an ideal ASSB shows both high specific energy and high specific power. The target region marks a cell with more than 250 Wh kg^{-1} specific energy and a cycling rate of more than 1C, which is the performance of state-of-the-art lithium-ion battery technology (including cell casing)[45,46]. The corresponding Ragone diagram for the energy density and power density is shown in Supplementary Fig. 10, in which the target region marks more than 700 Wh l^{-1} energy density and a cycling rate of more than 1C. Supplementary Fig. 11 also shows a corresponding plot of the area capacity against the current density.

Considering only the specific energy, E_m, obtained at ambient temperature, so far there are no ASSBs that reach the value of lithium-ion batteries. ASSBs with graphite AAM and thiophosphate solid electrolyte lead the field, achieving almost 200 Wh kg^{-1} by either decreasing the thickness of the solid electrolyte separator down to 30 µm with the doctor-blade method[15], or by increasing the thickness of the cathode layer up to 600 µm in the thick electrode configuration[26]. The specific energy of thiophosphate-based ASSBs with lithium metal has been rather modest at ambient temperature (<27 Wh kg^{-1}). This is largely caused by the use of relatively thick lithium metal foils and solid electrolyte separators. Oxide/phosphate-based ASSBs show inferior specific energy compared with thiophosphate-based ASSBs, achieving up to 12 Wh kg^{-1}. ASSBs containing polymer or composite electrolytes achieve higher specific energy up to 288 Wh kg^{-1} using lithium and $LiFePO_4$ as active materials, but require elevated temperatures of 50 to 80 °C, at which the internal resistance of the cells is sufficiently low (Fig. 1b). Use of higher potential CAMs results in oxidative decomposition of the polymer electrolyte[47]. To circumvent this problem, cells using inorganic solid electrolyte in the cathode composite, and a polymer solid electrolyte separator, were developed, but most have comparatively modest specific energy at elevated temperature.

The cathode composite determines the maximum specific energy possible in the cell. It is hypothetically reached if no solid electrolyte separator and anode are considered, while assuming a cell voltage of the cathode composite against Li^+/Li. Therefore, we introduce $E_{m(Ca)}$ as the hypothetical specific energy of the cathode composite, which we define as the cell energy normalized only to the cathode composite mass, while assuming a cell voltage against Li^+/Li. This allows comparison of the performance of the cathode composite between different studies that is independent of the type and quantity of separator and anode material used in the respective study. The resulting literature analysis in Table 2 shows that the highest hypothetical specific energy of the cathode composite achieved was about 400 Wh kg^{-1} with an intercalation-type CAM and about 900 Wh kg^{-1} with a conversion-type CAM at ambient temperature. However, comparison of solely the hypothetical specific energy of the cathode composite probably favours studies with a thinner cathode layer. Therefore, it is especially important to keep the applied layer thicknesses in mind as well and moving towards cells with a higher area capacity. This is emphasized by the observation that most studies achieve similar hypothetical specific energy in the cathode composite (300–400 Wh kg^{-1}), indicating that the large spread of the cell-specific energy observed in Fig. 1 mostly originates simply from variations in the applied layer thicknesses (Fig. 2). Thus, the hypothetical specific energy is especially helpful when comparing model cell systems such as these. Similarly, the hypothetical energy density $E_{V(Ca)}$ can be calculated and compared.

Additionally, the area capacity Q_A (cell capacity divided by cell cross-sectional area) also needs to be high, as this is necessary to achieve cells of sufficient size. While most studies achieve up to 2 mAh cm^{-2}, some have demonstrated up to 14 mAh cm^{-2} (see Table 2). Correspondingly, the area energy E_A can be compared as well. It is obtained by dividing the energy of the cell by the cell cross-sectional area. Most studies achieve up to 75 Wh m^{-2}. Some have demonstrated up to 574 Wh m^{-2}. However, it is vital that the hypothetical specific energy and the area energy are increased simultaneously, as the former is a specific property of the cathode composite, while the latter is indicative of cell size.

Whereas the specific energy also depends on the density of the materials used in the cell, the energy density E_V is solely dependent on the layer thicknesses within the cell. While the hypothetical energy density of the cathode composite, analogous to the hypothetical specific energy, determines the maximum achievable energy density, the layer thicknesses of the anode and separator simply need to be minimized. Free-standing lithium foil as thin as 20 µm is currently available commercially and solid electrolyte layers of less than 50 µm have already been demonstrated (Fig. 2 and Supplementary Table 4)[15,31,48]. Due to the low density of lithium, the impact of the lithium foil thickness on energy density is larger than on the specific energy of a cell. Nonetheless, the trends discussed for the specific energy also apply when comparing energy density (Supplementary Fig. 10).

When using solid electrolytes with lithium transfer number close to unity and high ionic conductivity, ASSBs with intercalation-type electrodes can provide higher power than lithium-ion batteries normalized to the CAM content[3]. More than 1,000 W kg^{-1} specific power, P_m, was demonstrated, albeit at comparatively low specific energy using a graphite anode. Polymer-based ASSBs struggle to achieve similar specific power, even at elevated temperatures. Generally, specific power depends on the cell potential, area density (mass of cell divided by cell area) and current density (see Supplementary Table 1). As the cell potential changes during cycling, specific power at any given point during discharge is dependent on the state of charge. Therefore, we plot the average specific power during discharge at constant current density in the Ragone diagram.

Sometimes, the C-rate (specific current of CAM divided by specific capacity of CAM) is stated instead of the current density, j (current divided by cell area). Both parameters are important descriptors, but for different aspects. Whereas the current density through the cross-section area of the cell is directly comparable between cells, the C-rate also depends on the cell capacity obtained, which varies between studies. For example, a cell with smaller area capacity requires a lower current density to achieve the same C-rate. Consequently, the C-rate remains ambiguous if the capacity to which it refers is not explicit. Therefore, current density should be preferred as the value stated in the experimental section. The C-rate may be reported in the results section on the basis of the obtained capacity. It is listed as such in Table 2.

Current density is a critical parameter to evaluate the occurrence of a short-circuit due to lithium penetration of the solid electrolyte

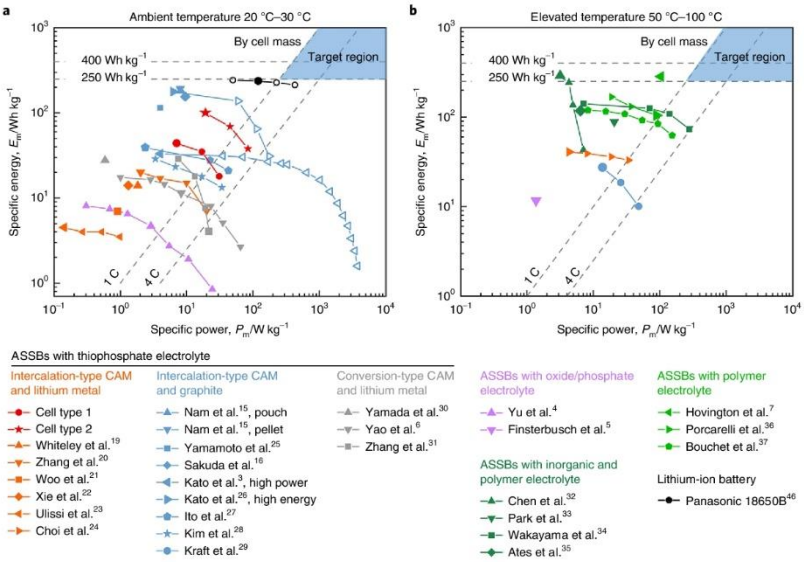

Fig. 1 | Ragone plots for cells cycled at different temperatures. a,**b**, Ambient (20–30 °C) (**a**) and elevated (50–100 °C) (**b**) temperature. Dashed lines indicate targets for specific energy and C-rate. The area in blue depicts the target region where both energy and rate performance excel. The specific energy shown here is the energy delivered by the cell during discharge, normalized to the cell mass. The specific power is the average power delivered by the cell during discharge, normalized to the cell mass. For ASSBs, the weight of the cell casing and current collectors is omitted here. Literature data for the performance comparison of cells were obtained as indicated in Table 1. ASSBs with thiophosphate solid electrolyte, intercalation-type CAM and lithium metal (orange); ASSBs with thiophosphate solid electrolyte, intercalation-type CAM and graphite (blue); ASSBs with thiophosphate solid electrolyte, conversion-type CAM and lithium metal (grey); ASSBs with polymer electrolyte (light green); ASSBs with inorganic and polymer electrolyte (dark green); and ASSBs with oxide/phosphate electrolyte (violet) and a commercial lithium-ion battery (black) are compared. Our own data for the Ragone plot were obtained from the discharge curves of cell type 1 and cell type 2 cycled at 25 °C (red). Large symbols indicate conditions under which prolonged cycling was demonstrated and correspond to data detailed in Table 1. Small symbols indicate data points of the corresponding rate test if available. Filled symbols indicate data of cells that were charged and discharged at equal current density. Empty symbols indicate cycling data in which the rate test was only applied to discharge, whereas charging was carried out at lower current.

separator. Whereas a current density exceeding 20 mA cm^{-2} has been demonstrated with graphite-type ASSBs[3], applying a prolonged current density of 1 mA cm^{-2} and more with a lithium metal anode is usually accompanied by internal shorting of the cell, often referred to as lithium dendrite formation. Nonetheless, prolonged cycling of an ASSB with lithium metal anode at 1.27 mA cm^{-2}, and up to 12.7 mA cm^{-2} in a rate test, has been demonstrated at ambient temperature. In another study, the critical current density at which the short-circuit occurs in LPS was increased from 0.7 mA cm^{-2} to 2.0 mA cm^{-2} by introducing a LiF-rich solid electrolyte interphase between Li_3PS_4 and lithium[39]. The C-rate and specific current (current per gram of CAM) are most important for studies investigating the CAM and cathode composite performance. However, this requires that CAM-related processes dominate the factors limiting cell performance.

The internal resistance R influences the overpotential, η, energy efficiency and power capability of the cell during cycling. It can be directly compared between cells, when noted as area-normalized resistance in Ω cm^2, simply using the cross-section area of the cell. However, care needs to be taken as it is dependent on the state of charge. As little as 14 Ω cm^2 internal resistance at ambient temperature was demonstrated for an ASSB with graphite AAM, thiophosphate solid electrolyte and $LiCoO_2$[3]. Via Ohm's law, the overpotential of the cell is directly linked with the applied current density and the internal resistance. A substantial overvoltage in the cell leads to a large discrepancy between the energy required for charge and that released during discharge.

The energy efficiency of the charge–discharge sequence, $\Phi_{E(ch\text{-}dis)}$ (energy of nth discharge divided by energy of nth charge), needs to be maximized in the interests of reducing energy loss during battery cycling. It is the product of the corresponding Coulomb efficiency, $\Phi_{Q(ch\text{-}dis)}$ (capacity of nth discharge divided by capacity of nth charge), and voltage efficiency, $\Phi_{V(ch\text{-}dis)}$ (average voltage of nth discharge divided by average voltage of nth charge). As the Coulomb efficiency must necessarily be high to allow long-term cycling of a secondary battery, the voltage efficiency is usually the critical factor that determines the energy efficiency of each cycle (Supplementary Fig. 12).

Estimating the energy efficiency of the surveyed literature was often only possible by extracting the average charge and discharge voltages from the voltage profiles presented. Cells with intercalation-type CAM mostly exceed 90% energy efficiency from the 2nd cycle onwards, and so far surpass that of cells with conversion-type CAM (Table 2 and Supplementary Table 5). This is in part explained by the higher cell voltages of the intercalation-type CAMs, as any

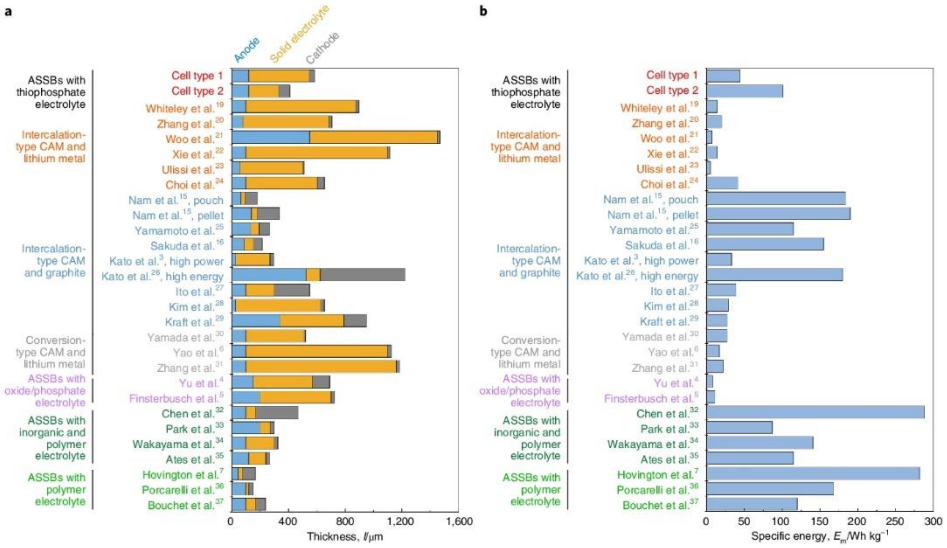

Fig. 2 | Relationship between layer thicknesses and specific energies of analysed ASSBs. a,b, Representation of layer thicknesses of ASSBs (**a**) and the corresponding cell-specific energies as histograms (**b**). Corresponding data are available in Supplementary Tables 2 and 4.

overvoltage will affect energy efficiency less for cells operating at higher voltage. Analysis of the minimalistic cells shows that voltage efficiency decreases during cycling, indicating an increase in overpotential of the cell (Supplementary Fig. 12).

When it comes to battery cycling analysis, energy retention, $\Phi_{E(dis/dis1)}$ (energy of discharge of nth cycle divided by energy of discharge of first cycle), is the key parameter as it covers both contributions to energy loss: capacity loss and overpotential increase. Generally, capacity loss is the dominant factor, with the additional influence of the change in overpotential typically having less effect on energy retention (Supplementary Fig. 12). Therefore, cell ageing is often reported by plotting capacity as a function of the cycle number, as shown in Supplementary Fig. 13. Additionally, the development of the specific energy of the cell during cycling, as plotted in Fig. 3a, also indicates high and low specific energy cells and allows the comparison of cells with different types of CAM in one diagram.

Still, the number of cycles tested and the area energy delivered by the tested cell per cycle vary strongly between studies. On the cell level, the goal is to maintain high specific energy per cycle while delivering greater area energy. Hence, Fig. 3b plots the specific energy of cycle n against the area energy delivered during all discharges up to cycle n (delivered area energy $\Sigma_n E_A$), which is more indicative of the overall cell performance. Comparison of the two types of plots shows that a low cycle number can still translate into a substantial area-normalized energy being delivered, depending on the area capacity[26]. The total delivered area energy ($\Sigma_{tot} E_A$) over all cycles shown in the original references is listed in Table 2.

In terms of energy retention during cycling at ambient temperature, ASSBs with a protected lithium anode, thiophosphate-based solid electrolyte and intercalation-type CAM[20], as well as with conversion-type CAM[6], excel, achieving 1.26 Wh cm^{-2} and 1.93 Wh cm^{-2}, respectively, for delivered area energy ($\Sigma_{tot} E_A$) with little capacity loss over 500 and 1,000 cycles, respectively. These examples demonstrate the importance of protective layers in preventing battery degradation. Pretreatment of lithium metal with 80 wt% H_3PO_4 solution to form a LiH_2PO_4 protective layer was shown to improve the energy retention of the lithium metal anode[20]. Similarly, the addition of 1% P_2O_5 to Li_2S–P_2S_5 glass stabilized the lithium–thiophosphate interface over 1,000 cycles[6]. Amongst the high specific energy cells at ambient temperature, cells with $LiNbO_3$-coated $LiCoO_2$ and graphite show the most stable cycling[26]. At elevated temperatures, the energy retention of cells with polymer electrolytes is excellent with $LiFePO_4$ and lithium, achieving 8.45 Wh cm^{-2} delivered area energy over 1,400 cycles[7]. Also, the $Li_{6.6}La_3Zr_{1.6}Ta_{0.4}O_{12}$-based cell showed excellent energy retention with $LiCoO_2$ and lithium at 100 °C (ref. [3]). On the cathode side, $LiNbO_3$ is a suitable coating for $LiCoO_2$, allowing excellent energy retention, as demonstrated in cells with thiophosphate-based solid electrolytes and lithium metal[20] as well as graphite AAM[3,26].

There is as yet no singular set of parameters commonly used for the characterization of ASSBs and their performance across different studies. On the basis of the fundamental definitions and equations describing battery performance (Supplementary Table 1), we identified a practical set of parameters that can be directly compared, and from which all others can be calculated. These are listed and commented on in Table 3. Supplementary Data 1 demonstrates how the performance measures can be calculated from this set of parameters by modifying the values of the input parameters as described in the Methods.

Amongst the less commonly reported values, the average voltage and its development during cycling is most critical, as without it neither specific energy nor specific power can be calculated from the capacity alone. Impedance measurements are required to evaluate solid electrolyte ionic conductivity and charge transfer resistances of the electrodes. Cycling performance is also reported inconsistently, varying over a large range of cycles, time, current density and

Table 2 | Comparison of battery performance of cell type 1 and cell type 2 with previously reported ASSB cells

Reference	Results of initial cycle(s)									Cycling test			
	j_1[a] (mA m^{-2})	q_{dis} (mAh g^{-1})	C-rate (h^{-1})	E_m (Wh kg^{-1})	$E_{m(Ca)}$[b] (Wh kg^{-1})	Q_A (mAh cm^{-2})	E_A (Wh m^{-2})	$\Phi_{E(ch-dis)}$[c] (%)	j_2[a] (mA cm^{-2})	P_m (W kg^{-1})	j_3[a] (mA cm^{-2})	Cycles (in total)	$\Sigma_{cyc}E_A$ (Wh cm^{-2})
ASSBs with thiophosphate electrolyte													
Minimalistic cell													
Cell type 1	0.178	128	0.16	44	328	1.14	42	92	0.89	30.9	0.178	211	0.56
Cell type 2	0.356	107	0.19	100	276	1.91	71	91	1.78	84.0	0.356	230	0.93
Intercalation-type CAM and lithium metal													
Whiteley et al.[19]	0.082	125[d]	0.13	14[e]	308[e]	0.64[d]	23[e]	95[d]	0.082	1.8[e]	0.082	75	0.17
Zhang et al.[20]	0.075[e]	133	0.1	20[d,e]	308[e]	0.83	28[d,e]	98[d]	0.75	20.0[e]	0.075[e]	500	1.26
Woo et al.[21]	0.045	121[d]	0.13	7[d]	175[d]	0.46[d]	17[d]	91[d]	0.045	0.9[d]	0.045	25	0.03
Xie et al.[22]	0.066	134	0.09	14[e]	411[e]	0.79	26[e]	97[d]	0.066	1.3[e]	0.066	50	0.12
Ulissi et al.[23]	0.004	100	0.03	5[d]	197[d]	0.14	5[d]	91[d]	0.032	1.0[d]	0.004	100	0.03
Choi et al.[24]	0.12	170	0.1	42	440	1.19	44	93	1.2	34.0	0.12	40	0.15
Intercalation-type CAM and graphite													
Nam et al.[15]	0.147[e]	121	0.04	190[f]	377	3.55	136	96[d]	0.147	7.9[e,f]	0.147[e]	19	0.25
Nam et al.[15]	0.072[e]	112	0.04	184[f]	350	1.60	72	97[d]	0.072	8.2[e,f]	0.072[e]	13	0.07
Yamamoto et al.[25]	0.064	116	0.03	115	319	1.85	65	59[d]	0.064	4.0	0.064	ND	ND
Sakuda et al.[16]	0.064	114	0.06	155	397[e]	1.08	56	92[d]	0.064	9.2[e]	0.064	15	0.06
Kato et al.[3]	0.067	114[d]	0.12	33	266[e]	0.55[d]	21	97[d]	91.31	3,745.0[d]	0.067	30	0.06
Kato et al.[26]	0.50	123	0.04	180	311[e]	14.18	574	98[d]	20.0	175.7[e]	0.50	10	0.53
Ito et al.[27]	0.05	121[d]	0.06	39[d]	268[d]	0.82[d]	29[d]	ND	1.0	42.6[d]	0.05	100	0.28
Kim et al.[28]	0.14	119	0.1	29[e]	388[e]	1.19	44[e]	84[d]	1.4	33.9[e]	0.14	ND	ND
Kraft et al.[29]	1.71	99	0.51	27[d]	249[d,e]	3.40	71[d]	89[d]	6.84	48.0[d]	1.71	50	0.40
Conversion-type CAM and lithium metal													
Yamada et al.[30]	0.025	1,600	0.02	27[d,e]	912[d,e]	0.96	22[d,e]	84[d]	0.025	0.6[d,e]	0.025	10	0.02
Yao et al.[6]	0.13	647	0.06	17[d,e]	386	2.33	33[d,e]	78[d]	12.73	64.9[d,e]	1.27	1,000	1.93
Zhang et al.[31]	0.57	550	0.18	22[d,e]	359[d,e]	3.14	46[d,e]	71[d]	5.73	28.8[d,e]	5.73	150	0.18
ASSBs with oxide/phosphate electrolyte													
Yu et al.[4]	0.043	102	0.04	8	166[e]	1.01	11	ND	4.29	24.4	0.43	500	0.44
Finsterbusch et al.[5]	0.10	118	0.12	11[e]	232[e]	0.83	32[e]	92	0.1	1.4[e]	0.10	70	0.16
ASSBs with inorganic and polymer electrolyte													
Chen et al.[32]	0.10	155	0.01	288[e]	362[e]	9.42	294[e]	81[d]	0.3	7.1[e]	0.10	11	0.29
Park et al.[33]	0.24[e]	170	0.24	87[e]	377[e]	1.02	37[e]	95[f]	0.24	21[e]	0.24[e]	100	0.33
Wakayama et al.[34]	0.08[e]	136	0.05	141[e]	471[e]	1.59	59[e]	95	3.08	278.8[e]	0.08[e]	ND	ND
Ates et al.[35]	0.06	136	0.06	115[e]	341[e]	1.01	39[e]	95	0.06	6.3[e]	0.06	50	0.23
ASSBs with polymer electrolyte													
Hovington et al.[7]	0.81[e]	158	0.36	282[e]	364[e]	2.32	73[e]	87[d]	0.81	100.3[e]	0.81[e]	1,400	8.45
Porcarelli et al.[36]	0.09[e]	152	0.11	168[e]	336[e]	0.79	25[e]	ND	0.43	91.4[e]	0.43	300	0.43
Bouchet et al.[37]	0.05[e]	162	0.07	120[e]	329[e]	0.78	26[e]	ND	1.6	153.6[e]	0.05[e]	ND	ND
Lithium-ion battery													
Panasonic LIB[46]	ND	ND	0.2	243	ND	ND	ND	ND	ND	50	ND	ND	ND

Panasonic LIB, lithium-ion battery NCR18650B (specific energy and specific power values also take cell casing into account); ND, no data available. Unless indicated otherwise, values represent the performance of the initial discharge cycle(s) and were either specified or calculated (Supplementary Table 1) entirely from values specified in the respective reference. [a]j_1: lowest available current density; j_2: highest available current density; j_3: current density at which prolonged cycling was demonstrated. [b]Hypothetical specific energy of the cathode composite. $E_{m(Ca)}$ is based solely on the cathode composite weight and assumes that the anode potential is equivalent to Li^+/Li. For graphite 0.1 V, for $Li_4Ti_5O_{12}$ 1.5 V and for $LiTi_2(PO_4)_3$ 2.5 V average potential versus Li^+/Li was assumed. [c]The energy efficiency of the charge–discharge sequence was obtained from the second cycle, except for Whitely et al.[19], Yamamoto et al.[25], Kraft et al.[29] and Yamada et al.[30], where it was obtained from the first cycle, and Woo et al.[21], where it was obtained from the third cycle. [d]Not all data were available as number values in the respective reference. Data were extracted from figures in the respective reference, as detailed in Supplementary Tables 2 and 3. [e]Not all data were available in the respective references to calculate these values. Approximations had to be made as detailed in Supplementary Tables 2 and 3. [f]Weight of cell also includes weight of current collectors.

discharge capacity. Whenever possible, the area-normalized energy delivered until 80% of the original specific energy is reached, as well as the retained specific capacity after 100 cycles, should be reported. Correlating energy retention during cycling with the development of internal resistance may provide further insights into the degradation mechanism. A plot of the resistances obtained from impedance analysis against the cycle number can help to identify the cause for an increase in overpotential that may occur during cycling[27]. However, care needs to be taken in this analysis, as the internal resistance is also dependent on the state of charge.

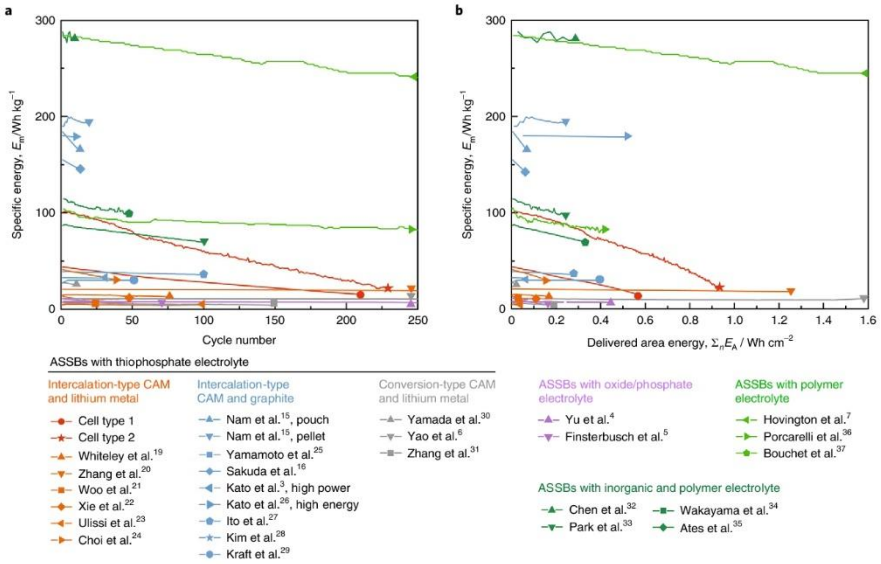

Fig. 3 | Cycling results of analysed ASSBs. a,**b**, Specific energy per cycle versus cycle number (**a**) and specific energy per cycle versus the sum of cell area-normalized energies (**b**) delivered by the cell during all discharges up to the respective cycle number. The applied current densities and obtained specific energies of the first discharge are detailed in Table 2. Because data for the development of the overpotential during cycling are mostly not available, we solely applied the capacity loss proportionally to the initial specific energy of the respective cell. This means assuming that the overpotential remains constant during cycling, which is acceptable here, as energy retention is usually dominated by capacity retention. To ensure clarity of the images, the cycling results extending beyond the *x* axis scale were truncated at 250 cycles or 1.6 Wh cm^{-2}, respectively. Each line is composed of as many data points as numbers of cycles available for each cell. Individual points were omitted for clarity. Symbol meanings are the same as in Fig. 1. The sole purpose of the symbol at the end of each line is as a cell identifier.

Performance prediction

Estimating cell performance measures on the basis of idealized assumptions is helpful to specify targets for research, while maintaining all parameters within reasonable margins. For example, increasing the CAM fraction in the cell is suitable to achieve higher energy density. However, this inherently means that the current density needs to be increased to maintain a high C-rate, requiring lower internal resistance of the cell. Hence, the cell performance and cell requirements can simply be estimated for any cell system using the fundamental equations for the specific energy, energy density, specific power, energy efficiency and Ohm's law (Supplementary Table 1). Several examples of these back-of-the-envelope-style calculations of cell performance are given in Supplementary Data 2. For the purposes of simplification, the internal resistance is assumed to be independent of the state of charge and the corresponding overvoltage applied equally to charge and discharge. Minority components, such as polymer binder and conducting carbon, are omitted in the following thought experiments. Three examples are described here. The corresponding boundary conditions and input parameters are discussed in Supplementary Table 9.

Example 1 in Supplementary Data 2 describes variants of an ASSB with lithium, thiophosphate solid electrolyte and NCM with an area capacity of 5 mAh cm^{-2} by variable layer thicknesses and weight fraction of CAM. To have a chance to exceed 400 Wh kg^{-1} energy density with NCM, the specific discharge capacity needs to exceed 170 mAh g_{CAM}^{-1} in an 89-µm-thick cathode composite containing 85 wt% CAM, in a cell with 40 µm thiophosphate solid electrolyte separator and 20 µm lithium metal anode. Also, the maximum allowed internal resistance can be calculated. To achieve a cell with 5 mAh cm^{-2}, 90% energy efficiency and a cycling rate of 1C, the internal resistance must be less than 40 Ω cm^2. Varying the lithium thickness of said cell demonstrates its substantial influence on the energy density. The same argument is valid for varying the solid electrolyte thickness. Without solid electrolyte and lithium metal, the hypothetical energy density of the composite cathode is obtained, which corresponds to the maximum attainable value with the respective cathode composite.

Following the same procedure, lithium and $LiNi_{0.5}Mn_{1.5}O_4$ (LNMO, example 2 in Supplementary Data 2) as well as lithium and Li_2S (example 3 in Supplementary Data 2) cells were evaluated. While the high potential of LNMO allows for higher internal resistance of the cell (<49 Ω cm^2) at similar specific energy, the conversion-type ASSBs promise to substantially increase specific energy, but require much lower internal resistance. With the assumed limitation of 5 mA cm^{-2} (see Supplementary Table 9), a lithium–sulfur cell can reach about 700 Wh kg^{-1} if the internal resistance is below 23 Ω cm^2 (assuming: 20 µm lithium foil, 40 µm thiophosphate solid electrolyte, 31 µm cathode composite, 70 wt% sulfur in the cathode composite, 90% energy efficiency and a 1C rate).

For a general comparison of ASSBs, we calculate the maximum allowed internal resistance and achievable specific energy (Supplementary Data 3) for each CAM (NCM, LNMO, Li_2S) and

Table 3 | A set of parameters necessary for an overall characterization of battery performance

Parameter	Frequency of reporting and parameter description
Cell components	Widely reported; describes the composition.
Cell area, *A*	Mostly reported; indicates the size of the cell.
Layer mass, *m*, or area density, ρ_A	Mostly reported; required to calculate specific energy and specific power. Area density is to be preferred over the absolute layer mass used in the experiment as it is directly comparable between cells of different area.
Layer thickness, *l*	Often reported; required to calculate energy density and power density. Useful to directly compare different cell types and sizes of cells.
Applied pressure, *p*	Often reported; important for cell preparation and cycling conditions.
Temperature, *T*	Widely reported; important for cycling conditions, as it influences the internal resistance.
Current, *I*, or current density, *j*	Mostly reported; indicates conditions of cycling. To be preferred over the C-rate as it is independent of cell design and CAM specific capacity.
Average voltage, *U*	Rarely reported as a value; it is mostly available from the charge–discharge curves, but very cumbersome to extract for the reader. It should always be reported as it is required to calculate energy, power and energy efficiency. Its development over time contains information on cell degradation.
Specific capacity, *q*	Mostly reported for charge and discharge; sometimes only available from a graph.
Internal resistance, *R*	Although the ionic conductivity of the solid electrolyte is widely reported, the charge transfer resistances are less analysed and the internal resistance of ASSBs is often only available from the impedance plots. If possible, the resistances of the solid electrolyte separator and the charge transfer processes at anode and cathode are to be distinguished. Its development over time contains information on cell degradation and can be placed in context with the development of the overvoltage during cycling.
Rate test	Inconsistently reported; the specific energy at a current density of 0.1 mA cm^{-2} and a rate test to indicate power performance should be reported.
Energy retention	Inconsistently reported; mostly demonstrated as plots of capacity versus cycle number. Additionally, a plot of the specific energy against the delivered area energy of the cell allows a more general comparison between cells. As values, the energy retention after 100 cycles and the delivered area energy (in Wh cm^{-2}) until 80% of the original specific energy remains can be stated.

solid electrolyte (PEO–LiTFSI, Li_6PS_5Cl, $Li_7La_3Zr_2O_{12}$) combination, dependent on the area capacity (1–10 mAh cm^{-2}), while maintaining a 1C rate and 90% energy efficiency. We assume the theoretical capacity for each CAM and that all cells contain a 20-µm lithium metal foil anode. In the input parameters, we vary the volume fraction of CAM in the cathode composite (25 vol%, 50 vol%, 75 vol%), separator thickness (200 µm, 50 µm, 20 µm) and the use of current collectors (15 µm aluminium, 15 µm copper). Figure 4 shows the results. The smaller the internal resistance needs to be, the more challenging it is to develop such a system. Supplementary Fig. 14 plots the required current density against the specific energy following the same analysis.

For example, viewing the data in Fig. 4 shows that at a separator thickness of 200 µm the lower cell voltage conversion-type systems are at a disadvantage to intercalation-type systems with higher cell voltage. Lower internal resistance and higher current density must be achieved to obtain the same specific energy and cycling performance. Most ASSBs to date use even thicker separators than this, which may explain the superior performance of ASSBs with intercalation-type CAMs observed so far (Fig. 1).

At 50-µm separator thickness, it depends on the density of the solid electrolyte as to whether the resistance advantage lies with intercalation- or conversion-type cells. Exceptionally high specific energy beyond 500 Wh kg^{-1} can only be achieved with the conversion-type systems. Regarding the required current density, the advantage of conversion-type cells demonstrates itself already at 50-µm separator thickness (Supplementary Fig. 14). Likewise, higher volume fraction of CAM in the cathode composite benefits conversion-type systems, such as Li–S ASSBs.

With exceptionally thin (20 µm) and low-density separators (PEO–LiTFSI), conversion systems offer a substantial advantage over intercalation-type cells to achieve very high specific energy. However, the trends so far only consider the bare cells without current collectors. The additional weight introduced when current-collector foils are required affects the conversion-type cells more than the higher voltage intercalation-type cells. The influence is so strong that any Li–S ASSB that uses a copper and an aluminium current collector of 15-µm thickness each per cell, must achieve lower cell resistance than a higher voltage intercalation-type cell for the same specific energy.

Due to the reasons stated above, we have so far focused on the specific energy of ASSBs. However, depending on the application, volume limitations may be critical, thus making the attainable energy density the decisive factor. Our equivalent analysis of the energy density versus the required internal resistance is shown in Supplementary Fig. 15. The results demonstrate that, here, conversion-type cell systems are at a striking disadvantage over higher voltage systems, underlining the emphasis that the automotive industry places on high-voltage cell systems.

Overall, this comparison demonstrates the importance of developing cells with thinner separators and better processing techniques to achieve the internal resistance and current density requirements for high energy and high power ASSBs. At 200-µm separator thickness, achieving this appears improbable unless substantial advances in solid electrolyte ionic conductivity are made. Reducing excess cell weight, for example, by bipolar stacking, might prove especially important for conversion-type cells to achieve exceptionally high specific energy where cell weight plays a critical role, such as in aerospace applications.

Research targets

From the above analysis, it seems that all the necessary tools are now at hand to obtain a pellet-type ASSB with more than 250 Wh kg^{-1} and stable cycling by combining $LiNbO_3$-protected $LiCoO_2$ as the positive electrode[26], a thiophosphate solid electrolyte[13,15] and protected lithium

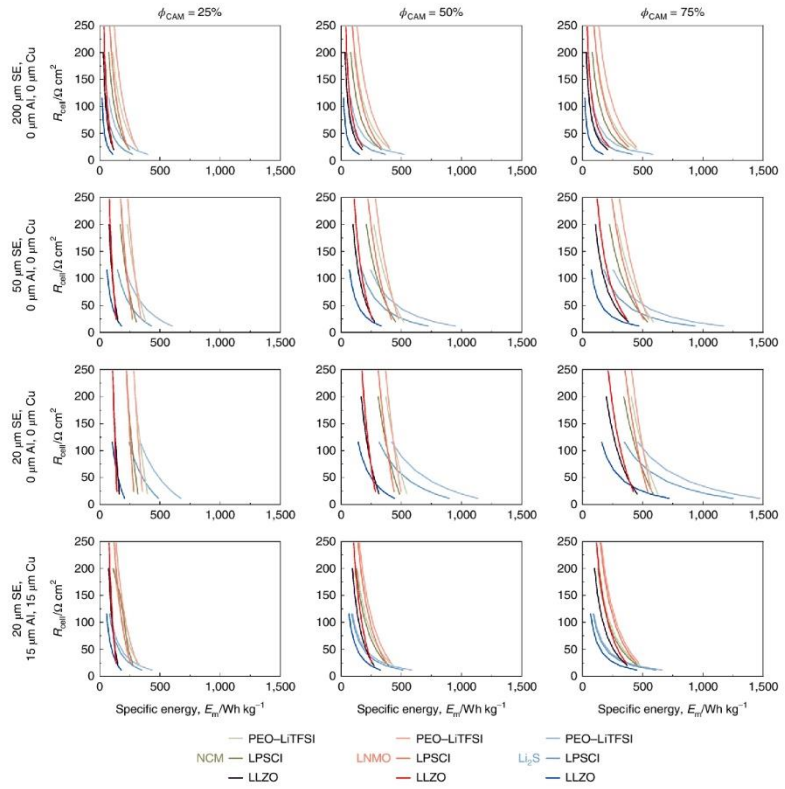

Fig. 4 | The maximum allowed internal resistance and achievable specific energy for intercalation- and conversion-type cell systems. These are calculated by varying the area capacity using Supplementary Data 3. NCM, LNMO and Li_2S cathode materials and solid electrolytes PEO–LiTFSI (density of 1.2 g cm^{-3}), Li_6PS_5Cl (LPSCl, density of 1.87 g cm^{-3}) and $Li_7La_3Zr_2O_{12}$ (LLZO, density of 5.14 g cm^{-3}) are compared. Theoretical specific capacity of each CAM is assumed. Each point (area capacity) indicates the achievable specific energy and the internal resistance requirement for 90% energy efficiency at a rate of 1C. A thickness of 20 µm of lithium foil is used for this calculation. Comparison is carried out at equal current density, that is, equal area capacity. Hence, variation of the cathode composite thickness is required to set cell capacity to 1.0, 1.3, 1.8, 2.7, 4.0, 6.0 or 10.0 mAh cm^{-2} (low to high specific energy). Values of 200, 50 or 20 µm solid electrolyte, 25 vol%, 50 vol% or 75 vol% volume fraction φ_{CAM} of CAM in the cathode composite and the addition of aluminium and copper foil current collectors (each 15 µm thick) are compared by modifying the input parameters in Supplementary Data 3.

metal as the negative electrode[30] (see example 4 in Supplementary Data 2). However, the specific energy is not the only parameter of importance. A high specific power beyond 250 W kg^{-1} requires cells with less than about 40 Ω cm^2 of internal resistance. Optimizing cell design will play an important role in achieving these targets.

Comparing the requirements obtained from performance prediction with our literature survey indicates what has already been achieved and which targets still need to be met. This identifies the research goals listed in Table 4. An important problem yet to be solved in the solid state is accessing the theoretical specific capacity of CAMs. For example, the theoretical specific capacity of NCM has been shown to be about 200 mAh g^{-1} in cells using liquid electrolytes[50], while ASSBs with NCM struggle to exceed 150 mAh g^{-1} at ambient temperature. Furthermore, CAM content in the composite cathode needs to be increased to maximize hypothetical specific energy[51,52]. The development of highly conducting (>10 mS cm^{-1}), electrochemically compatible solid electrolytes will help with these targets. Also, new coatings for NCM-type CAMs are to be developed to reduce charge transfer resistance and increase capacity retention. New processing methods will allow creation of larger cells. Important targets for conversion-type cells are increased cell voltage, reduced internal resistance, increased CAM content, decreased separator thickness and increased current density.

On the anode side, formation of a lithium metal anode in situ, without the initial addition of lithium foil, would substantially increase energy density and facilitate cell manufacturing[53]. Also, lithium dendrite growth is expected to occur at higher current densities. Therefore, it is important to develop reliable methods

Table 4 | Research targets to achieve high energy and power ASSBs

Parameter	Target description
Cell voltage, V	Lithium metal has been identified as the key anode material. Development of intercalation-type CAMs, such as NCM or LNMO, to achieve high energy density, and conversion-type CAMs, to achieve high specific energy, is ongoing.
Specific capacity, q	Practical specific capacity needs to reach theoretical values at ambient temperature, for example, NCM ~200 mAh g^{-1}, Li_2S 1,166 mAh g^{-1}, LNMO 147 mAh g^{-1}.
Volume fraction of CAM in cathode composite, $\phi_{CAM/Ca}$	Most studies apply a volume fraction of CAM of 40–60 vol% in the cathode composite. Increasing this to more than 70 vol% is an important target to increase specific energy and energy density[51,52].
Hypothetical specific energy, $E_{m(Ca)}$, and area capacity, Q_A	These are the key to maximize specific energy and energy density. Cathode composites exceeding 500 Wh kg^{-1} (versus Li^+/Li by weight of cathode composite only) and 5 mAh m^{-2} are desired.
Current density, j	Dendrite formation needs to be prevented at a current density of at least 5 mA cm^{-2} (refs. [49,54]).
Energy efficiency, Φ_E	The desired energy efficiency determines the allowed overvoltage. Using Ohm's law, the maximum allowed internal resistance of the cell is estimated from the allowed overvoltage and the desired current density. More than 90% should be achieved.
Internal resistance, R	A high specific energy cell requires less than about 40 Ω cm^2 internal resistance to allow cycling at 1C with more than 90% energy efficiency[3].
Lithium thickness, l_{An}	Concepts of reducing lithium layer thickness are under development[50]. Ideally, introduction of excess lithium would not be required and lithium would stem solely from the CAM.
Solid electrolyte thickness, l_{SE}	Solid electrolyte thickness of as little as 30 µm has been demonstrated[15,48]. Further reducing layer thickness increases specific energy and reduces internal resistance.
Cathode composite thickness, l_{Ca}	The thickness of the composite cathode requires a balance of increasing specific energy of the cell by increasing thickness, while remaining within a practical window for the required current density.
Cell area, A	Thin composite cathodes and solid electrolyte separators can be prepared at small scale. Creation of the lithium metal anode in a pouch-type set-up with inorganic electrolytes remains a challenge. Large-area cells with more than 200 cm^2 remain to be demonstrated for ASSBs with inorganic electrolytes[15,52].
Pressure, p	The most successful ASSBs so far applied external pressure during cycling of the cell. For practical applications, the requirement for excessive pressure should be avoided.
Additives	The roles of binders and conductive carbon additives need to be investigated further[55–57].
Energy retention	Cycling tests aim to demonstrate a cell that maintains more than 80% of its original specific energy over 1,000 cycles and at least 5 Wh cm^{-2} delivered area energy.

to prevent lithium dendrite formation up to at least 10 mA cm^{-2} (ref. [54]). Finally, a discussion of binders and conductive carbon additives was beyond the scope of our analysis, but their influence on cell performance and cell degradation must also be investigated further[55–57]. With these challenges solved, excluding cell casing, ASSBs with specific energy beyond 400 Wh kg^{-1}, energy density beyond 1,000 Wh l^{-1} and more than 90% energy efficiency at a 1C rate are within reach (Fig. 4 and Supplementary Fig. 15).

Conclusions

Starting out with a survey of the ASSB literature, it is evident that a comparison of cell performance is not always directly accessible. Therefore, we present an extensive analysis of the performance measures of the best-performing all-solid-state batteries in our literature overview. This demonstrates that the differences in specific energy and specific power of the multitude of available ASSBs mostly originate from differences in layer thicknesses and internal resistance. To compare these with a basic reference system, we present an all-solid-state battery using only a lithium metal anode, β-Li_3PS_4 solid electrolyte and $Li(Ni_{0.6}Co_{0.2}Mn_{0.2})O_2$ cathode active material. We intentionally did not apply material coatings or carbon additives so that these cells can serve as minimalistic references. The Ragone plot and the plot of the cycle-dependent specific discharge energy offer direct comparison of different cell chemistries and varying cycling protocols relative to our minimalistic cells. This demonstrates that high specific energy and high specific power ASSBs using lithium metal remain elusive as long as thick separators are used. Cycling tests show that further research is required to develop protective coatings, especially for high-voltage CAMs. Using the fundamental equations that determine battery performance, we identify and quantify key research targets, such as achieving less than 40 Ω cm^2 internal resistance, less than 50 µm separator thickness, in-situ generation of the anode, more than 5 mAh cm^{-2} area capacity and 500 Wh kg^{-1} hypothetical cathode specific energy. Thus, our analysis projects a pathway to lithium metal ASSBs and highlights the remaining challenges still to be overcome in order to surpass the performance of state-of-the-art lithium-ion batteries.

Methods

Literature analysis. We include all ASSBs from the literature that allowed us to carry out a consistent full cell analysis (Tables 1 and 2). In some cases, we selected representative examples, as the inclusion of all reports would have exceeded the scope of this analysis. Most of the cells included in our analysis are not optimized for energy and power, which we ask the reader to bear in mind when interpreting the results. To obtain all parameters for the literature overview, we identified the parameters available in each publication individually and calculated the remaining parameters one by one to complete the set. In some cases, we had to make assumptions to approximate unavailable parameters, as described in Supplementary Table 2.

Calculating performance measures. As summarized in Supplementary Data 1, the experimental data obtained for cell type 1 and 2 are used as input parameters (highlighted in grey) to calculate the corresponding performance measures (highlighted in colour) in the same line. The underlying formula can be identified by double-clicking on the respective cell. The calculation is set up such that the performance measures are automatically calculated from the input parameters of the same row. Exception: at least two consistent consecutive lines of data are required to correctly calculate efficiency, cumulative and retention parameters for cell cycling analysis. An explanation of the symbols and columns is given in the tab labelled 'legend' of the Supplementary Data 1.

Using Supplementary Data 1, the reader can easily analyse their own experiments by replacing the data for the input parameters with the corresponding complete set of their own data. The resulting performance indicators are then automatically calculated using the embedded formula and cell references. To add additional rows with full functionality for analysis, simply copy complete rows of data into rows without data or select the filled cells to be used for the calculation and drag the fill handle upwards or downwards.

To gauge the performance potential of solid-state batteries by calculating examples 1 to 4 described in the section on 'Performance prediction', we demonstrate thought experiments for all-solid-state lithium batteries in Supplementary Data 2. Supplementary Data 2 functions, in principle, in the same way as Supplementary Data 1. However, instead of experimental data used as the input parameters, values are varied within reason to predict the corresponding performance measures.

In Supplementary Data 3, we calculate the achievable specific energy for intercalation- and conversion-type lithium ASSBs and the corresponding maximum allowed internal resistance and the minimum required current density. The results are used to calculate the data for Fig. 4 and Supplementary Figs. 14 and 15 by varying the input parameters within reason (see Supplementary Table 9). Supplementary Data 3 functions, in principle, in the same way as Supplementary Data 1. The reader can modify the input parameters, to match their interest. The figures included in the spreadsheet table are updated automatically, as are the corresponding performance measures.

All three spreadsheets can, in principle, also be applied to other battery types and can be modified to accommodate additional performance measures of interest.

Materials. BASF SE provided the crystalline solid electrolyte β-Li_3PS_4 (1.2×10^{-4} S cm^{-1}) and the $Li(Ni_{0.6}Co_{0.2}Mn_{0.2})O_2$ (NCM) active material for this study. All chemicals were stored in an argon-filled glovebox ($H_2O < 0.1$ ppm and $O_2 < 0.1$ ppm). X-ray diffraction patterns and scanning electron microscopy (SEM) images of LPS and NCM are available in Supplementary Figs. 16–19. The NCM active material was dried in a vacuum at 250 °C (Büchi furnace) overnight. A disc of lithium foil of approximately 120 µm thickness and 9 mm diameter was used as the anode. The composite cathode consists of dried NCM ($\rho = 4.78$ g cm^{-3})[58] and β-Li_3PS_4 ($\rho = 1.83$ g cm^{-3})[59] in a mass ratio of 70:30 (volume ratio 47:53). The NCM and LPS powders were ground in an agate mortar for 15 min by hand before cell assembly, forming the cathode mixture.

Li | LPS | NCM cell assembly. The cell casing was manufactured in-house as described in detail previously[42,43]. The Li | β-Li_3PS_4 | NCM:β-Li_3PS_4 (Li | LPS | NCM:LPS) cells (Supplementary Fig. 1) were assembled within an argon-filled glovebox. For cell assembly, one of the stainless steel stamp current collectors was used to close one side of a polyether ether ketone cylinder with a diameter of 10 mm, into which all materials were added via the remaining opening. First, 60 mg of the β-Li_3PS_4 solid electrolyte was added and the powder was uniformly compressed manually with the second stainless steel stamp current collector. Then, 10 mg of cathode composite (NCM:LPS was 70:30 by weight; 8.9 mg cm^{-2}) was distributed evenly on top of the smooth LPS surface, corresponding to an area capacity of 1.78 mAh cm^{-2} on the basis of a theoretical specific capacity of 200 mAh g_{CAM}^{-1} (ref. [60]). For cells with higher area capacity, the amounts of LPS and cathode composite were modified as specified in the respective section. The stack was then compressed uniaxially between the stainless steel stamp current collectors at 30 kN (that is, ~380 MPa, for cells with higher area capacity the pressure needed to be reduced to 25 kN) for 3 min before adding the lithium disc anode (thickness: 120 µm, diameter: 9 mm) and a copper foil disc (thickness: 40 µm, diameter: 10 mm) to the cell illustrated in Supplementary Fig. 1. The copper foil is used for stabilization of the battery stack during disassembly. Without copper foil, lithium would stick to the steel current collectors and complete removal of the battery would be impossible, complicating post-experiment analysis. Finally, a pressure of approximately 50 MPa was applied using an external frame, which remained in place during all electrochemical measurements.

Electrochemical characterization. Charge and discharge tests were performed using a VMP-300 Biologic and a MACCOR potentiostat/galvanostat. Cells using lithium as anode material were repeatedly charged galvanostatically to 4.3 V and discharged to 2.6 V versus Li^+/Li at 25 °C. The applied current density was 0.178 mA cm^{-2} corresponding to a 0.1C rate for cells with an area capacity of 1.78 mAh cm^{-2}. For the rate test and cells with higher area capacity, the current density was modified accordingly. Electrochemical impedance spectroscopy (EIS) was performed using an EC-Lab Electrochemistry VMP-300 Biologic before the first charge step and for the first five cycles after reaching the cut-off voltages and 10 min of pause (open circuit voltage measurement). EIS was conducted in the frequency range 7 MHz to 1 Hz, applying a 10-mV signal amplitude.

X-ray photoelectron spectroscopy. X-ray photoelectron spectroscopy (XPS) was employed to identify decomposition products and the binding states of the used battery materials. The measurements were carried out using a PHI5000 Versa Probe II with an Al anode. Exposure to air was avoided by using a transfer vessel filled with argon, which was loaded inside the argon-filled glovebox. A surface area of 100 µm × 1,400 µm (X-ray spot size) was investigated and an X-ray power of 100 W was used. The pass energy of the analyser was set to 187.9 eV for survey scans and 23.5 eV for detailed spectra. A charge correction was carried out for all spectra, to a binding energy of 284.8 eV referring to the C 1s line corresponding to adventitious carbon. CasaXPS v.2.3.17 software was used to evaluate the received spectra.

SEM of battery cross-sections. The all-solid-state battery was cut in half using an ultrasonic knife (Sonofile, SF-0102) and the received cross-section was analysed by SEM. The SEM images of the cross-sections did not show signs of mixing of the different battery materials due to the cutting process, that is, clean cross-sections were obtained, the cutting area was sharp and there was no smearing of materials. Microstructure images of disassembled battery components were obtained on a high-resolution scanning electron microscope (Merlin, Carl Zeiss AG). An acceleration voltage of 3 kV and a sample current of 150 pA were applied. The secondary electron detector was used to record the images.

Distribution of relaxation times (DRT) analysis. Previous publications[61,62] have shown that it is favourable to deconvolute impedance data in the space of relaxation times. This so-called DRT method enables a refined separation of physical processes even if they are strongly overlapping in the Nyquist diagram. Each process is represented as a local maximum in a continuous distribution function. The advantage is that processes with close time constants can be separated and a physically motivated equivalent circuit model can be established. Furthermore, Schönleber et al.[63] proved that any non-oscillating electrochemical system can be correctly described using the DRT.

Data availability

All data generated or analysed during this study are included in this Analysis and its Supplementary Information files.

Received: 14 May 2019; Accepted: 24 January 2020;
Published online: 09 March 2020

References

1. Schmuch, R., Wagner, R., Hörpel, G., Placke, T. & Winter, M. Performance and cost of materials for lithium-based rechargeable automotive batteries. *Nat. Energy* **3**, 267–278 (2018).
2. Hayashi, A., Noi, K., Sakuda, A. & Tatsumisago, M. Superionic glass-ceramic electrolytes for room-temperature rechargeable sodium batteries. *Nat. Commun.* **3**, 856 (2012).
3. Kato, Y. et al. High-power all-solid-state batteries using sulfide superionic conductors. *Nat. Energy* **1**, 16030 (2016).
4. Yu, S. et al. Monolithic all-phosphate solid-state lithium-ion battery with improved interfacial compatibility. *ACS Appl. Mater. Interfaces* **10**, 22264–22277 (2018).
5. Finsterbusch, M. et al. High capacity garnet-based all-solid-state lithium batteries: fabrication and 3D-microstructure resolved modeling. *ACS Appl. Mater. Interfaces* **10**, 22329–22339 (2018).
6. Yao, X. et al. High-energy all-solid-state lithium batteries with ultralong cycle life. *Nano Lett.* **16**, 7148–7154 (2016).
7. Hovington, P. et al. New lithium metal polymer solid state battery for an ultrahigh energy: nano C-$LiFePO_4$ versus nano $Li_{1.2}V_3O_8$. *Nano Lett.* **15**, 2671–2678 (2015).
8. Krauskopf, T., Hartmann, H., Zeier, W. G. & Janek, J. Toward a fundamental understanding of the lithium metal anode in solid-state batteries—an electrochemo-mechanical study on the garnet-type solid electrolyte $Li_{6.25}Al_{0.25}La_3Zr_2O_{12}$. *ACS Appl. Mater. Interfaces* **11**, 14463–14477 (2019).
9. Zhu, G.-L. et al. Fast charging lithium batteries: recent progress and future prospects. *Small* **15**, 1805389 (2019).
10. Liu, J. et al. Pathways for practical high-energy long-cycling lithium metal batteries. *Nat. Energy* **4**, 180–186 (2019).
11. Takeda, Y., Yamamoto, O. & Imanishi, N. Lithium dendrite formation on a lithium metal anode from liquid, polymer and solid electrolytes. *Electrochemistry* **84**, 210–218 (2016).
12. Porz, L. et al. Mechanism of lithium metal penetration through inorganic solid electrolytes. *Adv. Energy Mater.* **7**, 1–12 (2017).
13. Zhu, Y., He, X. & Mo, Y. Strategies based on nitride materials chemistry to stabilize Li metal anode. *Adv. Sci.* **4**, 1–11 (2017).
14. Culver, S. P., Koerver, R., Zeier, W. G. & Janek, J. On the functionality of coatings for cathode active materials in thiophosphate-based all-solid-state batteries. *Adv. Energy Mater.* **9**, 1900626 (2019).
15. Nam, Y. J., Oh, D. Y., Jung, S. H. & Jung, Y. S. Toward practical all-solid-state lithium-ion batteries with high energy density and safety: comparative study for electrodes fabricated by dry- and slurry-mixing processes. *J. Power Sources* **375**, 93–101 (2018).
16. Sakuda, A. et al. All-solid-state battery electrode sheets prepared by a slurry coating process. *J. Electrochem. Soc.* **164**, A2474–A2478 (2017).
17. Ma, J., Chen, B., Wang, L. & Cui, G. Progress and prospect on failure mechanisms of solid-state lithium batteries. *J. Power Sources* **392**, 94–115 (2018).

18. Kerman, K., Luntz, A., Viswanathan, V., Chiang, Y.-M. & Chen, Z. Review—practical challenges hindering the development of solid state Li ion batteries. *J. Electrochem. Soc.* **164**, A1731–A1744 (2017).
19. Whiteley, J., Woo, J. H., Hu, E., Nam, K. & Lee, S. Empowering the lithium metal battery through a silicon-based superionic conductor. *J. Electrochem. Soc.* **161**, A1812–A1817 (2014).
20. Zhang, Z. et al. Interface re-engineering of $Li_{10}GeP_2S_{12}$ electrolyte and lithium anode for all-solid-state lithium batteries with ultralong cycle life. *ACS Appl. Mater. Interfaces* **10**, 2556–2565 (2018).
21. Woo, J. et al. Nanoscale interface modification of $LiCoO_2$ by Al_2O_3 atomic layer deposition for solid-state Li batteries. *J. Electrochem. Soc.* **159**, A1120–A1124 (2012).
22. Xie, D. et al. High ion conductive Sb_2O_5-doped β-Li_3PS_4 with excellent stability against Li for all-solid-state lithium batteries. *J. Power Sources* **389**, 140–147 (2018).
23. Ulissi, U., Agostini, M., Ito, S., Aihara, Y. & Hassoun, J. All solid-state battery using layered oxide cathode, lithium-carbon composite anode and thio-LISICON electrolyte. *Solid State Ionics* **296**, 13–17 (2016).
24. Choi, S.-J. et al. LiI-doped sulfide solid electrolyte: enabling a high-capacity slurry-cast electrode by low-temperature post-sintering for practical all-solid-state lithium batteries. *ACS Appl. Mater. Interfaces* **10**, 31404–31412 (2018).
25. Yamamoto, M., Terauchi, Y., Sakuda, A. & Takahashi, M. Binder-free sheet-type all-solid-state batteries with enhanced rate capabilities and high energy densities. *Sci. Rep.* **8**, 1212 (2018).
26. Kato, Y. et al. All-solid-state batteries with thick electrode configurations. *J. Phys. Chem. Lett.* **9**, 607–613 (2018).
27. Ito, S. et al. A rocking chair type all-solid-state lithium ion battery adopting Li_2O-ZrO_2 coated $LiNi_{0.8}Co_{0.15}Al_{0.05}O_2$ and a sulfide based electrolyte. *J. Power Sources* **248**, 943–950 (2014).
28. Kim, D. et al. Infiltration of solution-processable solid electrolytes into conventional Li-ion-battery electrodes for all-solid-state Li-ion batteries. *Nano Lett.* **17**, 3013–3020 (2017).
29. Kraft, M. A. et al. Inducing high ionic conductivity in the lithium superionic argyrodites $Li_{6+x}P_{1-x}Ge_xS_5I$ for all-solid-state batteries. *J. Am. Chem. Soc.* **140**, 16330–16339 (2018).
30. Yamada, T. et al. All solid-state lithium–sulfur battery using a glass-type P_2S_5–Li_2S electrolyte: benefits on anode kinetics. *J. Electrochem. Soc.* **162**, A646–A651 (2015).
31. Zhang, Q. et al. Nickel sulfide anchored carbon nanotubes for all-solid-state lithium batteries with enhanced rate. *J. Mater. Chem. A* **6**, 12098–12105 (2018).
32. Chen, R. et al. Addressing the interface issues in all-solid-state bulk-type lithium ion battery via an all-composite approach. *ACS Appl. Mater. Interfaces* **9**, 9654–9661 (2017).
33. Park, M., Jung, Y. & Kim, D. Hybrid solid electrolytes composed of poly(1,4-butylene adipate) and lithium aluminum germanium phosphate for all-solid-state $Li/LiNi_{0.6}Co_{0.2}Mn_{0.2}O_2$ cells. *Solid State Ionics* **315**, 65–70 (2018).
34. Wakayama, H., Yonekura, H. & Kawai, Y. Three-dimensional bicontinuous nanocomposite from a self-assembled block copolymer for a high-capacity all-solid-state lithium battery cathode. *Chem. Mater.* **28**, 4453–4459 (2016).
35. Ates, T., Keller, M., Kulisch, J., Adermann, T. & Passerini, S. Development of an all-solid-state lithium battery by slurry-coating procedures using a sulfidic electrolyte. *Energy Storage Mater.* **18**, 31261–31264 (2018).
36. Porcarelli, L. et al. Single-ion triblock copolymer electrolytes based on poly(ethylene oxide) and methacrylic sulfonamide blocks for lithium metal batteries. *J. Power Sources* **364**, 191–199 (2017).
37. Bouchet, R. et al. Single-ion BAB triblock copolymers as highly efficient electrolytes for lithium-metal batteries. *Nat. Mater.* **12**, 452–457 (2013).
38. Kim, J., Hong, Y., Ryu, K. S., Kim, M. G. & Cho, J. Washing effect of a $LiNi_{0.83}Co_{0.15}Al_{0.02}O_2$ cathode in water. *Electrochem. Solid-State Lett.* **9**, A19–A23 (2006).
39. Visbal, H. et al. The influence of the carbonate species on $LiNi_{0.8}Co_{0.15}Al_{0.05}O_2$ surfaces for all-solid-state lithium ion battery performance. *J. Power Sources* **269**, 396–402 (2014).
40. Liu, Z. et al. Anomalous high ionic conductivity of nanoporous β-Li_3PS_4. *J. Am. Chem. Soc.* **135**, 975–978 (2013).
41. Phuc, N. H. H., Morikawa, K., Mitsuhiro, T., Muto, H. & Matsuda, A. Synthesis of plate-like Li_3PS_4 solid electrolyte via liquid-phase shaking for all-solid-state lithium batteries. *Solid State Ionics* **23**, 2061–2067 (2017).
42. Zhang, W. et al. Interfacial processes and influence of composite cathode microstructure controlling the performance of all-solid-state lithium batteries. *ACS Appl. Mater. Interfaces* **9**, 17835–17845 (2017).
43. Koerver, R. et al. Capacity fade in solid-state batteries: interphase formation and chemomechanical processes in nickel-rich layered oxide cathodes and lithium thiophosphate solid electrolytes. *Chem. Mater.* **29**, 5574–5582 (2017).
44. Ragone, D. V. *Review of Battery Systems for Electrically Powered Vehicles* SAE Technical Paper 680453 (SAE, 1968).
45. van Noorden, R. A better battery. *Nature* **507**, 26–28 (2014).
46. Sanyo Energy. *Panasonic NCR18650B Specification* (2012); https://www.batteryspace.com/prod-specs/NCR18650B.pdf.
47. Keller, M., Varzi, A. & Passerini, S. Hybrid electrolytes for lithium metal batteries. *J. Power Sources* **392**, 206–225 (2018).
48. Fu, K. (K). Three-dimensional bilayer garnet solid electrolyte based high energy density lithium metal-sulfur batteries. *Energy Environ. Sci.* **10**, 1568–1575 (2017)..
49. Fan, X. et al. Fluorinated solid electrolyte interphase enables highly reversible solid-state Li metal battery. *Sci. Adv.* **4**, eaau9245 (2018).
50. Chen, S. et al. High-efficiency lithium metal batteries with fire-retardant electrolytes. *Joule* **2**, 1–11 (2018).
51. Sakuda, A., Hayashi, A., Ohtomo, T., Hama, S. & Tatsumisago, M. All-solid-state lithium secondary batteries using $LiCoO_2$ particles with pulsed laser deposition coatings of Li_2S–P_2S_5 solid electrolytes. *J. Power Sources* **196**, 6735–6741 (2011).
52. Hippauf, F. et al. Overcoming binder limitations of sheet-type solid-state cathodes using a solvent-free dry-film approach. *Energy Storage Mater.* **21**, 390–398 (2019).
53. Krauskopf, T. et al. Lithium-metal growth kinetics on LLZO garnet-type solid electrolytes. *Joule* **3**, 2030–2049 (2019).
54. Albertus, P., Babinec, S., Litzelman, S. & Newman, A. Status and challenges in enabling the lithium metal electrode for high-energy and low-cost rechargeable batteries. *Nat. Energy* **3**, 16–21 (2018).
55. Yoon, K., Kim, J.-J., Seong, W. M., Lee, M. H. & Kang, K. Investigation on the interface between $Li_{10}GeP_2S_{12}$ electrolyte and carbon conductive agents in all-solid-state lithium battery. *Sci. Rep.* **8**, 8066 (2018).
56. Zhang, W. et al. The detrimental effects of carbon additives in $Li_{10}GeP_2S_{12}$-based solid-state batteries. *ACS Appl. Mater. Interfaces* **9**, 35888–35896 (2017).
57. Hakari, T., Sato, Y., Yoshimi, S., Hayashi, A. & Tatsumisago, M. Favorable carbon conductive additives in Li_3PS_4 composite positive electrode prepared by ball-milling for all-solid-state lithium batteries. *J. Electrochem. Soc.* **164**, A2804–A2811 (2017).
58. Huang, Z. et al. Structural and electrochemical properties of Mg-doped nickel based cathode materials $LiNi_{0.8}Co_{0.2}Mn_{0.2-x}Mg_xO_2$ for lithium ion batteries. *RSC Adv.* **5**, 88773–88779 (2015).
59. Homma, K. et al. Crystal structure and phase transitions of the lithium ionic conductor Li_3PS_4. *Solid State Ionics* **182**, 53–58 (2011).
60. Nitta, N., Wu, F., Lee, J. T. & Yushin, G. Li-ion battery materials: present and future. *Mater. Today* **18**, 252–264 (2015).
61. Schichlein, H., Müller, A. C., Voigts, M., Krügel, A. & Ivers-Tiffée, E. Deconvolution of electrochemical impedance spectra for the identification of electrode reaction mechanisms in solid oxide fuel cells. *J. Appl. Electrochem.* **32**, 875–882 (2002).
62. Ivers-Tiffée, E. & Weber, A. Evaluation of electrochemical impedance spectra by the distribution of relaxation times. *J. Ceram. Soc. Jpn* **125**, 193–201 (2017).
63. Schönleber, M. & Ivers-Tiffée, E. Approximability of impedance spectra by RC elements and implications for impedance analysis. *Electrochem. Commun.* **58**, 15–19 (2015).

Acknowledgements

Financial support from the Federal Ministry of Education and Research (BMBF) within the FELIZIA project (grant nos. 03XP0026G and 03XP0026J) and the FESTBATT consortium (grant no. 03XP0177A) is acknowledged. We acknowledge discussions with T. Ates, S. Culver, C. Dietrich, M. Keller, P. Minnmann, C. Pompe, N. Riphaus, J. Sann and M. Weiß.

Author contributions

S.R., D.A.W., W.G.Z., F.H.R. and J.J. designed the experimental work. S.R. and O.K. conducted the experimental work. R.K. carried out and analysed the XPS measurements. P.B., A.W. and E.I.-T. carried out the DRT analysis. T.A. and J.K. provided the solid electrolyte and cathode active material. S.R. and F.H.R. analysed the literature data and cell performance prediction. S.R., F.H.R. and J.J. wrote the manuscript. F.H.R. and J.J. directed this work. All authors commented on the manuscript.

Competing interests

D.A.W. is now employed by Volkswagen AG and R.K. is now employed by BMW group.

Additional information

Supplementary information is available for this paper at https://doi.org/10.1038/s41560-020-0565-1.

Correspondence and requests for materials should be addressed to F.H.R. or J.J.

Reprints and permissions information is available at www.nature.com/reprints.

Publisher's note Springer Nature remains neutral with regard to jurisdictional claims in published maps and institutional affiliations.

3.2 Publication 2: On the Additive Microstructure in Composite Cathodes and Alumina-Coated Carbon Microwires for Improved All-Solid-State Batteries

Carbon-based conductive additives improve the performance of conventional lithium ion batteries. However, their influence in solid-state batteries is yet not fully understood. In the second publication the influence of several carbon additives with different morphologies and surface areas were investigated on the cell performance. Cycling tests and microstructure-resolved simulations show that a higher utilization of the cathode active material can be achieved with fiber-shaped additives. However, carbon additives generally lead to an increased capacity loss during cycling and an enhanced formation of decomposition products. The latter was studied in more detail using cyclovoltammetry, X-ray photoelectron spectroscopy and cycling experiments. To overcome the issues caused by the use of carbon additives, a protection concept is developed.

The publication was written by the author and edited by the co-authors. A. Neumann, K. Becker-Steinberger, T. Danner, S. Hein and A. Latz conducted the simulation experiments and wrote the respective sections. The experiments were designed by the author and F. Walther under the supervision of B. Mogwitz, J. Sann, F.H. Richter and J. Janek. The author and Y. Schneider carried out the experiments. R. S. Negi applied the carbon coating by ALD. F. Walther carried out the XPS analysis.

CHEMISTRY OF MATERIALS

pubs.acs.org/cm Article

On the Additive Microstructure in Composite Cathodes and Alumina-Coated Carbon Microwires for Improved All-Solid-State Batteries

Simon Randau, Felix Walther, Anton Neumann, Yannik Schneider, Rajendra S. Negi, Boris Mogwitz, Joachim Sann, Katharina Becker-Steinberger, Timo Danner, Simon Hein, Arnulf Latz, Felix H. Richter, and Jürgen Janek*

Cite This: https://dx.doi.org/10.1021/acs.chemmater.0c04454 Read Online

ACCESS | Metrics & More | Article Recommendations | Supporting Information

ABSTRACT: All-solid-state batteries promise to enable lithium metal anodes and outperform state-of-the-art lithium-ion battery technology. To achieve high battery capacity, utilization of the active material in the cathode must be maximized. Carbon-based conductive additives are known to improve the capacity and rate performance of electrode composites. However, their influence on cathode composites in all-solid-state batteries is yet not fully understood. Here, we study the influence of several carbon additives with different morphologies and surface areas on the performance of an all-solid-state battery cell Li|β-Li_3PS_4|$Li(Ni_{0.6}Co_{0.2}Mn_{0.2})O_2$/$\beta$-$Li_3PS_4$/carbon. Cycling tests and microstructure-resolved simulations show that higher utilization of the cathode active material can be achieved using fiber-shaped vapor-grown carbon additives, whereas particle-shaped carbons show a minor influence. Unfortunately, carbon additives generally lead to an accelerated capacity loss during cycling and an enhanced formation of solid electrolyte decomposition products. The latter was studied in more detail using cyclic voltammetry, X-ray photoelectron spectroscopy, and cycling experiments. The results show that carbon additives with a small surface area and a fiber-like morphology result in the lowest degree of decomposition. To completely overcome electrolyte degradation caused by the use of carbon additives, a protection concept is developed. A thin alumina coating with a few nanometers thickness was deposited on the carbon fibers by atomic layer deposition, which successfully prevents decomposition reactions, reduces long-term capacity fading, and leads to an enhanced overall all-solid-state battery performance.

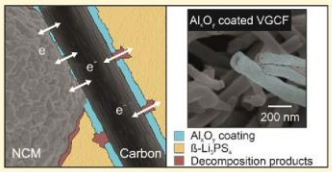

INTRODUCTION

The search for next-generation battery systems with increased energy and power density, longer cycle life, and improved safety has attracted significant interest in recent years, especially in the automotive sector.[1] The currently well-established lithium-ion batteries are limited by degradation as well as safety risks and rate limitations arising from the use of organic liquid electrolytes. These challenges include, for example, flammability of the organic liquid electrolytes, reactivity with the electrode materials, and a low lithium-ion transport number.[2] All-solid-state batteries (ASSBs) are considered as a promising alternative, however, presenting their own challenges on the way to commercial use.[3,4]

With the use of a solid electrolyte (SE), the overall safety of the device is expected to improve because SEs are more stable at higher temperatures and are less flammable.[4] The SE may also lead to an increase in energy and power density, if lithium metal can be used as anode.[5] Finally, the ionic conductivity of several SEs is meanwhile competitive with those of organic liquid electrolytes.[6−8] Thiophosphate-based SEs seem to be particularly promising because of their high ionic conductivities, good mechanical compatibility, and relatively low costs.[9] Nonetheless, it is still a great challenge to achieve high-performing ASSBs that can compete with LIBs.

In general, poor thermodynamic stability of the SE,[10,11] chemo-mechanical coupling,[12,13] and interface kinetics[14] are the remaining major challenges. At the anode, the reduction of thiophosphate SEs by lithium metal occurs and a solid electrolyte interphase (SEI) forms.[11,15] In the cathode composite, side reactions take place at three locations. First, decomposition takes place at the current collector/SE interface at high potentials.[16] Second, reactions occur between cathode active materials (CAM), such as $Li(Ni_{0.6}Co_{0.2}Mn_{0.2})O_2$ (NCM), and the SE resulting in resistive interfacial layers.[17−19] Third, once a carbon conductive additive is used, decomposition reactions are induced at the carbon/SE interface.[20]

Received: November 18, 2020
Revised: January 23, 2021

https://dx.doi.org/10.1021/acs.chemmater.0c04454
Chem. Mater. XXXX, XXX, XXX−XXX

To achieve high charge and discharge current densities and effectively utilize all CAM particles, a homogeneous current distribution and balance between ionic (SE particles) and electronic percolation pathways with low impedance is crucial.[21−23] The limited intrinsic electronic conductivity of CAMs can be rate-limiting,[24,25] especially because the often spherical shape of CAM particles means that the electronic contact area between particles in the cathode composite is small. To overcome this limitation, carbon additives play a central role to improve the electronic percolation network.

Beside experimental studies, simulations[22,26] on the continuum scale allow to analyze the effect of the electrode composition, conductive additives, and microstructure on battery performance and lifetime.[27] This approach was recently demonstrated for ASSB cells using two different classes of SEs, namely, LLZO[28] and thiophosphates.[25] Moreover, physico-chemical models enable to discriminate the contributions of different degradation mechanisms. With these results, the characteristics for an ideal carbon additive for ASSBs can be identified.

Recent reports indicate that carbon additives lead to an additional decomposition reaction of the SE at the carbon surface, especially during charge (within typical the potential range for NCM-based ASSBs), which can have a strong influence on cell performance.[29−32] However, in these studies only one type of additive was considered, the influence of different morphologies and surfaces was not considered in detail. Furthermore, in some cases only small amounts of the additive were used (1 wt %). Here, we will show that a threshold fraction of the vapor-grown carbon fiber (VGCF) additive (3 wt %) has to be exceeded to form a sufficient percolation network. The sample preparation also influences the percolation network, and the use of a ball mill leads to high energy input into the composite and can already induce first decomposition reactions, which can interfere with cyclic voltammetry (CV) investigations. This forms the basis for the first part of this publication.

Recently, the decomposition mechanism of β-Li_3PS_4 as prototype thiophosphate SE at VGCF was investigated in more detail by X-ray photoelectron spectroscopy (XPS).[20,33,34] Coating strategies are widely used to overcome stability limitations, especially at the interface between CAM and SE.[35] There are also efforts to transfer the same coating strategies already established for CAM to carbon additives.[36] Thus, an electronically conductive polymer coating for carbon nanotubes was presented, recently.[37] Analyzing the CV results, the electronic contact of carbon additives to the SE is responsible for the decomposition, and an electronically conductive polymer coating may not prevent degradation completely. Therefore, we decided to investigate an electronically insulating coating of a fiber- or "wire"-type carbon additive.

Testing various carbon additives, we investigate the influence of the specific surface area and the morphology in cathode composites for ASSB applications. By combining CV, XPS depth profiling, and battery cycling experiments, the surface area and morphology dependence of the decomposition reaction of the thiophosphate-based SE on the carbon additives is shown. Moreover, the microstructure resolved simulations confirm the increase in active material (AM) utilization when using fibrous carbon additives, by creating electronic networks more effectively. Finally, we present cycling data using an alumina-coated carbon additive, which reduces cell degradation.

■ EXPERIMENTAL SECTION

Materials. BASF SE provided the AM $Li(Ni_{0.6}Co_{0.2}Mn_{0.2})O_2$ and the thiophosphate SE β-Li_3PS_4 (LPS, $\sigma_{bulk} = 1.2 \times 10^{-4}$ S·cm^{-1}). The VGCF (Sigma-Aldrich Inc., iron-free) showed an average specific surface area of 24 $m^2 \cdot g^{-1}$ with a diameter of 100 nm and a length of 20−200 μm. The Super C65 graphite-type carbon was ordered from Imerys Graphite & Carbon Switzerland Ltd. and showed an average specific surface of 62 $m^2 \cdot g^{-1}$. The used Ketjenblack EC600JD (KBC) graphite type carbon was purchased from Lion Specialty Chemicals Co., Ltd., showing an average surface of 1270 $m^2 \cdot g^{-1}$. The carbon nanotubes (CNT) NC7000 were obtained from Nanocyl SA, showing an average surface area of 300 $m^2 \cdot g^{-1}$, with an average diameter of 9.5 nm and an average length of 1.5 μm. We compare fiber- and particle-shaped carbons with small and large surface areas. VGCF is selected because of the fiber morphology and a small surface area. CNT is an example for a high surface area fiber-shaped carbon. Super C65 and KBC are commonly used for lithium-ion batteries and represent small and high surface area particulate carbon additives, respectively. NCM AM and carbon additives were dried in a Büchi furnace at 200 °C overnight. A 120 μm thick Li foil disc (Albemarle, Rockwood Lithium GmbH) or an indium foil disc (chemPUR GmbH) with 125 μm thickness were used as the anode/reference electrode. The lithium−metal foil was mechanically polished, indium was used as received. All chemicals were stored in an argon filled glovebox (<0.1 ppm O_2, <0.1 ppm H_2O).

Preparation of the Solid-State Battery Cell. *Cathode Composite.* Two types of composites were investigated. The reference composite consists only of dried NCM and LPS with a mass ratio of 70:30 (volume ratio 47:53). The second composite contains additionally a conductive carbon additive, as stated above. First, 100 mg of a NCM/LPS composite, with a mass ratio of 70:30, were mixed and ground briefly. Afterward, 3 mg of carbon were added, resulting in a carbon content of 2.9 wt % in the cathode composite. The different composites were then ground by hand with an agate mortar for 15 min to achieve a uniform cathode composite mixture. For all investigations, the cathode composites were freshly prepared.

Cell Assembly. The cell tests were carried out using a pellet-type cell casing manufactured in house.[14,18] To assemble the cell, one stainless steel stamp was used for closing the polyether ether ketone (PEEK) cylinder. LPS (60 mg) were added into a 10 mm diameter cylinder. The powder was compressed uniformly by a second steel stamp. The 10 mg cathode composite was added subsequently. The cathode composite corresponds to an AM loading of 8.92 mg·cm^{-2} and 1.78 mA h·cm^{-2} (Q_{theo} = 200 mA h·g^{-1}) for a composite without a carbon additive. For a composite with a 2.9 wt % carbon additive 10 mg of composite refer to 8.65 mg·cm^{-2} and 1.73 mA h·cm^{-2}, respectively. The resulting pellet was uniaxially compressed at 30 kN (approx. 380 MPa) for 3 min. The lithium metal anode was placed on the remaining side, on top of the LPS. Copper foil was added for an easy extraction of the pellet after the experiments. An external frame was used during all electrochemical tests, applying a constant pressure of approximately 50 MPa.

Preparation of SE/Carbon Cells for CV. *Composite for the CV Cell.* For this type of cell, no NCM was used in the composite. Only LPS and conductive carbon were mixed. The aim was to identify solely the influence of the carbon additives on the LPS. Therefore, the ratio between both components was the same as in the ASSBs with CAM. The conductive carbon content was 9.1 wt %. LPS was mixed with the carbon additive in an agate mortar for 15 min.

Cell Assembly. At first, 30 mg of the pure LPS were placed in a PEEK cylinder and briefly compressed with both steel stamps. Then, 30 mg of the LPS/conductive carbon composite were added as the working electrode. The pellet was compressed uniaxially at 30 kN (approx. 380 MPa) for 3 min. The counter electrode was pure indium foil with 8 mm diameter. The pressure of the used external frame (50 MPa) and indium foil ductility is sufficient to fully cover the LPS surface. Pure indium was used to exclude any decomposition at the counter electrode/SE interface. A schematic of the CV cell and a

https://dx.doi.org/10.1021/acs.chemmater.0c04454
Chem. Mater. XXXX, XXX, XXX−XXX

Table 1. Overview of the Properties of the Investigated Carbon Additives

	morphology	specific surface area/$m^2 \cdot g^{-1}$	$D \times L$/primary particle size	distributor
VGCF	fiber	24	100 nm × 20−200 μm	Sigma-Aldrich
Super C65	particle	62	<50 nm (particle size)	Imerys Ltd.
CNT	fiber	300	9.5 nm × 1.5 μm	Nanocyl/BASF SE
KB EC600JD	particle	1270	68 nm (particle size)	Lion Ltd.

detailed discussion on the anode materials can be found in the Supporting Information S1 and S3.

Electrochemical Characterization. *Battery Test.* VMP-300 or MACCOR potentiostat/galvanostat were used to perform the charge and discharge tests. The VMP-300 potentiostat was used in the first cycles to perform cell cycling in combination with impedance measurements. Prolonged cycling was carried out afterward with the MACCOR potentiostat. Batteries with the lithium metal anode are charged to an upper cut-off potential of 4.3 V and discharged to a lower cut-off potential of 2.6 V versus Li^+/Li. The battery tests were carried out at 25 °C. Charge and discharge experiments were conducted with 0.1 C, which corresponds to 1.78 $mA \cdot cm^{-2}$ for cells with 8.9 $mg \cdot cm^{-2}$ (1.78 mA $h \cdot cm^{-2}$) AM loading. Electrochemical impedance spectroscopy (EIS) was carried out with a VMP-300 potentiostat. For relaxation of the system, 10 min open circuit voltage measurement was carried out before any EIS experiment. A 10 mV sinus amplitude and a frequency range of 7 MHz to 1 Hz define the EIS experiment.

CV Experiments. The CV experiments were performed using a VMP-300 or SP-150 Biologic potentiostat in a two-electrode arrangement (anode as reference electrode). Starting from the OCV, the first sweep was carried out to 5.5 V versus the reference electrode, corresponding to the oxidative sweep. From 5.5 V, the reverse sweep was carried out till 0 V and afterward back to the cell OCV. The scan speed was 1 $mV \cdot s^{-1}$.

X-ray Photoelectron Spectroscopy. XPS was carried out using a PHI5000 Versa Probe II (Physical Electronics GmbH). All samples were transferred from the glovebox into the XPS system using a transfer vessel under an argon atmosphere. Monochromatic Al K_α radiation (1486.6 eV) was used for analysis. The X-ray source was operated with a power of 50 W at 15 kV. The spot size of the analysis beam was 200 μm in diameter. For sputtering, a sputter gun with Ar^+ ions was used, which was operated with an acceleration voltage of 0.5 kV. The sputtered area was (2 × 2) mm^2. For charge compensation, a dual beam charge neutralization (ion beam combined with low-energy electrons) was applied. The pass energy of the analyzer was set to 23.50 eV for all detail spectra shown in the manuscript. Because the surface oriented toward the current collector was analyzed, we performed depth profiling experiments in order to clean the surface and to minimize the influence of the degradation processes toward the current collector/SE interface.[16,20] We monitored the change of the signals as a function of the sputtering time. From the depth, where no signal change was observed with further sputtering time, we assume that the influence of the current collector is minimized and the signals are representative for the bulk material. The data were evaluated with software CasaXPS (version 2.3.22, Casa Software Ltd).

First, the XP spectra of the β-Li_3PS_4 reference were calibrated in relation to the signal of adventitious carbon at 284.8 eV. Afterward, the signal position of the main component of the S 2p signal was determined (PS_4^{3-} units) and the XP spectra of the composite cathodes were calibrated in relation to the main component of the β-Li_3PS_4 reference. In this way, detrimental effects because of surface effects were minimized.[38,39] We used Shirley backgrounds and GL(30) line-shapes for signal fitting. In addition, commonly used fitting constraints were applied, including theoretical signal area ratios (e.g., for p orbitals 1:2), full width at half-maximum constraints, and reported values for spin orbit splitting.

Preparation of the Coating. The ALD-based Al_xO_y coating was directly performed on VGCF powder in a SUNALE R-200 Advanced (Picosun; Finland) system at 120 °C, by using $Al(CH_3)_3$ (trimethyl aluminum) and H_2O as precursors with a pulse time of 10 s. Nitrogen was used as a flow gas and was purged in between two consecutive pulses for 100 s in order to ensure the complete removal of reaction byproducts and unreacted excess precursor. The vacuum conditions in the reaction chamber were controlled <10 hPa.

Computational. We refer to Supporting Information S11−S16 for details on simulation parameters like simulation framework, input parameters for Battery and Electrochemistry Simulation Tool (BEST), model parameterization, effective conductivity calculation with GeoDict, analysis of virtual reference electrode, and the effective electronic conductivity calculation for conductive additive.

Simulation Methodology. The length scale of the additives given by the fiber or particle diameter is in the order of 100 nm. This very fine morphology cannot be resolved in the cell level electrochemical simulations because of the resulting computational load. Therefore, a new multiscale concept was required for both virtual electrode generation and the electrochemical modeling of the carbon additives inside the electrode. In the electrochemical simulations, we treated the SE and the carbon as a mixed phase in which both transport of ions and electrons occurs, respectively. The effective electronic and ionic transport properties in the mixed phase are characterized by the volume fraction and tortuosity of the SE and carbon phase. Both parameters are estimated by the structural analysis of high-resolution microstructure models.

Cathode Generation and Virtual Cell Assembly. In analogy to the experimental setup, we used in our simulations virtual cells consisting of a composite cathode, a LPS separator, and a lithium metal anode. The lithium metal and the separator were modeled as isotropic layers (Supporting Information Table S3). The virtual composite cathode microstructures were generated in software tool GeoDict.[40] The voxel resolution was set to 1 μm and the resulting virtual composite electrodes had a dimension of 40 × 150 × 150 μm^3. The first dimension corresponds to the composite cathode thickness of 40 μm. The structure generator randomly fills the simulation domain (40 × 150 × 150 μm^3) with spherical particles based on a defined particle size distribution until the particles exceed the preset solid volume fraction (SVF) of the AM of 45%. The selected Gaussian particle size distribution with an average diameter $d = (10 \pm 3)$ μm also accounts for the AM particle cracking occurring during the mixing and pressing of the electrode.[41,42]

High-Resolution Microstructure Models. To resolve the carbon morphology (about 100 nm feature size), we selected a cubic cutout (40 × 40 × 40 μm^3) from the virtual electrode sample (cf. previous paragraph) without carbon and increased the voxel resolution to 31.25 nm. The resulting high-resolution structure consists of 1280 × 1280 × 1280 voxels. We selected Super C65 as a representative for the class of granular additives and VGCF for fibrous additives. For Super C65, the scanning electron microscopy (SEM) images did not show an agglomeration of primary particles in the electrode. Therefore, we model Super C65 in the SE by polyhedron-shaped particles with a diameter of 93.75 nm. For the VGCF, we set the fiber diameter to 100 nm and the fiber length to (25 ± 5) μm, which corresponds to the dimensions given by the material manufacturer (see Table 1). In the next step, the carbon additives were randomly distributed until the volume fraction agreed with the electrode composition. In the VGCF model, we did not account for fiber bending or specific surface clustering of the carbon additives, but we allow for the additive overlap and direct contact to the AM. In order to create a statistically more reliable data set, we generated multiple electrodes with the same composition and porosity.

Structural Analysis of the Carbon Additive Network. For each class of carbon additive, we performed a structural analysis of the

https://dx.doi.org/10.1021/acs.chemmater.0c04454
Chem. Mater. XXXX, XXX, XXX−XXX

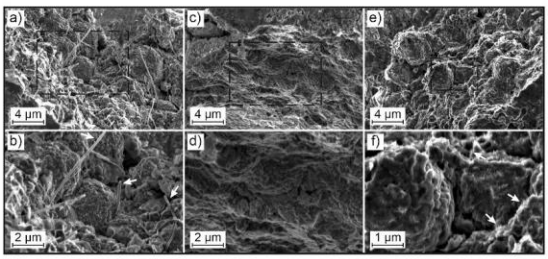

Figure 1. SEM cross sections for cathode composites with (a,b) VGCF, (c,d) Super C65, and (e,f) CNT carbon additives. Arrows exemplarily highlight carbon additives. VGCF enables a homogenous percolation network in the entire cathode composite. Super C65 is not visible because of the small particle dimensions in combination with the relatively weak material contrast. It can be assumed that isolated domains have formed within the composite and the percolation network is smaller compared to VGCF. CNTs are only visible in high magnification images and appear as bright and fiber-like. KBC is shown in the Supporting Information Figure S2.

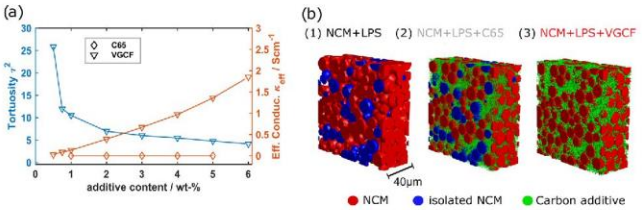

Figure 2. (a) Calculated effective electronic conductivity (orange) and tortuosity factor for selected carbon additives in the electrode with varying mass content: $\kappa_{eff}^{elec,VGCF}$, $\kappa_{eff}^{elec,C65}$, and tortuosity factor τ_{VGCF}^2 (blue). For nonpercolating Super C65, the tortuosity factor is calculated to infinity, therefore, these results are not included in the graph. (b) Schematics for the various conductive additive distributions generated for the virtual electrode: (1) without carbon, (2) C65, and (3) VGCF. Color code: isolated CAM particles in blue, carbon additive in green, CAM in red and the SE is transparent.

high-resolution simulation in GeoDict. Because this analysis is purely geometric and neglects any electrochemical effects, the computational costs were drastically reduced. The obtained structural parameters such as porosity and tortuosity of the ionic and electronic network were inputs for the electrochemical simulations. For the calculation of the effective conductivities, we assume that the ionic conductivity of the carbon phase and the electronic conductivity of LPS are negligible. Therefore, we use only the introduced additive phase for the calculation of the effective electronic conductivity κ_{eff}^{elec} and only the LPS phase for the effective ionic conductivity κ_{eff}^{ion}, respectively. Knowing the SVF of the respective phase, we calculate the corresponding tortuosity factor τ^2 and porosity ε. More details on the effective transport parameters are given in the Supporting Information S14−S16.

Electrochemical Simulations. The multiscale approach outlined above allows us to include the effect of conductive additives on cell performance, without the necessity of resolving the additive within the SE network. Following the procedures of the electrochemical measurements, we performed discharge simulations in order to evaluate the effect of additives in the first cycle. Further details on the modified transport equations in the mixed SE phase, the simulation framework BEST, and model parametrization are given in the Supporting Information S11−S13.

■ RESULTS AND DISCUSSION

Structural Analysis of ASSBs. Conductive carbon additives are used in lithium-ion batteries to achieve sufficient electronic percolation pathways. For solid-state batteries, the use of carbon additives has long been considered as unnecessary because of sufficient electronic conductivity of the original CAM (e.g., LCO).[24] Current research highlights the importance of optimized ionic and electronic pathways for the overall battery performance.[22] Of major importance is the proper ionic and electronic connection of the AM, see Usiskin and Maier.[43] The properties of the investigated carbon additives are summarized in Table 1.

In order to better characterize the microstructure of the composite cathodes and to get an impression of the carbon additive distribution, SEM images of cross sections of the composite cathodes were recorded. The VGCF are homogeneously distributed throughout the cathode composite (Figure 1a,b) and electronically contact the NCM AMs. Different fibers are in contact with each other, resulting in an extended electronically conducting network. In the cathode composite with Super C65 (Figure 1c,d), it is not possible to distinguish the carbon particles from the SE because of the small particle dimensions and the relatively small contrast. Based on the particulate character of Super C65, it is reasonable to assume that nonconnected domains exist within the composite cathode, which do not constitute part of the percolation network.[22]

The CNTs (Figure 1e,f) are visible in high magnification images, appearing bright and fiber-like. Based on the dimensions and the specific surface area, the CNTs have probably good contact with the NCM particles as well as the SE. Because of the fiber morphology, the probability of

https://dx.doi.org/10.1021/acs.chemmater.0c04454
Chem. Mater. XXXX, XXX, XXX−XXX

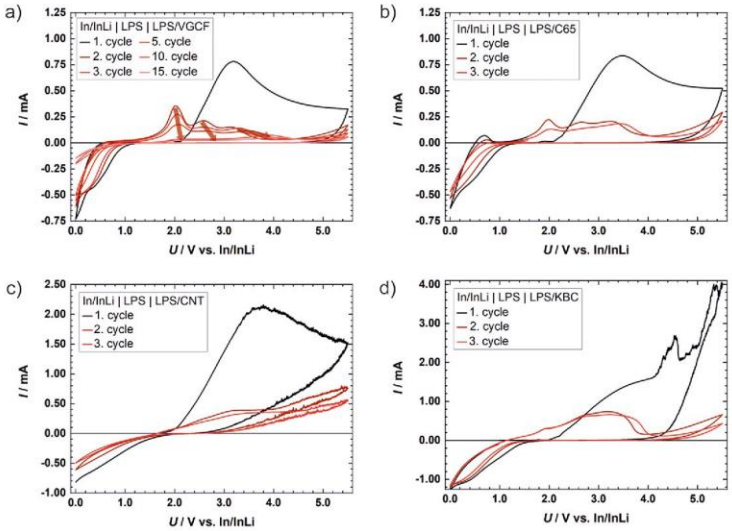

Figure 3. Comparison of the CV cells containing the four investigated carbon additives. (a) VGCF carbon additive and long-term cyclic voltammogram. The change in the peak position of the redox pair is highlighted. (b) CV for C65 carbon additive in the composite. (c) KBC additive in the composite leads to a stronger decomposition reaction in the first CV cycle. From the second cycle, the formed redox pair is barely visible. (d) For CV cells with the CNT additive a strong first oxidation is visible, present in further cycles and overlapping with the formed redox pair. The potential difference between the In/InLi anode and the lithium metal anode is 0.62 V vs Li^+/Li. By adding this offset, the voltage against lithium metal is obtained.

forming a continuous electronically conducting network is higher compared to particulate additives. However, the mean fiber length of CNTs is shorter than that of VGCF. Therefore, the question arises whether the CNT fiber network can contact the current collector with distant AM particles. The cross-section images for KBC are shown in the Supporting Information S2. The KBC particles are not visible in the SE micrographs as Super C65 and because of its small particle size a noncontinuous electronically conductive network is assumed as well.

The structural analysis of virtual electrodes without conductive additives reveals that 5 vol % of CAM is not connected electronically with the current collector (Figure 2b; isolated particles are highlighted in blue). This is in fair agreement with the experimental findings.[42,44]

The structural simulation of high-resolution data sets, including spherical carbon particles representing Super C65 in different mass ratios from 1 to 6 wt %, shows no improvement of the effective electronic conductivity $\kappa_{eff}^{elec,C65}$. Because the particles are distributed uniformly inside the SE phase, no substantial percolating network is established ($\kappa_{eff}^{elec,C65} = 0$ and $\tau_{C65}^2 = \infty$). Consequently, the electronic transport network is provided predominantly by the CAM (Figure 2b).

The fiber-like particles representing VGCF form a well-connected network in the volume between the CAM particles. The resulting virtual structures are in qualitative agreement with SEM images of real samples (Figure 1). In contrast to Super C65, VGCF have a beneficial effect on the effective electronic conductivity ($\kappa_{eff}^{elec,VGCF}$), establishing a network throughout the whole electrode. As shown in Figure 2a (right axis), the improved percolation leads to a nearly linear growth for $\kappa_{eff}^{elec,VGCF}$ with increasing VGCF content. This relates to the increasing number of intercepting fibers, providing more conduction pathways and thereby reducing the electronic resistance. The virtual electrode structure with added VGCF, as shown in Figure 2b, indicates the preferential orientation of the longer fibers enabling long-range electronic pathways.

Furthermore, the structural analysis indicates a lower limit of the tortuosity with increasing VGCF content. As soon as a percolating network is established, the gain in effective electronic conductivity with increasing VGCF content is less pronounced. In Figure 2a (left axis), the VGCF tortuosity factor τ_{VGCF}^2 is shown for different wt % of VGCF in the electrode structure. Although the effective conductivity $\kappa_{eff}^{elec,VGCF}$ increases linearly, the tortuosity factor levels off at around $\tau_{VGCF}^2 \sim 5$. This indicates that the percolation threshold is at around 3 wt % because of a constant tortuosity factor of around 5. A further introduction of VGCF has no significant impact on the conductive network. This observation is confirmed by discharge experiments, as discussed below. A summary of the structural analysis including volume fractions and effective conductivities for each additive class are given in the Supporting Information Table S2.

The structural analysis provides strong evidence that electronic transport is the kinetic bottleneck for the investigated cathode composites. Fiber-shaped carbon additives can have a positive influence on the electronic percolation

https://dx.doi.org/10.1021/acs.chemmater.0c04454
Chem. Mater. XXXX, XXX, XXX−XXX

network, increasing the battery performance. In contrast, up to 5 wt % granular carbon additives seem to have no or only minor influence on cathode performance. Beside the influence of the microstructure, the decomposition of the SE at the carbon additive surface needs to be discussed in detail. CV and XPS investigations are therefore performed in the following. Cycling experiments are added to evaluate the combined influence of the carbon microstructure and SE decomposition at the carbon surface.

Electrochemical Analysis of Carbon Additives. The CV experiments (In/InLi|LPS|LPS/C) were primarily performed to induce decomposition reactions at the carbon-SE interface for the following XPS study. Additional discussions on the choice of the anode material and a detailed discussion on the reversibility of the occurring redox pair can be found in the Supporting Information S3 and S4. The theoretical concepts of CV are based on a typical liquid-state system with a mobile redox couple. In solid-state cells, reaction conditions (e.g., limited mobility but also energetic or kinetic changes) are different to the liquid counterpart. As a result, the theoretical analysis of diffusion-controlled CV peaks is strictly no longer applicable and a quantitative analysis of reversibility can easily be misleading.[45,46] Therefore, we do not identify decomposition products and possible mechanisms from the CV data but refer to our XPS analysis.

CV experiments show that the onset of the first oxidation and the degree of decomposition depend on the morphology and surface area of the carbon additives (Figure 3). We define the onset of oxidation as a current of 0.03 mA. This value was chosen considering the resolution of the potentiostat and the experimental settings. This excludes errors because of the noise in the measurement. The average values for the decomposition onset of all analyzed cells are listed in Table 2. A shift of up to 0.2 V between the carbons with different specific surface areas was detected. A discussion on the normalization of the current on the surface area of the carbons can be found in Supporting Information S5.

Table 2. Different Investigated Carbon Additives and the Onset Potentials for the Oxidative Decomposition in the First CV Cycle

	morphology	surface area/$m^2 \cdot g^{-1}$	E vs In/InLi/V
VGCF	fiber	24	2.18
Super C65	particle	62	2.16
CNT	fiber	300	1.94
KB EC600JD	particle	1270	2.00

Figure 3a shows the cyclic voltammogram for a cell with VGCF as a carbon additive. In the first positive potential sweep, a broad peak (oxidation reaction) with the absolute current maximum (at 3.2 V vs In/InLi) is passed, preceded by a small current peak at approx. 1.9 V versus In/InLi. In the cathodic run of the first cycle, a drop in current at approx. 1.2 V versus In/InLi indicates a reduction reaction. In the second anodic potential sweep, three clearly separated peaks are now visible (2.1 V, 2.6 V, 3.2 V vs In/InLi). The third and following sweeps show no significant changes in shape. However, the intensity of the current maximum decreases and the peak potential shifts toward higher voltages for the oxidation process and toward lower voltages for the reduction process. For Super C65, a similar observation can be made for the peaks' sequence (Figure 3b).

For cells with Super C65, the three times higher surface area compared to VGCF should lead to a noticeable increased decomposition current. The maximum currents measured are in a similar range—0.84 mA with Super C65 and 0.78 mA with VGCF. Despite this fact, the surface dependence does not need to be revised. The presence of an intact electronic percolation network is crucial for the decomposition. A change of the morphology can have significant influence. The simulation results show a connected percolation network for VGCF. With particulate carbons, like Super C65, the particles can agglomerate and result in domain formation. Certain domains can be isolated from the percolation network. In this case, these particles are completely surrounded by the almost electrically insulating LPS and thus have no influence during the electrochemical analysis. This explains the lower currents observed because of the reduced surface, where a decomposition can take place.

The additives CNT (300 $m^2 \cdot g^{-1}$) and KBC (1270 $m^2 \cdot g^{-1}$) (Figure 3c,d) show much higher specific surface areas compared to VGCF and Super C65. A significant increase in the currents for the oxidation reactions is observed, as the higher surface area leads to increased electronic contact with the SE. However, for both types of carbon, no linear increase between the maximum current and surface area was observed as well. The increase from 0.78 mA (VGCF) to 2.2 mA (CNT) or 1.8 mA (KBC) is not proportional to the theoretical specific surface area. Additionally, the area of the reduction peaks is much smaller for CNT and KBC compared to VGCF. The massive oxidation reaction observed with CNT and KBC is the reason for the differences. It leads to a fast and massive formation of a cathode electrolyte interphase (CEI),[47] isolating the carbon additives and self-limiting further oxidation of the CEI and blocking redox pair formation. Additionally, CNTs are considerably smaller in length and diameter than VGCF, and KBC is a particular carbon, resulting in isolated domains and the reduction of electronic contact area, similar to Super C65. In both CVs (Figure 3c,d), the noise was recognized from a current of 1.8 mA onward. This noise could be caused by abrupt changes in the electrical contact surface, caused by the insulating products of the decomposition and a breaking of the CEI layer, followed by a locally increased decomposition reaction and high currents.

The previously discussed simulation of the cathode composite focused on its structure and the influence on the electronic contact. The CV experiments have revealed another aspect of the interaction between carbon conductive additives and the SE, the small stability window of the SE. The decomposition of the SE was observed with all carbons. Apparently, VGCF shows the lowest degree of decomposition, which is confirmed in the following XPS investigations.

Analysis of Degradation Products. Using XPS, the cathode composites were examined to draw conclusions of the existing decomposition. To induce degradation, cells were disassembled at 5.5 V versus In/InLi in the oxidized state after four CV cycles. The XPS analyses were performed on the current collector-oriented side of the cathode composites. We performed depth profiling experiments in order to exclude effects of the current collector and to ensure that the decomposition signals are because of the degradation at the carbon additive/SE interface (see Experimental Section).

As a measure of decomposition, we have exemplarily analyzed the oxidation products in the S 2p spectrum. For all composite cathodes, the same components could be

https://dx.doi.org/10.1021/acs.chemmater.0c04454
Chem. Mater. XXXX, XXX, XXX−XXX

Chemistry of Materials pubs.acs.org/cm Article

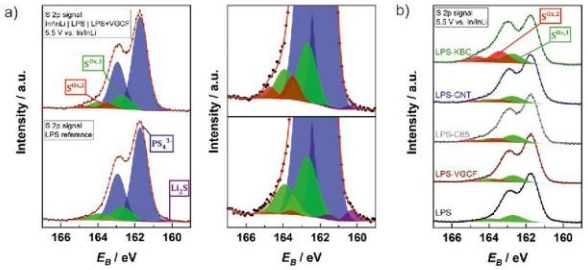

Figure 4. (a) Normalized detail spectra for the S 2p signal. The upper XP spectra reflects the used system In/InLiLPSlLPS/VGCF. The cell went through four complete CV cycles and was disassembled at 5.5 V vs In/InLi, thus the cathode is in the oxidized state. The lower spectrum shows pure LPS, which serves as a reference for the assignment of the components. (b) Stacked view of all normalized S 2p detail spectra of the different composites after the CV experiment. For comparison, the S 2p spectrum of the pristine LPS is shown. The red signal indicates the decomposition products.

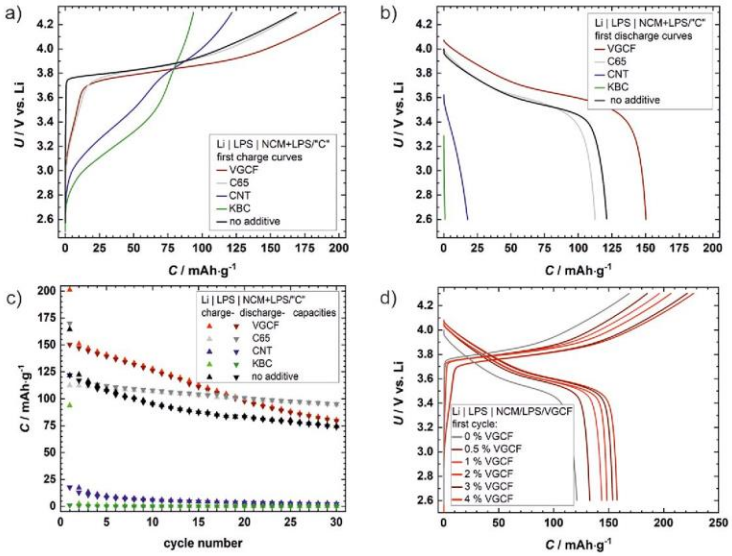

Figure 5. (a) First cycle charge curves for ASSBs with different carbon additives (2.9 wt %) in the cathode composite. The surface area and morphology of the carbon additives lead to a first decomposition region in the potential range from 2.8 to 3.7 V. (b) First cycle discharge curves for ASSBs with different carbon additives in the composite cathode. For VGCF, a positive effect is noticeable. Higher discharge capacities and lower over voltages are noticeable. Cells with Super C65 do not perform significantly different from cells without any conductive additive. Batteries with CNT and KBC show a bad battery performance because of massive decomposition reactions at the carbon/SE interface. (c) Charge and discharge capacities of ASSBs with different carbon additives. The trend described in the context of Figure 5a applies also here. (d) Variation of the VGCF carbon additive mass fraction for different ASSBs. The first charge and discharge curves for every cell are shown.

determined in the S 2p spectrum, independent of the carbon type. Differences can be seen in the relative signal areas, that is, the concentration of the species. Therefore, we give a more detailed description of the S 2p signal contributions using the example of the VGCF/SE composite (Figure 4a). The main component at 161.7 eV can be assigned to the PS_4^{3-} tetrahedron of the LPS structure.[16] The doublet at lower binding energies can be assigned to Li_2S. As this also occurs in the LPS reference, we assume Li_2S residues from the LPS synthesis. For the VGCF/SE composite, the fraction of Li_2S is lower, indicating the oxidizing conditions (disassembled at 5.5 V vs In/InLi). The signals in the higher binding energy range (green and red) are often reported to be correlated with degradation phenomena for thiophosphates.[16,32,33,48,49] It can

https://dx.doi.org/10.1021/acs.chemmater.0c04454
Chem. Mater. XXXX, XXX, XXX−XXX

be seen that the content of these species increases for the VGCF/SE composite after the CV experiment, indicating a degradation at the VGCF/SE interface. Based on very recent reports, we assume that a major contribution is because of the formation of polysulfides with different chain lengths.[20,50] However, the elucidation of the decomposition mechanism was not in the focus of this work. For more details concerning the decomposition pathways in composite cathodes, we refer to our previous study by Walther et al.[20]

Figure 4b shows a comparison of the S 2p signals for all tested composites (VGCF, CNT, KBC, and C65). We marked the decomposition signals $S^{ox,1}$ and $S^{ox,2}$ in the higher binding energy region in green and red. In summary, Figure 4b shows that the lowest fraction of decomposition products is obtained for cells with VGCF. Its small specific surface area seems to be the main reason for this. Hence, we expect VGCF to be most beneficial for the ASSB cycling performance, as demonstrated in the following sections.

For Super C65, CNT, and KBC the fraction of decomposition products is higher, of which KBC shows the highest fraction. Except for the CNTs, a systematic increase in decomposition signals with increasing specific surface area of the carbon additive is observed. However, the cell with CNT in the cathode composite showed strong variations in the peak currents of the decomposition reaction, resulting in a heterogeneous distribution of decomposition products (Supporting Information S8). Taking this into account, the qualitative statement on the surface area dependence of the decomposition reaction is reasonable.

Cycling Performance and Simulation of ASSBs. The four different carbons were used in otherwise identical cells (LiIβ-Li_3PS_4|Li($Ni_{0.6}Co_{0.2}Mn_{0.2}$)O_2/β-Li_3PS_4/carbon) in order to evaluate the individual effects discussed above regarding their influence on cell performance. The carbon content was 2.9 wt %, and the voltage range was limited from 2.6 to 4.3 V versus Li^+/Li. This voltage window corresponds to 2.0 to 3.7 V versus In/InLi in the CV tests. A discussion of the CV cell with this smaller potential window can be found in the Supporting Information S7. The microstructure simulation suggests a positive influence of fibrous carbons, as they form a conducting network, unlike particular carbons. The CV and XPS experiments showed a more severe oxidation for carbon additives with a higher specific surface area, which is expected to cause inferior cell performance. We like to emphasize that it is not the carbon additive that decomposes. Rather the SE in electronic contact with the carbon additive electrochemically decomposes. This lowers the volume fraction of ionic conducting phase in the composite cathode, which increases the internal resistance of the cell, thus degrading cell performance.

Figure 5a shows the first charge curve for the different composite cathodes. The slope at the beginning can be seen as an indicator for side reactions at the carbon/SE interface (<3.7 V). One charge cycle corresponds to one anodic sweep in the cyclic voltammogram, therefore, the oxidation of the SE also occurs during battery cycling. The detected reduction in the cyclic voltammogram does not occur for the ASSBs, as the electrode potential never drops below 1.00 V versus In/InLi.

The curve shapes of the sample with VGCF (red) and Super C65 (grey) are comparable. In both cases, the plateau for the CAM delithiation is visible, which is at a slightly lower potential in the case of VGCF. Overall, the composite cathode with the VGCF reaches the highest charge capacity. The fiber-like structure of VGCF connects all NCM particles electronically with the current collector, leading to a small number of isolated NCM particles. In addition, the electronic percolation network creates a uniform current distribution, resulting in a reduction of the overpotential.

In contrast to VGCF and Super C65, CNT and KBC lead to significantly different charge curves, which indicates a large increase in side reactions. In addition, for the cell with CNT, the plateau indicating CAM delithiation is blurred but still visible, whereas it is no longer visible for the cell with KBC. Overall, these observations correspond very well to the results of the CV experiments, showing the tendency of a stronger degradation with an increasing specific surface area of the carbon additives. A higher specific surface area of the carbon additives corresponds to more reaction sites for SE decomposition reactions.

Figure 5b clearly reflects the already discussed findings for the charging cycles. Cells with VGCF and Super C65 can be discharged. VGCF shows the highest discharge capacity. Cells with CNT and KBC show very low discharge capacities. The plateau of the AM is not visible. It is therefore possible that further decomposition takes place during the discharge step.

The loss of specific capacity during cycling has several reasons. Besides possible chemo-mechanical degradation such as contact loss[13] of the AM or structural degradation by intercalation and place changes,[19,51] we expect a main contribution because of (electro)chemical degradation of the SE: first, CEI formation takes place at the NCM/SE interface (mainly during first charge), the CC/SE interface, as well as SEI formation at the Li/SE interface. These phenomena occur in every ASSB without coating or protective layers.[18,19,52,53] Second, decomposition reactions occur within the composite cathode at the carbon additive/SE interfaces during charge (oxidation), resulting in the slope during charge reaction at low potentials (<3.7 V) and an additional charge capacity during delithiation of NCM (3.7−4.3 V). The dependence of the degree of this decomposition on the carbon surface area was already shown above.

Figure 5c compares the cycling stability for ASSBs with the different carbon additives in the composite cathode. The strong decomposition reactions with CNT and KBC probably prohibit reasonable cell cycling, confirming that a higher specific surface is bad for the battery performance. For the two other carbon additives (VGCF, Super C65), the capacity difference (30 mA h·g^{-1}) in the first cycles is most probably based on the different CAM utilizations. However, because the fading of the cell with VGCF is more pronounced, both ASSBs show the same specific capacity after 18 cycles. This seems counterintuitive at first because the CV cells indicate a stronger decomposition when Super C65 is used and the carbon particles are in contact with each other and the current collector. However, the simulations indicate the presence of isolated domains. Within these domains, no reaction takes place at the carbon/SE interface. When VGCF is used, decomposition takes place at all carbon/SE interfaces. The formed products isolate the CAM, and thus increase the cathode resistance and impair the lithium ion transport and battery properties for prolonged cycling.

In order to check whether the initial slope (<3.7 V, charge step) depends on the fraction of carbon additives, we exemplarily investigated the influence of the VGCF mass fraction on the first charge and discharge curves (Figure 5d). The slope seems to have a mass fraction threshold and is

https://dx.doi.org/10.1021/acs.chemmater.0c04454
Chem. Mater. XXXX, XXX, XXX−XXX

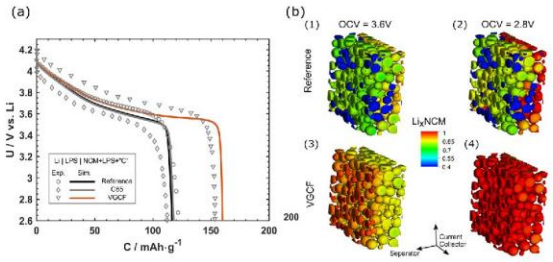

Figure 6. (a) Comparison between experimental (open symbols) and simulated 0.1 C discharge curves for the virtual electrode: electrode without carbon (black), C65 electrode (grey), and VGCF electrode (red). The modified electrode parameterization represents an additive content of 3 wt %. (b) Lithium concentration distribution for the electrode without carbon at (1) 3.6 and (2) 2.8 V. (3,4) Concentration distribution in the VGCF-electrode under the same conditions.

clearly visible for VGCF mass fractions of 3 wt %. This is in good agreement with the simulated effective conductivity. For smaller mass fractions, more NCM secondary particles can already be accessed, but the isolated VGCF domains may also be present within the composite cathode, as indicated by the microstructure analysis. Above the threshold, statistically all VGCF are electronically contacted, resulting in a fully connected network. Decomposition can then occur on almost all VGCF/SE interfaces, leading to more decomposition products and further capacity contributions. Clearly, the discharge capacity rises with increasing mass fraction of VGCF. For smaller mass fractions, the capacity rise is higher and gets smaller with higher VGCF mass fractions. This capacity increase has two main reasons: the main contribution is because of more AM being addressed. In addition, taking the reactions at the VGCF/SE into account, we suspect further capacity contributions because of additionally introduced VGCF/SE interfaces. After the mass threshold is reached, the capacity increases proportionally with carbon mass and the resulting increase of decomposition sites. The recent literature suggests a redox activity of the decomposition products of thiophosphate-based SE.[50,54]

The composition of the cathode composite (e.g., weight fractions, additives, morphology, and distribution) determines the maximum capacity of the cell. To understand the complex interplay of the different parameters and allow predictions of the battery performance, we combine our experimental cycling data with the corresponding simulations. We compare the performance of the cathode composite with Super C65, the composite with VGCF, and the cathode composite without carbon. In the electrochemical simulations, we focus on a conductive additive content of 3 wt %, which is close to the best performance in the experiments. The simulated discharge curves of the corresponding virtual electrodes are shown in Figure 6a. For the cathode without carbon, the simulated cell voltage (solid black line) is in qualitative agreement with the experimental data (open triangles). Some deviation is expected because our model does not account for additional loss mechanisms like SE delamination or inhomogeneous particle distribution. Moreover, we assume a perfect contact of the electrode to the current collector. For a more detailed study of the interface effects and structure modifications, we refer to Neumann et al.[25]

The model qualitatively predicts the effect of carbon additives on discharge performance. The addition of Super C65 is not able to significantly improve the discharge capacity. This is in line with our predictions based on the microstructure analysis. Because no percolating network is established, isolated CAM particles remain inactive. Additionally, the simulations reproduce the higher overpotential attributed to a reduction of ionic conductivity.

On the other hand, electrodes with VGCF show a clear increase in capacity. The improved electronic conductivity because of the VGCF network enables a high CAM utilization, which increases the capacity by ∼27%. Almost full electrode utilization is achieved. Furthermore, the better conductivity and the corresponding increase in active surface area reduce the overpotential and improve the energy density of the cell. This effect is still more pronounced in the experiments.

In order to illustrate the role of the VGCF, Figure 6b presents the spatial distribution of Li in the AM for both the cathode without carbon [Figure 6b(1,2)] and the cathode with VGCF [Figure 6b(3,4)] at cell voltages of 3.6 and 2.8 V (after the discharge process). The inhomogeneous distribution of lithium in the electrode without carbon demonstrates that the low electronic conductivity of NCM622 is a major limitation for CAM utilization. This is discussed in detail in ref 25. By adding VGCF to the electrodes, the percolating electronic network is extended and activates previously isolated CAM particles. CAM particles that appear in blue color in the cathode without carbon now contribute to cell capacity. The differences are clearly visible in the Li distribution of the VGCF electrodes. With VGCF, we observe a homogeneous lithiation of the electrode starting from the separator, advancing toward the current collector. This demonstrates that with VGCF, the electronic conductivity is no longer rate limiting.

The combination of the experiment and simulation results emphasizes the need for percolating electronic networks in order to achieve an optimized electrode performance. Our analysis shows that fibrous additives, such as VGCF, are suitable conductive additives to create a percolating conductive network. Because the fibers inherently tend to form overlapping flexible networks during processing and are uniformly distributed throughout the electrode, they clearly improve the cycling performance. However, oxidative degradation at the carbon/SE interface prevents a useful application of bare VGCF in battery cells during prolonged cycling. Our results indicate that VGCF may be the best choice, if the stronger fading during cycling can be moderated.

https://dx.doi.org/10.1021/acs.chemmater.0c04454
Chem. Mater. XXXX, XXX, XXX−XXX

Alumina Coating of Carbon Additives. We assume that the potential drop at the carbon/SE interface is the main driving force for degradation reactions. A protective coating on the carbon surface should lead to suppressed degradation and thus to an improved overall ASSB performance. To prevent or at least reduce these reactions, we coated the VGCF carbon additive with electronically insulating aluminum oxide (Al_xO_y) by ALD. However, electronic contact of the carbon core to the CAM and between the VGCF cores must be ensured.

Figure 7a shows SEM images of Al_xO_y-coated VGCF, prepared by 20 ALD cycles. The micrographs reveal a relatively rough surface, which indicates island-like growth. However, the thickness of the particulate coating is homogeneous (2−3 nm) and covers almost the entire carbon surface, which indicates a high deposition conformity of the ALD process. Only the tips of the VGC fibers do not show a complete coverage with the ALD coating. However, the particulate character of the coating still allows small uncovered areas, where an electronically conductive contact to the CAM is possible and where decomposition of the SE may still occur to a small extent. The fiber core appears transparent because of SEM analysis parameters and the high material contrast. Accordingly, the electrons transit through the carbon, making it difficult to determine the coating thickness because of edge effects. The morphology of the coated fibers resembles jacketed wires with their ends bare. In these microwires, an insulating layer surrounds the electronically conductive core (Figure 7b).

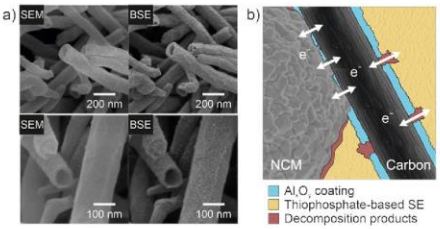

Figure 7. (a) Scanning electron images of Al_xO_y-coated VGCF. The fibers were each coated with 20 ALD cycles. On the left side, images with a secondary electron micrograph are shown, while images with a back-scatter electron(s) detector are shown on the right side. The inside of the fiber (carbon core) appears transparent because of the selected analysis parameters and the material contrast. (b) Schematic of the morphology of coated fibers. The coated carbon resembles jacketed wires. In these microwires, an insulating layer surrounds the electronically conductive core. A degradation of the carbon/SE interface is only possible in areas where the coating is not homogeneous.

In order to test the influence of the protection concept on the ASSB performance, cells with alumina-coated VGCF were built and tested. Because the composite materials are hand-ground in an agate mortar before cell assembly, we hypothesize that small amounts of coated VGCF break into smaller fragments, leading to an opening of additional uncoated surface areas. Additionally, during battery preparation the cathode composite is compacted at around 380 MPa. The mechanically rigid NCM particles apply high forces to the surrounding VGCF, potentially resulting in the local breaking of the coating. Accordingly, electronic contact is achieved.

Figure 8a shows a comparison of the cycling stability between ASSBs with composite cathodes without VGCF, with uncoated, and with alumina-coated VGCF (2.9 wt %). The used cell setup is Li|β-Li_3PS_4|Li($Ni_{0.6}Co_{0.2}Mn_{0.2}$)O_2/β-Li_3PS_4/VGCF. The discharge capacities of a cell without conductive additive in the composite cathode are shown in black. They serve as a reference to demonstrate the influence of the conductive additive. The fading of the discharge capacity of this sample is because of the morphological/structural and (electro-)chemical degradation phenomena in the cell.[18,19,52,53] If VGCF is added to the composite cathode, higher initial capacities can already be observed in the untreated case (dark red) because more AM is addressed. In the following cycles, however, a pronounced reduction in capacity is noticeable, whereby the initial capacity advantage over the cell without carbon is lost after 35 cycles. After 50 cycles, the cell with untreated VGCF has only 29% of its initial capacity left. The protective concept of the conductive additive significantly

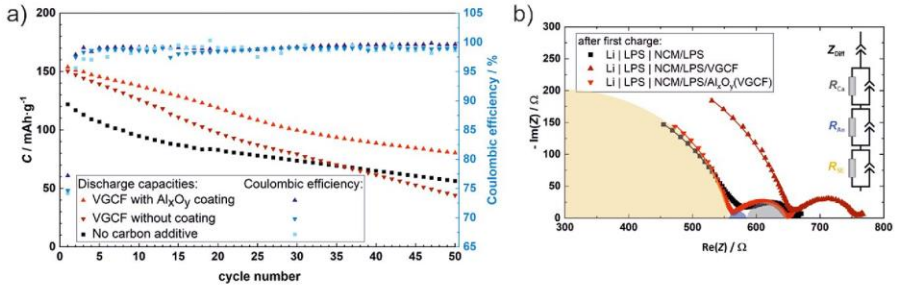

Figure 8. (a) Discharge capacity as a function of the number of cycles. Shown is a comparison of Li|β-Li_3PS_4|Li($Ni_{0.6}Co_{0.2}Mn_{0.2}$)O_2/β-Li_3PS_4/VGCF cells depending on the influence of the conductive additive (2.9 wt %) in the composite cathode. All cells were galvanostatically charged to 4.3 V (vs Li^+/Li) and discharged to 2.6 V. Assuming a theoretical capacity of 200 mA h·g^{-1}, the current density was 178 μA·m^{-2} (equivalent to 0.1 C). Overall, the cell with Al_xO_y-coated VGCF shows the highest discharge capacities and improved cycle stability. (b) Nyquist plot for different cells after the first charge step. During the first charge, the influence of decomposition reactions is the strongest. Through the microwire-like coating of VGCF, the decomposition between carbon and SE is effectively reduced, resulting in comparable resistances to cells without the carbon additive. The use of uncoated carbon fibers leads to increased LPS bulk (R_{SE}) and NCM-LPS (R_{Ca}) charge transfer resistances.

https://dx.doi.org/10.1021/acs.chemmater.0c04454
Chem. Mater. XXXX, XXX, XXX−XXX

reduces the drop in capacity, so that after 50 cycles 52% of the initial capacity is retained. Compared to the cell without the conductive additive, the modified VGCF cell has 1.4 times higher capacity after 50 cycles.

Interestingly, the slopes of the ASSBs with coated VGCF and without carbon in Figure 8a are comparable. We therefore assume that the remaining capacity fading is mainly due to the effects at the uncoated CAM surface, which occur also within the reference ASSB and only to a minor extent because of the partially uncoated VGCF surface areas. Regarding the composite cathode, these include previously reported morphological/structural and (electro-)chemical degradation phenomena.[18,19,52,53]

Figure 8b shows the corresponding Nyquist plots for the cells after the first charge process. As already mentioned, the strongest decomposition is expected during the first charge process. This should lead to a change of the LPS bulk resistance (R_{SE}). The Nyquist plot further shows the charge transfer process at the lithium-LPS interface (R_{An}), the charge transfer process at the NCM-LPS interface (R_{Ca}) and the diffusion in the cathode particles (Z_{Diff}). For a detailed interpretation of impedance data for this battery setup, with DRT analysis for the assignment of the processes, we refer to Randau et al.[55]

The data for R_{SE} of the cells without carbon and with the microwire-coated VGCF show comparable values (≈560 Ω), highlighting that no additional decomposition reactions are present. The R_{SE} of the battery with the bare VGCF is increased to about 650 Ω. This increase is explained by the decomposition of the SE induced by carbon. R_{An} shows no differences between the different batteries, as expected. R_{Ca} is also comparable in the cells without and with coated VGCF (≈74 Ω) but slightly increased (≈93 Ω) for the cell with the uncoated VGCF. This as well indicates a negative influence of the carbon/SE decomposition on the NCM-LPS charge transfer process.

Our concept of using microwires in ASSBs should be generally applicable to all types of fiber-based carbons, thus creating an isolated wire with an internal conductive part. For particle-shaped carbons, like carbon black, Super C 65, or Ketjenblack, this concept appears to be useless. After coating, the individual particles will be isolated, preventing a conductive network. Additionally, isolated domains will remain in the composite cathode, limiting cell performance of ASSBs. According to the assumed mechanism, all electronically insulating materials should form suitable coatings. Important properties are small electronic conductivity, high stability toward oxidation, and a high dielectric constant. Furthermore, we assume that the coating layer needs to be very thin (nanometer scale) but has to block electron tunneling effectively. Therefore, numerous oxides easily applicable by ALD may be suitable coating materials, for example, SiO_2, ZrO_2, TiO_2, SnO_2, and MgO.[56]

■ CONCLUSIONS

We investigated the influence of different conductive carbon additives on the stability of β-Li_3PS_4 and on the performance of all-solid-state lithium batteries. The presented combination of simulation and experiment highlights that the balance of ionic and electronic percolation is crucial for the performance of ASSBs. Microstructure resolved electrochemical simulations of the cathode composite indicate a strong influence of the carbon morphology (fiber vs particle) on cell performance. Additionally, the results of CV show that all investigated carbons increase the cathode degradation, which decreases the cycling performance of full cells. XPS analysis indicates the formation of oxidized sulfur species such as polysulfides. With higher surface areas of the carbons, the volume fraction of the decomposition products increases. ASSBs with VGCF as the conductive additive in the cathode composite show the highest initial discharge capacity and the lowest overpotential of the tested carbons. However, the decomposition of the SE in contact with VGCF still leads to substantial fading—more severe than without the carbon additive. This was addressed by a nanometer thin, electronically insulating alumina coating on VGCF. This coating decreased the fading of the discharge capacity, without decreasing the initial battery performance. The resulting microwire concept for carbon additives reduces cell decomposition effectively and may be crucial to realize high power ASSBs.

■ ASSOCIATED CONTENT

Supporting Information

The Supporting Information is available free of charge at https://pubs.acs.org/doi/10.1021/acs.chemmater.0c04454.

SEM images of a composite cathode with Ketjenblack EC600JD conductive carbon, discussion on different anode materials for CV, discussion on reversibility of the redox pair in the CV cells, discussion if a surface normalization is reasonable, CV data of cells with a first reductive sweep and reduced potential window, further ASSB data, like charge/discharge curves and onset potentials for the decomposition in the first charge step, and further details on the simulation parameters like simulation framework, input parameters for BEST, model parameterization, effective conductivity calculation with GeoDict, analysis of virtual reference electrode, and the effective electronic conductivity calculation for conductive additive (PDF)

■ AUTHOR INFORMATION

Corresponding Author

Jürgen Janek − *Institute of Physical Chemistry, Justus Liebig University Giessen, D-35392 Giessen, Germany; Center for Materials Research (LaMa), Justus Liebig University Giessen, D-35392 Giessen, Germany;* orcid.org/0000-0002-9221-4756; Email: jürgen.janek@phys.chemie.uni-giessen.de

Authors

Simon Randau − *Institute of Physical Chemistry, Justus Liebig University Giessen, D-35392 Giessen, Germany; Center for Materials Research (LaMa), Justus Liebig University Giessen, D-35392 Giessen, Germany*

Felix Walther − *Institute of Physical Chemistry, Justus Liebig University Giessen, D-35392 Giessen, Germany; Center for Materials Research (LaMa), Justus Liebig University Giessen, D-35392 Giessen, Germany*

Anton Neumann − *Institute of Engineering Thermodynamics, German Aerospace Center (DLR), 70569 Stuttgart, Germany; Helmholtz Institute for Electrochemical Energy Storage (HIU), 89081 Ulm, Germany;* orcid.org/0000-0002-4575-8697

Yannik Schneider − *Institute of Physical Chemistry, Justus Liebig University Giessen, D-35392 Giessen, Germany;*

https://dx.doi.org/10.1021/acs.chemmater.0c04454
Chem. Mater. XXXX, XXX, XXX−XXX

Center for Materials Research (LaMa), Justus Liebig University Giessen, D-35392 Giessen, Germany

Rajendra S. Negi − *Institute of Physical Chemistry, Justus Liebig University Giessen, D-35392 Giessen, Germany; Center for Materials Research (LaMa), Justus Liebig University Giessen, D-35392 Giessen, Germany*

Boris Mogwitz − *Institute of Physical Chemistry, Justus Liebig University Giessen, D-35392 Giessen, Germany; Center for Materials Research (LaMa), Justus Liebig University Giessen, D-35392 Giessen, Germany*

Joachim Sann − *Institute of Physical Chemistry, Justus Liebig University Giessen, D-35392 Giessen, Germany; Center for Materials Research (LaMa), Justus Liebig University Giessen, D-35392 Giessen, Germany*

Katharina Becker-Steinberger − *Institute of Engineering Thermodynamics, German Aerospace Center (DLR), 70569 Stuttgart, Germany; Helmholtz Institute for Electrochemical Energy Storage (HIU), 89081 Ulm, Germany*

Timo Danner − *Institute of Engineering Thermodynamics, German Aerospace Center (DLR), 70569 Stuttgart, Germany; Helmholtz Institute for Electrochemical Energy Storage (HIU), 89081 Ulm, Germany*

Simon Hein − *Institute of Engineering Thermodynamics, German Aerospace Center (DLR), 70569 Stuttgart, Germany; Helmholtz Institute for Electrochemical Energy Storage (HIU), 89081 Ulm, Germany;* orcid.org/0000-0002-6728-9983

Arnulf Latz − *Institute of Engineering Thermodynamics, German Aerospace Center (DLR), 70569 Stuttgart, Germany; Helmholtz Institute for Electrochemical Energy Storage (HIU), 89081 Ulm, Germany; Institute of Electrochemistry, Ulm University, 89081 Ulm, Germany*

Felix H. Richter − *Institute of Physical Chemistry, Justus Liebig University Giessen, D-35392 Giessen, Germany; Center for Materials Research (LaMa), Justus Liebig University Giessen, D-35392 Giessen, Germany*

Complete contact information is available at: https://pubs.acs.org/10.1021/acs.chemmater.0c04454

Notes

The authors declare no competing financial interest.

■ ACKNOWLEDGMENTS

Financial support from the Federal Ministry of Education and Research (BMBF) within the FELIZIA project (03XP0026G, 03XP0026J) and the FESTBATT consortium (03XP0177A, 03XP0176D) is gratefully acknowledged. The authors acknowledge support with computational resources provided by the state of Baden-Württemberg through bwHPC (bwForCluster JUSTUS). The authors (JLU Giessen) also acknowledge support by BASF SE within the International Network for Batteries and Electrochemistry.

■ REFERENCES

(1) Etacheri, V.; Marom, R.; Elazari, R.; Salitra, G.; Aurbach, D. Challenges in the Development of Advanced Li-Ion Batteries: A Review. *Energy Environ. Sci.* **2011**, *4*, 3243−3262.

(2) Thackeray, M. M.; Wolverton, C.; Isaacs, E. D. Electrical Energy Storage for Transportation - Approaching the Limits of, and Going beyond, Lithium-Ion Batteries. *Energy and Environmental Science*; Royal Society of Chemistry, 2012; pp 7854−7863.

(3) Janek, J.; Zeier, W. G. A Solid Future for Battery Development. *Nat. Energy* **2016**, *1*, 16141.

(4) Kato, Y.; Hori, S.; Saito, T.; Suzuki, K.; Hirayama, M.; Mitsui, A.; Yonemura, M.; Iba, H.; Kanno, R. High-Power All-Solid-State Batteries Using Sulfide Superionic Conductors. *Nat. Energy* **2016**, *1*, 16030.

(5) Bachman, J. C.; Muy, S.; Grimaud, A.; Chang, H.-H.; Pour, N.; Lux, S. F.; Paschos, O.; Maglia, F.; Lupart, S.; Lamp, P.; Giordano, L.; Shao-Horn, Y. Inorganic Solid-State Electrolytes for Lithium Batteries: Mechanisms and Properties Governing Ion Conduction. *Chem. Rev.* **2016**, *116*, 140−162.

(6) Murugan, R.; Thangadurai, V.; Weppner, W. Fast Lithium Ion Conduction in Garnet-Type Li7La 3Zr2O12. *Angew. Chem. Int. Ed.* **2007**, *46*, 7778−7781.

(7) Busche, M. R.; Weber, D. A.; Schneider, Y.; Dietrich, C.; Wenzel, S.; Leichtweiss, T.; Schröder, D.; Zhang, W.; Weigand, H.; Walter, D.; Sedlmaier, S. J.; Houtarde, D.; Nazar, L. F.; Janek, J. In Situ Monitoring of Fast Li-Ion Conductor Li7P3S11 Crystallization Inside a Hot-Press Setup. *Chem. Mater.* **2016**, *28*, 6152−6165.

(8) Buschmann, H.; Dölle, J.; Berendts, S.; Kuhn, A.; Bottke, P.; Wilkening, M.; Heitjans, P.; Senyshyn, A.; Ehrenberg, H.; Lotnyk, A.; Duppel, V.; Kienle, L.; Janek, J. Structure and Dynamics of the Fast Lithium Ion Conductor "Li 7La3Zr2O12.". *Phys. Chem. Chem. Phys.* **2011**, *13*, 19378−19392.

(9) Liu, Z.; Fu, W.; Payzant, E. A.; Yu, X.; Wu, Z.; Dudney, N. J.; Kiggans, J.; Hong, K.; Rondinone, A. J.; Liang, C. Anomalous High Ionic Conductivity of Nanoporous *β*-Li 3PS4. *J. Am. Chem. Soc.* **2013**, *135*, 975−978.

(10) Zhu, Y.; He, X.; Mo, Y. Origin of Outstanding Stability in the Lithium Solid Electrolyte Materials: Insights from Thermodynamic Analyses Based on First-Principles Calculations. *ACS Appl. Mater. Interfaces* **2015**, *7*, 23685−23693.

(11) Wenzel, S.; Randau, S.; Leichtweiß, T.; Weber, D. A.; Sann, J.; Zeier, W. G.; Janek, J. Direct Observation of the Interfacial Instability of the Fast Ionic Conductor Li10GeP2S12 at the Lithium Metal Anode. *Chem. Mater.* **2016**, *28*, 2400−2407.

(12) Whiteley, J. M.; Kim, J. W.; Kang, C. S.; Cho, J. S.; Oh, K. H.; Lee, S.-H. Tin Networked Electrode Providing Enhanced Volumetric Capacity and Pressureless Operation for All-Solid-State Li-Ion Batteries. *J. Electrochem. Soc.* **2015**, *162*, A711−A715.

(13) Zhang, W.; Schröder, D.; Arlt, T.; Manke, I.; Koerver, R.; Pinedo, R.; Weber, D. A.; Sann, J.; Zeier, W. G.; Janek, J. (Electro)Chemical Expansion during Cycling: Monitoring the Pressure Changes in Operating Solid-State Lithium Batteries. *J. Mater. Chem. A* **2017**, *5*, 9929−9936.

(14) Zhang, W.; Weber, D. A.; Weigand, H.; Arlt, T.; Manke, I.; Schröder, D.; Koerver, R.; Leichtweiss, T.; Hartmann, P.; Zeier, W. G.; Janek, J. Interfacial Processes and Influence of Composite Cathode Microstructure Controlling the Performance of All-Solid-State Lithium Batteries. *ACS Appl. Mater. Interfaces* **2017**, *9*, 17835−17845.

(15) Bron, P.; Roling, B.; Dehnen, S. Impedance Characterization Reveals Mixed Conducting Interphases between Sulfidic Superionic Conductors and Lithium Metal Electrodes. *J. Power Sources* **2017**, *352*, 127−134.

(16) Koerver, R.; Walther, F.; Aygün, I.; Sann, J.; Dietrich, C.; Zeier, W. G.; Janek, J. Redox-Active Cathode Interphases in Solid-State Batteries. *J. Mater. Chem. A* **2017**, *5*, 22750−22760.

(17) Tian, Y.; Shi, T.; Richards, W. D.; Li, J.; Kim, J. C.; Bo, S.-H.; Ceder, G. Compatibility Issues between Electrodes and Electrolytes in Solid-State Batteries. *Energy Environ. Sci.* **2017**, *10*, 1150−1166.

(18) Koerver, R.; Aygün, I.; Leichtweiß, T.; Dietrich, C.; Zhang, W.; Binder, J. O.; Hartmann, P.; Zeier, W. G.; Janek, J. Capacity Fade in Solid-State Batteries: Interphase Formation and Chemomechanical Processes in Nickel-Rich Layered Oxide Cathodes and Lithium Thiophosphate Solid Electrolytes. *Chem. Mater.* **2017**, *29*, 5574−5582.

(19) Walther, F.; Koerver, R.; Fuchs, T.; Ohno, S.; Sann, J.; Rohnke, M.; Zeier, W. G.; Janek, J. Visualization of the Interfacial Decomposition of Composite Cathodes in Argyrodite-Based All-

Solid-State Batteries Using Time-of-Flight Secondary-Ion Mass Spectrometry. *Chem. Mater.* **2019**, *31*, 3745−3755.
(20) Walther, F.; Randau, S.; Schneider, Y.; Sann, J.; Rohnke, M.; Richter, F. H.; Zeier, W. G.; Janek, J. Influence of Carbon Additives on the Decomposition Pathways in Cathodes of Lithium Thiophosphate-Based All-Solid-State Batteries. *Chem. Mater.* **2020**, *32*, 6123−6136.
(21) Shi, T.; Tu, Q.; Tian, Y.; Xiao, Y.; Miara, L. J.; Kononova, O.; Ceder, G. High Active Material Loading in All-Solid-State Battery Electrode via Particle Size Optimization. *Adv. Energy Mater.* **2020**, *10*, 1902881.
(22) Bielefeld, A.; Weber, D. A.; Janek, J. Microstructural Modeling of Composite Cathodes for All-Solid-State Batteries. *J. Phys. Chem. C* **2019**, *123*, 1626−1634.
(23) Zhu, C.; Usiskin, R. E.; Yu, Y.; Maier, J. The Nanoscale Circuitry of Battery Electrodes. *Science* **2017**, *358*, No. eaao2808.
(24) Ménétrier, M.; Saadoune, I.; Levasseur, S.; Delmas, C. The Insulator-Metal Transition upon Lithium Deintercalation from LiCoO2: Electronic Properties and 7Li NMR Study. *J. Mater. Chem.* **1999**, *9*, 1135−1140.
(25) Neumann, A.; Randau, S.; Becker-Steinberger, K.; Danner, T.; Hein, S.; Ning, Z.; Marrow, J.; Richter, F. H.; Janek, J.; Latz, A. Analysis of Interfacial Effects in All-Solid-State Batteries with Thiophosphate Solid Electrolytes. *ACS Appl. Mater. Interfaces* **2020**, *12*, 9277−9291.
(26) Ruess, R.; Schweidler, S.; Hemmelmann, H.; Conforto, G.; Bielefeld, A.; Weber, D. A.; Sann, J.; Elm, M. T.; Janek, J. Influence of NCM Particle Cracking on Kinetics of Lithium-Ion Batteries with Liquid or Solid Electrolyte. *J. Electrochem. Soc.* **2020**, *167*, 100532.
(27) Latz, A.; Zausch, J. Multiscale Modeling of Lithium Ion Batteries: Thermal Aspects. *Beilstein J. Nanotechnol.* **2015**, *6*, 987−1007.
(28) Finsterbusch, M.; Danner, T.; Tsai, C.-L.; Uhlenbruck, S.; Latz, A.; Guillon, O. High Capacity Garnet-Based All-Solid-State Lithium Batteries: Fabrication and 3D-Microstructure Resolved Modeling. *ACS Appl. Mater. Interfaces* **2018**, *10*, 22329−22339.
(29) Zhang, W.; Leichtweiß, T.; Culver, S. P.; Koerver, R.; Das, D.; Weber, D. A.; Zeier, W. G.; Janek, J. The Detrimental Effects of Carbon Additives in Li10GeP2S12-Based Solid-State Batteries. *ACS Appl. Mater. Interfaces* **2017**, *9*, 35888−35896.
(30) Park, S. W.; Oh, G.; Park, J. W.; Ha, Y. C.; Lee, S. M.; Yoon, S. Y.; Kim, B. G. Graphitic Hollow Nanocarbon as a Promising Conducting Agent for Solid-State Lithium Batteries. *Small* **2019**, *15*, 1900235.
(31) Strauss, F.; Stepien, D.; Maibach, J.; Pfaffmann, L.; Indris, S.; Hartmann, P.; Brezesinski, T. Influence of Electronically Conductive Additives on the Cycling Performance of Argyrodite-Based All-Solid-State Batteries. *RSC Adv.* **2019**, *10*, 1114−1119.
(32) Swamy, T.; Chen, X.; Chiang, Y.-M. Electrochemical Redox Behavior of Li Ion Conducting Sulfide Solid Electrolytes. *Chem. Mater.* **2019**, *31*, 707−713.
(33) Tan, D. H. S.; Wu, E. A.; Nguyen, H.; Chen, Z.; Marple, M. A. T.; Doux, J.-M.; Wang, X.; Yang, H.; Banerjee, A.; Meng, Y. S. Elucidating Reversible Electrochemical Redox of Li6PS5Cl Solid Electrolyte. *ACS Energy Lett.* **2019**, *4*, 2418−2427.
(34) Yoon, K.; Kim, J. J.; Seong, W. M.; Lee, M. H.; Kang, K. Investigation on the Interface between Li10GeP2S12 Electrolyte and Carbon Conductive Agents in All-Solid-State Lithium Battery. *Sci. Rep.* **2018**, *8*, 8066.
(35) Jung, Y. S.; Oh, D. Y.; Nam, Y. J.; Park, K. H. Issues and Challenges for Bulk-Type All-Solid-State Rechargeable Lithium Batteries Using Sulfide Solid Electrolytes. *Isr. J. Chem.* **2015**, *55*, 472−485.
(36) Liang, J.; Sun, Y.; Zhao, Y.; Sun, Q.; Luo, J.; Zhao, F.; Lin, X.; Li, X.; Li, R.; Zhang, L.; Lu, S.; Huang, H.; Sun, X. Engineering the Conductive Carbon/PEO Interface to Stabilize Solid Polymer Electrolytes for All-Solid-State High Voltage LiCoO2 Batteries. *J. Mater. Chem. A* **2020**, *8*, 2769−2776.
(37) Deng, S.; Sun, Y.; Li, X.; Ren, Z.; Liang, J.; Doyle-Davis, K.; Liang, J.; Li, W.; Norouzi Banis, M.; Sun, Q.; Li, R.; Hu, Y.; Huang, H.; Zhang, L.; Lu, S.; Luo, J.; Sun, X. Eliminating the Detrimental Effects of Conductive Agents in Sulfide-Based Solid-State Batteries. *ACS Energy Lett.* **2020**, *5*, 1243−1251.
(38) Maibach, J.; Lindgren, F.; Eriksson, H.; Edström, K.; Hahlin, M. Electric Potential Gradient at the Buried Interface between Lithium-Ion Battery Electrodes and the SEI Observed Using Photoelectron Spectroscopy. *J. Phys. Chem. Lett.* **2016**, *7*, 1775−1780.
(39) Lindgren, F.; Rehnlund, D.; Källquist, I.; Nyholm, L.; Edström, K.; Hahlin, M.; Maibach, J. Breaking Down a Complex System: Interpreting PES Peak Positions for Cycled Li-Ion Battery Electrodes. *J. Phys. Chem. C* **2017**, *121*, 27303−27312.
(40) GeoDict Startseite. https://www.math2market.com/?Language=de (accessed Nov 16, 2020).
(41) Haselrieder, W.; Ivanov, S.; Christen, D. K.; Bockholt, H.; Kwade, A. Impact of the Calendering Process on the Interfacial Structure and the Related Electrochemical Performance of Secondary Lithium-Ion Batteries. *ECS Trans.* **2013**, *50*, 59−70.
(42) Strauss, F.; Bartsch, T.; De Biasi, L.; Kim, A.-Y.; Janek, J.; Hartmann, P.; Brezesinski, T. Impact of Cathode Material Particle Size on the Capacity of Bulk-Type All-Solid-State Batteries. *ACS Energy Lett.* **2018**, *3*, 992−996.
(43) Usiskin, R. E.; Maier, J. Guidelines for Optimizing the Architecture of Battery Insertion Electrodes Based on the Concept of Wiring Lengths. *Phys. Chem. Chem. Phys.* **2018**, *20*, 16449−16462.
(44) Hlushkou, D.; Reising, A. E.; Kaiser, N.; Spannenberger, S.; Schlabach, S.; Kato, Y.; Roling, B.; Tallarek, U. The Influence of Void Space on Ion Transport in a Composite Cathode for All-Solid-State Batteries. *J. Power Sources* **2018**, *396*, 363−370.
(45) Pöpke, H.; Mutoro, E.; Luerssen, B.; Janek, J. Oxidation of Platinum in the Epitaxial Model System Pt(111)/YSZ(111): Quantitative Analysis of an Electrochemically Driven PtO x Formation. *J. Phys. Chem. C* **2012**, *116*, 1912−1920.
(46) Mutoro, E.; Luerßen, B.; Günther, S.; Janek, J. The Electrode Model System Pt(O2)|YSZ: Influence of Impurities and Electrode Morphology on Cyclic Voltammograms. *Solid State Ionics* **2009**, *180*, 1019−1033.
(47) Wenzel, S.; Weber, D. A.; Leichtweiss, T.; Busche, M. R.; Sann, J.; Janek, J. Interphase Formation and Degradation of Charge Transfer Kinetics between a Lithium Metal Anode and Highly Crystalline Li7P3S11 Solid Electrolyte. *Solid State Ionics* **2016**, *286*, 24−33.
(48) Richards, W. D.; Miara, L. J.; Wang, Y.; Kim, J. C.; Ceder, G. Interface Stability in Solid-State Batteries. *Chem. Mater.* **2016**, *28*, 266−273.
(49) Auvergniot, J.; Cassel, A.; Foix, D.; Viallet, V.; Seznec, V.; Dedryvère, R. Redox Activity of Argyrodite Li6PS5Cl Electrolyte in All-Solid-State Li-Ion Battery: An XPS Study. *Solid State Ionics* **2017**, *300*, 78−85.
(50) Nagai, E.; Arthur, T. S.; Bonnick, P.; Suto, K.; Muldoon, J. The Discharge Mechanism for Solid-State Lithium-Sulfur Batteries. *MRS Adv.* **2019**, *4*, 2627−2634.
(51) Zhang, W.; Richter, F. H.; Culver, S. P.; Leichtweiss, T.; Lozano, J. G.; Dietrich, C.; Bruce, P. G.; Zeier, W. G.; Janek, J. Degradation Mechanisms at the Li10GeP2S12/LiCoO2 Cathode Interface in an All-Solid-State Lithium-Ion Battery. *ACS Appl. Mater. Interfaces* **2018**, *10*, 22226−22236.
(52) Koerver, R.; Zhang, W.; De Biasi, L.; Schweidler, S.; Kondrakov, A. O.; Kolling, S.; Brezesinski, T.; Hartmann, P.; Zeier, W. G.; Janek, J. Chemo-Mechanical Expansion of Lithium Electrode Materials-on the Route to Mechanically Optimized All-Solid-State Batteries. *Energy Environ. Sci.* **2018**, *11*, 2142−2158.
(53) Kondrakov, A. O.; Schmidt, A.; Xu, J.; Geßwein, H.; Mönig, R.; Hartmann, P.; Sommer, H.; Brezesinski, T.; Janek, J. Anisotropic Lattice Strain and Mechanical Degradation of High- and Low-Nickel NCM Cathode Materials for Li-Ion Batteries. *J. Phys. Chem. C* **2017**, *121*, 3286−3294.
(54) Dewald, G. F.; Ohno, S.; Kraft, M. A.; Koerver, R.; Till, P.; Vargas-Barbosa, N. M.; Janek, J.; Zeier, W. G. Experimental

https://dx.doi.org/10.1021/acs.chemmater.0c04454
Chem. Mater. XXXX, XXX, XXX−XXX

Assessment of the Practical Oxidative Stability of Lithium Thiophosphate Solid Electrolytes. *Chem. Mater.* **2019**, *31*, 8328−8337.
(55) Randau, S.; Weber, D. A.; Kötz, O.; Koerver, R.; Braun, P.; Weber, A.; Ivers-Tiffée, E.; Adermann, T.; Kulisch, J.; Zeier, W. G.; Richter, F. H.; Janek, J. Benchmarking the Performance of All-Solid-State Lithium Batteries. *Nat. Energy* **2020**, *5*, 259−270.
(56) Marichy, C.; Pinna, N. Carbon-Nanostructures Coated/Decorated by Atomic Layer Deposition: Growth and Applications. *Coordination Chemistry Reviews*; Elsevier, December 1, 2013; pp 3232−3253.

https://dx.doi.org/10.1021/acs.chemmater.0c04454
Chem. Mater. XXXX, XXX, XXX−XXX

3.3 Contribution to Publications

3.3.1 Li^+-Ion Dynamics in β-Li_3PS_4 Observed by NMR: Local Hopping and Long-Range Transport

In this publication the Li^+-ion dynamic in β-Li_3PS_4 was investigated. The aim was to elucidate the local and long-range transport mechanisms of Li^+-ions in this material. Besides ^6Li and ^{31}P magic-angle spinning NMR, X-ray and neutron diffusion, high temperature X-ray diffraction and impedance measurements were performed.

The long-range crystal structure was probed by X-ray and neutron diffraction techniques, whereas the local environments around Li and P could be investigated by MAS NMR spectroscopy. The phase transition from β-Li_3PS_4 to α-Li_3PS_4 was determined by XRD. The β-phase is present in the temperature range from 298 to 773 K. Above 773 K the transformation to the high temperature alpha phase occurs. This phase is stable up to 873 K and above 923 K the material is completely melted and no Bragg reflections are present.

The transport of the Li^+-ions takes place locally in the nanosecond range and a long-range transport occurs on the much longer timescale. The activation energy of this transport was determined to be 0.24 eV. A room temperature Li diffusion constant was determined to be $9 \cdot 10^{-14}$ $m^2 \cdot s^{-1}$, the corresponding Li conductivity is $1 \cdot 10^{-4}$ $S \cdot cm^{-1}$ and was calculated using the Nernst-Einstein relation. Electrochemical impedance measurements confirmed these results. Furthermore, the diffusion path of the Li^+-ions was elucidated by the combination of X-ray and neutron diffraction. This involves a 2D diffusion using two of the three available Li sites.

The work was written by Heike Stöffler and the SEM images (Figure 11), impedance measurements and Arrhenius plot (Figure 12) were performed by Simon Randau at the JLU. Images reprinted with permission from *The Journal of Physical Chemistry C* 2018 American Chemical Society.

H. Stöffler, T. Zinkevich, M. Yavuz, A. Senyshyn, J. Kulisch, P. Hartmann, T. Adermann, S. Randau, F. H. Richter, J. Janek, S. Indris, and H. Ehrenberg, Li^+-Ion Dynamics in β-Li_3PS_4 Observed by NMR: Local Hopping and Long-Range Transport, *The Journal of Physical Chemistry C*, **2018**, 122 (28), 15954-15965.

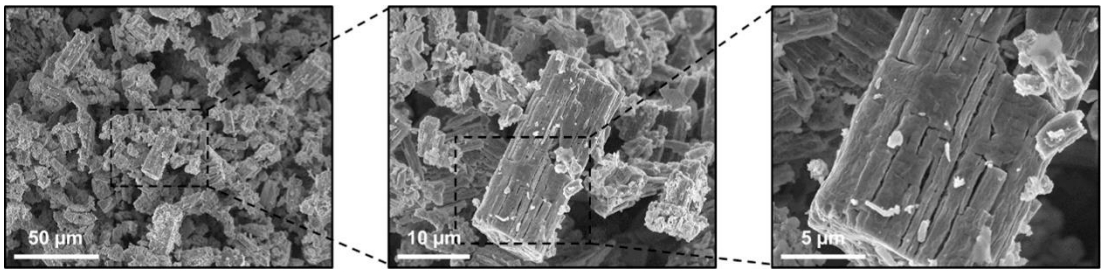

Figure 11: Scanning electron microscopy images of β-Li_3PS_4 powder. Reprinted with permission from The Journal of Physical Chemistry C 2018 American Chemical Society[127]

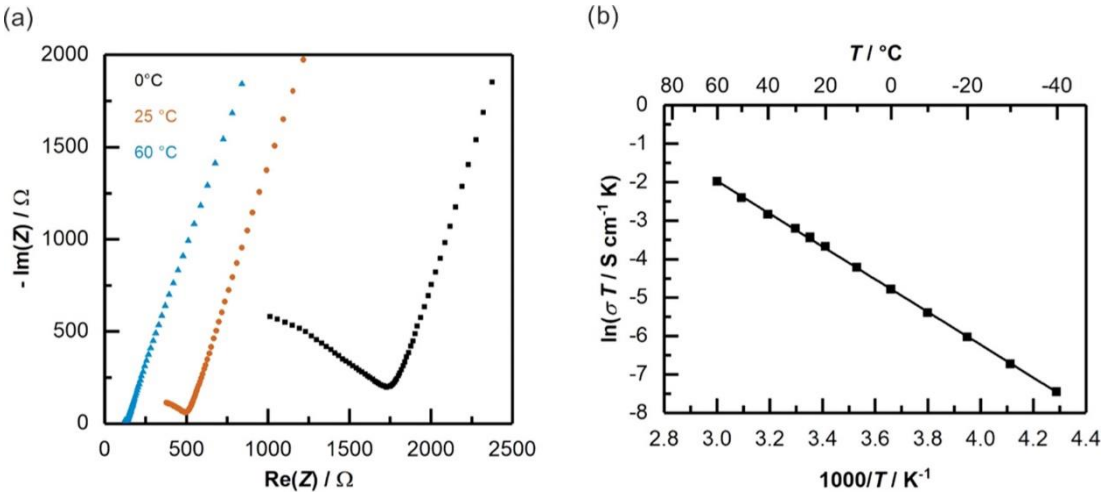

Figure 12: a) Impedance plot of β-Li_3PS_4 at selected temperatures (60 mg, 425 µm thickness, 10 mm diameter). b) Arrhenius plot of the ionic conductivity, as obtained from temperature dependent impedance measurements. Reprinted with permission from The Journal of Physical Chemistry C 2018 American Chemical Society[127]

3.3.2 Amorphous versus Crystalline Li_3PS_4: Local Structural Changes during Synthesis and Li Ion Mobility

In this paper the synthesis of Li_3PS_4 is discussed in detail. The focus was on the identification of the different structural building blocks and in which stage of the synthesis they occur. In a first step the starting materials have to be amorphized with a ball mill. The amorphous Li_3PS_4 is compared with the crystallized β-Li_3PS_4. The crystallization kinetics were investigated using the intensities of Bragg reflections. ^{7}Li NMR relaxometry and pulsed field-gradient (PFG) NMR was used to study the short-range and long-range Li^+ dynamics in both materials.

The formation mechanism during amorphization was elucidated. During ball milling of the educts the amorphization process involves several anionic building blocks such as $[PS_4]^{3-}$, $[P_2S_6]^{4-}$, and $[P_2S_7]^{4-}$, as confirmed by ^{31}P MAS NMR and Raman spectroscopy. Phase pure crystallization of β-Li_3PS_4 was achieved at 548 K.

For the glassy sample and the glass-ceramic β-Li_3PS_4, a Li^+ bulk conductivity σ_{Li} of $1.6 \cdot 10^{-4}$ $S \cdot cm^{-1}$ (298 K) was obtained by PFG NMR, showing that for this system a well-crystalline material is not essential to achieve fast Li-ion dynamics. Impedance measurements reveal a slightly higher overall conductivity for the amorphous sample, suggesting that the influence of grain boundaries is small in this case. The results show that a certain nanostructure is not essential to obtain a good ionic conductivity in Li_3PS_4, not even a crystalline material is necessary. This might facilitate future upscaling of the synthesis procedure because a sintering step is not necessary.

This publication was written by Heike Stöffler. The impedance measurements and Arrhenius calculations were performed by Simon Randau at the JLU. The physisorption experiments were performed by Simon Randau and Felix H. Richter.

H. Stöffler, T. Zinkevich, M. Yavuz, A. Hansen, M. Knapp, J. Bednarčík, S. Randau, F. H. Richter, J. Janek, H. Ehrenberg, and S. Indris, Amorphous versus Crystalline Li3PS4: Local Structural Changes during Synthesis and Li Ion Mobility, *J. Phys. Chem. C*, **2019**, 123 (16) 10280–10290.

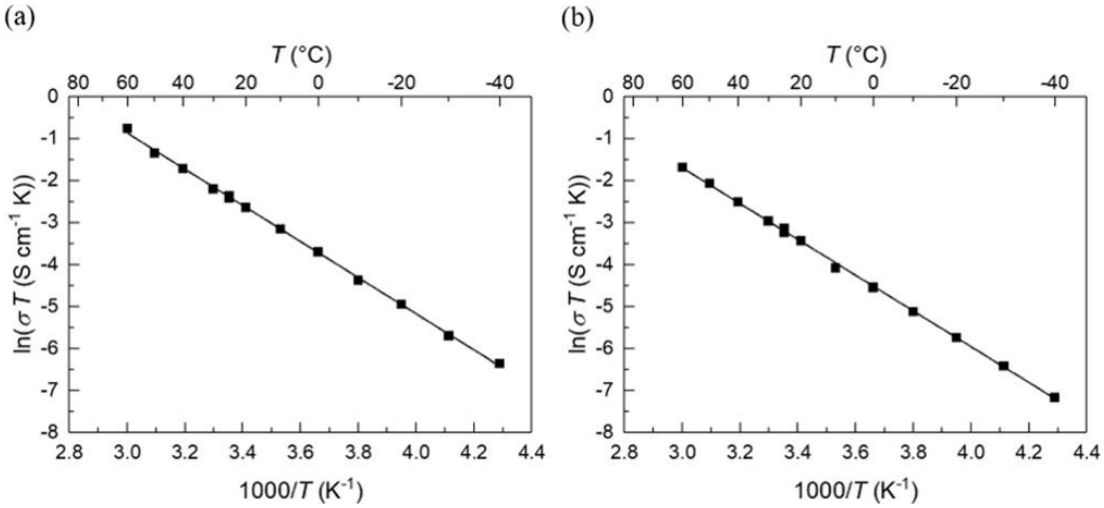

Figure 13: Arrhenius plots from impedance measurements for the (a) amorphous and (b) calcined samples. Reprinted with permission from The Journal of Physical Chemistry C 2018 American Chemical Society.[128]

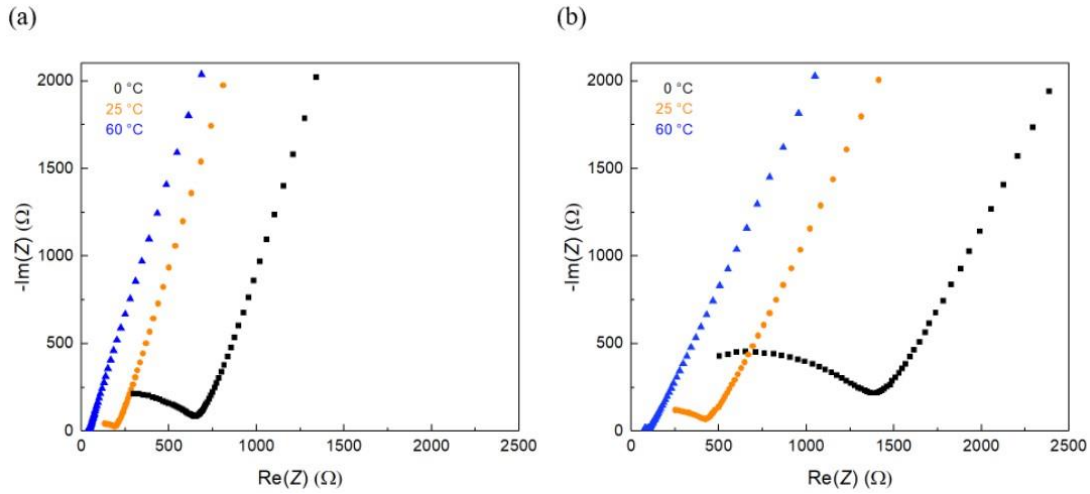

Figure 14: Nyquist plot of electrochemical impedance for the (a) amorphous and (b) calcined sample various temperatures. Reprinted with permission from The Journal of Physical Chemistry C 2018 American Chemical Society.[128]

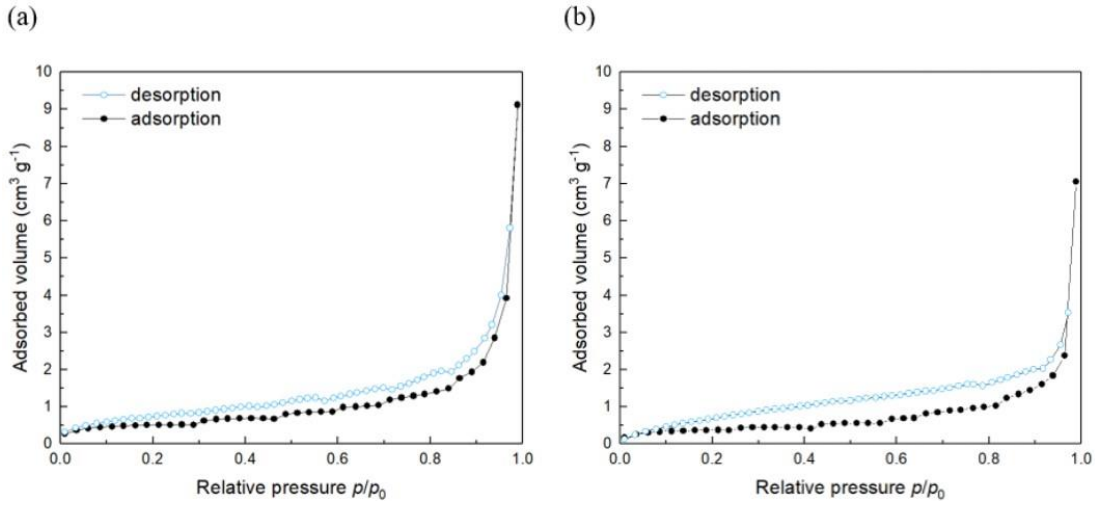

Figure 15: Nitrogen physisorption isotherm of (a) amorphous and (b) calcined sample. Reprinted with permission from The Journal of Physical Chemistry C 2018 American Chemical Society.[128]

3.3.3 Analysis of Interfacial Effects in All-Solid-State Batteries with Thiophosphate Solid Electrolytes

Current cathodes in SSBs have a lower utilization of the active material than in batteries with liquid electrolytes, so a significant increase in energy density can be achieved by optimizing the composite cathodes. The common understanding is that interface processes between the active material and solid electrolyte are responsible for the reduced performance. To further understand the origin of this problem, 3D microstructure-resolved simulations were combined with electrochemical investigations of batteries. The 3D microstructure was obtained by X-ray tomography of cathode composites. Cell data were obtained by cyclization, impedance experiments and symmetrical cells.

The 3D micro- structure-resolved simulations were run on reconstructed electrodes obtained by CT measurements of β-LPS/NMC-622 composite cathodes. By this simulation conclusions on tortuosity effects and structural inhomogeneities can be drawn. The computational results are validated by the experimental data. Two competing mechanism were identified. First, capacity losses are caused by the decreased electronic conductivity of the CAM during lithiation. This results in a self-accelerated electronic blocking of the cathode, especially for high rates lowering the CAM utilization. Second, the low ionic conductivity of LPS promotes an inhomogeneous intercalation of the CAM close to the separator. The competition of both mechanisms leads to an inhomogeneous and imperfect utilization of the active material, resulting in an interesting sandwich like lithiation of the active material, especially pronounced in thicker electrodes with higher energy density. These inherent material properties can be potentially enhanced by morphological inhomogeneities.

Two morphological changes were investigated in more detail, which can occur during the cell operation. First, a reduced contact of the electrode layer to the current collector and second the delamination of the solid electrolyte from the active particle surface. For the first case the small contact area between the active material and current collector reduces the specific capacity at high currents. The enhanced local currents enhance an inhomogeneous lithiation close to the current collector, which pronounces the mentioned local reduction of electronic conductivity. For the second case of the particle delamination large overpotentials at high discharge rates might be coupled to the reduced active surface caused by volume changes of the active material within the composite cathode during cycling. Still, this effect does not give a complete explanation for the capacity loss at high currents. A study combining this effect with the formation of space charge layers seems to be necessary. This publication demonstrates that both the internal and external interfaces of the composite cathode influence cell performance.

This work was written by Anton Neumann. Simon Randau is the Coauthor and wrote the description of the electrochemical experiments. Furthermore, the electrochemical experiments, material parameters and data for the simulation were provided by Simon Randau. The samples for the CT measurements were provided by Simon Randau.

A. Neumann, S. Randau, K. Becker-Steinberger, T. Danner, S. Hein, Z. Ning, J. Marrow, F. H. Richter, J. Janek, A. Latz, Analysis of Interfacial Effects in All-Solid-State Batteries with Thiophosphate Solid Electrolytes, *ACS Appl. Mater. Interfaces*, **2020**, 12 (8), 9277-9291.

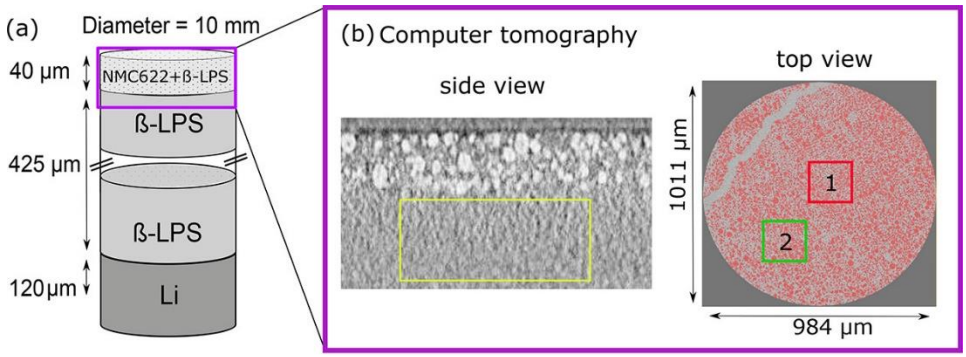

Figure 16: a) Schematic of the cell setup and corresponding layer thicknesses. (b) CT images inside (xy-plane) and top view (yz-plane) showing the pristine composite cathode and parts of the compressed separator (yellow inset). Reprinted with permission from ACS Appl. Mater. Interfaces C 2020 American Chemical Society.[118]

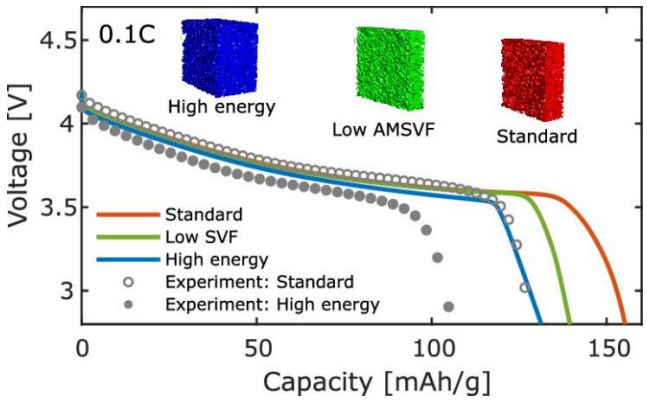

Figure 17: Comparison between experimental (gray symbols) and simulated 0.1C discharge curves for the virtual standard (solid red), low-AMSVF (solid green), and high-energy electrodes (solid blue). Reprinted with permission from ACS Appl. Mater. Interfaces C 2020 American Chemical Society.[118]

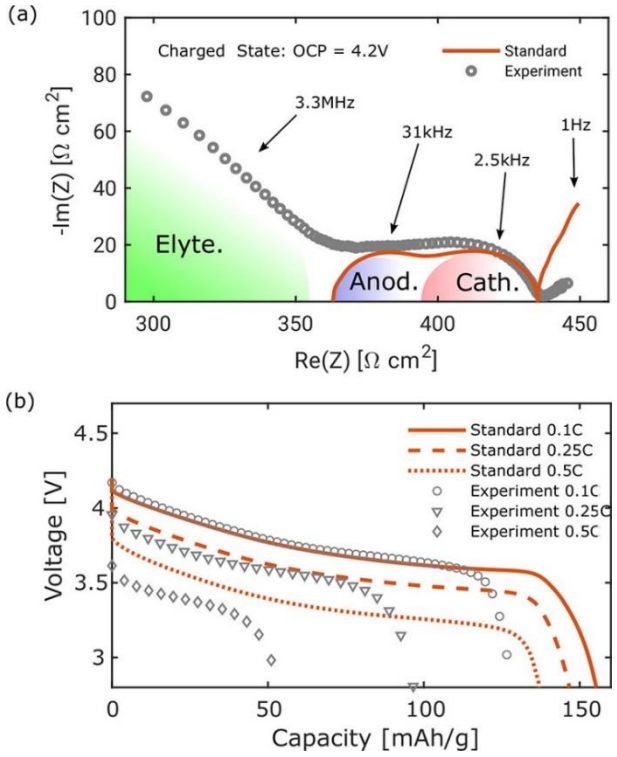

Figure 18: a) Simulation (line) and measured (symbol) impedance spectra for a charged cell (OCP = 4.2 V) with the standard electrode. b) Results of the C-rate test measured (symbols) and simulated (lines) on the standard electrode. Reprinted with permission from ACS Appl. Mater. Interfaces C 2020 American Chemical Society.[118]

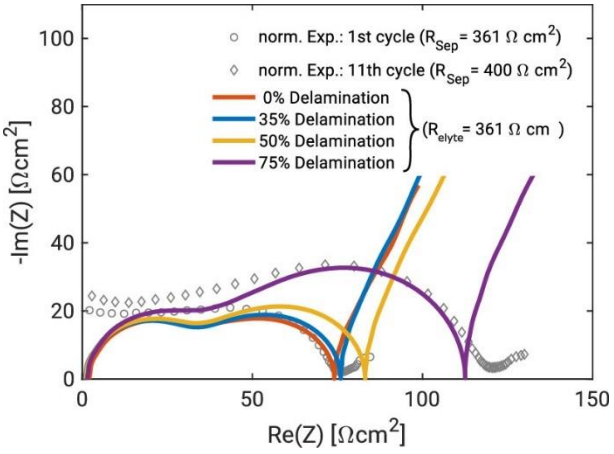

Figure 19: Simulated impedance for each delamination scenario (solid lines) and experimental impedance spectra after cycles 1 and 11. All data are shifted by the corresponding solid electrolyte bulk resistance R_{Elyte} as indicated in the legend. Reprinted with permission from ACS Appl. Mater. Interfaces C 2020 American Chemical Society.[118]

3.3.4 Influence of Carbon Additives on the Decomposition Pathways in Cathodes of Lithium Thiophosphate-Based All-Solid-State Batteries

The fact that the CAM cannot be completely addressed in the composite cathode is a known challenge within SSBs. In liquid electrolyte batteries it is common to add carbon-based conductive additives for better CAM contacting. Due to a pronounced long-term capacity fade the beneficial effect of carbon additives is not maintained for SSBs. This capacity fade is due to several decomposition mechanism and the formed products show bad ionic conductivities, resulting in a buildup of resistances. So far, these effects have not been analyzed in depth and are not fully understood because of the complexity of the composite cathode structure. Together with overlap of the occurring degradation paths, this makes a separation of the individual decomposition processes challenging.

Cycling experiments highlight the influence of the carbon additives on the battery performance. These experiments are also used to induce the degradation by prolonged cycling. The influence of VGCF as carbon-based conductive additive on the degradation within the cathode composite is investigated by XPS and Tof-SIMS. Surface and bulk analyses were combined to separate the overlapping degradation mechanism.

The electrochemical studies revealed a higher initial capacity by using VGCF, which is not only attributed to a higher utilization of active material but also to a contribution from redox-active decomposition products of the SE. At the same time the capacity fading was significantly increased with VGCF, making the additive detrimental for higher charge/discharge cycles. By XPS and ToF-SIMS three independent degradation path were distinguished for the composite cathode. These degradations are located (i) at the current collector, (ii) at the active material and (iii) at the carbon-based conductive additive. The decomposition reactions show a high degree of similarity. With regard to sulfur-containing decomposition products, sulfate/sulfite formation (e.g., Li_2SO_4 seems plausible) and polysulfide formation were observed. The polysulfide formation is dominant and could be verified by long-chain S_x^- fragments. Phosphate formation is dominant for the phosphorus-containing decomposition and Li_3PO_4 seems to be reasonable.

This work was written by Felix Walther. The electrochemical experiments and SEM images were performed and the description of the electrochemical experiments was written by Simon Randau. Felix Walther and Simon Randau planed the analysis experiments. Simon Randau prepared the analyzed samples. Felix Walther conducted the analytical experiments and performed the interpretation.

F. Walther, S. Randau, Y. Schneider, J. Sann, M. Rohnke, F. H. Richter, W. G. Zeier, and J. Janek, Influence of Carbon Additives on the Decomposition Pathways in Cathodes of Lithium Thiophosphate-Based All-Solid-State Batteries, *Chem. Mater.*, **2020**, 32 (14), 6123-6136.

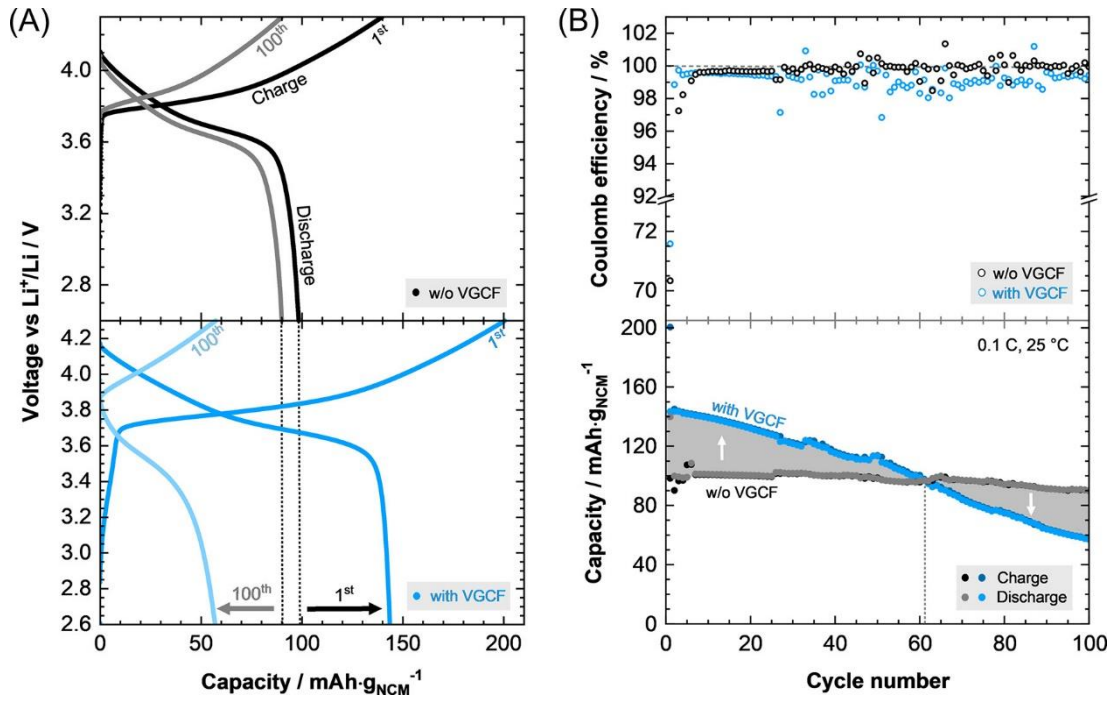

Figure 20: a) Charge and discharge curves for the first and the hundredth cycle of a Li|β-Li_3PS_4|$LiNi_{0.6}Co_{0.2}Mn_{0.2}O_2$/β-$Li_3PS_4$ ASSB with 3 wt.% and without (w/o) VGCF in the composite cathode. b) Charge and discharge capacity and Coulomb efficiency as a function of the cycle number. Adding VGCF results in higher initial capacities, but at the same time in a significantly increased capacity fading. Reprinted with permission from Chemistry of Materials 2020 American Chemical Society.[19]

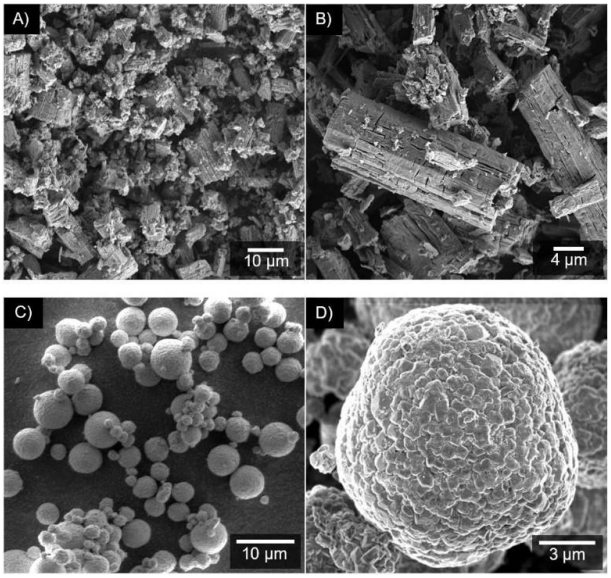

Figure 21: Scanning electron micrographs showing the microstructure and the morphology of the solid electrolyte β-Li_3PS_4 and the active material NCM-622. a) Overview image of the solid electrolyte, b) Large-magnification image of the solid electrolyte, c) Overview image showing the particle size distribution, d) Large-magnification image of single NCM-622 secondary particles formed by several primary particles. Reprinted with permission from Chemistry of Materials 2020 American Chemical Society.[19]

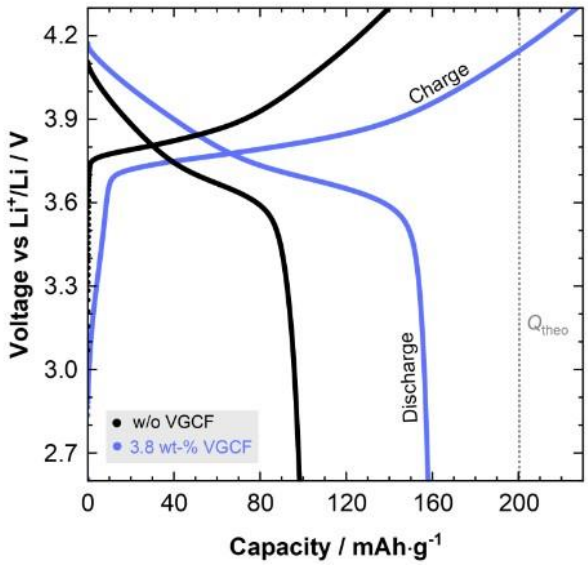

Figure 22: Charge and discharge curve for the first cycle of a Li|β-Li_3PS_4|$LiNi_{0.6}Co_{0.2}Mn_{0.2}$/β-$Li_3PS_4$ ASSB cell with 3.8 wt.% VGCF in the composite cathode. The slope at the beginning of the first charge curve is smaller compared to the reference without VGCF, indicating an increase in side reactions. Additionally, the charge and discharge capacity are further increased compared to the sample with 3 wt.% VGCF, supporting the hypothesis of further capacity contributions due to decomposition reactions. Reprinted with permission from Chemistry of Materials 2020 American Chemical Society.[19]

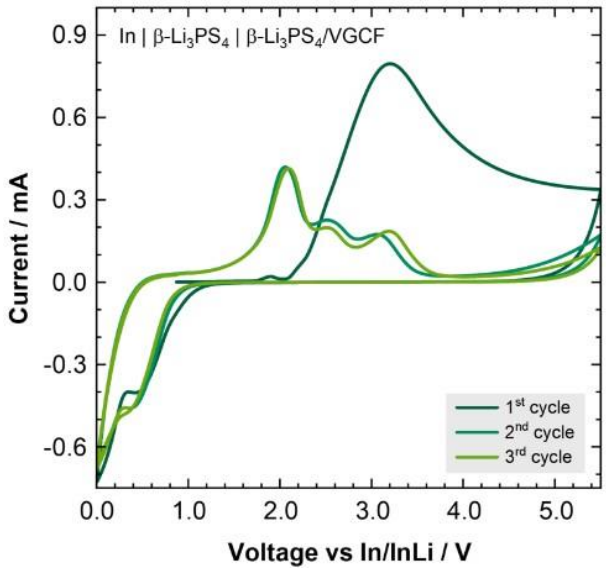

Figure 23: Cyclic voltammogram for a In|β-Li_3PS_4|VGCF/β-Li_3PS_4 cell. Reprinted with permission from Chemistry of Materials 2020 American Chemical Society.[19]

3.3.5 Macroscopic Displacement Reaction of Copper Sulfide in Lithium Solid-State Batteries

Copper sulfide (CuS) is due to its intrinsic mixed conductivity and high theoretical capacity of 560 mAh·g^{-1} an attractive electrode material. Additionally, its ductility and possibility for low temperature synthesis makes it appealing for use in SSBs. In this publication the electrochemical properties of respective SSBs (Li | Li_3PS_4 | Li_3PS_4/CuS) are investigated. The galvanostatic cycling is combined with SEM, EDX and XPS measurements.

The initial discharge capacity at 0.1 C was 498 mAh·g^{-1}, i.e. 84% of its theoretical capacity. After 100 cycles, the capacity reached 310 mAh·g^{-1}. The cell delivered an energy density of 58.2 Wh·kg^{-1} at a power density of 7 W·kg^{-1}. Furthermore, the macroscopic phase separation between the discharge products (Cu and Li_2S) was investigated. CuS underwent a displacement reaction with lithium, leading to the macroscopic phase separation. In particular, Cu formed a network of µm-sized, well-crystallized particles that seems to percolate through the electrode. This separation was reversed upon charging. The displacement mechanism is in agreement with literature based on liquid electrolyte batteries, although the Cu crystals are larger for SSBs. A comparison with literature in a Ragone plot shows that the cells are among the best conversion-type SSBs reported so far.

This study shows that the use of CuS can mitigate two limitations of the conversion reaction, named the polarization and the low Coulombic efficiency in the first cycle. The displacement reaction of the active material is reversible enough for rechargeable batteries at

room temperature. The ductility of the active material and SE, the electrochemical stability of the active material and the SE, the intrinsic conductivity of copper and the displacement mechanism benefit the SSB properties.

The publication was written by Aggunda L. Santhosha. The benchmarking of the battery data, comparison with the literature and Ragone plot were provided by Simon Randau.

A. L. Santhosha, N. Nazer, R. Koerver, S. Randau, F. H. Richter, D. A. Weber, J. Kulisch, T. Adermann, J. Janek and P. Adelhelm, Macroscopic Displacement Reaction of Copper Sulfide in Lithium Solid-State Batteries, *Adv. Energy Mater*, 2020, 10, 2002394

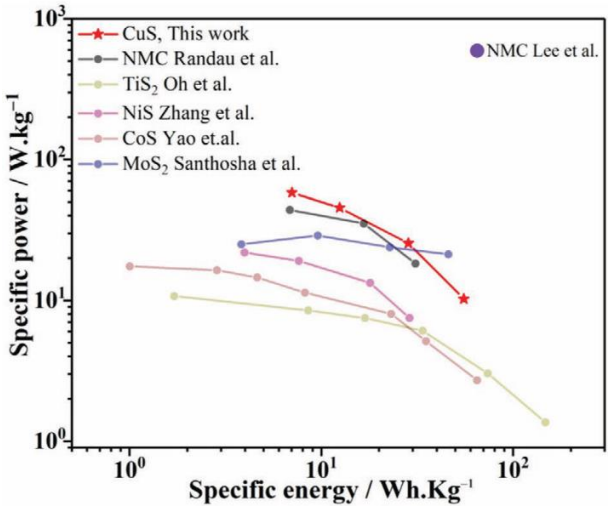

Figure 24: Ragone plot of the ambient temperature performance of solid-state batteries with transition metal sulfides CoS, TiS_2, FeS_2, NiS, MoS_2 and CuS (this work) as cathode, lithium as counter electrode and thiophosphates as solid electrolyte. The performance of the SSBs is estimated from the current density, average charge/discharge voltage and cell mass excluding current collectors and casing. Reprinted with permission from Wiley-VCH GmbH 2020.[129]

4 Conclusion and Outlook

In this Ph.D. thesis the current literature for SSBs was reviewed and evaluated from a quantitative perspective. A comparison between different cell concepts and to a minimalistic cell was performed. From this the current state of the art could be derived and specific research goals for the further development of SSBs with lithium anode could be derived. It is demonstrated that the differences in specific energy and specific power of the multitude of available ASSBs mostly originate from differences in layer thicknesses and internal resistance. The Ragone plot and the plot of the cycle-dependent specific discharge energy offer direct comparison of different cell concepts and varying cycling protocols relative to the minimalistic cell. This comparison clearly shows that currently the large thicknesses of the separator are mainly responsible for a reduction of the energy density in SSBs. From the comparison it could also be concluded that protection concepts, especially for CAM, will be necessary. Furthermore, key research targets were identified using fundamental equations. These are: achieving less than 40 Ω cm^2 internal resistance, less than 50 µm separator thickness, in-situ generation of the anode, more than 5 mAh cm^{-2} area capacity and 500 Wh kg^{-1} hypothetical cathode specific energy. This analysis projects a pathway to lithium metal SSBs and highlights the remaining challenges still to be overcome in order to surpass the performance of state-of-the-art lithium-ion batteries.

Based on this, the battery performance was optimized. For this purpose, the influence of different carbon conducting additives in the cathode composite was considered. Their morphology and specific surface area have a strong influence on battery performance. The presented combination of simulation and experiment highlights that the balance of ionic and electronic percolation is crucial for the performance of SSBs. In addition, it was found that fiber-like carbons form interconnected conduction networks, which leads to a better contact between CAM and current collector. Particular carbons form a multitude of isolated areas which are contacted within the area, but long-range contacting is not guaranteed. The particular carbons showed no positive influence on the battery performance. Additionally, the results of cyclic voltammetry show that all investigated carbons increase the cathode degradation, which decreases the cycling performance of full cells. XPS analysis indicates the formation of oxidized sulfur species such as polysulfides. With higher surface areas of the carbons, the volume fraction of the decomposition products increases. Although batteries with VGCF initially showed the highest discharge capacities, this positive effect was used up during prolonged cycling by the constant decomposition of the SE. This was addressed by a nanometer thin, electronically insulating alumina coating on VGCF. This coating decreased fading of the discharge capacity, without decreasing the initial battery performance. The

resulting microwire concept for carbon additives reduces cell decomposition effectively and may be crucial to realize high power ASSBs.

In summary, this thesis shows that for a useful optimization of SSBs, the entire cell must be considered. A battery cell is a system of anode, separating electrolyte and cathode composite. In the future, the focus should therefore be on a reduction of the separating electrolyte thickness and thus a reduction of the resistances within the battery. In addition to the material thickness, the overall cell resistance needs to be reduced. This can be influenced by the contacting of the individual components. Especially within the cathode composite there are possibilities for optimization by means of carbon conducting additives. However, the decomposition of the SE induced by the carbons must be effectively prevented. For this purpose, it will be necessary to understand the mechanism of the Al_2O_3 coating for carbon fibers presented in this thesis. Suitable layer thicknesses have to be identified. Furthermore, it may be possible to further vary the coating material. Alternative oxides or insulating polymers can also result in increased performance.

Solid-state batteries still face a variety of challenges, which need to be solved for a successful commercial application. The achieved progress in academia and industry as well as the emerging drive towards expanding renewable energy use by politics and society allow an optimistic outlook

5 Bibliography

(1) Raupach, M. R.; Marland, G.; Ciais, P.; Le Quéré, C.; Canadell, J. G.; Klepper, G.; Field, C. B. Global and Regional Drivers of Accelerating CO_2 Emissions. *Proc. Natl. Acad. Sci. U. S. A.* **2007**, *104* (24), 10288–10293.

(2) AOAN. Global Monitoring Laboratory - Carbon Cycle Greenhouse Gases. *US Dep. Commer. NOAA, Glob. Monit. Lab.* **2019**.

(3) Ellabban, O.; Abu-Rub, H.; Blaabjerg, F. Renewable Energy Resources: Current Status, Future Prospects and Their Enabling Technology. *Renewable and Sustainable Energy Reviews*. Elsevier Ltd November 1, 2014, pp 748–764.

(4) Statistics, I. Germany - CO_2 emissions from transport (% of total fuel combustion) https://data.worldbank.org/indicator/EN.CO2.TRAN.ZS?locations=DE&type=points (accessed Dec 31, 2020).

(5) Vilchez, J. J. G.; Smyth, A.; Kelleher, L.; Lu, H.; Rohr, C.; Harrison, G.; Thiel, C. Electric Car Purchase Price as a Factor Determining Consumers' Choice and Their Views on Incentives in Europe. *Sustain.* **2019**, *11* (22), 6357.

(6) Curry, C. *Lithium-Ion Battery Costs and Market*; 2017; Vol. 5.

(7) Volkswagen AG. Supervisory Board and Board of Management take important decisions for future of Volkswagen Group https://www.volkswagenag.com/en/news/2019/05/Important_decisions_for_future_of_Volkswagen_Group.html (accessed Dec 31, 2020).

(8) Janek, J.; Zeier, W. G. A Solid Future for Battery Development. *Nat. Energy* **2016**, *1* (9), 1–4.

(9) Han, F.; Westover, A. S.; Yue, J.; Fan, X.; Wang, F.; Chi, M.; Leonard, D. N.; Dudney, N. J.; Wang, H.; Wang, C. High Electronic Conductivity as the Origin of Lithium Dendrite Formation within Solid Electrolytes. *Nat. Energy* **2019**, *4* (3), 187–196.

(10) Krauskopf, T.; Dippel, R.; Hartmann, H.; Peppler, K.; Mogwitz, B.; Richter, F. H.; Zeier, W. G.; Janek, J. Lithium-Metal Growth Kinetics on LLZO Garnet-Type Solid Electrolytes. *Joule* **2019**, *3* (8), 2030–2049.

(11) Krauskopf, T.; Hartmann, H.; Zeier, W. G.; Janek, J. Toward a Fundamental

Understanding of the Lithium Metal Anode in Solid-State Batteries - An Electrochemo-Mechanical Study on the Garnet-Type Solid Electrolyte $Li_{6.25}Al_{0.25}La_3Zr_2O_{12}$. *ACS Appl. Mater. Interfaces* **2019**, *11* (15), 14463–14477.

(12) Wenzel, S.; Randau, S.; Leichtweiß, T.; Weber, D. A.; Sann, J.; Zeier, W. G.; Janek, J. Direct Observation of the Interfacial Instability of the Fast Ionic Conductor $Li_{10}GeP_2S_{12}$ at the Lithium Metal Anode. *Chem. Mater.* **2016**, *28* (7), 2400–2407.

(13) Zhu, Y.; He, X.; Mo, Y. Origin of Outstanding Stability in the Lithium Solid Electrolyte Materials: Insights from Thermodynamic Analyses Based on First-Principles Calculations. *ACS Appl. Mater. Interfaces* **2015**, *7* (42), 23685–23693.

(14) Zhang, W.; Leichtweiß, T.; Culver, S. P.; Koerver, R.; Das, D.; Weber, D. A.; Zeier, W. G.; Janek, J. The Detrimental Effects of Carbon Additives in $Li_{10}GeP_2S_{12}$-Based Solid-State Batteries. *ACS Appl. Mater. Interfaces* **2017**, *9* (41), 35888–35896.

(15) Dewald, G. F.; Ohno, S.; Kraft, M. A.; Koerver, R.; Till, P.; Vargas-Barbosa, N. M.; Janek, J.; Zeier, W. G. Experimental Assessment of the Practical Oxidative Stability of Lithium Thiophosphate Solid Electrolytes. *Chem. Mater.* **2019**, *31* (20), 8328–8337.

(16) Swamy, T.; Chen, X.; Chiang, Y. M. Electrochemical Redox Behavior of Li Ion Conducting Sulfide Solid Electrolytes. *Chem. Mater.* **2019**, *31* (3), 707–713.

(17) Bielefeld, A.; Weber, D. A.; Janek, J. Microstructural Modeling of Composite Cathodes for All-Solid-State Batteries. *J. Phys. Chem. C* **2019**, *123* (3), 1626–1634.

(18) Shi, T.; Tu, Q.; Tian, Y.; Xiao, Y.; Miara, L. J.; Kononova, O.; Ceder, G. High Active Material Loading in All-Solid-State Battery Electrode via Particle Size Optimization. *Adv. Energy Mater.* **2020**, *10* (1).

(19) Walther, F.; Randau, S.; Schneider, Y.; Sann, J.; Rohnke, M.; Richter, F. H.; Zeier, W. G.; Janek, J. Influence of Carbon Additives on the Decomposition Pathways in Cathodes of Lithium Thiophosphate-Based All-Solid-State Batteries. *Chem. Mater.* **2020**, *32* (14), 6123–6136.

(20) Lee, Y. G.; Fujiki, S.; Jung, C.; Suzuki, N.; Yashiro, N.; Omoda, R.; Ko, D. S.; Shiratsuchi, T.; Sugimoto, T.; Ryu, S.; Ku, J. H.; Watanabe, T.; Park, Y.; Aihara, Y.; Im, D.; Han, I. T. High-Energy Long-Cycling All-Solid-State Lithium Metal Batteries Enabled by Silver–Carbon Composite Anodes. *Nat. Energy* **2020**, *5* (4), 299–308.

(21) Kato, A.; Yamamoto, M.; Sakuda, A.; Hayashi, A.; Tatsumisago, M. Mechanical

Properties of Li_2S-P_2S_5 Glasses with Lithium Halides and Application in All-Solid-State Batteries. *ACS Appl. Energy Mater.* **2018**, *1* (3), 1002–1007.

(22) Yu, S.; Schmidt, R. D.; Garcia-Mendez, R.; Herbert, E.; Dudney, N. J.; Wolfenstine, J. B.; Sakamoto, J.; Siegel, D. J. Elastic Properties of the Solid Electrolyte $Li_7La_3Zr_2O_{12}$ (LLZO). *Chem. Mater.* **2016**, *28* (1), 197–206.

(23) Wolfenstine, J.; Allen, J. L.; Sakamoto, J.; Siegel, D. J.; Choe, H. Mechanical Behavior of Li-Ion-Conducting Crystalline Oxide-Based Solid Electrolytes: A Brief Review. *Ionics (Kiel).* **2018**, *24* (5), 1271–1276.

(24) Kato, A.; Suyama, M.; Hotehama, C.; Kowada, H.; Sakuda, A.; Hayashi, A.; Tatsumisago, M. High-Temperature Performance of All-Solid-State Lithium-Metal Batteries Having Li/Li_3PS_4 Interfaces Modified with Au Thin Films. *J. Electrochem. Soc.* **2018**, *165* (9), A1950–A1954.

(25) Doyle, M.; Fuller, T. F.; Newman, J. The Importance of the Lithium Ion Transference Number in Lithium/Polymer Cells. *Electrochim. Acta* **1994**, *39* (13), 2073–2081.

(26) Yonemoto, F.; Nishimura, A.; Motoyama, M.; Tsuchimine, N.; Kobayashi, S.; Iriyama, Y. Temperature Effects on Cycling Stability of Li Plating/Stripping on Ta-Doped Li7La3Zr2O12. *J. Power Sources* **2017**, *343*, 207–215.

(27) Krauskopf, T.; Mogwitz, B.; Rosenbach, C.; Zeier, W. G.; Janek, J. Diffusion Limitation of Lithium Metal and Li–Mg Alloy Anodes on LLZO Type Solid Electrolytes as a Function of Temperature and Pressure. *Adv. Energy Mater.* **2019**, *9* (44), 1902568.

(28) Whiteley, J. M.; Woo, J. H.; Hu, E.; Nam, K.-W.; Lee, S.-H. Empowering the Lithium Metal Battery through a Silicon-Based Superionic Conductor. *J. Electrochem. Soc.* **2014**, *161* (12), A1812–A1817.

(29) Zhang, Z.; Chen, S.; Yang, J.; Wang, J.; Yao, L.; Yao, X.; Cui, P.; Xu, X. Interface Re-Engineering of $Li_{10}GeP_2S_{12}$ Electrolyte and Lithium Anode for All-Solid-State Lithium Batteries with Ultralong Cycle Life. *ACS Appl. Mater. Interfaces* **2018**, *10* (3), 2556–2565.

(30) Woo, J. H.; Trevey, J. E.; Cavanagh, A. S.; Choi, Y. S.; Kim, S. C.; George, S. M.; Oh, K. H.; Lee, S.-H. Nanoscale Interface Modification of LiCoO 2 by Al 2 O 3 Atomic Layer Deposition for Solid-State Li Batteries . *J. Electrochem. Soc.* **2012**, *159* (7), A1120–A1124.

(31) Xie, D.; Chen, S.; Zhang, Z.; Ren, J.; Yao, L.; Wu, L.; Yao, X.; Xu, X. High Ion Conductive Sb_2O_5-Doped β-Li_3PS_4 with Excellent Stability against Li for All-Solid-State Lithium Batteries. *J. Power Sources* **2018**, *389* (January), 140–147.

(32) Ulissi, U.; Agostini, M.; Ito, S.; Aihara, Y.; Hassoun, J. All Solid-State Battery Using Layered Oxide Cathode, Lithium-Carbon Composite Anode and Thio-LISICON Electrolyte. *Solid State Ionics* **2016**, *296*, 13–17.

(33) Choi, S.-J.; Choi, S.-H.; Bui, A. D.; Lee, Y.-J.; Lee, S.-M.; Shin, H.-C.; Ha, Y.-C. LiI-Doped Sulfide Solid Electrolyte: Enabling a High-Capacity Slurry-Cast Electrode by Low-Temperature Post-Sintering for Practical All-Solid-State Lithium Batteries. *ACS Appl. Mater. Interfaces* **2018**, *10* (37), 31404–31412.

(34) Nam, Y. J.; Oh, D. Y.; Jung, S. H.; Jung, Y. S. Toward Practical All-Solid-State Lithium-Ion Batteries with High Energy Density and Safety: Comparative Study for Electrodes Fabricated by Dry- and Slurry-Mixing Processes. *J. Power Sources* **2018**, *375* (November 2017), 93–101.

(35) Yamamoto, M.; Terauchi, Y.; Sakuda, A.; Takahashi, M. Binder-Free Sheet-Type All-Solid-State Batteries with Enhanced Rate Capabilities and High Energy Densities. *Sci. Rep.* **2018**, *8* (1), 1212.

(36) Sakuda, A.; Kuratani, K.; Yamamoto, M.; Takahashi, M.; Takeuchi, T.; Kobayashi, H. All-Solid-State Battery Electrode Sheets Prepared by a Slurry Coating Process. *J. Electrochem. Soc.* **2017**, *164* (12), A2474–A2478.

(37) Kato, Y.; Hori, S.; Saito, T.; Suzuki, K.; Hirayama, M.; Mitsui, A.; Yonemura, M.; Iba, H.; Kanno, R. High-Power All-Solid-State Batteries Using Sulfide Superionic Conductors. *Nat. Energy* **2016**, *1* (4), 16030.

(38) Kato, Y.; Shiotani, S.; Morita, K.; Suzuki, K.; Hirayama, M.; Kanno, R. All-Solid-State Batteries with Thick Electrode Configurations. *J. Phys. Chem. Lett.* **2018**, *9* (3), 607–613.

(39) Ito, S.; Fujiki, S.; Yamada, T.; Aihara, Y.; Park, Y.; Kim, T. Y.; Baek, S.-W.; Lee, J.-M.; Doo, S.; Machida, N. A Rocking Chair Type All-Solid-State Lithium Ion Battery Adopting Li_2O-ZrO_2 Coated $LiNi_{0.8}Co_{0.15}Al_{0.05}O_2$ and a Sulfide Based Electrolyte. *J. Power Sources* **2014**, *248*, 943–950.

(40) Kim, D. H.; Oh, D. Y.; Park, K. H.; Choi, Y. E.; Nam, Y. J.; Lee, H. A.; Lee, S.-M.; Jung, Y. S. Infiltration of Solution-Processable Solid Electrolytes into Conventional Li-Ion-

Battery Electrodes for All-Solid-State Li-Ion Batteries. *Nano Lett.* **2017**, *17* (5), 3013–3020.

(41) Kraft, M. A.; Ohno, S.; Zinkevich, T.; Koerver, R.; Culver, S. P.; Fuchs, T.; Senyshyn, A.; Indris, S.; Morgan, B. J.; Zeier, W. G. Inducing High Ionic Conductivity in the Lithium Superionic Argyrodites $Li_{6+x}P_{1-X}Ge_xS_5I$ for All-Solid-State Batteries. *J. Am. Chem. Soc.* **2018**, *140* (47), 16330–16339.

(42) Yamada, T.; Ito, S.; Omoda, R.; Watanabe, T.; Aihara, Y.; Agostini, M.; Ulissi, U.; Hassoun, J.; Scrosati, B. All Solid-State Lithium–Sulfur Battery Using a Glass-Type P_2S_5–Li_2S Electrolyte: Benefits on Anode Kinetics. *J. Electrochem. Soc.* **2015**, *162* (4), A646–A651.

(43) Yao, X.; Liu, D.; Wang, C.; Long, P.; Peng, G.; Hu, Y. S.; Li, H.; Chen, L.; Xu, X. High-Energy All-Solid-State Lithium Batteries with Ultralong Cycle Life. *Nano Lett.* **2016**, *16* (11), 7148–7154.

(44) Zhang, Q.; Peng, G.; Mwizerwa, J. P.; Wan, H.; Cai, L.; Xu, X.; Yao, X. Nickel Sulfide Anchored Carbon Nanotubes for All-Solid-State Lithium Batteries with Enhanced Rate Capability and Cycling Stability. *J. Mater. Chem. A* **2018**, *6* (25), 12098–12105.

(45) Yu, S.; Mertens, A.; Tempel, H.; Schierholz, R.; Kungl, H.; Eichel, R. A. Monolithic All-Phosphate Solid-State Lithium-Ion Battery with Improved Interfacial Compatibility. *ACS Appl. Mater. Interfaces* **2018**, *10* (26), 22264–22277.

(46) Finsterbusch, M.; Danner, T.; Tsai, C. L.; Uhlenbruck, S.; Latz, A.; Guillon, O. High Capacity Garnet-Based All-Solid-State Lithium Batteries: Fabrication and 3D-Microstructure Resolved Modeling. *ACS Appl. Mater. Interfaces* **2018**, *10* (26), 22329–22339.

(47) Chen, R. J.; Zhang, Y. B.; Liu, T.; Xu, B. Q.; Lin, Y. H.; Nan, C. W.; Shen, Y. Addressing the Interface Issues in All-Solid-State Bulk-Type Lithium Ion Battery via an All-Composite Approach. *ACS Appl. Mater. Interfaces* **2017**, *9* (11), 9654–9661.

(48) Park, M. S.; Jung, Y. C.; Kim, D. W. Hybrid Solid Electrolytes Composed of Poly(1,4-Butylene Adipate) and Lithium Aluminum Germanium Phosphate for All-Solid-State $Li/LiNi_{0.6}Co_{0.2}Mn_{0.2}O_2$ Cells. *Solid State Ionics* **2018**, *315* (December 2017), 65–70.

(49) Wakayama, H.; Yonekura, H.; Kawai, Y. Three-Dimensional Bicontinuous Nanocomposite from a Self-Assembled Block Copolymer for a High-Capacity All-Solid-State Lithium Battery Cathode. *Chem. Mater.* **2016**, *28* (12), 4453–4459.

(50) Ates, T.; Keller, M.; Kulisch, J.; Adermann, T.; Passerini, S. Development of an All-Solid-State Lithium Battery by Slurry-Coating Procedures Using a Sulfidic Electrolyte. *Energy Storage Mater.* **2019**, *17*, 204–210.

(51) Hovington, P.; Lagacé, M.; Guerfi, A.; Bouchard, P.; Mauger, A.; Julien, C. M.; Armand, M.; Zaghib, K. New Lithium Metal Polymer Solid State Battery for an Ultrahigh Energy: Nano C-$LiFePO_4$ versus Nano $Li_{1.2}V_3O_8$. *Nano Lett.* **2015**, *15* (4), 2671–2678.

(52) Porcarelli, L.; Aboudzadeh, M. A.; Rubatat, L.; Nair, J. R.; Shaplov, A. S.; Gerbaldi, C.; Mecerreyes, D. Single-Ion Triblock Copolymer Electrolytes Based on Poly(Ethylene Oxide) and Methacrylic Sulfonamide Blocks for Lithium Metal Batteries. *J. Power Sources* **2017**, *364*, 191–199.

(53) Bouchet, R.; Maria, S.; Meziane, R.; Aboulaich, A.; Lienafa, L.; Bonnet, J.-P.; Phan, T. N. T.; Bertin, D.; Gigmes, D.; Devaux, D.; Denoyel, R.; Armand, M. Single-Ion BAB Triblock Copolymers as Highly Efficient Electrolytes for Lithium-Metal Batteries. *Nat. Mater.* **2013**, *12* (5), 452–457.

(54) Randau, S.; Weber, D. A.; Kötz, O.; Koerver, R.; Braun, P.; Weber, A.; Ivers-Tiffée, E.; Adermann, T.; Kulisch, J.; Zeier, W. G.; Richter, F. H.; Janek, J. Benchmarking the Performance of All-Solid-State Lithium Batteries. *Nat. Energy* **2020**, *5* (3), 259–270.

(55) Neudecker, B. J.; Dudney, N. J.; Bates, J. B. "Lithium-Free" Thin-Film Battery with In Situ Plated Li Anode. *J. Electrochem. Soc.* **2000**, *147* (2), 517.

(56) Julien, C.; Mauger, A.; Vijh, A.; Zaghib, K. *Lithium Batteries: Science and Technology*; 2015.

(57) Peters, J. F.; Baumann, M.; Zimmermann, B.; Braun, J.; Weil, M. The Environmental Impact of Li-Ion Batteries and the Role of Key Parameters – A Review. *Renewable and Sustainable Energy Reviews*. Elsevier Ltd January 1, 2017, pp 491–506.

(58) Herold, A. Bull. Soc. Chim. France. **1955**.

(59) Juza, R.; Wehle, V. Lithium-Graphit-Einlagerungsverbindungen. *Naturwissenschaften* **1965**, *52* (20), 560.

(60) Aurbach, D.; Markovsky, B.; Weissman, I.; Levi, E.; Ein-Eli, Y. On the Correlation between Surface Chemistry and Performance of Graphite Negative Electrodes for Li Ion Batteries. *Electrochim. Acta* **1999**, *45* (1), 67–86.

(61) Besenhard, J. O.; Eichinger, G. High Energy Density Lithium Cells. Part I. Electrolytes

and Anodes. *J. Electroanal. Chem.* **1976**, *68* (1), 1–18.

(62) Eichinger, G.; Besenhard, J. O. High Energy Density Lithium Cells. Part II. Cathodes and Complete Cells. *J. Electroanal. Chem.* **1976**, *72* (1), 1–31.

(63) Shukla, A. K.; Prem Kumar, T. Materials for Next-Generation Lithium Batteries. *Curr. Sci.* **2008**, *94* (3), 314–331.

(64) Liang, Y.; Tao, Z.; Chen, J. Organic Electrode Materials for Rechargeable Lithium Batteries. *Adv. Energy Mater.* **2012**, *2* (7), 742–769.

(65) Kasavajjula, U.; Wang, C.; Appleby, A. J. Nano- and Bulk-Silicon-Based Insertion Anodes for Lithium-Ion Secondary Cells. *J. Power Sources* **2007**, *163* (2), 1003–1039.

(66) Brissot, C.; Rosso, M.; Chazalviel, J. N.; Lascaud, S. Dendritic Growth Mechanisms in Lithium/Polymer Cells. *J. Power Sources* **1999**, *81*, 925–929.

(67) Kerman, K.; Luntz, A.; Viswanathan, V.; Chiang, Y.-M.; Chen, Z. Review—Practical Challenges Hindering the Development of Solid State Li Ion Batteries. *J. Electrochem. Soc.* **2017**, *164* (7), A1731–A1744.

(68) Kamaya, N.; Homma, K.; Yamakawa, Y.; Hirayama, M.; Kanno, R.; Yonemura, M.; Kamiyama, T.; Kato, Y.; Hama, S.; Kawamoto, K.; Mitsui, A. A Lithium Superionic Conductor. *Nat. Mater.* **2011**, *10* (9), 682–686.

(69) Murugan, R.; Thangadurai, V.; Weppner, W. Fast Lithium Ion Conduction in Garnet-Type $Li_7La_3Zr_2O_{12}$. *Angew. Chemie - Int. Ed.* **2007**, *46* (41), 7778–7781.

(70) Kganyago, K. R.; Ngoepe, P. E. Structural and Electronic Properties of Lithium Intercalated Graphite LiC_6. *Phys. Rev. B - Condens. Matter Mater. Phys.* **2003**, *68* (20), 1–16.

(71) Randau, S.; Walther, F.; Neumann, A.; Schneider, Y.; Negi, R. S.; Mogwitz, B.; Sann, J.; Becker-Steinberger, K.; Danner, T.; Hein, S.; Latz, A.; Richter, F. H.; Janek, J. On the Additive Microstructure in Composite Cathodes and Alumina-Coated Carbon Microwires for Improved All-Solid-State Batteries. *Chem. Mater.* **2021**, acs.chemmater.0c04454.

(72) Harry, K. J.; Hallinan, D. T.; Parkinson, D. Y.; MacDowell, A. A.; Balsara, N. P. Detection of Subsurface Structures underneath Dendrites Formed on Cycled Lithium Metal Electrodes. *Nat. Mater.* **2014**, *13* (1), 69–73.

(73) Albertus, P.; Babinec, S.; Litzelman, S.; Newman, A. Status and Challenges in Enabling the Lithium Metal Electrode for High-Energy and Low-Cost Rechargeable Batteries. *Nat. Energy* **2018**, *3* (1), 16–21.

(74) Naudin, C.; Bruneel, J. L.; Chami, M.; Desbat, B.; Grondin, J.; Lassègues, J. C.; Servant, L. Characterization of the Lithium Surface by Infrared and Raman Spectroscopies. *J. Power Sources* **2003**, *124* (2), 518–525.

(75) Qian, J.; Adams, B. D.; Zheng, J.; Xu, W.; Henderson, W. A.; Wang, J.; Bowden, M. E.; Xu, S.; Hu, J.; Zhang, J. G. Anode-Free Rechargeable Lithium Metal Batteries. *Adv. Funct. Mater.* **2016**, *26* (39), 7094–7102.

(76) Jote, B. A.; Beyene, T. T.; Sahalie, N. A.; Weret, M. A.; Olbassa, B. W.; Wondimkun, Z. T.; Berhe, G. B.; Huang, C. J.; Su, W. N.; Hwang, B. J. Effect of Diethyl Carbonate Solvent with Fluorinated Solvents as Electrolyte System for Anode Free Battery. *J. Power Sources* **2020**, *461* (March), 228102.

(77) Zhang, S. S.; Fan, X.; Wang, C. A Tin-Plated Copper Substrate for Efficient Cycling of Lithium Metal in an Anode-Free Rechargeable Lithium Battery. *Electrochim. Acta* **2017**, *258*, 1201–1207.

(78) Assegie, A. A.; Cheng, J. H.; Kuo, L. M.; Su, W. N.; Hwang, B. J. Polyethylene Oxide Film Coating Enhances Lithium Cycling Efficiency of an Anode-Free Lithium-Metal Battery. *Nanoscale* **2018**, *10* (13), 6125–6138.

(79) Wondimkun, Z. T.; Beyene, T. T.; Weret, M. A.; Sahalie, N. A.; Huang, C. J.; Thirumalraj, B.; Jote, B. A.; Wang, D.; Su, W. N.; Wang, C. H.; Brunklaus, G.; Winter, M.; Hwang, B. J. Binder-Free Ultra-Thin Graphene Oxide as an Artificial Solid Electrolyte Interphase for Anode-Free Rechargeable Lithium Metal Batteries. *J. Power Sources* **2020**, *450* (December 2019), 227589.

(80) Zheng, F.; Kotobuki, M.; Song, S.; Lai, M. O.; Lu, L. Review on Solid Electrolytes for All-Solid-State Lithium-Ion Batteries. *J. Power Sources* **2018**, *389*, 198–213.

(81) Yue, L.; Ma, J.; Zhang, J.; Zhao, J.; Dong, S.; Liu, Z.; Cui, G.; Chen, L. All Solid-State Polymer Electrolytes for High-Performance Lithium Ion Batteries. *Energy Storage Materials*. Elsevier B.V. October 1, 2016, pp 139–164.

(82) Takada, K. Progress in Solid Electrolytes toward Realizing Solid-State Lithium Batteries. *J. Power Sources* **2018**, *394*, 74–85.

(83) Homma, K.; Yonemura, M.; Kobayashi, T.; Nagao, M.; Hirayama, M.; Kanno, R. Crystal Structure and Phase Transitions of the Lithium Ionic Conductor Li_3PS_4. *Solid State Ionics* **2011**, *182* (1), 53–58.

(84) Liu, Z.; Fu, W.; Payzant, E. A.; Yu, X.; Wu, Z.; Dudney, N. J.; Kiggans, J.; Hong, K.; Rondinone, A. J.; Liang, C. Anomalous High Ionic Conductivity of Nanoporous β-Li_3PS_4. *J. Am. Chem. Soc.* **2013**, *135* (3), 975–978.

(85) Deiseroth, H.-J.; Kong, S.-T.; Eckert, H.; Vannahme, J.; Reiner, C.; Zaiß, T.; Schlosser, M. Li_6PS_5X: A Class of Crystalline Li-Rich Solids With an Unusually High Li^+ Mobility. *Angew. Chemie* **2008**, *120* (4), 767–770.

(86) Wang, H.; Hood, Z. D.; Xia, Y.; Liang, C. Fabrication of Ultrathin Solid Electrolyte Membranes of β-Li_3PS_4 Nanoflakes by Evaporation-Induced Self-Assembly for All-Solid-State Batteries. *J. Mater. Chem. A* **2016**, *4* (21), 8091–8096.

(87) Wang, H.; Hood, Z. D.; Xia, Y.; Liang, C. Fabrication of Ultrathin Solid Electrolyte Membranes of β-Li_3PS_4 Nanoflakes by Evaporation-Induced Self-Assembly for All-Solid-State Batteries. *J. Mater. Chem. A* **2016**, *4* (21), 8091–8096.

(88) Hood, Z. D.; Wang, H.; Pandian, A. S.; Peng, R.; Gilroy, K. D.; Chi, M.; Liang, C.; Xia, Y. Fabrication of Sub-Micrometer-Thick Solid Electrolyte Membranes of β-Li_3PS_4 via Tiled Assembly of Nanoscale, Plate-Like Building Blocks. *Adv. Energy Mater.* **2018**, *8* (21), 1800014.

(89) Schnell, J.; Günther, T.; Knoche, T.; Vieider, C.; Köhler, L.; Just, A.; Keller, M.; Passerini, S.; Reinhart, G. All-Solid-State Lithium-Ion and Lithium Metal Batteries – Paving the Way to Large-Scale Production. *J. Power Sources* **2018**, *382*, 160–175.

(90) Lenze, G.; Röder, F.; Bockholt, H.; Haselrieder, W.; Kwade, A.; Krewer, U. Simulation-Supported Analysis of Calendering Impacts on the Performance of Lithium-Ion-Batteries. *J. Electrochem. Soc.* **2017**, *164* (6), A1223–A1233.

(91) Hu, M.; Pang, X.; Zhou, Z. Review Recent Progress in High-Voltage Lithium Ion Batteries. *J. Power Sources* **2013**, *237*, 229–242.

(92) Daniel, C.; Mohanty, D.; Li, J.; Wood, D. L. Cathode Materials Review. *AIP Conf. Proc.* **2014**, *1597*, 26–43.

(93) Chebiam, R. V.; Prado, F.; Manthiram, A. Structural Instability of Delithiated $Li_{1-x}N_{1-y}Co_yO_2$ Cathodes. *J. Electrochem. Soc.* **2001**, *148* (1), A49.

(94) Wild, M.; O'Neill, L.; Zhang, T.; Purkayastha, R.; Minton, G.; Marinescu, M.; Offer, G. J. Lithium Sulfur Batteries, a Mechanistic Review. *Energy Environ. Sci.* **2015**, *8* (12), 3477–3494.

(95) Nitta, N.; Wu, F.; Lee, J. T.; Yushin, G. Li-Ion Battery Materials: Present and Future. *Mater. Today* **2015**, *18* (5), 252–264.

(96) Buchmann, I. Types of Lithium-ion Batteries – Battery University Types of Lithium-ion Batteries.

(97) Mizushima, K.; Jones, P. C.; Wiseman, P. J.; Goodenough, J. B. Li_xCoO_2 (0<x<-1): A New Cathode Material for Batteries of High Energy Density. *Mater. Res. Bull.* **1980**, *15* (6), 783–789.

(98) Nishi, Y. Lithium Ion Secondary Batteries; Past 10 Years and the Future. *J. Power Sources* **2001**, *100* (1–2), 101–106.

(99) Ohzuku, T.; Makimura, Y. Layered Lithium Insertion Material of $LiNi_{1/2}Mn_{1/2}O_2$: A Possible Alternative to $LiCoO_2$ for Advanced Lithium-Ion Batteries. *Chem. Lett.* **2001**, *30* (8), 744–745.

(100) Van Der Ven, A.; Ceder, G. Ordering in $Li_x(Ni_{0.5}Mn_{0.5})O_2$ and Its Relation to Charge Capacity and Electrochemical Behavior in Rechargeable Lithium Batteries. *Electrochem. commun.* **2004**, *6* (10), 1045–1050.

(101) Bréger, J.; Dupré, N.; Chupas, P. J.; Lee, P. L.; Proffen, T.; Parise, J. B.; Grey, C. P. Short- and Long-Range Order in the Positive Electrode Material, $Li(NiMn)_{0.5}O_2$: A Joint X-Ray and Neutron Diffraction, Pair Distribution Function Analysis and NMR Study. *J. Am. Chem. Soc.* **2005**, *127* (20), 7529–7537.

(102) Ohzuku, T.; Makimura, Y. Layered Lithium Insertion Material of $LiCo_{1/3}Ni_{1/3}Mn_{1/3}O_2$ for Lithium-Ion Batteries. *Chem. Lett.* **2001**, *30* (7), 642–643.

(103) Shaju, K. M.; Bruce, P. G. Macroporous $Li(Ni_{1/3}Co_{1/3}Mn_{1/3})O_2$: A High-Power and High-Energy Cathode for Rechargeable Lithium Batteries. *Adv. Mater.* **2006**, *18* (17), 2330–2334.

(104) Venkatraman, S.; Manthiram, A. Comparison of the Phase Relationships of Chemically Delithiated Layered $Li_{1-X}Co_{1-Y}O_2$ (M=A1 and Mg) Oxides. *Solid State Ionics* **2005**, *176* (3–4), 291–298.

(105) Padhi, A. K.; Nanjundaswamy, K. S.; Goodenough, J. B. Phospho-olivines as Positive-

Electrode Materials for Rechargeable Lithium Batteries. *J. Electrochem. Soc.* **1997**, *144* (4), 1188–1194.

(106) Yamada, A.; Chung, S. C.; Hinokuma, K. Optimized $LiFePO_4$ for Lithium Battery Cathodes. *J. Electrochem. Soc.* **2001**, *148* (3), A224-229.

(107) Whittingham, M. S. Lithium Batteries and Cathode Materials. *Chem. Rev.* **2004**, *104* (10), 4271–4301.

(108) Wang, G. X.; Bewlay, S.; Needham, S. A.; Liu, H. K.; Liu, R. S.; Drozd, V. A.; Lee, J.-F.; Chen, J. M. Synthesis and Characterization of $LiFePO_4$ and $LiTi_{0.01}Fe_{0.99}PO_4$ Cathode Materials. *J. Electrochem. Soc.* **2006**, *153* (1), A25.

(109) Xia, Y.; Yoshio, M.; Noguchi, H. Improved Electrochemical Performance of $LiFePO_4$ by Increasing Its Specific Surface Area. *Electrochim. Acta* **2006**, *52* (1), 240–245.

(110) Ellis, B.; Kan, W. H.; Makahnouk, W. R. M.; Nazar, L. F. Synthesis of Nanocrystals and Morphology Control of Hydrothermally Prepared $LiFePO_4$. *J. Mater. Chem.* **2007**, *17* (30), 3248–3254.

(111) Goodenough, J. B.; Kim, Y. Challenges for Rechargeable Li Batteries. *Chemistry of Materials*. American Chemical Society February 9, 2010, pp 587–603.

(112) Ge, Y.; Yan, X.; Liu, J.; Zhang, X.; Wang, J.; He, X.; Wang, R.; Xie, H. An Optimized Ni Doped $LiFePO_4$/C Nanocomposite with Excellent Rate Performance. *Electrochim. Acta* **2010**, *55* (20), 5886–5890.

(113) Thackeray, M. M.; David, W. I. F.; Bruce, P. G.; Goodenough, J. B. Lithium Insertion into Manganese Spinels. *Mater. Res. Bull.* **1983**, *18* (4), 461–472.

(114) Aurbach, D.; Levi, M. D.; Gamulski, K.; Markovsky, B.; Salitra, G.; Levi, E.; Heider, U.; Heider, L.; Oesten, R. Capacity Fading of LixMn2O4 Spinel Electrodes Studied by XRD and Electroanalytical Techniques. *J. Power Sources* **1999**, *81–82*, 472–479.

(115) Shin, Y.; Manthiram, A. Factors Influencing the Capacity Fade of Spinel Lithium Manganese Oxides. *J. Electrochem. Soc.* **2004**, *151* (2), A204.

(116) Gummow, R. J.; de Kock, A.; Thackeray, M. M. Improved Capacity Retention in Rechargeable 4 V Lithium/Lithium-Manganese Oxide (Spinel) Cells. *Solid State Ionics* **1994**, *69* (1), 59–67.

(117) Ohzuku, T.; Takeda, S.; Iwanaga, M. Solid-State Redox Potentials for $Li[Me_{1/2}Mn_{3/2}]O_4$

(Me: 3d-Transition Metal) Having Spinel-Framework Structures: A Series of 5 Volt Materials for Advanced Lithium-Ion Batteries. *J. Power Sources* **1999**, *81–82*, 90–94.

(118) Neumann, A.; Randau, S.; Becker-Steinberger, K.; Danner, T.; Hein, S.; Ning, Z.; Marrow, J.; Richter, F. H.; Janek, J.; Latz, A. Analysis of Interfacial Effects in All-Solid-State Batteries with Thiophosphate Solid Electrolytes. *ACS Appl. Mater. Interfaces* **2020**, *12* (8), 9277–9291.

(119) Zhang, W.; Weber, D. A.; Weigand, H.; Arlt, T.; Manke, I.; Schröder, D.; Koerver, R.; Leichtweiss, T.; Hartmann, P.; Zeier, W. G.; Janek, J. Interfacial Processes and Influence of Composite Cathode Microstructure Controlling the Performance of All-Solid-State Lithium Batteries. *ACS Appl. Mater. Interfaces* **2017**, *9* (21), 17835–17845.

(120) Strauss, F.; Bartsch, T.; De Biasi, L.; Kim, A. Y.; Janek, J.; Hartmann, P.; Brezesinski, T. Impact of Cathode Material Particle Size on the Capacity of Bulk-Type All-Solid-State Batteries. *ACS Energy Lett.* **2018**, *3* (4), 992–996.

(121) Koerver, R.; Walther, F.; Aygün, I.; Sann, J.; Dietrich, C.; Zeier, W. G.; Janek, J. Redox-Active Cathode Interphases in Solid-State Batteries. *J. Mater. Chem. A* **2017**, *5* (43), 22750–22760.

(122) Walther, F.; Koerver, R.; Fuchs, T.; Ohno, S.; Sann, J.; Rohnke, M.; Zeier, W. G.; Janek, J. Visualization of the Interfacial Decomposition of Composite Cathodes in Argyrodite-Based All-Solid-State Batteries Using Time-of-Flight Secondary-Ion Mass Spectrometry. *Chem. Mater.* **2019**, *31* (10), 3745–3755.

(123) Culver, S. P.; Koerver, R.; Zeier, W. G.; Janek, J. On the Functionality of Coatings for Cathode Active Materials in Thiophosphate-Based All-Solid-State Batteries. *Adv. Energy Mater.* **2019**, *9* (24), 1–14.

(124) Ruess, R.; Schweidler, S.; Hemmelmann, H.; Conforto, G.; Bielefeld, A.; Weber, D. A.; Sann, J.; Elm, M. T.; Janek, J. Influence of NCM Particle Cracking on Kinetics of Lithium-Ion Batteries with Liquid or Solid Electrolyte. *J. Electrochem. Soc.* **2020**, *167* (10), 100532.

(125) Yang, J.; Huang, B.; Yin, J.; Yao, X.; Peng, G.; Zhou, J.; Xu, X. Structure Integrity Endowed by a Ti-Containing Surface Layer towards Ultrastable $LiNi_{0.8}Co_{0.15}Al_{0.05}O_2$ for All-Solid-State Lithium Batteries. *J. Electrochem. Soc.* **2016**, *163* (8), A1530–A1534.

(126) Study on sintered temperature and performance of nickel base cathode $LiNi_{0.90}Co_{0.05}Mn_{0.05}O_2$ coated with Co and Mn components

http://en.cnki.com.cn/Article_en/CJFDTotal-DYJS200705008.htm (accessed Dec 31, 2020).

(127) Stöffler, H.; Zinkevich, T.; Yavuz, M.; Senyshyn, A.; Kulisch, J.; Hartmann, P.; Adermann, T.; Randau, S.; Richter, F. H.; Janek, J.; Indris, S.; Ehrenberg, H. Li+-Ion Dynamics in β-Li_3PS_4 Observed by NMR: Local Hopping and Long-Range Transport. *J. Phys. Chem. C* **2018**, *122* (28), 15954–15965.

(128) Stöffler, H.; Zinkevich, T.; Yavuz, M.; Hansen, A. L.; Knapp, M.; Bednarčík, J.; Randau, S.; Richter, F. H.; Janek, J.; Ehrenberg, H.; Indris, S. Amorphous versus Crystalline Li_3PS_4: Local Structural Changes during Synthesis and Li Ion Mobility. *J. Phys. Chem. C* **2019**, *123* (16), 10280–10290.

(129) Santhosha, A. L.; Nazer, N.; Koerver, R.; Randau, S.; Richter, F. H.; Weber, D. A.; Kulisch, J.; Adermann, T.; Janek, J.; Adelhelm, P. Macroscopic Displacement Reaction of Copper Sulfide in Lithium Solid-State Batteries. *Adv. Energy Mater.* **2020**, *10* (41), 2002394.

6 Appendix

6.1 Supporting Information Publication I

nature energy

SUPPLEMENTARY INFORMATION

https://doi.org/10.1038/s41560-020-0565-1

In the format provided by the authors and unedited.

Benchmarking the performance of all-solid-state lithium batteries

Simon Randau[1], Dominik A. Weber[1,4], Olaf Kötz[1], Raimund Koerver[1,5], Philipp Braun[2], André Weber[2], Ellen Ivers-Tiffée[2], Torben Adermann[3], Jörn Kulisch[3], Wolfgang G. Zeier[1], Felix H. Richter[1]✉ and Jürgen Janek[1]✉

[1]Institute of Physical Chemistry & Center for Materials Research,Justus-Liebig-University Giessen, Giessen, Germany. [2]Karlsruhe Institute of Technology, Institute for Applied Materials, Karlsruhe, Germany. [3]BASF SE, Ludwigshafen am Rhein, Germany. [4]Present address: Volkswagen AG, Group Research, Wolfsburg, Germany. [5]Present address: BMW Group, München, Germany. ✉e-mail: felix.h.richter@phys.chemie.uni-giessen.de; Juergen.Janek@phys.Chemie.uni-giessen.de

Supplementary information to

Benchmarking the performance of all-solid-state lithium batteries

Simon Randau[a], Dominik A. Weber[a,b], Olaf Kötz[a], Raimund Koerver[a,c], Philipp Braun[d], André Weber[d], Ellen Ivers-Tiffée[d], Torben Adermann[e], Jörn Kulisch[e], Wolfgang G. Zeier[a], Felix H. Richter[a],*, Jürgen Janek[a],*

[a]Institute of Physical Chemistry & Center for Materials Research (ZFM), Justus-Liebig-University Giessen, Heinrich-Buff-Ring 17, 35392 Giessen, Germany
[b]current affiliation: Volkswagen AG, Group Research, 38436 Wolfsburg, Germany
[c]current affiliation: BMW Group, 80788 München, Germany
[d]Karlsruhe Institute of Technology (KIT), Institute for Applied Materials (IAM-WET), Adenauerring 20b, 76131 Karlsruhe, Germany
[e]BASF SE, 67056 Ludwigshafen am Rhein, Germany

Supplementary Table 1. Selected cell performance measures and equations.

$$\textbf{specific energy } E_{\mathrm{m}} = \frac{UIt}{m_{\mathrm{cell}}} = \frac{Uqm_{\mathrm{CAM}}}{m_{\mathrm{cell}}} = U\frac{qm_{\mathrm{CAM}}}{A}\frac{A}{m_{\mathrm{cell}}} = UQ_{\mathrm{A}}\rho_{\mathrm{A}}^{-1} = E_{\mathrm{A}}\rho_{\mathrm{A}}^{-1}$$

$$\textbf{energy density } E_{\mathrm{V}} = \frac{UIt}{V_{\mathrm{cell}}} = UQ_{\mathrm{A}}l^{-1}$$

$$\textbf{specific power } P_{\mathrm{m}} = \frac{UI}{m_{\mathrm{cell}}} = U\frac{I}{A}\frac{A}{m_{\mathrm{cell}}} = Uj\rho_{\mathrm{A}}^{-1}$$

$$\textbf{power density } P_{\mathrm{V}} = \frac{UI}{V_{\mathrm{cell}}} = Ujl^{-1}$$

$$\textbf{C rate} = \frac{j}{Q_{\mathrm{A}}}$$

$$\textbf{Coulomb efficiency } \phi_{\mathrm{Q(ch-dis)}} = \frac{q_{\mathrm{dis}}}{q_{\mathrm{ch}}}$$

$$\textbf{voltage efficiency } \phi_{\mathrm{U(ch-dis)}} = \frac{U_{\mathrm{dis}}}{U_{\mathrm{ch}}}$$

$$\textbf{energy efficiency } \phi_{\mathrm{E(ch-dis)}} = \frac{E_{\mathrm{dis}}}{E_{\mathrm{ch}}} = \phi_{\mathrm{U}}\phi_{\mathrm{Q}}$$

$$\textbf{overpotential } \eta = jRA$$

$$U_{dis} = U - \eta \quad \textit{and} \quad U_{\mathrm{ch}} = U + \eta$$

$$\textbf{internal resistance } R \approx R_{\mathrm{An}} + R_{\mathrm{SE}} + R_{\mathrm{Ca}} + R_{\mathrm{diff}} + R_{\mathrm{el}}$$

U	Average voltage (of discharge or charge)
I	Current
t	Time of discharge/charge
m	Mass (of CAM or cell)
q	Specific capacity of CAM
A	Area of a battery pellet
j	Current density
Q_A	Area capacity
E_A	Area energy
ρ_A	Surface density
V	Volume of cell
l	Thickness of cell
R	Resistance (anode interface, solid electrolyte, cathode interface, diffusion in CAM, electronic)

Supplementary Table 2: Description of approximations and assumptions made to calculate data for comparison where indicated.

Reference*	Comment	Assumptions
Whiteley *et al.*[19]	Layer thicknesses unavailable; Calculation of Ca and SE thicknesses by CAM and SE densities and weight fraction of CAM	CAM density (4.78 g·cm^{-3}); SE density (1.94 g·cm^{-3}); 100 µm thickness of lithium
Zhang *et al.*[20]	Layer thicknesses unavailable; Calculation of Ca and SE thicknesses by CAM and SE densities and weight fraction of CAM; Current density calculated from C-rate	CAM density (5.05 g·cm^{-3}); SE density (2.1 g·cm^{-3}); C-rate based on 137 mAh·g^{-1} theoretical capacity of $LiCoO_2$
Woo *et al.*[21]	-	-
Xie *et al.*[22]	Thickness of lithium unavailable; weight fraction of CAM contradictory: the paper states 70 wt.% weight fraction of CAM was used in the cathode mixture, however, it also states 7 mg·cm^{-2} cathode composite and 5.5 mg·cm^{-2} CAM were applied, which corresponds to 78.5 wt.% CAM.	100 µm thickness of lithium; 5.5 mg·cm^{-2} assumed to be the CAM loading
Ulissi *et al.*[23]	Layer thicknesses unavailable; Calculation of Ca, SE and An thicknesses by Ca, SE and An densities and weight fraction of CAM	CAM density (4.75 g·cm^{-3}); SE density (1.9 g·cm^{-3}); An density (0.53 g·cm^{-3})
Choi *et al.*[24]	SE thickness unavailable, estimated by SE mass and SE density	Density (SE) = Density (β-Li_3PS_4 in cell type 1)
Nam *et al.*[25]	Current density calculated from C-rate	C-rate based on 200 mAh·g^{-1} theoretical capacity of NCM
Yamamoto *et al.*[25]	-	-
Sakuda *et al.*[16]	*m*(SE) unavailable; Estimated from SE thickness	Density (SE) = Density (β-Li_3PS_4 in cell type 1)
Kato *et al.*[3]	*m*(SE) and *m*(An) unavailable; Estimated from SE and An thickness and total cell mass; Total cell mass was calculated from the values given in the reference for the specific energy based on mass of $LiCoO_2$, the specific energy based on mass of cell and the mass of $LiCoO_2$ in the cell and its content in the cathode composite	Density (SE) = Density (An) = Density (β-Li_3PS_4 in cell type 1)
Kato *et al.*[26]	m(SE) unavailable; Estimated from SE thickness	Density (SE) = Density (β-Li_3PS_4 in cell type 1)
Ito *et al.*[27]	-	-
Kim *et al.*[28]	Layer thicknesses of Ca and anode composite unavailable; Calculation of Ca and anode composite thicknesses by CAM and A density and weight fraction of CAM	CAM density (5.05 g·cm^{-3}); An density (1.9 g·cm^{-3})
Kraft *et al.*[29]	Average charge/discharge voltage for 0.5C and 1C not shown	M. Kraft personal communication: U_{ch}(0.5C) = 2.63 V, U_{dis}(0.5C) = 1.98 V, U_{ch}(1C) = 2.50 V, U_{dis}(1C) = 1.84 V
Yamada *et al.*[30]	Layer thicknesses of Ca and SE unavailable; Calculation of thicknesses by Ca and SE densities and weight fraction of CAM	CAM density (2.0 g·cm^{-3}); SE density (1.85 g·cm^{-3})
Yao *et al.*[6]	Layer thickness of Ca and mass of SE unavailable; Calculation of Ca thickness by Ca density and weight fraction of CAM; Calculation of mass of SE from SE thickness and density	CAM density (5.45 g·cm^{-3}); Density (SE) = Density (β-Li_3PS_4 in cell type 1)
Zhang *et al.*[31]	Calculation of Ca thickness by Ca density and weight fraction of CAM; An thickness unavailable	CAM density (5.66 g·cm^{-3}); Ca density (4.82 g·cm^{-3}); Density (SE) = Density (β-Li_3PS_4 in cell type 1); 100 µm thickness of lithium
Yu *et al.*[4]	Current density calculated from C-rate	C-rate based on 200 mAh·g^{-1} theoretical capacity of NCM
Finsterbusch *et al.*[5]	Mass of SE and anode unavailable; Calculation by SE and An densities and thicknesses	SE density (5.2 g·cm^{-3}), An density (0.53 g·cm^{-3})
Chen *et al.*[32]	Cell area and mass of Ca, SE and anode unavailable; Calculation by SE and An densities and layer thicknesses	Area assumed to be 3.14 cm^2 as LIR 2032 coin cell was used; Ca density (2.7 g·cm^{-3}), SE density (2.2 g·cm^{-3}), An density (0.53 g·cm^{-3})
Park *et al.*[33]	Cell area and mass of SE and anode unavailable; Calculation of thicknesses by Ca and SE densities and weight fraction of CAM; Current density calculated from C-rate	Area assumed to be 3.14 cm^2 as CR 2032 coin cell was used; CAM density (4.78 g·cm^{-3}), SE density (3.0 g·cm^{-3}), An density (0.53 g·cm^{-3}); C-rate based on 200 mAh·g^{-1} theoretical capacity of NCM
Wakayama *et al.*[34]	Anode thickness and mass of Ca, SE and anode unavailable; Calculation of mass of Ca, SE and anode by density, thickness and weight fraction of CAM	100 µm thickness of lithium; Ca density (5 g·cm^{-3}), SE density (1.2 g·cm^{-3}), An density (0.53 g·cm^{-3})
Ates *et al.*[35]	Mass of polymer electrolyte unavailable; Calculation by layer thickness and density	Polymer electrolyte density (1.2 g·cm^{-3})
Hovington *et al.*[7]	Mass of Ca, SE and anode unavailable; Calculation of mass Ca, SE and An by densities, layer thicknesses and weight fraction of CAM	CAM density (3.53 g·cm^{-3}), Ca density (2.23 g·cm^{-3}), SE density (1.2 g·cm^{-3}), An density (0.53 g·cm^{-3})
Porcarelli *et al.*[36]	Anode thickness and mass of Ca, SE and anode unavailable; Calculation of mass Ca, SE and anode by densities, layer thicknesses and weight fraction of CAM	100 µm thickness of lithium; CAM density (3.53 g·cm^{-3}), SE density (1.2 g·cm^{-3}), An density (0.53 g·cm^{-3})
Bouchet *et al.*[37]	Anode thickness and mass of Ca, SE and anode unavailable; Calculation of mass Ca, SE and anode by densities, layer thicknesses and weight fraction of CAM	100 µm thickness of lithium; CAM density (3.53 g·cm^{-3}), SE density (1.2 g·cm^{-3}), An density (0.53 g·cm^{-3})

Ca: cathode composite; CAM: cathode active material; SE: solid electrolyte; An: anode (composite)

*References refer to numbers in the main text for consistency.

Supplementary Table 3: Description of values taken from graphics and illustrations.

Reference*	Comment
Whiteley *et al.*[19]	Average voltage for charge and discharge extracted from graph
Zhang *et al.*[20]	Average voltage for charge and discharge extracted from graph
Woo *et al.*[21]	Average voltage for charge and discharge extracted from graph
Xie *et al.*[22]	Average voltage for charge and discharge extracted from graph
Ulissi *et al.*[23]	Average voltage for charge and discharge extracted from graph
Choi *et al.*[24]	Average voltage for charge and discharge extracted from graph
Nam *et al.*[15]	Average voltage for charge and discharge extracted from graph
Yamamoto *et al.*[25]	Average voltage for charge and discharge extracted from graph
Sakuda *et al.*[16]	Average voltage for charge and discharge extracted from graph; thickness for Ca, SE, A obtained from an SEM image of the cell cross-section
Kato *et al.*[3]	Average voltage for charge and discharge extracted from graph; Data for Ragone plot extracted from a Ragone plot displayed in the paper
Kato *et al.*[26]	Average voltage for charge and discharge extracted from graph; Data for Ragone plot calculated from discharge curves shown in graph
Ito *et al.*[27]	Average voltage for charge and discharge extracted from graph
Kim *et al.*[28]	Average voltage for charge and discharge extracted from graph
Kraft *et al.*[29]	Average voltage for charge and discharge and 0.25C extracted from graph
Yamada *et al.*[30]	Average voltage for charge and discharge extracted from graph
Yao *et al.*[6]	Average voltage for charge and discharge extracted from graph; Data for Ragone plot extracted a Ragone plot displayed in the paper
Zhang *et al.*[31]	Average voltage for charge and discharge extracted from graph;
Yu *et al.*[4]	Average voltage for charge and discharge extracted from graph
Finsterbusch *et al.*[5]	Average voltage for charge and discharge extracted from graph
Chen *et al.*[32]	Average voltage for charge and discharge extracted from graph
Park *et al.*[33]	Average voltage for charge and discharge extracted from graph
Wakayama *et al.*[34]	Average voltage for charge and discharge extracted from graph
Ates *et al.*[35]	Average voltage for charge and discharge extracted from graph
Hovington *et al.*[7]	Average voltage for charge and discharge extracted from graph
Porcarelli *et al.*[36]	Average voltage for charge and discharge extracted from graph
Bouchet *et al.*[37]	Average voltage for charge and discharge extracted from graph

*References refer to numbers in the main text for consistency.

Supplementary Table 4: Composition and thickness of the cells. Unless specified otherwise, values were either obtained or calculated from values specified in the respective reference.

Reference*	A / cm²	l_{Ca} / µm	l_{SE} / µm	l_{An} / µm	$\rho_{A(CAM)}$ / mg·cm⁻²	w_{CAM} / wt.%	w_{SE} / wt.%	w_{Carbon} / wt.%	w_{Binder} / wt.%	$\rho_{A(Ca)}$ / mg·cm⁻²	$\rho_{A(SE)}$ / mg·cm⁻²	$\rho_{A(An)}$ / mg·cm⁻²	$\rho_{A(cell)}$ / mg·cm⁻²
Cell type 1	0.785	40	425	120	8.9	70.0	30.0	0.0	0.0	12.7	76.4	6.4	95.6
Cell type 2	0.785	80	210	120	17.8	70.0	30.0	0.0	0.0	25.5	38.2	6.4	70.1
Whiteley *et al.*[19]	1.327	19[#]	777[#]	100[†]	5.2	68.6	29.4	2.0	0.0	7.5	151	5.3[†]	163.6[†]
Zhang *et al.*[20]	0.785	21[#]	607[#]	80	5.5	70.0	30.0	0.0	0.0	8.9	127.4	4.3	140.6
Woo *et al.*[21]	1.327	20	900	550	2.8	37.7	56.6	5.7	0.0	10	200	39	249
Xie *et al.*[22]	0.785	17	1000	100[†]	5.5	78.5[#]	21.5[#]	0.0	0.0	7.5	150.7	29.4	187.6[†]
Ulissi *et al.*[23]	1.327	9[#]	446[#]	57[#]	1.4	60.0	35.0	5.0	0.0	2.3	90.4	3.0	95.7
Choi *et al.*[24]	1.327	50	503[#]	100	7.0	70	25	2.5	2.5	10	90.4	5.3	105.8
Nam *et al.*[15]	1.327	155	45	138	29.3	79.2	19.5	1.3	0.0	37	7.5	27	71.5
Nam *et al.*[15]	48.0	88	30	65	14.3	68.1	29.2	1.3	1.4	21	4.9	13	38.9
Yamamoto *et al.*[25]	0.785	74	59	134	15.9	76.2	19.0	1.9	2.9	20.9	13.9	21.5	56.3
Sakuda *et al.*[16]	4.84	63[§]	63[§]	89[§]	9.5	66.0	28.3	2.8	2.8	14.4	11.3[#]	10.2	35.9[#]
Kato *et al.*[3]	1.0	28	240	29	4.9	60.0	34.0	6.0	0.0	8.1	49.8[#]	6.0[#]	63.9
Kato *et al.*[26]	1.0	600	100	524	115.4	61.0	36.0	3.0	0.0	189	18[#]	112	319[#]
Ito *et al.*[27]	1.327	250	200	100	6.8	60.0	35.0	5.0	0.0	11.3	52.7	11.3	75.3
Kim *et al.*[28]	1.3	25.3[#]	600	28[#]	10.0	86.3	11.0	1.8	0.9	11.6	134.6	6[#]	152.2
Kraft *et al.*[29]	1.13	160	450	340	34.1	70.0	30.0	0.0	0.0	49	133	81	262
Yamada *et al.*[30]	1.327	13[#]	407[#]	100	0.7	30.0	60.0	10.0	0.0	2	75	5	83
Yao *et al.*[6]	0.785	26[#]	1000	100	3.5	40.0	50.0	10.0	0.0	9	180[#]	5	194[#]
Zhang *et al.*[31]	0.785	26[#]	1061[#]	100[†]	5.7	45.0	50.0	5.0	0.0	12.7	191.1	5[#]	208.8
Yu *et al.*[4]	0.503	150	420	120	9.9	45.0	25.0	15.0	15.0	22	101	18	141
Finsterbusch *et al.*[5]	1.13	25	500	200	7.1	50.0	50.0	0.0	0.0	14	263[#]	11[#]	287
Chen *et al.*[32]	3.14	300	70	100	60.8	75.0	15.0	10.0	0.0	81	15[#]	5[#]	102
Park *et al.*[33]	3.14[#]	31[#]	75	200	6.0	60.0	30.0	10.0	0.0	10	23[#]	11[#]	43
Wakayama *et al.*[34]	1.54	25	200	100[†]	11.3	90.0	10.0	0.0	0.0	13[#]	24[#]	5[#]	42
Ates *et al.*[35]	0.76	26	121	120	7.6	67.2	28.8	2.0	2.0	11	16	6	34
Hovington *et al.*[7]	3.8	92	29	46	14.4[#]	70.0	25.0	5.0	0.0	21[#]	3[#]	2[#]	26
Porcarelli *et al.*[36]	0.78	30[#]	20[#]	100[†]	5.0	65.0	20.0	15.0	0.0	8[#]	2[#]	5[#]	15
Bouchet *et al.*[37]	3.14	70	70	100[†]	4.7[#]	60.0	32.0	8.0	0.0	8[#]	8[#]	5[#]	22

Abbreviations: CAM: cathode active material; Ca: cathode composite; SE: solid electrolyte; An: anode (composite); nd: no data available.

*References refer to numbers in the main text for consistency.

[#] Not all necessary data was available in the respective reference to calculate these values; these values include approximations.

[§] Not all necessary data was available as numbers in the respective reference; these values include data extracted from figures in the respective reference.

[†] Data unavailable, values estimated.

Supplementary Table 5: Data for the calculation of the energy efficiency.

Reference*	j / mA·cm^{-2}	q_{dis} of 2nd charge / mAh·g^{-1}	q_{dis} of 2nd discharge / mAh·g^{-1}	U of 2nd charge / V	U of 2nd discharge / V	$\Phi_{E(ch-dis)}$ / %
Cell type 1	0.178	130	128	3.98	3.69	92
Cell type 2	0.356	111	109	3.96	3.66	91
Whiteley *et al.*[19]	0.082	125§,†	125†	3.79§,†	3.59§,†	95§,†
Zhang *et al.*[20]	0.075#	134§,†	131†	3.76§,†	3.76§,†	98§,†
Woo *et al.*[21]	0.045	124§,‡	120‡	4.07§,‡	3.85§,‡	91§,‡
Xie *et al.*[22]	0.066	131§	130	3.97§	3.92§	97§
Ulissi *et al.*[23]	0.004	105§	100	3.42§	3.28§	91§
Choi *et al.*[24]	0.12	170	168	3.88	3.70	93
Nam *et al.*[15]	0.147#	122§	120	3.67§	3.57§	96§
Nam *et al.*[15]	0.072#	112§	110	3.71§	3.67§	97§
Yamamoto *et al.*[25]	0.064	189§,†	122†	3.68§,†	3.51*,†	59§,†
Sakuda *et al.*[16]	0.064	115§	111	3.81§	3.62§	92§
Kato *et al.*[3]	0.067	117§	110	3.74§	3.71§	97§
Kato *et al.*[26]	0.50	123§	123	3.84§	3.75§	98§
Ito *et al.*[27]	0.05	nd	121†	nd	3.59§,†	nd
Kim *et al.*[28]	0.14	133§	119	3.92§	3.69§	84§
Kraft *et al.*[29]	1.71	120†,§	89†,§	2.25†,§	2.11†,§	89†,§
Yamada *et al.*[30]	0.025	1585§	1640	2.40§	1.94§	84§
Yao *et al.*[6]	0.13	642	646	1.94§,†	1.5§,†	78§,†
Yao *et al.*[6]	1.27	500§,†	501†	2.15§,†	1.25§,†	58§,†
Zhang *et al.*[31]	0.57	537†	550†	2.05†	1.45†	71†
Yu *et al.*[4]	0.043	nd	102	nd	1.13§	nd
Finsterbusch *et al.*[5]	0.10	122§	116	4.03	3.91	92
Chen *et al.*[32]	0.10	171§,†	155†	3.49§,†	3.11§,†	81§,†
Park *et al.*[33]	0.24#	168§,†	165†	3.81§,†	3.68§,†	95§,†
Wakayama *et al.*[34]	0.08#	139§,†	136†	3.98†	3.85†	95†
Ates *et al.*[35]	0.06	145§	139	3.81§	3.73§	85
Hovington *et al.*[7]	0.81#	168§	165	3.60§	3.27§	87§
Porcarelli *et al.*[36]	0.09#	nd	152†	nd	3.4§,†	nd
Bouchet *et al.*[37]	0.05#	nd	162†	nd	3.38§,†	nd

*References refer to numbers in the main text for consistency.
#Not all necessary data was available in the respective reference to calculate these values; these values include approximations.
§ Not all necessary data was available as numbers in the respective reference; these values include data extracted from figures in the respective reference.
†Data unavailable, values estimated.

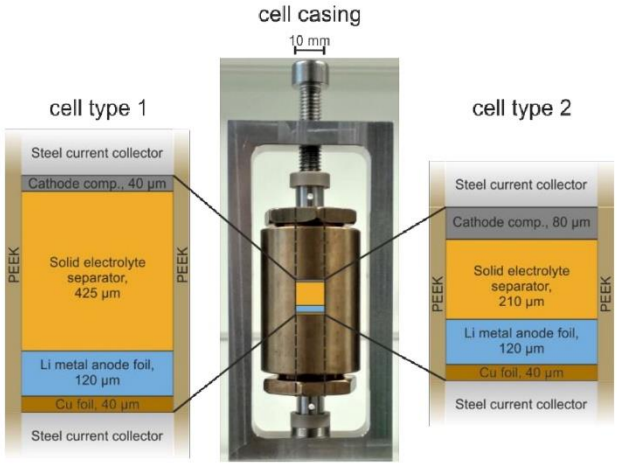

Supplementary Figure 1: Image of the ASSB cell setup and casing along with schematics of the layer thicknesses of cell type 1 and cell type 2.

We prepared two types of Li|LPS|NCM pellet-type cells with 10 mm diameter and cycled them galvanostatically to 4.3 V during charge and 2.6 V during discharge vs Li^+/Li at various current densities. In brief, the cell casing and layer thicknesses of cell type 1 and cell type 2 are depicted in Supplementary Figure 1. Cell type 1 contains an LPS separator thickness of 425 µm and a cathode composite thickness of 40 µm. Excluding the cell casing and current collectors, the first discharge specific energy of cell type 1 is 44 $Wh \cdot kg^{-1}$ and the energy density is 72 $Wh \cdot L^{-1}$. Specific energy and energy density are increased by decreasing the thickness of the solid electrolyte separator and increasing the amount of cathode mixture. Therefore, we prepared cell type 2, which has half of the LPS separator thickness, and double the thickness of cathode composite. The first discharge specific energy of cell type 2 is 100 $Wh \cdot kg^{-1}$ and the energy density is 172 $Wh \cdot L^{-1}$. Even though the employed LPS has only moderate ionic conductivity, the cells presented here show sufficiently low resistance to demonstrate high specific power up to 100 $W \cdot kg^{-1}$. Cell specifications and cycling results are summarized in Supplementary Table 6.

Supplementary Table 6: Overview of cell specifications and cycling results.

	Cell type 1	Cell type 2
CAM mass, m_{CAM}	10 mg	20 mg
LPS separator mass, m_{SE}	60 mg	30 mg
Lithium mass, m_{An}	5 mg	5 mg
Thickness of cathode layer, l_{Ca}	40 µm	80 µm
Thickness of solid electrolyte, l_{SE}	425 µm	210 µm
Thickness of anode, l_{An}	120 µm	120 µm
Thickness of copper foil, l_{Cu}	40 µm	40 µm
Current density for 0.1C (theory), j	0.178 mA·cm^{-2}	0.356 mA·cm^{-2}
Surface density of CAM, $\rho_{A(CAM)}$	8.9 mg·cm^{-2}	17.8 mg·cm^{-2}
Initial charge capacity, q_{ch}	176 mAh·g^{-1}	153 mAh·g^{-1}
Initial discharge capacity, q_{dis}	128 mAh·g^{-1}	107 mAh·g^{-1}
Specific energy based on first discharge, E_m	44 Wh·kg^{-1}	100 Wh·kg^{-1}
Energy density based on first discharge, E_V	72 Wh·L^{-1}	172 Wh·L^{-1}

The cycling data of cell type 1 and cell type 2 are shown in Supplementary Figure 2. The first charge capacity of cell type 1 is 176 mAh·g_{CAM}^{-1} (1.5 mAh·cm^{-2}) and the first discharge capacity is 128 mAh·g_{CAM}^{-1} (1.1 mAh·cm^{-2}), resulting in a Coulomb efficiency of 73 %. The average Coulomb efficiency up to 200 cycles is 99.8 %, excluding the first cycle. The first charge capacity of cell type 2 is 153 mAh·g_{CAM}^{-1} (2.7 mAh·cm^{-2}) and the first discharge capacity is 107 mAh·g_{CAM}^{-1} (1.9 mAh·cm^{-2}), resulting in a Coulomb efficiency of 71 %. The average Coulomb efficiency up to 200 cycles is 99.2 %, excluding the first cycle.

The rate tests were performed by applying current densities of 0.178 mA·cm^{-2}, 0.445 mA·cm^{-2}, 0.89 mA·cm^{-2} and 1.78 mA·cm^{-2}, which correspond to 0.1C, 0.25C, 0.5C, and 1.0C, respectively, based on a theoretical capacity of 200 mAh·g^{-1}. For cell type 1, the specific capacities reduce from 128 mAh·g^{-1} to 98 mAh·g^{-1}, 54 mAh·g^{-1} and 0 mAh·g^{-1} at 0.178 mA·cm^{-2}, 0.445 mA·cm^{-2}, 0.89 mA·cm^{-2} and 1.78 mA·cm^{-2}, respectively. Due to the lowering of accessible capacity, these current densities correspond to a true C-rate of 0.16C, 0.48C, 1.71C, and n.d., respectively. For cell type 2, the specific capacities reduce from 106 mAh·g^{-1} to 78 mAh·g^{-1}, 46 mAh·g^{-1} and 0 mAh·g^{-1} at 0.356 mA·cm^{-2}, 0.89 mA·cm^{-2}, 1.78 mA·cm^{-2}, and 3.56 mA·cm^{-2} respectively. Due to the lowering of accessible capacity, these correspond to a true C-rate of 0.19C, 0.66C, 2.22C, n.d., respectively.

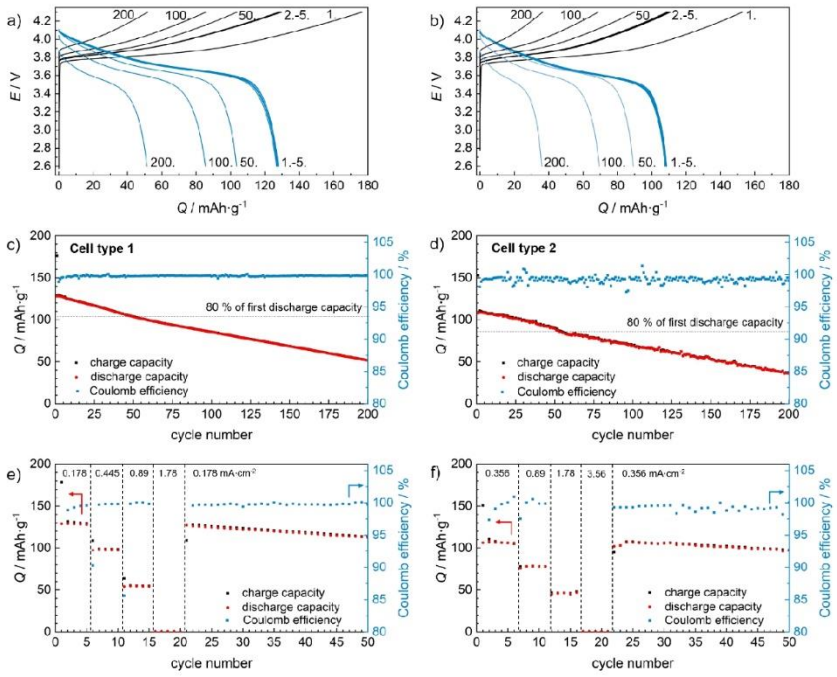

Supplementary Figure 2: Charge (black) and discharge (blue) curves of Li|β-Li_3PS_4|NCM cell type 1 (a) and cell type 2 (b). Coulomb efficiency over 200 cycles of cell type 1 (c) and cell type 2 (d). Rate tests for cell type 1 (e) and cell type 2 (f).

The minimalistic cells showed comparable loss of capacity over 200 cycles. We attribute the irreversible capacity loss that occurs during cycling to interfacial reactions at the cathode with the solid electrolyte. This is confirmed by X-ray photoelectron spectroscopy of the cathode composite (Supplementary Figure 3), which is in line with previous reports.[i,ii] The interfacial reactions on the cathode side upon cycling were investigated by X-ray photoelectron spectroscopy (XPS). The surface of the cathode composite (cell type 1) in contact with the stainless steel current collector after 200 charge and discharge cycles at 0.178 mA·cm^{-2} was compared to a freshly prepared cathode mixture without electrochemical treatment. The signals for the cycled cathode composite broaden toward higher binding energies, indicating the formation of an oxidized sulfur species and degradation of the solid electrolyte. These results are in good agreement with previous investigations of the cathode composite in combination with an indium anode.[i] It is evident that the major fraction of the oxidized species is formed during the first charge step, which mainly explains the low Coulomb efficiency of the first charge-discharge cycle.[iii] In addition, the volume contraction of the NCM particles during charge leads to a contact loss of the CAM, further limiting capacity.[iv]

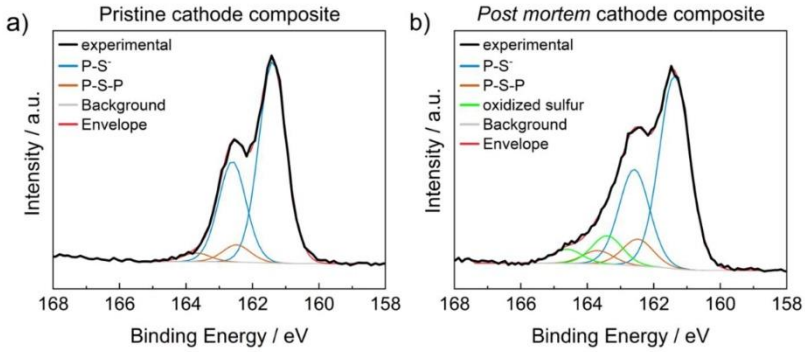

Supplementary Figure 3: XPS S2p spectra of a) a pristine cathode composite and b) a cathode composite after 200 cycles at 0.178 mA·cm^{-2}.

Scanning electron microscopy (SEM) images (Supplementary Figure 4) of a cross-section of the all-solid-state Li|LPS|NCM battery of cell type 1 after 200 cycles at 0.178 mA·cm^{-2} show that the 60 mg LPS solid electrolyte resulted in a 425 µm thick solid electrolyte separator layer. The cathode composite was approximately 40 µm thick. The roughly 10 µm sized NCM particles are embedded in LPS. Supplementary Figure 4 also shows that LPS and lithium are in intimate contact, forming a continuous interface. However, LPS is known to react with lithium metal and forms an interphase consisting of Li_2S and Li_3P.[v,vi] The impact of such an interphase can be analyzed in symmetric lithium cells (Supplementary Figure 5). Whereas cycling at 0.178 mA·cm^{-2} causes the resistance of a symmetric lithium cell to increase with time, ramping of the current density resulted in a short-circuit above 0.713 mA·cm^{-2}. During the first cycles, cell type 1 reached 128 mAh·g^{-1} discharge capacity, which corresponds to a 6.1 µm thick lithium layer, which is transferred per step in this setup (area 0.785 cm^2). After 200 cycles, the observed discharge capacity has reduced to 52 mAh·g^{-1}, which corresponds to 2.4 µm of transferred lithium per step.

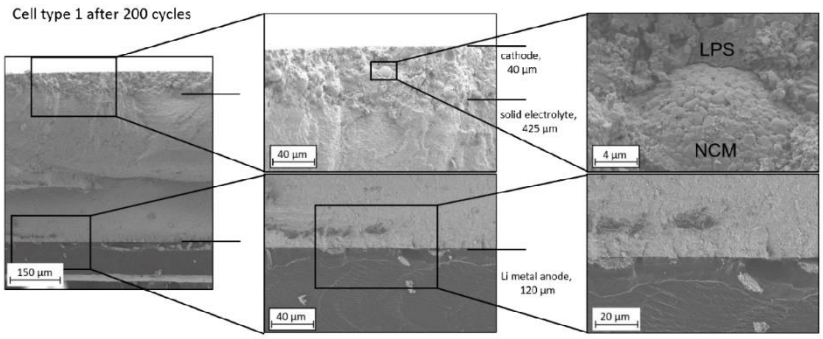

Supplementary Figure 4: Cross-sectional SEM images of Li|β-Li_3PS_4|NCM cell type 1 after 200 cycles. The change in contrast through the solid electrolyte is likely due to changes in sample height caused by an uneven cut through the sample.

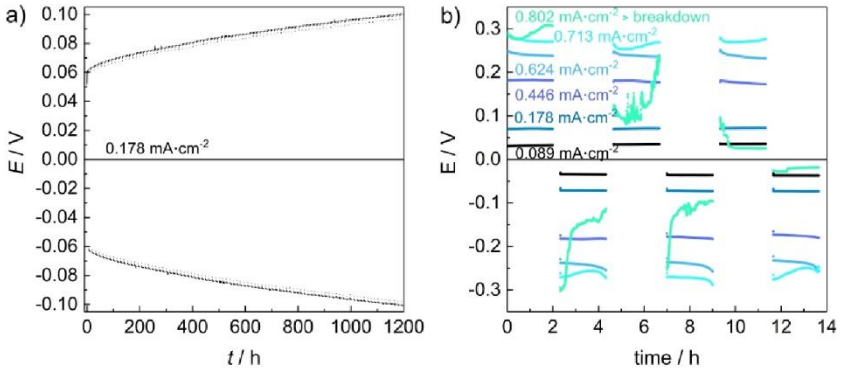

Supplementary Figure 5: a) Galvanostatic cycling of a symmetric lithium cell with β-Li_3PS_4 of 425 µm thickness at a current density of 0.178 mA·cm^{-2}. Every step length was 6.5 h, corresponding to 6 µm lithium stripping/plating. These conditions correspond to those of cycling of cell type 1 with a discharge capacity of 130 mAh·g^{-1}. b) Determination of the critical current density of a symmetric lithium cell with β-Li_3PS_4 between current densities of 0.089 mA·cm^{-2} and 0.802 mA·cm^{-2}.

A distribution of relaxation times (DRT) analysis of electrochemical impedance spectroscopy (EIS) measurements was carried out for the cells to monitor the processes governing each impedance contribution. In the state-of-charge (SOC) dependent DRT analysis of cell type 1, four processes were detected (Supplementary Figure 6). We attribute the SOC independent high frequency process to the LPS separator. As shown in the Nyquist (Supplementary Figure 7) and Bode (Supplementary Figure 8) plots, the impedance of a pellet of LPS with stainless steel blocking electrodes (σ_{LPS} = 1.2·10^{-4} S·cm^{-1}) agrees well with the high frequency process. The SOC independent process with a peak at 20 kHz is attributed to charge transfer at the lithium-LPS interface. As shown in Supplementary Figure 7, the impedance of a symmetric transference cell with LPS also shows a peak at 20 kHz, which clearly represents the charge-transfer process at the lithium-LPS interface. We then attribute the strongly SOC dependent peak between about 100 Hz and 1 kHz, in the discharged and charged states, respectively, to the charge transfer process at the NCM-LPS interface (Supplementary Figure 7), which is in line with previous reports.[vii,viii] Finally, the fourth contribution is attributed to lithium diffusion in the cathode particles.[ix] Fitting of the impedance data can thus be carried out using the equivalent circuit: (R_0)(R_1/Q)(R_2/Q)(R_3/Q)(Z_{DIFF}), in which (R_0)(R_1/Q) represents the solid electrolyte, (R_2/Q) the lithium-LPS interface, (R_3/Q) the cathode-LPS interface and (Z_{DIFF}) lithium diffusion in the CAM, fitted with a Finite Space Warburg element. Supplementary Table 7 and Supplementary Table 8 respectively list the fitted circuit parameters for cell type 1 and cell type 2.

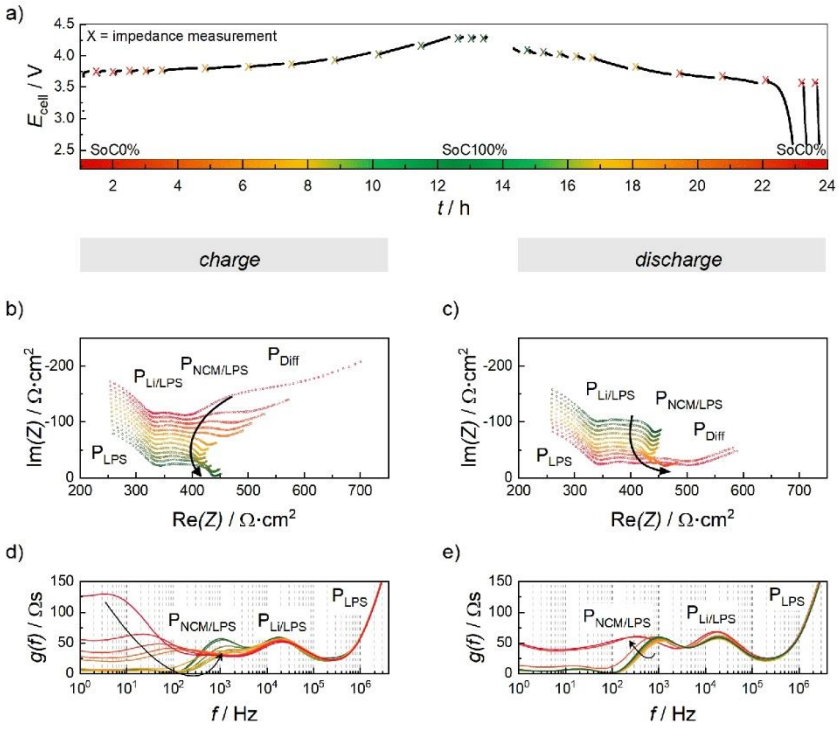

Supplementary Figure 6: First charge and discharge curve for a Li|β-Li_3PS_4|NCM-622+β-Li_3PS_4 battery of cell type 1. The cell was cycled in several steps (charge: 5x10 min, 7x60 min, 3x until cut-off potential; discharge: 5x10 min, 5x60 min, 2x until cut-off potential). After each step and a 10 min rest time, impedance measurements were carried out for b) charge and c) discharge. For clarity, the corresponding Nyquist plots are each stacked by a 10 Ω·cm² shift on the y-axes with respect to the previous one and the last two were omitted. Graphs (d) and (e) present the DRT analysis of the impedance data shown in (b) and (c), allowing one to clearly determine the characteristic frequency of each polarization contribution.

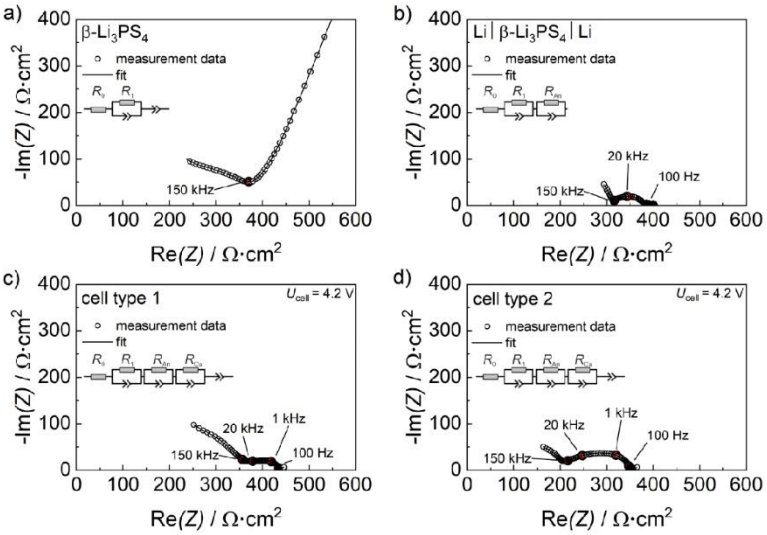

Supplementary Figure 7: Impedance data: a) Nyquist plot and corresponding fit of a pellet of 60 mg β-Li_3PS_4 (stainless steel stamp current collectors); b) Nyquist plot for a symmetrical Li|β-Li_3PS_4|Li cell with 425 µm thickness of LPS; c) Nyquist Plot for cell type 1 ASSB at 4.2 V after first charge; d) Nyquist plot for cell type 2 ASSB at 4.2 V after first charge.

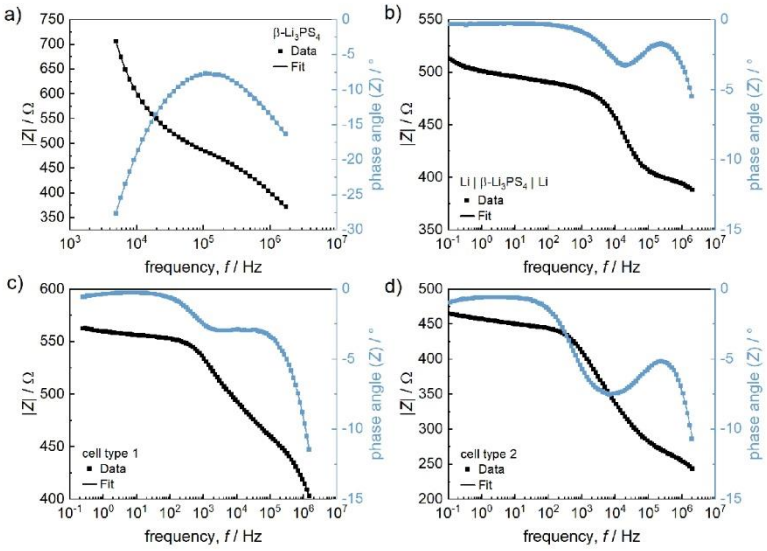

Supplementary Figure 8: Bode plots corresponding to the impedance data shown in Supplementary Figure 7.

Supplementary Table 7: List of circuit parameters for the resistance contributions for Li|β-Li_3PS_4|NCM ASSB of cell type 1. The solid electrolyte resistance (R_{SE}) is the sum of the resistance R_0 and the resistance of the first R_1/CPE element.

Cycle #	R_0* / Ω	R_1 / Ω	α_1	f_1 / $\cdot 10^6$ Hz	Q_1 / $\cdot 10^{-11}$ C	R_{SE} / Ω	R_{An} / Ω	α_{An}	f_{An} / Hz	Q_{An} / $\cdot 10^{-7}$ C	R_{Ca} / Ω	α_{Ca}	f_{Ca} / Hz	Q_{Ca} / $\cdot 10^{-6}$ C	$Z_{Diff,R}$ / Ω	$Z_{Diff,T}$ / $\cdot 10^6$ s	$Z_{Diff,P}$
1	37.0	418.6	0.71	9.40	3.72	455.6	45.1	0.70	29482	1.71	53.3	0.83	1675	2.15	1853.7	1.09	0.36
2	37.7	422.7	0.70	9.42	3.67	460.4	45.5	0.70	26875	1.86	56.7	0.83	1527	2.22	1943.6	1.09	0.36
3	45.4	419.4	0.71	9.09	3.77	464.8	47.3	0.70	24501	1.96	58.4	0.84	1392	2.33	1765.8	1.14	0.35
4	50.1	420.2	0.71	8.68	3.90	470.3	49.6	0.70	24501	1.87	61.8	0.84	1269	2.40	1964.4	1.09	0.36
5	52.1	426	0.70	9.00	3.70	478.1	47.8	0.70	24501	1.94	68.0	0.83	1269	2.22	1986.1	1.08	0.36
6	66.1	416.8	0.71	8.25	3.99	482.9	51.3	0.70	24501	1.81	71.3	0.84	1157	2.30	2259.6	1.08	0.36
7	62.3	427	0.71	8.37	3.89	489.3	49.9	0.70	24501	1.86	77.6	0.83	1157	2.14	2202.1	1.08	0.36
8	24.4	466.8	0.74	8.99	3.60	491.2	54.1	0.70	26876	1.56	82.1	0.84	1054	2.20	2819.3	1.00	0.38
9	54.4	445.8	0.71	8.50	3.75	500.2	52.2	0.70	22336	1.95	85.5	0.84	1054	2.11	1983.8	1.07	0.35
10	49.0	454.2	0.73	7.93	3.99	503.2	56.9	0.70	22336	1.79	88.3	0.85	961	2.21	2291.5	1.02	0.36
11	0.1	509.5	0.71	8.84	3.53	509.6	54.5	0.70	22336	1.87	94.5	0.84	961	2.09	2336.7	1.01	0.36
12	0.0	514.5	0.71	8.83	3.50	514.5	58.4	0.70	20362	1.91	96.2	0.85	876	2.21	2376.3	1.00	0.36
13	0.0	519.7	0.72	8.67	3.53	519.7	57.5	0.70	20362	1.94	102.1	0.85	876	2.10	2267.4	1.05	0.35
14	0.0	525.1	0.72	8.59	3.53	525.1	56.4	0.70	20362	1.98	108.2	0.84	876	1.99	2220.8	1.02	0.35

*From cycle 11 onwards, R_0 becomes zero, as the RelaxIS software combines R_0 and R_1 to receive a more precise fit result. Reasons for this can be small changes in the α value or in the capacitance Q. Unfortunately, there are not enough data points within the measurement range to reliably distinguish R_0 and R_1 in these cycles. However, R_{SE} can be determined well as the sum of R_0 and R_1.

Supplementary Table 8: List of circuit parameters for the resistance contributions for Li|β-Li_3PS_4|NCM ASSB of cell type 2. The solid electrolyte resistance (R_{SE}) is the sum of the first resistance R_0 and the resistance of the first R_1/CPE element.

Cycle #	R_0 / Ω	R_1 / Ω	α_1	f_1 / $\cdot 10^7$ Hz	Q_1 / $\cdot 10^{-11}$ C	R_{SE} / Ω	R_{An} / Ω	α_{An}	f_{An} / Hz	Q_{An} / $\cdot 10^{-7}$ C	R_{Ca} / Ω	α_{Ca}	f_{Ca} / Hz	Q_{Ca} / $\cdot 10^{-6}$ C	$Z_{Diff,R}$ / Ω	$Z_{Diff,T}$ / $\cdot 10^{10}$ s	$Z_{Diff,P}$
1	65.9	190.9	0.80	1.04	5.96	256.8	75.8	0.70	27645	1.08	100.2	0.77	2015	1.02	2909.5	1.10	0.21
2	54.8	207.4	0.79	1.12	5.40	262.2	76.4	0.71	27606	1.07	104.4	0.77	2015	0.98	2956.7	1.08	0.21
3	45.8	221	0.77	1.20	4.97	266.8	75.6	0.72	28090	1.05	108.5	0.77	2015	0.95	3081.5	1.10	0.22
4	48.5	222.1	0.78	1.17	5.02	270.6	74.9	0.72	28993	1.02	112.4	0.76	2015	0.92	3451.7	1.09	0.22
5	50.1	223.5	0.78	1.14	5.11	273.6	84.4	0.70	25466	1.06	105.7	0.77	1837	1.06	3098.6	1.10	0.21
6	48.9	228.3	0.79	1.12	5.12	277.2	82.7	0.70	26398	1.03	109.8	0.76	1837	1.03	3246.2	1.08	0.22
7	51.9	226.3	0.79	1.08	5.28	278.2	83.2	0.70	24990	1.09	99.4	0.78	1837	1.12	3040.7	1.09	0.22
8	54.8	225.2	0.80	1.05	5.41	280.0	82.8	0.70	25430	1.08	100.3	0.78	1837	1.11	2883.1	1.10	0.22
9	53.7	228.1	0.80	1.05	5.38	281.8	82.0	0.70	25612	1.08	101.7	0.77	1837	1.10	3011.2	1.14	0.22
10	51.9	233.8	0.79	1.06	5.26	285.7	88.2	0.70	24747	1.04	108.5	0.77	1675	1.14	3182.5	1.09	0.22
11	37.2	252.5	0.77	1.17	4.70	289.7	94.0	0.70	21865	1.11	103.3	0.78	1527	1.29	2443.4	83.1	0.21
12	39.2	253.3	0.78	1.14	4.77	292.5	93.6	0.70	22151	1.10	106.5	0.78	1527	1.26	2627.8	77.8	0.21
13	29.7	266.3	0.77	1.20	4.47	296.0	100.1	0.70	19840	1.14	100.3	0.80	1392	1.43	2125	1.13	0.19
14	30.5	268.3	0.77	1.18	4.50	298.8	99.5	0.70	20146	1.13	103.4	0.79	1392	1.40	2233.1	91.2	0.20

The resistances R_{SE}, R_{An} and R_{Ca} are shown as function of cycle number (see Supplementary Table 7 and Supplementary Table 8 and Supplementary Figure 9). Comparing cell type 2 with cell type 1, the resistance contribution of the solid electrolyte ($R_{SE} = R_0 + R_1$) is about half as large – as expected – whereas the cathode transfer resistance R_{Ca} appears to be almost twice as large. Also, the anodic transfer resistance R_{An} was observed to be slightly larger in cell type 2, but is still within experimental error. Overall, the analysis of the impedance data recorded in the charged state shows that cell degradation occurs in all parts of the cell (Supplementary Figure 9). For both cells, the solid electrolyte and the Li/LPS resistance contributions increase with the same rate, which may be caused by decomposition reactions in the cathode composite, decreasing the content of conducting phase, thus decreasing ion transport. However, whereas the NCM/LPS interface resistance of cell type 1 almost doubles within 15 cycles, the cathodic interface resistance of cell type 2 hardly shows any change in the interface resistance. These apparently contradicting trends may simply originate from differences in the state of charge between these two cells measured here, from the margin of experimental error, or from yet unidentified factors requiring further investigation.

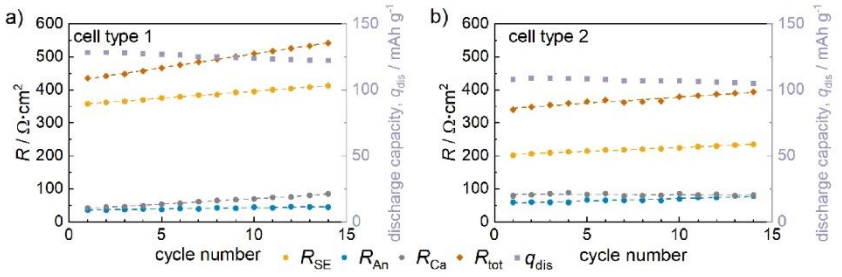

Supplementary Figure 9: Resistance contributions for Li|β-Li_3PS_4|NCM ASSB of a) cell type 1 and b) cell type 2. The impedance data for the charged state were analyzed. Additionally, the internal resistance (R_{tot}) as the sum of the three contributions and the discharge charge capacities for every cycle is shown.

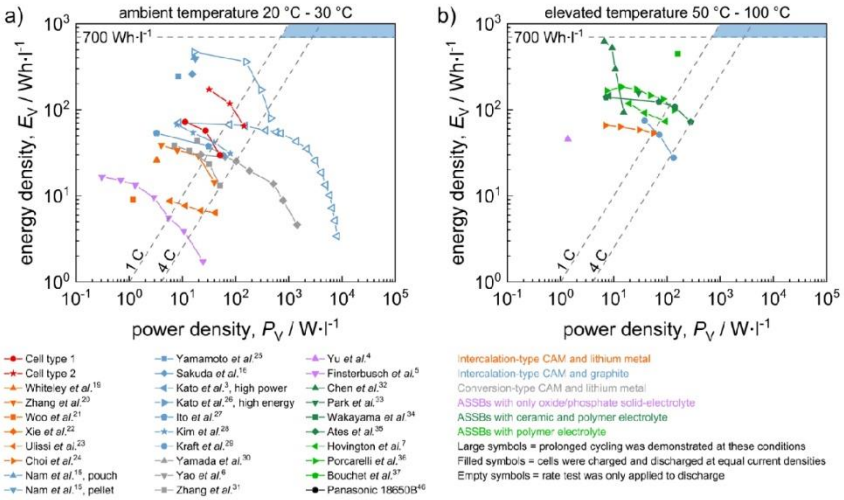

Supplementary Figure 10: Ragone diagrams by cell volume (energy density versus power density) for cells tested at a) ambient and b) elevated temperature. Symbols and references as indicated in Figure 2 of main text. Marked area (blue) represents the target region with more than 700 Wh·l^{-1} energy density and a cycling rate of more than 1C.

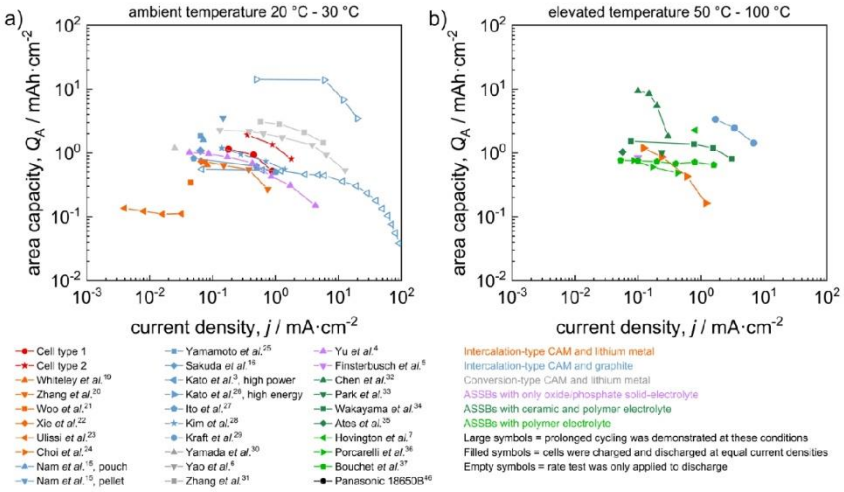

Supplementary Figure 11: Plots of the area capacity against the current density at a) ambient and b) elevated temperature.

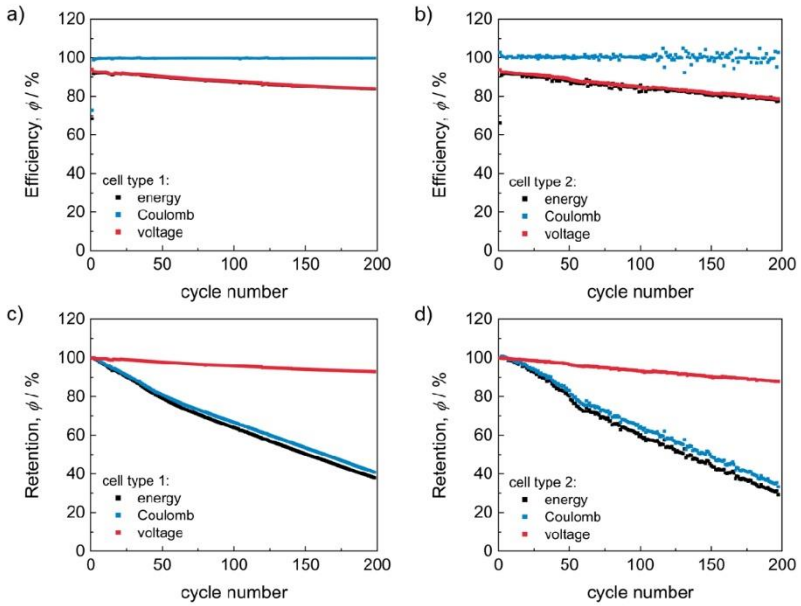

Supplementary Figure 12: Energy, Coulomb and voltage efficiencies for a) cell type 1 at a current density of 0.178 mAh·cm^{-2} and b) cell type 2 at a current density of 0.356 mAh·cm^{-2}. Energy, Coulomb and voltage retention for c) cell type 1 at a current density of 0.178 mAh·cm^{-2} and d) cell type 2 at a current density of 0.356 mAh·cm^{-2}.

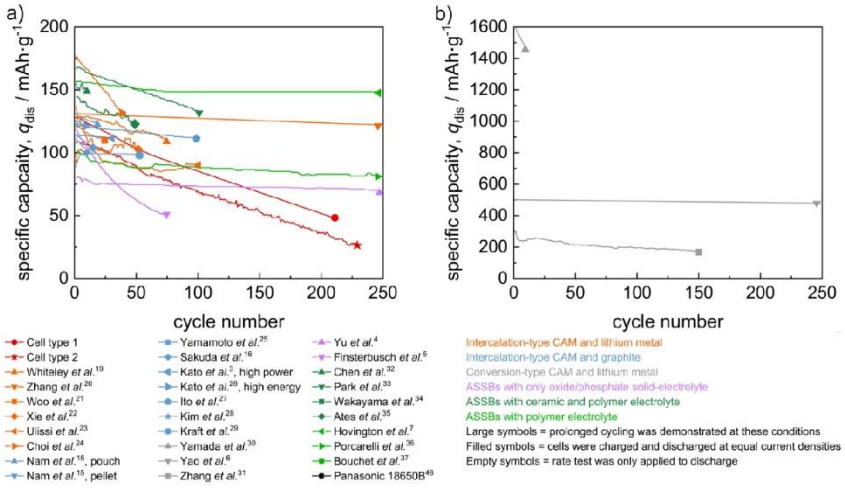

Supplementary Figure 13: Cycling tests of a) intercalation and b) conversion-type cells.

Supplementary Table 9: List of parameters to predict battery performance and impedance requirements (compare SD 2).

Parameter	Comments
Cell system	The choice of anode and cathode material determines the OCV of the cell as well as specific capacity and the density of the CAM. Lithium is used in this comparison as anode material. The OCV determines the allowed overpotential to achieve a certain energy efficiency at a certain current density. The lower the OCV, the lower the internal resistance must be.
C-rate	Fixes the desired rate at which the cells are to be cycled.
Solid electrolyte	Choice of the solid electrolyte determines the density of the solid electrolyte, e.g. Li_6PS_5Cl with a density of about 1.87 $g \cdot cm^{-3}$.
Layer thicknesses, l	Anode and solid electrolyte only contribute to the weight of the cell. The weight fraction of CAM and cathode layer thickness determine the area capacity of the cell.
Area capacity, Q_A	Having fixed the C-rate at 1C, the area capacity determines the required current density. From comparing the literature data, a current density of 5 $mA \cdot cm^{-2}$ without dendrite growth appears to be an ambitious target. Dependent on the specific capacity and the weight fraction of CAM in the cathode composite, the cathode thickness needs to be adapted to obtain the desired area capacity of the cell. In this context, 80 µm to 120 µm cathode layer thickness appears to be the most realistic range for intercalation type CAMs.
Energy efficiency, Φ_E	Finally, the desired energy efficiency determines the allowed overvoltage. Using Ohm's law, the maximum allowed internal resistance of the cell is estimated from the overvoltage and current density.

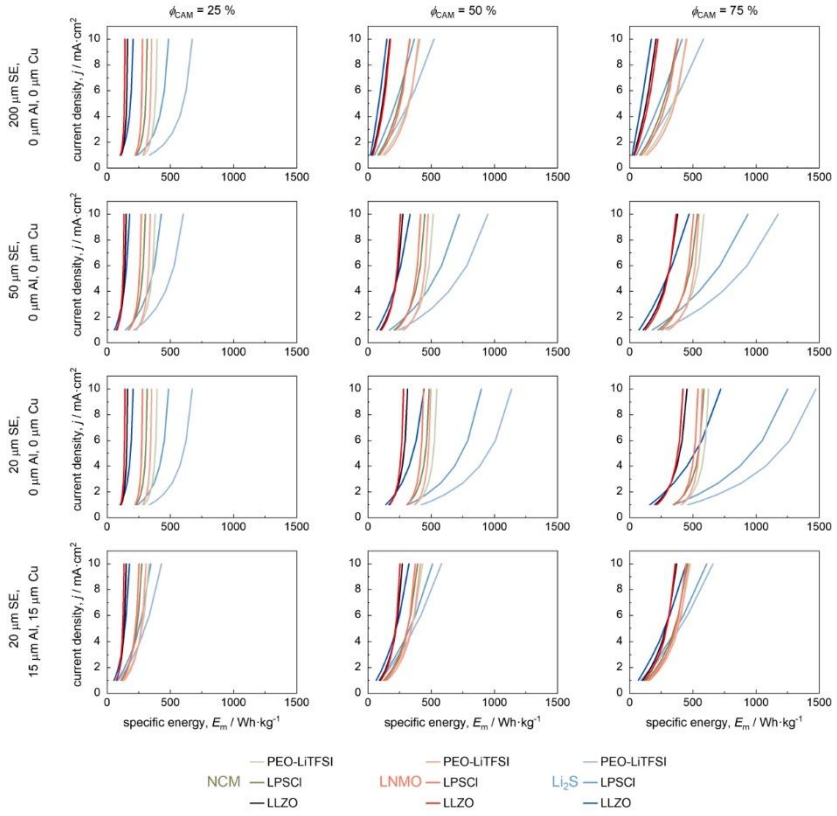

Supplementary Figure 14: Calculation of the current density required for intercalation- and conversion-type cell systems. NCM, LNMO, and Li_2S cathode materials and solid electrolytes PEO-LiTFSI (density of 1.2 g·cm^{-3}), Li_6PS_5Cl (LPSCl, density of 1.87 g·cm^{-3}), and $Li_7La_3Zr_2O_{12}$ (LLZO, density of 5.14 g·cm^{-3}) are compared. Each point indicates the achievable specific energy and the current density requirement at a rate of 1C. 20 µm of lithium foil are used for this calculation. Comparison is carried out at equal current density, i.e. equal cell capacity. Hence, variation of the cathode composite thickness is required to set cell capacity to 1.0, 1.3, 1.8, 2.7, 4.0, 6.0, 10.0 mAh·cm^{-2} (low to high specific energy) as indicated in SD 3. 200 µm, 50 µm or 20 µm solid electrolyte, 25 vol.%, 50 vol.% or 75 vol.% volume fraction φ_{CAM} of CAM in cathode composite and the addition of aluminum and copper foil current collectors (each 15 µm thick) are compared.

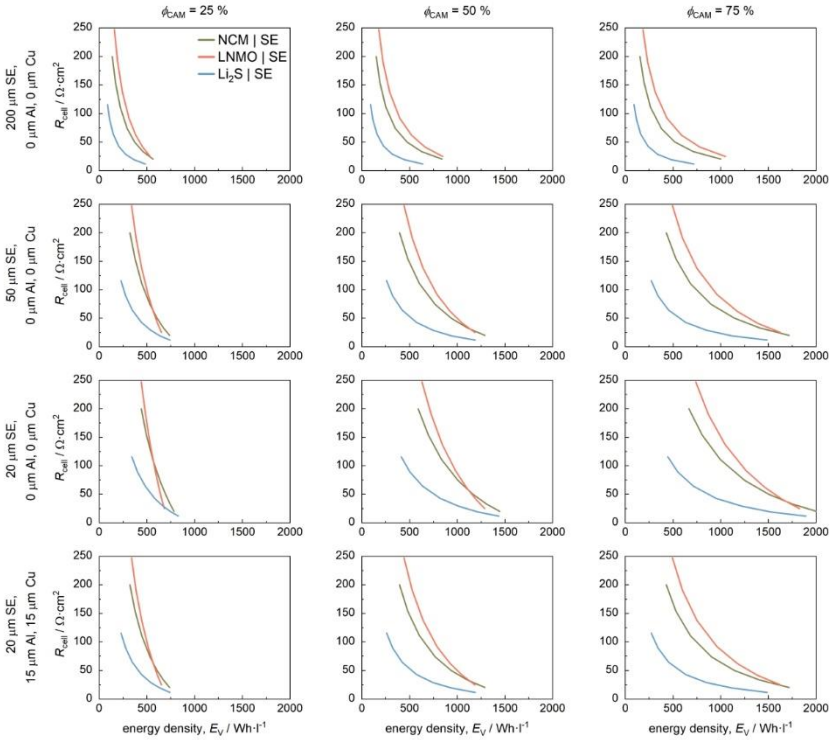

Supplementary Figure 15: Calculation of the maximum internal resistance for intercalation- and conversion-type cell systems dependent on the energy density. NCM, LNMO, and Li_2S cathode materials and solid electrolytes PEO-LiTFSI (density of 1.2 g·cm^{-3}), Li_6PS_5Cl (LPSCl, density of 1.87 g·cm^{-3}), and $Li_7La_3Zr_2O_{12}$ (LLZO, density of 5.14 g·cm^{-3}) are compared. Each point indicates the achievable specific energy and the internal resistance requirement for 90 % energy efficiency at a rate of 1C. 20 µm of lithium foil are used for this calculation. Comparison is carried out at equal current density, i.e. equal area capacity. Hence, variation of the cathode composite thickness is required to set cell capacity to 1.0, 1.3, 1.8, 2.7, 4.0, 6.0, 10.0 mAh·cm^{-2} (low to high specific energy) as indicated in SD 3. 200 µm, 50 µm or 20 µm solid electrolyte, 25 vol.%, 50 vol.% or 75 vol.% volume fraction φ_{CAM} of CAM in cathode composite and the addition of aluminum and copper foil current collectors (each 15 µm thick) are compared.

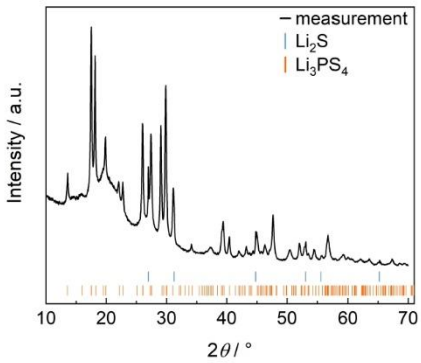

Supplementary Figure 16: XRD pattern of the used β-Li_3PS_4 solid electrolyte. The content of Li_2S side phase is about 7 %.

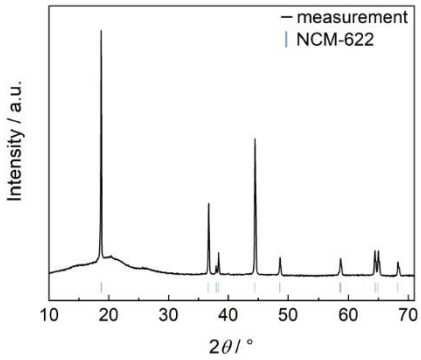

Supplementary Figure 17: XRD pattern of the used NCM-622 active material.

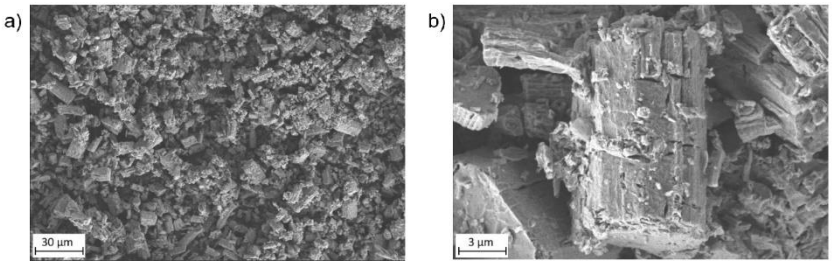

Supplementary Figure 18: SEM images for the β-Li_3PS_4 solid electrolyte at a) small and b) large magnification. The average particle size is about 10 µm.

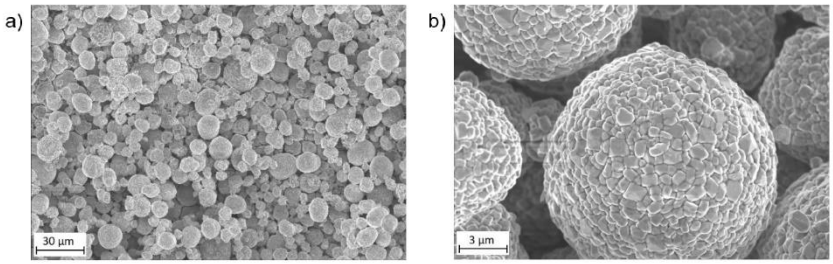

Supplementary Figure 19: SEM images of NCM. The average particle size is about 10 µm.

Additionally, Supplementary Data (SD) are available:

SD 1 Calculation table to evaluate lithium SSB performance from experimental data

SD 2 Prediction of performance characteristics of lithium solid state batteries

SD 3 Prediction of the maximum allowed internal resistance and the required current density for intercalation- and conversion-type cell systems versus Li^+/Li

Supplementary References

[i] R. Koerver, F. Walther, I. Aygün, J. Sann, C. Dietrich, W. G. Zeier, J. Janek, Redox-active cathode interphases in solid-state batteries, *J. Mater. Chem. A*, **2017**, *5*, 22750.

[ii] A. Sakuda, A. Hayashi, M. Tatsumisago, Interfacial Observation between $LiCoO_2$ Electrode and Li_2S-P_2S_5 Solid Electrolytes of All-Solid-State Lithium Secondary Batteries Using Transmission Electron Microscopy, *Chem. Mater.*, **2010**, 22, 949-956.

[iii] R. Koerver, I. Aygün, T. Leichtweiß, C. Dietrich, W. Zhang, J. O. Binder, P. Hartmann, W. G. Zeier, J. Janek, Capacity Fade in Solid-State Batteries: Interphase Formation and Chemomechanical Processes in Nickel-Rich Layered Oxide Cathodes and Lithium Thiophosphate Solid Electrolytes, *Chem. Mater.*, **2017**, 29, 13, 5574–5582.

[iv] A. O. Kondrakov, A. Schmidt, J. Xu, H. Geßwein, R. Mönig, P. Hartmann, H. Sommer, T. Brezesinski, J. Janek, Anisotropic Lattice Strain and Mechanical Degradation of High- and Low-Nickel NCM Cathode Materials for Li-Ion Batteries, *J. Phys. Chem. C*, **2017**, 121, 6, 3286-3294.

[v] S. Wenzel, D. A. Weber, T. Leichtweiss, M. R. Busche, J. Sann, J. Janek, Interphase formation and degradation of charge transfer kinetics between a lithium metal anode and highly crystalline $Li_7P_3S_{11}$ solid electrolyte, *Solid State Ionics*, **2016**, 286, 24-33.

[vi] A. Kato, H. Kowada, M. Deguchi, C. Hotehama, A. Hayashi, M. Tatsumisago, XPS and SEM analysis between Li/Li_3PS_4 interface with Au thin film for all-solid-state lithium batteries, *Solid State Ionics*, **2018**, 322, 1-4.

[vii] Z. Zhang, S. Chen, J. Yang, J. Wang, L. Yao, X. Yao, P. Cui, X. Xu, Interface Re-Engineering of $Li_{10}GeP_2S_{12}$ Electrolyte and Lithium anode for All-Solid-State Lithium Batteries with Ultralong Cycle Life, *ACS Appl. Mater. Interfaces*, **2018**, 10, 3, 2556-2565.

[viii] S. H. Jung K. Oh, Y. J. Nam, D. Y. Oh, P. Brüner, K. Kang, Y. S. Jung, Li_3BO_3–Li_2CO_3: Rationally Designed Buffering Phase for Sulfide All-Solid-State Li-Ion Batteries, *Chem. Mater.*, **2018**, 30 (22), 8190-8200.

[ix] P. Braun, C. Uhlmann, M. Weiss, A. Weber, E. Ivers-Tiffée, Assessment of all-solid-state lithium-ion batteries, *J. Power Sources*, **2018**, 393, 119-127.

6.2 Supporting Information Publication II

Supporting Information

On the Additive Microstructure in Composite Cathodes and Alumina-Coated Carbon Microwires for Improved All-Solid-State Batteries

Simon Randau[a,b], Felix Walther[a,b], Anton Neumann[c,d], Yannik Schneider[a,b], Rajendra S. Negi[a,b], Boris Mogwitz[a,b], Joachim Sann[a,b], Katharina Becker-Steinberger[c,d], Timo Danner[c,d], Simon Hein[c,d], Arnulf Latz[c,d,e], Felix H. Richter[a,b] and Jürgen Janek[a,b,*]

[a] *Institute of Physical Chemistry, Justus Liebig University Giessen, Heinrich-Buff-Ring 17, D-35392 Giessen, Germany.*

[b] *Center for Materials Research (LaMa), Justus Liebig University Giessen, Heinrich-Buff-Ring 16, D-35392 Giessen, Germany.*

[c] *German Aerospace Center (DLR), Institute of Engineering Thermodynamics, Pfaffenwaldring 38-40,70569 Stuttgart, Germany*

[d] *Helmholtz Institute for Electrochemical Energy Storage (HIU), Helmholtzstraße 11, 89081 Ulm, Germany*

[e] *Institute of Electrochemistry, Ulm University, Albert-Einstein-Allee 47, 89081 Ulm, Germany*

S1. Schematic for a cyclic voltammetry cell

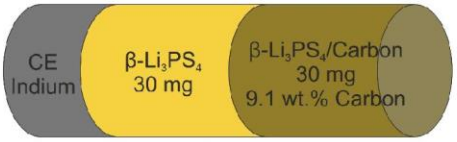

Supplementary Figure 1: Schematics of the cyclic voltammetry test cell setup. For this work the counter electrode (CE) is indium metal (125 µm). The separating electrolyte is β-Li_3PS_4. The composite cathode consists of β-Li_3PS_4 and one of the carbon additives.

S2. SEM Cross-Section of KBC cathode composite

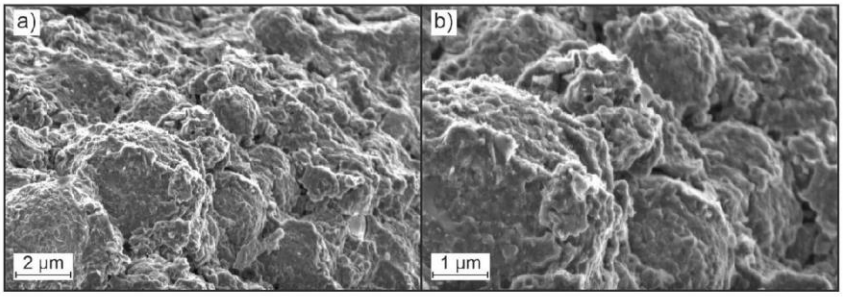

Supplementary Figure 2: SEM cross section for a cathode composite with KBC as conductive additive. Due to the particular character and presence of not conducting carbon domains, carbon is not visible in the images.

S3. Reference electrode material for cyclic voltammetry cells

A counter electrode with a stable potential is needed to perform the cyclic voltammetry experiments. Three types of anode are possible, a pure lithium anode, an *ex situ* formed indium-lithium alloy (*ex situ* In/InLi) and indium metal, which forms a lithium-indium alloy during the experiment (*in situ* In/InLi).

A lithium metal anode combined with a thiophosphate-based SE results in a reduction of the SE and the formation of an isolating SEI layer.[1,2] By using an InLi alloy the negative influence of the direct contact with lithium metal can be avoided. In the region of < 1 at.% to 47 at.% lithium the In/InLi two-phase mixture shows a stable potential of 0.62 V vs. Li^+/Li.[3] This two-phase alloy is typically prepared by applying a thin lithium foil onto a thick indium foil. During further assembly, a contact between lithium

metal and SE may occur, a reduction of the SE is possible. If an indium foil is used during cell assembly, it is necessary that the alloy is formed *in situ*. During the first positive sweep of CV cells the SE is oxidized at the SE/carbon interface. The resulting lithium ions migrate to the anode and form the InLi alloy shortly after the beginning of the experiment, which then forms a stable potential in the presence of unreacted In.[4]

When shifting the cell potentials for CV cells with alloy reference electrodes by 0.62 V vs Li^+/Li, the present peak position overlays with the lithium metal CV cell (Supplementary Figure 3). This is also visible for the first cycle, but the influence of the first oxidative decomposition of the SE leads to an additional variation of the peak positions hindering an easy comparison.

Since the *ex situ* and *in situ* formed In/InLi two-phase alloy electrodes are comparable, for all CV cells in this work an *in situ* formed In/InLi alloy mixture is used as reference electrode. For simplicity the *in situ* formed anode is indicated as In/InLi in all further figures.

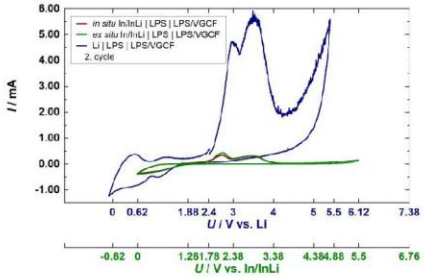

Supplementary Figure 3: By comparing the open circuit potentials of CV cells with different anodes the necessary potential shifts for cells with an ex situ formed In/InLi anode and an in situ formed In/InLi anode can be shown. Both CV cell potentials needed to be shifted by 0.62 V vs Li^+/Li for comparison. The shift for both In/InLi anodes agrees with literature data.[3] To receive an in situ formed In/InLi anode a lithium ion source is needed. We assume an oxidation of the SE during the first positive potential sweep.

S4. Reversibility of the cathode redox couple in the CV cells

Recurring peak sequences can be seen beginning with the second cycle of the cyclic voltammograms (see Figure 3a,b). When VGCF and C65 are used as carbon additives, the course over several cycles shows a reduction of the current maxima for the individual peaks and a shift of the peak positions to higher potentials for oxidation and to lower potentials for reduction. The presence of oxidation and reduction peaks suggests that a redox pair is present. Due to the mentioned changes, the underlying reaction does not seem to be completely reversible. This can be explained by changes in ion mobility as

well as kinetic barriers due to the oxidation products formed, resulting in an incomplete reduction of the formed oxidation products. Leading to an increase of cell resistance and the observed peak position shift.

CV cells with CNT and KBC as carbon additive show a different behavior, which has already been discussed in the manuscript.

S5. Discussion on surface normalization: Steel stamp vs. fiber carbon vs. particular carbon

A first comparison between a cell with carbon additive and a cell without additive is useful (Supplementary Figure 4). For the cell without carbon additive, an active area of 0.79 cm^2 is assumed, since only the steel stamp acts as a current collector. For the cell with carbon additive, the surface of the VGCF is added. Here the assumption is made that all fibers are in contact with the steel stamp. However, this will result in an overestimation of the electronic contact area for this setup, because of the complex 3D structure and presence of isolated domains of the conductive carbons. Therefore, a surface normalization for these experiments is limited. The calculated contact areas, peak currents and calculated ratios for the two setups are shown in Supplementary Table 1. When the ratios for the maximum peak current and surface area are compared for the first cycle, a similar order of magnitude is noticed. Consequently, a surface area dependence of the oxidation can be assumed. In the second cycle the maximum current of the peaks is significantly lower, which is also reflected in the calculated ratio. The reactions can be kinetically and energetically inhibited and reduced contact surfaces by isolated carbon fibers may be the reason. In addition, the changed peak sequence, with three peaks for the second cycle must be taken into account.

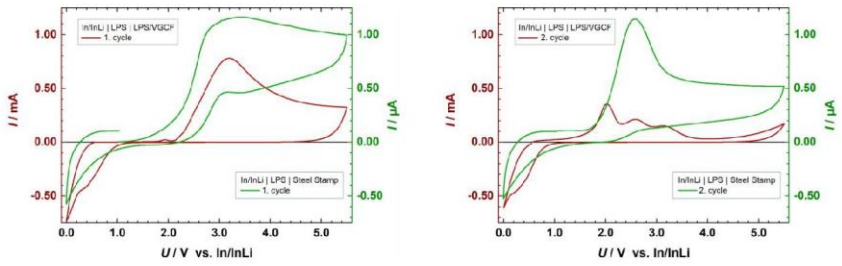

Supplementary Figure 4: Cyclovoltammogram for a) the first and b) second CV cycles of CV cells with VGCF in the composite and without VGCF. The y-achis is scaled differently for a better comparison.

Supplementary Table 1: Overview of the calculated surface areas and the peak currents measured for the CV cells with VGCF composite and planar steel working electrodes. The surface areas in the cell composition with VGCF have been idealized and simplified, resukting in an overestimation. In addition, the ratios for the surface areas and peak currents for both electrode types are calculated.

Electrode setup:	VGCF composite	Steel stamp	Ratio
Area:	656 cm^2	0.79 cm^2	830
I_{max} (1. cycle):	780.4 µA	1.16 µA	673
I_{max} (2. cycle):	212.5 µA	1.15 µA	185

S6. Cyclic voltammetry cell with first reductive sweep

The standard CV test starts with a positive sweep toward high potentials, with an initial oxidative peak. Tests were carried out, performing at first a negative sweep towards low potentials (0 V vs. In/InLi). Supplementary Figure 5 shows the corresponding voltammograms. In the negative potential sweep no peaks are observed. In the following positive potential sweep the first oxidation starts at ca. 2.2 V vs. In/InLi. The formed oxidation products are the starting materials for the redox pair, observed in the following cycles. The further cycles do not differ from CV cell, beginning with a positive potential sweep.

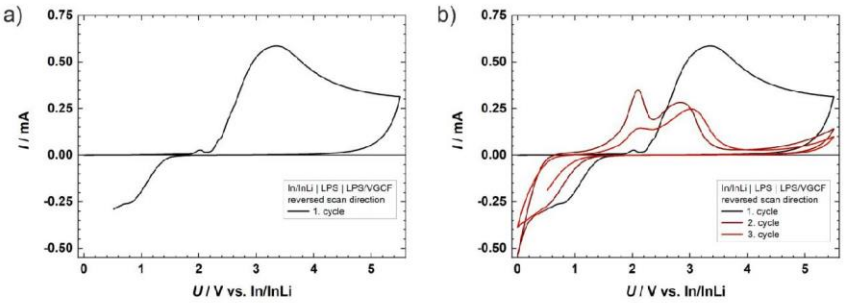

Supplementary Figure 5: Cyclic voltammogram of a cell with VGCF as conductive additive. This cell performed a reversed potential sweep, with a first sweep to negative potentials (reductive region) and afterwards a positive potential sweep. When the reductive sweep performed first, no peaks are visible in this area. The first peak is always the oxidative peak seen in all CV cells first cycles. This peak form the educts of the later observed redox pair.

S7. Cyclic voltammetry cell narrow potential window

Starting from the OCV a first positive sweep was carried out to 3.68 V vs. In/InLi and the following negative sweep stops at 1.98 V vs. In/InLi, corresponding to the upper and lower cut-off potential of an ASSB (Supplementary Figure 6). The expected oxidative peak is present in the first cycle. Compared to cyclic voltammograms with higher reversal potentials, the first oxidation is not finalized. Furthermore, reduction peaks are absent, due to the high cut-off potential of the reductive sweep. For the second and third cycle the oxidation is reoccurring. However, the quantity of reaction decreases, a saturation of decomposition products at the SE/carbon interface can be assumed.

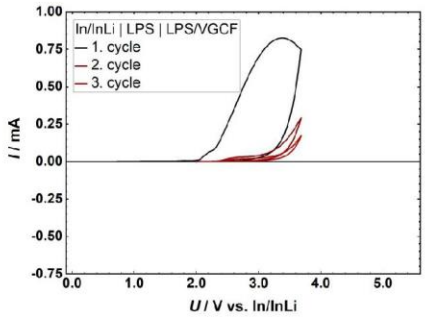

Supplementary Figure 6: CV of a model cell with VGCF carbon additive. For the CV experiment, a potential window of 3.68 V to 1.98 V vs. In/InLi is applied. This correlates to the potential window for an ASSB.

S8. CV of SE with CNT carbon additive

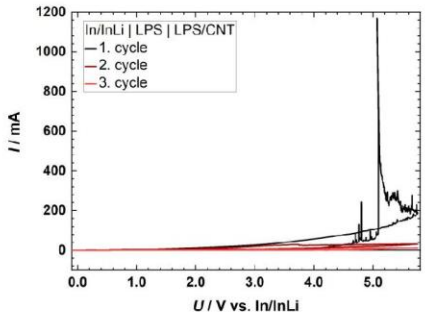

Supplementary Figure 7: CV spectra for a cell with CNT carbon additive. The high current in the first cycle indicates strong decomposition reactions.

S9. First three charge and discharge curves of a full cell with VGCF additive

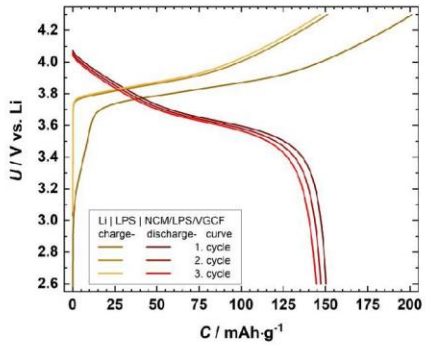

Supplementary Figure 8: The first three charge and discharge curves of a cell with VGCF as the conductive additive in the composite cathode (Li|LPS|NCM-622/LPS/VCGF). For the battery cycling, the potential limits have been set to 4.3 V during charging and 2.6 V during discharging.

S10. Onset for carbon additive induced oxidation in full cells

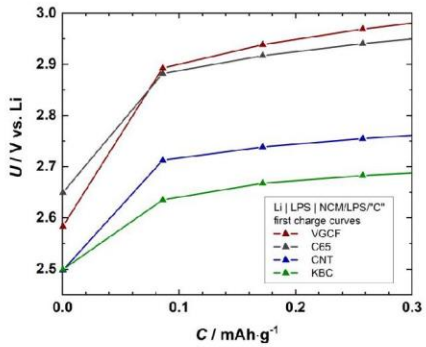

Supplementary Figure 9: Onset of the initial oxidation decomposition reaction in the first charge step induced by different carbon additives. A surface dependency for this onset is recognizable and is in agreement with the Onset discussion for the CV cells, mentioned in the manuscript.

S11. Simulation Framework

The microstructure resolved simulation framework Battery and Electrochemistry Simulation Tool (BEST) is based on a continuum model for lithium-ion batteries derived by Latz *et al.*[5]. The dynamic

evolution of the concentration and the potential in the simulated cell is described by a set of coupled partial differential equations resulting from the conservation equations for mass, charge, momentum, and energy. We continuously improved and modified the simulation framework to describe additional interfacial and material transport effects in solid-state battery cells[6,7]. In our recent work, we investigated the interface modification induced through SE delamination and the current-collector contact loss on the battery performance. An in-depth analysis of the parametrization of the material system NCM-622 and ß-LPS can be found in our recent work[7].

S12. Mixture of electronic and ionic properties in SE phase (BEST)

A prominent advantage of the microstructure resolved simulations is the ability to incorporate inherently the morphological properties of the cathode composite, as for example particle size and electrode tortuosity. The battery simulation studies are performed on virtually generated voxel-based electrodes, which are based on common experimental microstructural parameters like electrode thickness and particle size. Nevertheless, the growing interest in cell design optimization sets additional requirements also for model development. Additives, such as conducting agents, are just nanometers in size and more or less homogeneously dispersed in the cathode microstructure.[8] To maintain numerically efficient virtual electrode resolutions and simultaneously include the fine structural influences of the additive, we extended the BEST framework.

In Supplementary Table 2 the equations for the extended simulation framework implemented in our framework BEST[5] are summarized.

Supplementary Table 2: The constitutive equations of the Li-ion battery model used in this work. Indices are defined as electrolyte= El, active material= So and carbon additive = CB.

Phase	Material balance	Charge balance
Electrolyte	$\frac{\partial \varepsilon_{El} c_{El}}{\partial t} = -\vec{\nabla} \cdot \vec{N}_{El}$ (1a)	$0 = -\vec{\nabla} \cdot \vec{j}_{eff,El}$ (1b)
Carbon additive		$0 = -\vec{\nabla} \cdot \vec{j}_{eff,CB}$ (1c)
Active material	$\frac{\partial c_{So}}{\partial t} = -\vec{\nabla} \cdot \vec{N}_{So}$ (1d)	$0 = -\vec{\nabla} \cdot \vec{j}_{So}$ (1e)
Phase	**Lithium flux**	**Charge flux**
Electrolyte	$\vec{N}_{El} = \frac{\vec{j}_{eff,El}}{F}$ (1f)	$\vec{j}_{eff,El} = -\sigma_{eff} \vec{\nabla} (\varphi)$ (1g)
Carbon additive		$\vec{j}_{eff,CB} = -\kappa_{eff,CB} \vec{\nabla} \Phi_{So}$ (1h)

Active material	$\vec{N}_{So} = -D_{So}\vec{\nabla}c_{So}$ (1i)	$\vec{j}_{So} = -\kappa_{So}\vec{\nabla}\Phi_{So}$ (1j)

The new extended electrolyte model describes a homogenized electrolyte and conductive additive phase that has an ionic, as well as electronic conductivity. In general, we solve the additional charge conservation equation in the carbon additive phase to account for the electronic transport. The ionic conductivity κ_{bulk}^{ion} describes a property of the SE phase, while the electronic conductivity κ_{bulk}^{elec} characterizes the additive. The effective transport parameters in the mixed-phase are given by:

$$\kappa_{eff}^{ion} = \frac{\varepsilon}{\tau^2}\kappa_{bulk}^{ion}, \quad (2) \qquad \kappa_{eff}^{elec} = \frac{\varepsilon}{\tau^2}\kappa_{bulk}^{elec}, \quad (3)$$

where ε denotes the volume fraction and τ^2 the tortuosity of the respective phases within the homogenized SE phase. In our simulations, we assume a homogeneous mixture of the SE with the conductive additive. The morphology of the conductive networks is effectively taken into account by their respective tortuosity which allows the incorporation of the effect of conductive additives without the need for dissolving the additive at the microstructure level.

Reactions at the lithium interface as well as at the NCM-622 interface are parametrized via a Butler-Volmer type kinetic expressions.[9] The corresponding parameters for the interface reactions are given in the Supplementary Table 3. Through the finite porosity of the carbon additive phase ε a passivation of the active material surface is introduced, leading to a reduced interface reaction area.

S13. Model parametrization BEST

Supplementary Table 3 summarizes the parameters used for the battery cell simulation in BEST. The estimation of the transport kinetics for NCM-622 and LPS is based on the deconvolution of corresponding electrochemical impedance measurements of symmetric and full cells. A detailed discussion can be found in literature.[7] The general material parameters such as diffusion coefficients and conductivity were either measured or taken from literature. The state-of-charge-dependent transport correlations for NCM-622 are based on literature values extracted from Galvanostatic Intermittent Titration Technique measurements on half-cells with liquid electrolyte. A summary of all correlations is given in the work of Neumann *et al.*[7]. In this study, we additionally introduced conductive carbons with an assumed bulk conductivity of 83 $S \cdot cm^{-1}$.

Supplementary Table 3: Simulation Parameters in BEST. Values are measured by the authors (superscript [°]) or calculated (superscript [*]). The chemical diffusion coefficient of lithium and the electronic conductivity of NCM-622 are functional parameters dependent on the SOC of the material. Their values are given for the initial concentrations. All other parameters are constant during the simulations. If not indicated the references for the used parameters are given in Neumann et al[7].

Parameter, Unit	Description	Value
Electrolyte		
$c_{Li}^{elyte,0}$, mol·cm^{-3}	concentration of Li ions in LPS *	0.0103
κ_{Li}^{elyte}, S·cm^{-1}	Li-ion conductivity °	$1.20 \cdot 10^{-4}$
t_{Li}^{+}	transference number of Li ions	1
D_{Li}^{elyte}, cm^2·s^{-1}	Li-ion self-diffusion coefficient	$2.4 \cdot 10^{-9}$
f_{Li}^{elyte}	thermodynamic correction factor*	1.28
LPS, µm	electrolyte (separator) thickness °	425
Conductive carbons		
κ^{elyte}, S·cm^{-1}	electronic conductivity[10]	83
NCM-622		
$c_{Li}^{NCM,0}$, mol·cm^{-3}	initial Li concentration *	0.021
κ^{elyte}, S·cm^{-1}	electronic conductivity	Eq. S4.1
D_{Li}^{NCM}, cm^2·s^{-1}	Li-ion chemical diffusion coefficient	Eq. S4.2
U_0^{NCM}, V	open circuit potential	Eq. S4.3
α^{NCM}	symmetry factor	0.5
$c_{Li}^{NCM,max}$, mol·cm^{-3}	maximum Li concentration *	0.0519
i_{00}^{NCM}, A·cm^{-2}·mol$^{-1.5}$	exchange current density factor *	$4.98 \cdot 10^{-4}$
C_{DL}^{NCM}, F·cm^{-2}	double layer capacity *	$8 \cdot 10^{-7}$
L_{NCM}, µm	composite cathode thickness *	40
Li metal		
κ^{anode}, S·cm^{-1}	electronic conductivity *	$10 \cdot 10^{2}$
U_0^{Li}, V	open circuit potential	0
α^{NCM}	symmetry factor	0.5
i_{00}^{NCM}, A·cm^{-2}	exchange current density factor *	$8.87 \cdot 10^{-4}$

$C_{\mathrm{DL}}^{\mathrm{Li}}$, F·cm^{-2}	double layer capacity *	$2 \cdot 10^{-7}$

S14. Effective conductivity calculation with GeoDict

Effective conductivity tensors ($\overline{\overline{\kappa}}$) of electronic and ionic networks of the virtual electrodes and homogenized SE phase are calculated in Geodict[11] using microstructure-resolved input data.

$$\overline{\overline{\kappa}} = \begin{bmatrix} \kappa_{xx} & \kappa_{xy} & \kappa_{xz} \\ \kappa_{yx} & \kappa_{yy} & \kappa_{yz} \\ \kappa_{zx} & \kappa_{zy} & \kappa_{zz} \end{bmatrix} \quad (5)$$

The main diagonal elements define the effective conductivity in the main propagation axis (x-, y- and z-direction). For the effective conductivity κ_{eff} estimation, we use the mean value of the diagonal elements. By calculating the porosity ε based on the introduced solid volume fraction (SVF) of the conductive additive and using a common notation for the description of effective transport parameters

$$\kappa_{\mathrm{eff}} = \frac{\varepsilon}{\tau^2}\kappa, \quad (6)$$

we can evaluate the tortuosity τ^2 for each phase. Thereby, the conductivity value κ represents the ionic ($\kappa_{\mathrm{bulk}}^{\mathrm{ion}}$) or electronic ($\kappa_{\mathrm{bulk}}^{\mathrm{elec}}$) bulk conductivity of the bulk SE and conductive additive, respectively.

S15. Analysis of virtual reference electrode

The presented electrode generation algorithm randomly distributes the NCM-622 particles in the electrode volume of 40x150x150 µm^3 up to the desired 45 % SVF. The SVF is calculated based on material densities of NCM-622 and LPS, as well as the experimentally set mass ratio for the composite cathode of 70:30. The secondary NCM-622 particles are approximated by ideal spheres. The particle size is assumed to follow a gaussian distribution with particle diameter $d = 10 \pm 3$ µm. The standard deviation accounts for particle size reduction trough the initial manufacturing process as well as during the mixing and further pressing of the cell for the electrochemical characterization. Supplementary Figure 10 shows an exemplary electrode microstructure. The virtual sample contains isolated particles shown in blue color, which are not electronically connected to the rest of the electrode depicted in red color.

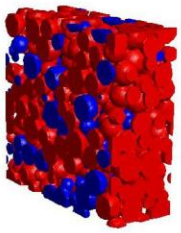

Supplementary Figure 10: Virtual electrode generated in GeoDict for the structure analysis and the electrochemical simulation in BEST. Electronically connected particles are depicted in red colour and isolated AM particles are given in blue colour.

We use a random seed for the structure generation which leads to statistical deviations between each generated structure. In order to quantify the potential statistical deviation, we created five structures with the same composition. The generated electrodes were structurally analyzed regarding their particle connectivity and effective conductivity, as well as their electrochemical performance, i.e. discharge capacity. The results are given in Supplementary Table 4.

Supplementary Table 4: Estimated isolated particle SVF, effective electronic conductivity, and simulated discharge capacity for five equally generated electrodes in GeoDict. The calculated mean value for each column is highlighted in yellow colour. The virtual electrode marked with [*] was selected as a representative for the electrochemical simulation in BEST.

Virtual Electrode No.	Isolated SVF / %	Effective conductivity κ_{eff}^{elec} / S·cm^{-1}	Discharge capacity / mAh·g^{-1}
1	9.0	0.026	100
2*	5.0	0.031	116
3	4.9	0.040	121
4	6.2	0.023	112
5	3.6	0.029	120
Mean value	5.74	0.029	113.8

The calculated average isolated SVF is 5.74 % and the mean discharge capacity is 113.8 mAh/g. Although we use the same generation method, we monitor significant fluctuations of isolated material for the five electrodes. Moreover, we observe a change in the effective electronic conductivity of up to 50% between the electrode with the highest isolated SVF compared to the one with the lowest isolated SVF. The relative change in effective conductivity is not proportional to the change in discharge capacity. Even though the effective electronic conductivity provides a first approximation for the electrode

transport properties, several structural aspects are neglected which are captured by the discharge simulation performed on the virtual electrode. These structural aspects are e.g. the inhomogeneous particle clustering of the AM, the distribution of the isolated AM particles, and the electrode morphology close to the current collector. All these influences together lead to the observed non-linear deviation between the calculated effective electronic conductivity and the performed microstructure resolved simulation. For a more rigorous study on this structural and interfacial effects, we refer to Neumann *et al.*[7].

Nevertheless, the introduction of carbon additives improves the effective electronic conductivity of the composite cathode and therefore increases the battery performance. Based on the calculated average isolated SVF and the mean effective electronic conductivity value, we selected the virtual structure No. 2 (indicated by [*]) for the electrochemical data presented in the manuscript.

S16. Effective electronic conductivity calculation cathodes with conductive additive

For the effective conductivity calculation, we select three electrodes from Supplementary Table 4 in order to create high-resolution cutouts of each electrode. Thereby, the selected electrodes represent the upper and the lower boundary for the isolated SVF deviation as well as the mean value. We chose a cubic volume (40x40x40 μm^3) in the center of each sample and generate a high-resolution cutout (1280x1280x1280 voxel) with a voxel resolution of 31.25 nm. By selecting the center part of the electrode, we reduce the influence of possible generation artifacts occurring atSVF the electrode boundaries.

In the next step, the conductive additive is randomly distributed in the remaining pore space up to the desired SVF based on the carbon additive mass content. In Supplementary Figure 11 the described workflow for the structural analysis is schematically shown.

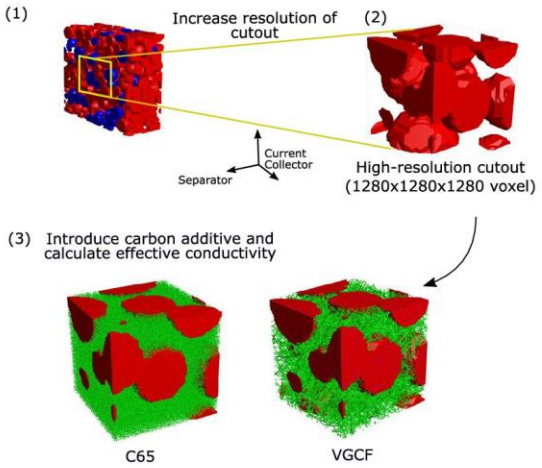

Supplementary Figure 11: Stepwise workflow for the structure analysis of the carbon additive. (1) cathode structure generation. (2) Selection of symmetric cutout and creation of high-resolution cutout. (3) Introduction of carbon additive and calculation of effective conductivity. We use only the introduced additive phase for the calculation of the effective electronic conductivity κ_{eff}^{elec}.

For the granular additive Super C65, we select a convex polyhedron as a representative particle shape with 93.75 nm diameter. The VGCFs are introduced with a diameter of 100 nm and a length distribution of 25 $\pm$ 5 µm to approximate the product specifications given by the manufacturer. We do not account for fiber bending or specific surface clustering of the carbon additives, but we allow for additive overlap and direct contact to the AM.

For each high-resolution cutout, we vary the mass content of the additives from 0.5 - 6 wt-% and calculate the effective conductivity matrix. We estimate the effective conductivity based on the mean value of the diagonal elements as described in the section above.

We summarize the relevant parameters for VGCF in Supplementary Table 5 and Super C65 in Supplementary Table 6. Electrochemical simulations in the manuscript use the corresponding values with 3 wt-% conductive additive content which is marked with [*].

Supplementary Table 5: Calculated parameters for VGCF with a mass density $\rho_{VGCF} = 1.9\ g \cdot ml^{-1}$: effective electronic conductivity κ_{eff}^{elec}, carbon additive SVF, tortuosity τ^2 and porosity ε in the solid electrolyte.

Mass content / mg	VGCF SVF / %	Effective conductivity $\kappa_{\text{eff}}^{\text{elec}}$ / S·cm^{-1}	Porosity in solid electrolyte ε	Tortuosity τ^2
0.5	0.9	0.00033	0.016	25.8
0.75	1.3	0.0011	0.023	12.0
1	1.7	0.0016	0.031	10.5
2	3.3	0.0047	0.061	7.0
3*	4.9	0.0081	0.089	6.0
4	6.4	0.012	0.12	5.5
5	7.9	0.016	0.15	4.8
6	9.3	0.022	0.17	4.4

Supplementary Table 6: Calculated parameters for C65 with a mass density $\rho_{C65} = 1.6\ g \cdot ml^{-1}$: effective electronic conductivity κ_{eff}^{elec}, carbon additive SVF, tortuosity τ^2 and porosity ε in the solid electrolyte. We excluded the 0.5, 0.75, and 6 wt-% since the calculations yield no meaningful results regarding the effective conductivity.

Mass content / mg	C65 SVF / %	Effective conductivity $\kappa_{\text{eff}}^{\text{elec}}$ / S·cm^{-1}	Porosity in solid electrolyte ε	Tortuosity τ^2
1	1.7	0	0.036	∞
2	3.3	0	0.072	∞
3*	4.9	0	0.11	∞
4	6.4	0	0.14	∞
5	7.9	0	0.17	∞

References:

(1) Liu, Z.; Fu, W.; Payzant, E. A.; Yu, X.; Wu, Z.; Dudney, N. J.; Kiggans, J.; Hong, K.; Rondinone, A. J.; Liang, C. Anomalous High Ionic Conductivity of Nanoporous β-Li 3PS4. *J. Am. Chem. Soc.* **2013**, *135* (3), 975–978. https://doi.org/10.1021/ja3110895.

(2) Zhu, Y.; He, X.; Mo, Y. Origin of Outstanding Stability in the Lithium Solid Electrolyte Materials: Insights from Thermodynamic Analyses Based on First-Principles Calculations. *ACS Appl. Mater. Interfaces* **2015**, *7* (42), 23685–23693. https://doi.org/10.1021/acsami.5b07517.

(3) Santhosha, A. L.; Medenbach, L.; Buchheim, J. R.; Adelhelm, P. The Indium–Lithium Electrode in

Solid-State Lithium-Ion Batteries: Phase Formation, Redox Potentials, and Interface Stability. *Batter. Supercaps* **2019**, *2* (6), 524–529. https://doi.org/10.1002/batt.201800149.

(4) Schwietert, T. K.; Arszelewska, V. A.; Wang, C.; Yu, C.; Vasileiadis, A.; de Klerk, N. J. J.; Hageman, J.; Hupfer, T.; Kerkamm, I.; Xu, Y.; van der Maas, E.; Kelder, E. M.; Ganapathy, S.; Wagemaker, M. Clarifying the Relationship between Redox Activity and Electrochemical Stability in Solid Electrolytes. *Nat. Mater.* **2020**, *19* (4), 428–435. https://doi.org/10.1038/s41563-019-0576-0.

(5) Latz, A.; Zausch, J. Multiscale Modeling of Lithium Ion Batteries: Thermal Aspects. *Beilstein J. Nanotechnol.* **2015**, *6* (1), 987–1007. https://doi.org/10.3762/bjnano.6.102.

(6) Finsterbusch, M.; Danner, T.; Tsai, C. L.; Uhlenbruck, S.; Latz, A.; Guillon, O. High Capacity Garnet-Based All-Solid-State Lithium Batteries: Fabrication and 3D-Microstructure Resolved Modeling. *ACS Appl. Mater. Interfaces* **2018**, *10* (26), 22329–22339. https://doi.org/10.1021/acsami.8b06705.

(7) Neumann, A.; Randau, S.; Becker-Steinberger, K.; Danner, T.; Hein, S.; Ning, Z.; Marrow, J.; Richter, F. H.; Janek, J.; Latz, A. Analysis of Interfacial Effects in All-Solid-State Batteries with Thiophosphate Solid Electrolytes. *ACS Appl. Mater. Interfaces* **2020**, *12* (8), 9277–9291. https://doi.org/10.1021/acsami.9b21404.

(8) Hein, S.; Danner, T.; Westhoff, D.; Prifling, B.; Scurtu, R.; Kremer, L.; Hoffmann, A.; Hilger, A.; Osenberg, M.; Manke, I.; Wohlfahrt-Mehrens, M.; Schmidt, V.; Latz, A. Influence of Conductive Additives and Binder on the Impedance of Lithium-Ion Battery Electrodes: Effect of Morphology. *J. Electrochem. Soc.* **2020**, *167* (1), 013546. https://doi.org/10.1149/1945-7111/ab6b1d.

(9) Latz, A.; Zausch, J. Thermodynamic Derivation of a Butler-Volmer Model for Intercalation in Li-Ion Batteries. *Electrochim. Acta* **2013**, *110*, 358–362. https://doi.org/10.1016/j.electacta.2013.06.043.

(10) VGCF™-H | Products | SHOWA DENKO K.K. https://www.sdk.co.jp/english/products/126/132/2094.html (accessed Nov 16, 2020).

(11) GeoDict Startseite https://www.math2market.com/?Language=de (accessed Nov 16, 2020).

6.3 List of Publications

2021 S. Randau, F. Walther, A. Neumann, Y. Schneider, R. S. Negi, B. Mogwitz, J. Sann, K. Becker-Steinberger, T. Danner, S. Hein, A. Latz, F. H. Richter, J. Janek, On the Additive Microstructure in Composite Cathodes and Alumina-Coated Carbon Microwires for Improved All-Solid-State Batteries, *Chem. Mater.*, **2021**, XXXX, XXX, XXX−XXX

2020 A. L. Santhosha, N. Nazer, R. Koerver, S. Randau, F. H. Richter, D. A. Weber, J. Kulisch, T. Adermann, J. Janek and P. Adelhelm, Macroscopic Displacement Reaction of Copper Sulfide in Lithium Solid-State Batteries, Adv. Energy Mater, 2020, 10, 2002394

F. Walther, S. Randau, Y. Schneider, J. Sann, M. Rohnke, F. H. Richter, W. G. Zeier, and J. Janek, Influence of Carbon Additives on the Decomposition Pathways in Cathodes of Lithium Thiophosphate-Based All-Solid-State Batteries, *Chem. Mater.*, **2020**, 32 (14), 6123-6136

S. Randau, D. A. Weber, D. A.; Kötz, O.; Koerver, R.; Braun, P.; Weber, A.; Ivers-Tiffée, E.; Adermann, T.; Kulisch, J.; Zeier, W. G.; Richter, F. H.; Janek, J., Benchmarking the Performance of All-Solid-State Lithium Batteries, *Nat. Energy*, **2020**, *5* (3), 259–270.

A. Neumann, S. Randau, K. Becker-Steinberger, T. Danner, S. Hein, Z. Ning, J. Marrow, F. H. Richter, J. Janek, A. Latz, Analysis of Interfacial Effects in All-Solid-State Batteries with Thiophosphate Solid Electrolytes, *ACS Appl. Mater. Interfaces*, **2020**, 12 (8), 9277-9291.

2019 H. Stöffler, T. Zinkevich, M. Yavuz, A. Hansen, M. Knapp, J. Bednarčík, S. Randau, F. H. Richter, J. Janek, H. Ehrenberg, and S. Indris, Amorphous versus Crystalline Li3PS4: Local Structural Changes during Synthesis and Li Ion Mobility, *J. Phys. Chem. C*, **2019**, 123 (16) 10280–10290.

2018 H. Stöffler, T. Zinkevich, M. Yavuz, A. Senyshyn, J. Kulisch, P. Hartmann, T. Adermann, S. Randau, F. H. Richter, J. Janek, S. Indris, and H. Ehrenberg, Li^+-Ion Dynamics in β-Li_3PS_4 Observed by NMR: Local Hopping and Long-Range Transport, *The Journal of Physical Chemistry C*, **2018**, 122 (28), 15954-15965.

6.4 List of Conference Contributions

2019 *22nd International Conference on Solid State Ionics*, June 2019, PyeongChang, South Korea, poster presentation: Methods for optimizing all solid battery performance based on the evaluation of a minimal cell system

2018 *Third Bunsen Colloquium on Solid-State Batteries*, November 2018, Frankfurt/Main, Germany, poster presentation: All-Solid-State Battery using NCM-622 and a Lithium Metal Anode for reference performance and literature overview with Ragone plot

19th International Meeting on Lithium Batteries, June 2018, Kyoto, Japan poster presentation: All-Solid-State Battery using NCM-622 and a Lithium Metal Anode